L-Band Radiometry for Sea-Ice Applications

Georg Heygster[1],
Stefan Hendricks[2], Lars Kaleschke[3], Nina Maass[3], Peter Mills[1],
Detlef Stammer[3], Rasmus T. Tonboe[4], and Christian Haas[5]

[1)] Institute of Environmental Physics, University of Bremen, Germany
[2)] Alfred-Wegener-Institute for Polar and Marine Research, Bremerhaven, Germany
[3)] Institute of Oceanography, University of Hamburg, Germany
[4)] Danish Meteorological Institute, Copenhagen, Denmark
[5)] University of Alberta, Edmonton, Canada

Final Report for ESA ESTEC Contract 21130/08/NL/EL

Institute of Environmental Physics, University of Bremen
November 2009

Universität Bremen Universität Hamburg AWI DMI

ESA STUDY CONTRACT REPORT - SPECIMEN

No ESA Study Contract Report will be accepted unless this sheet is inserted at the beginning of each volume of the Report.

ESA Contract No:	SUBJECT:	CONTRACTOR:
21130/08/NL/EL	L-Band Radiometry for Sea-Ice Applications	University of Bremen, Institute of Environmental Physics
* ESA CR( )No:	No. of Volumes:1 This is Volume No:1	CONTRACTOR'S REFERENCE: GH-ESA 2007/1

ABSTRACT:

See pages 1-2

The work described in this report was done under ESA Contract. Responsibility for the contents resides in the author or organisation that prepared it.

Names of authors:

Georg Heygster, Stefan Hendricks, Lars Kaleschke, Nina Maass, Peter Mills, Detlef Stammer, Rasmus Tonboe and Christian Haas

** NAME OF ESA STUDY MANAGER:	** ESA BUDGET HEADING:
DIV:	
DIRECTORATE:	

* Sections to be completed by ESA

** Information to be provided by ESA Study Manager

Contents

0.1 List of symbols

Symbol	description	first presented
R_v	reflection coeff. for vertical polarisation	(2.2)
R_h	reflection coeff. for horizontal polarisation	(2.2)
n	refractive index	2.2
θ	direction of travel of E-M radiation	(2.2)
T_v	vertically polarised brightness temperature	(2.4)
T_h	horizontally polarised brightness temperature	(2.4)
C	ice concentration	(2.4)
P	polarisation or polarisation ratio	(2.5)
GR	gradient ratio	(2.7)
ν	frequency	(2.7)
h	ice thickness	(2.10)
γ	scattering phase function	(2.12)
e	emissivity, ratio of brightness temperature to physical temperature	(4.3)
T	physical temperature	(4.1)
T_{water}	water temperature	(4.1)
T_{ice}	ice temperature	(4.1)
ϵ	complex permittivity ($= \epsilon' + \mathrm{i}\epsilon''$)	(4.3)
ϵ'	real part of complex permittivity	Section 6.2.1
ϵ''	imaginary part of complex permittivity	Section 6.2.1
σ	conductivity	(4.4)
ω	angular frequency ($= 2\pi\nu$)	(4.4)
R	reflection coefficient	Section (4.2.1)
c_0	speed of light in a vacuum	(4.9)
α	attenuation coefficient	(4.11)
β	phase coefficient	(4.10)
A	transmission coefficient ($= \tau^2$)	(4.12)
R_{ia}	reflection coefficient between ice and air	(4.12)
R_{wi}	reflection coefficient between water and ice	(4.12)
V_b	fractional brine volume	(4.20)
S	salinity	(4.21)
S_b	brine salinity	(4.21)
E	electric field	(6.1)
τ	transmission coefficient	(6.8)
Δz	layer thickness	(6.8)
$T\uparrow$	upwelling brightness temperature	(6.10)
$T\downarrow$	downwelling brightness temperature	(6.10)
T_b	brightness temperature	(6.22
I	radiance intensity	(6.15)
Q	polarisation difference	(6.15
U	polarisation difference at 45 degree rotation	(6.15)
V	circular polarisation	(6.15)

E_v	electric field along vertical polarisation axis	(6.15)
E_h	electric field along horisontal polarisation axis	(6.15)
s	path	(6.21)
$\hat{\mathbf{v}}$	viewing angle vector	(8.2)
$\hat{\mathbf{n}}$	surface normal	(8.3)
α	angle between surface- and instrument-defined polarisation axes	(8.5)
P	aircraft pitch	Section 9.2.2
ζ	angle of instrument relative to aircraft	Section 9.2.2
z	altitude	Section 9.2.2
R	aircraft roll	Section 9.2.2
ψ	longitude	Section 9.2.2
ϕ	latitude	Section 9.2.2
r_E	radius of the Earth	Section 9.2.2
X	distance parallel to flight track	Section 9.2.2
Y	distance perpendicular to flight track	Section 9.2.2
δ	angle from instrument boresight	Section 9.2.3
w	antenna pattern weighting coefficient	Section 9.2.3
δ'	see Figure 9.1	Section 9.2.3
δ_r	normal deviate of zero mean and unit variance	Section 9.2.3
t	line parameter in combined thickness-concentration retrieval	(10.1)

Abstract

The potential of the spaceborne, polar orbiting L-band radiometer SMOS (Soil Moisture and Ocean Salinity, scheduled for launch 2009) to retrieve sea ice parameters has been explored with emissivity models and by analyzing ice thickness and L-band emission taken during a field campaign in March 2007 in the Baltic. In spite of some imperfections of the observations (little temperature variations, sensor spikes), a variety of conclusion can be drawn if analyzed together with L-band emissivity models. The salinity much lower in the Northern part of the Baltic than in the global ocean influences the sea ice properties and emission. In order to draw conclusions from the campaign results about the SMOS retrievals over Arctic sea ice, they must be transferred from Baltic to Arctic conditions using emissivity models. Several model types have been used. All of them need the dielectric permittivity to calculate the emission. The first model type determines the permittivity from basic physical principles, like the Microwave Emission Model for Layered Snowpacks (MEMLS) and the Combined Strong Fluctuation Theory (CSFT) and may be used at the full microwave range. As at L-band volume scattering can be neglected, frequency-specific models are easier to establish. A simple three layer models (air, ice, water) is able to reproduce the observed brightness temperatures with a standard deviations around 7 K. It uses the different channels separately, allowing for one separate retrieval based on each of the the vertically (TBv) and horizontally (TBh) polarized brightness temperatures.

The second model type starts from the fact that the salinity and thus the permittivity of thin Arctic sea ice vary with thickness. Real and imaginary part of the permittivity are retrieved based on TBv and TBh together, and then the brightness temperatures are determined from the permittivity. Two versions of this model type have been used. In the first version, both real and imaginary part of the permittivity as function of sea ice thickness, are determined by empirical fits to the campaign data. In the second model, only the imaginary part is fit to the campaign values, and the real part is then determined using the Mixture Model, the empirical equations of Vant (1978b) and Hoekstra and Capallino (1971), allowing us to adjust for the higher salinity of the global ocean. At temperatures near melting, the influence of ice concentration and ice thickness may be distinguished, but at the same time retrieval of ice thickness becomes more uncertain because of the strongly increasing imaginary part of the permittivity. At low temperatures, the results suggest a sensitivity of the brightness temperatures to thicknesses up to 50 cm.

Output of a thermodynamic sea ice model, driven with ECMWF ERA 40 atmospheric data, served as input data for MEMLS. The sea ice model data at 85°N, 180°East over one complete winter season were used to simulate the L-band emission. Using these sea ice model data as input, most of the models showed for first-year ice consistently a sensitivity of the emitted L-band radiation to thickness up to about 0.5 m. The only exceptions are the mixture model

where already at about 0.2 m saturation is reached, and the CSFT, where the sensitivity reaches up to over 1 m. The sensitivity limit of about 0.5 m is also found for the campaign data when using the three layer model with constant permittivity. In real cases, we have to expect a lower limit for the detection ice thickness because (1) of the influences not accounted for in the models. These will lead to additional noise in the brightness temperatures, propagating into the retrieved geophysical parameters. (2) we have to expect that the ice conditions vary within the large footprint of about 50 km of the SMOS sensor. On the other hand, each surface region will be observed several times under different incidence angles during each overpass. This redundancy may be used to determine additional quantities if their variation with incidence angle is strong enough. Otherwise the multiple observations will serve to reduce the uncertainty in the retrieval by averaging. A consequence of the varying incidence angle is that the retrieval algorithms have to be developed for all of them.

For emission modeling, the sea ice permittivity is the most important quantity. Using the thermodynamic sea ice model data in conjunction with MEMLS, the real part varies between 4.5 and 5.5, and the imaginary part between 0.1 and 0.5 . For both the CSFT and the mixture model, the corresponding values are 3.5 to 7 and 0.002 to 1, a much larger range. The values determined from the campaign data range from 2 to 8 for the real part and from 0.03 to 0.1 for the the imaginary part. Thus, the values for the Arctic and the Baltic are rather similar, probably due to the high temperatures during the Baltic campaign. The campaign data show that the contrast between open water is high enough to discriminate both surface types and to determine the sea ice concentration.

Two studies have been devoted to the higher Stokes components. First, the influence of a deviation of the sensor attitude from horizontal orientation on the crosstalk from the first two Stokes components to the third one, U, has been quantified. Applying the resulting correction reduces the observed signal. Second, a model of horizontally anisotrope permittivities has shown that it can generate nonzero U and V Stokes components.

An investigation for a region with stable temperature and salinity values in high latitudes has been conducted where the surface temperature of the ocean could be used as an external calibration source for SMOS L-band radiances without adding any extra in situ observations. It has turned out that there is no location in the GIN Sea where SST is stable, and regions with low variability do not agree with regions of low SSS variability in a model simulation. External calibration.

It is concluded that SMOS has some potential to estimate thickness of thin ice and thus the lower boundary of ice volume. The sensitivity for Arctic ice thickness retrieval of up to half a meter is complementary to the capabilities of altimeter instruments like Cryosat. As thin ice plays an important role for heat exchange between the ocean and the atmosphere, a SMOS based ice thickness product will be certainly useful for sea ice applications in climate research, meteorology, and perhaps even for operational services for the assistance of ship navigation in polar waters.

Chapter 1

Introduction

Sea ice plays a significant role in the global climate. Monitoring both its extent and exchange processes is the challenge facing us in an uncertain twenty-first century. Passive microwave sensors are an excellent tool for this task. Amongst their advantages are frequent, global coverage in most or all weather conditions, and a lengthy record. The main disadvantage is a relatively poor horizontal resolution.

Plans are currently in the works to launch a new microwave radiometer called Soil Moisture and Ocean Salinity (SMOS). As its name implies, the chief focus of this instrument will be the pedosphere and the ocean surface. The angular field of view (FOV) of an antenna is directly proportional to the frequency and inversely proportional to the effective aperture area. By using a broad array of antennas that fold out upon deployment, SMOS will nonetheless have a horizontal resolution comparable to other microwave radiometers despite operating at a much lower frequency. SMOS is unique in measuring in the L-band range at 1.4 GHz, the first continuously operating passive instrument to do so. It will also be capable of detecting all four Stokes components.

Although explicitly being devoted to observation of soil moisture and ocean salinity, SMOS will also render information, when, during its polar orbit, it is pointing at the cryosphere instead.

In order to gain insight in the potential of extracting geophysical information about the cryosphere from the SMOS signals even before launch, ESA has initiated the present study. The original work plan consisted of the packages

WP 1: Literature Study

WP 2: Sea Ice Emissivity Models

WP 3: Sea Ice Processor

WP 4: External Target Calibration

While it was initially planned to organize the final report in the same way, it has turned out during the study to treat some fields in a more detailed way in dedicated special studies. The form separate chapters in this report. As a result, the chapter numbering differs from the work package numbering. In order to easily identify the work package number of the chapters, this is also given in the chapter names.

The single chapters are intended to be self-contained. Therefore, some overlap could not be avoided. In order to facilitate orientation within in the report, in the following an overview of the different chapters is given.

After the literature overview including the first-ever sea ice observation in L-band from space in Chapter 2, Chapter 3 describes the field campaign in the Baltic Bay of Bothnia where sea ice thickness and its L-band emissivity have been observed in coordinated flights of the EM-Bird of AWI, carried by a helicopter, and of the EMIRAD radiometer of the Technical University of Denmark, carried by the Sky Van airplane of the Helsinki University of Technology. While Chapter 3 describes the overall conditions of the campaign and the EM-Bird data, the radiometric data and the data preprocessing for Chapter 4 are described in Section 4.3 where they are needed.

Chapter 4 combines the sea ice thickness observations with the radiometric observations of the campaign (WP 2.1) and investigates the sensitivity of the SMOS signal to variations of thickness and ice concentration based on the Menashi three-layer slab forward model (WP2.5), which is presented including the basic physical and empirical relations. Also an attempt to retrieve the sea ice thickness data based on just on L-band intensities is given.

A more sophisticated method for obtaining the microphysical input data for the emissivity model is to use the output of thermodynamic sea ice models, as presented in Chapter 5, together with a sea ice adapted version of the Multi-layer Emissivity Model for Layered Snowpacks (MEMLS). Another layered model, the Strong Fluctuation Theory (SFT) in a version combined with incoherent radiative transfer (CSFT) is presented in Chapter 6 and applied to sets of microphysical parameters describing typical nilas, first-year, and multiyear ice conditions. Two more models are used in Section 6.3, a ridged Monte Carlo Model which takes into account the surface roughness of the sea ice and snow surfaces as observed during the campaign with the EM-Bird and combined laser altimeter (Chapter 3), and a closed solution of the three-layer model.

A word may be appropriate at this place about the general taxonomy of the models which is quite complicated because each model comprises two or more modules that can be re-combined in different ways. Because none of the models used in this study account for surface scattering and because volume scattering at L-band is weak, all the models reduce to a radiative transfer model (RT) with specular reflection at discontinuous boundaries, i.e. between the different interfaces (air-ice, snow-ice, ice-water, etc.) and between distinct ice layers. All models used in this study employ a plane-parallel geometry with the exception of two attempts to model large-scale surface roughness: one using an ensemble of plane-parallel models (Section 6.7) and the other using the Monte Carlo ray-tracing algorithm (Section 6.3.1).

Emissivity modelling can thus be divided into two steps: calculation of effective permittivities and the RT calculation over a vertical profile to determine final brightness temperature. For higher frequencies, volume scattering must also be determined and similarly vertically integrated. The examples of such ice emissivity models are the Microwave Emission of Layered Snow Packs (MEMLS) model, which includes all the required components in a single, easy-to-use MatLab program, and the Combined Strong Fluctuation Theory (CSFT) which calculates scattering and effective permittivities using Strong Fluctuation Theory and vertically integrates the permittivities using a simple RT model. The RT model has the advantage over a multi-layer SFT in that it produces a non-coherent solution, thus avoiding pronounced oscillations of emissivity with frequency or thickness. Since the RT model is programmed separately, it can take as input effective permittivities computed in a variety of ways, such as empirical models based

on actual measurements or mixture formulae based on the low-frequency limit. As these two models, MEMLS and the CSFT, include the volume scattering which no more be ignored at higher frequencies, they are also suitable for microwave emissivity modeling at higher frequencies, i.e. for other microwave sensors like AMSR-E and SSM/I, see Section 6.4 for some CSFT-based examples.

At its simplest, the RT model need only integrate a single ice layer, with uniform properties throughout, producing the three-layer (air, ice and water) dielectric slab model. In the Menashi model (Section 4.2.1, the derivation has been refined so as to produce a semi-coherent solution in which the thickness variations serve to cancel out coherency effects and the emissivity converges to the open water case as ice thickness approaches zero.

Chapters 7 and 8 are both devoted to the higher Stokes components which SMOS will be measuring in the Full-Pol mode. While Chapter 7 models the third and fourth Stokes components based on an azimuthally anisotropic permittivity, Chapter 7 analyzes the crosstalk from the first two components to the third one caused by a deviation of the sensor's attitude from the horizontal alignment. This cannot be avoided in the case of airborne sensors. For spaceborne sensors, this will not occur. But the equivalent case of a tilted surface is realistic even at scales of SMOS' footprint, e.g. over the Tibetan plateau or the ice sheets.

The salinity dependence of the SMOS signal is investigated in Chapter 9. As data of the POL-ICE campaign are used again, the calibration and functioning of the EMIRAD radiometer is described here independently of Chapter 4. Salinity profiles taken during a Polarstern campaign serve as examples of salinities of the global ocean. Methods to determine the permittivity of sea ice at L band from observations compared to bounds from model investigations, and the well-known relation between Arctic sea ice thickness and salinity is transferred to Baltic conditions.

Chapter 10 proposes a retrieval algorithm based on the vertically and horizontally polarized brightness temperatures, and describes incidence angle dependence, limits in sea ice thickness and concentration, and investigates some basic limitations in the retrieval of combinations of parameters.

The possibilities of an external calibration of the SMOS sensor using ocean regions of constant and low brightness temperatures are investigated in Chapter 11 by statistical analysis of the variability of sea surface temperature and salinity based on WOA climatologies, AMSR-E data and ocean circulation models. Finally, and Chapter 12 reviews the findings of the project and outlines the resulting recommendations for future research.

Chapter 2

WP1: Literature Review

Peter Mills and Georg Heygster

Institute for Environmental Physics, University of Bremen, Otto-Hahn-Allee 1, 28359 Bremen, Germany

2.1 Introduction

The purpose of this document is to present a broad overview of recent work on sea ice remote sensing, relating it back to detection in the L-band and, it is hoped, to point the way ahead with regards to the cryospheric component of the SMOS project. Existing ice detection algorithms will be presented, in particular those that use the two most common instruments for the task: Special Sensor Microwave Imager (SSM/I) and Advanced Microwave Scanning Radiometer on EOS (AMSR-E). Both are conical scanning radiometers with a fixed incidence angle of roughly 55 degrees. The SSM/I instrument has seven channels with central frequencies of about 19, 22, 37 and 85 GHz. Horizontal and vertical polarizations are distinguished at all frequencies but 22 GHz. The AMSR-E instrument shifts these frequencies somewhat and adds two new ones: 6.9, 10.65, 18.7, 23.8, 36.5 and 89.0 GHz. By using a larger reflector dish and sampling at a higher rate, it also gains a higher resolution. Thus algorithms originally developed for SSM/I can easily be adapted in improved form for AMSR-E. Both instruments adopt a higher scan rate in the near 90 GHz channels to take advantage the narrower FOV.

Other passive microwave sensors of relevance include SMMR, the SSM/T series, WindSat and the AMSU series. The Scanning Multi-channel Microwave Radiometer (SMMR) was the predecessor to SSM/I that operated between 1978 and 1987 and had five, dual-polarized frequencies: 6.6, 10.7, 18, 22 and 37 GHz, thus the new AMSR-E combines the cababilities of the two. WindSat is another conically scanning radiometer with the same resolution as AMSR-E and operating at most of the same frequencies: 6.8, 10.7, 18.7, 23.8, and 37.0 GHz. Its main advantage is that the 10.7, 18.7 and 37 GHz frequencies are fully polarimetric, but at present it seems to be under-utilized for sea-ice detection.

AMSU-A and SSM/T are both multi-channel, cross-track scanning radiometers sensitive to oxygen and designed primarily for temperature sounding. AMSU-B and SSM/T-2 are simi-

lar cross-track scanning radiometers designed for water vapour detection. In principal, these could be used for sea-ice detection since all have surface-looking channels, although this is hampered by the lack of polarisation data and strong atmospheric sensitivity, while the multiple viewing angles complicate algorithm development. There is no reason, however, that data from one or more of these instruments cannot either supplement or complement the surface-mapping radiometers –for instance by providing information on the current atmospheric state.

2.2 Physical properties of sea ice

2.2.1 Formation processes

Several formation mechanisms of sea ice have been identified. At its earliest stages, sea-ice consists of elongated, randomly oriented crystals. This is called frazil and mixed with water in the unconsolidated state is known as grease ice. If wave and wind conditions are calm, these crystals will consolidate at the surface and by selective pressure, begin to grow preferentially in the downward direction, forming nilas. In more turbulant conditions, the frazil will consolidate by mechanical action to form pancake ice, which has a more random structure (Maykut et al., 1992; Tucker et al., 1992; Fuhrhop et al., 1997). Another common formation mechanism, especially in the Antarctic where precipitation over sea ice is high, is from snow deposition: on thin ice, the snow will weigh down the ice enough to cause flooding. Subsequent freezing will form ice with a much more granular structure (Ehn et al., 2007; Maksym and Markus, 2008; Tang et al., 2007).

One of the more interesting processes to occur within consolidated ice packs is changes in the saline content. As the ice freezes, most of the salt content gets rejected and forms highly saline brine inclusions between the crystals. With decreasing temperatures in the ice sheet, the size of the brine pockets decreases while the salt content goes up. Since ice is less dense than water, increasing pressure causes some of the brine to be ejected from both the top and bottom, producing the characteristic 'C'-shaped profile of first year ice (Eicken, 1992). Brine will also drain through vertical channels, particularly in the melt season. Thus multi-year ice will tend to have both lower salinity and lower density than first-year ice (Vancoppenolle et al., 2007; Fuhrhop et al., 1997; Tucker et al., 1992).

Formation processes will determine the internal structure of sea ice which is important for at least two reasons. First, some knowledge of ice structure beyond simple fractional surface cover ("ice concentration") is necessary to accurately determine important climate variables like heat flux, heat capacity, salt flux and solar albedo. Thickness, brine volume and the presence of surface cover such as snow or melt ponds in particular have an influence on these variables. Second, it is this structure that ultimately determines the radiometric signature of the sea ice. Another reason, less relevant here, is to deduce its mechanical properties, such as tensile strength, for use in dynamic models.

At present, the only reliable method of determining the aggregate properties of sea ice is through field measurements. Some knowledge can be gained through laboratory experiments, but this does not capture the full variability of naturally occurring sea ice. Attempts have been made to model the formation processes, most notably by Cox and Weeks (1988), but this is difficult to do accurately because of the complexity involved.

2.2.2 Emissivity modelling

The primary challenge to determining sea ice emission properties is modelling the effective permittivity based on the configuration of the aggregates. In general, the permittivity will be different than that of the individual constituents and neither homogeneous, varying in particular with depth, nor isotropic, as both the crystal structure and brine inclusion geometry are often strongly directional. Common methods of modelling it are mean field theorems such as strong and weak fluctuation theory that seek an approximate solution to Maxwell's equations in the case of a randomly fluctuating dielectric constant (Fuhrhop et al., 1997; Stogryn, 1986, 1985). Far simpler are mixture models that use a combination of the dielectric constants of the components (Hoekstra and Cappillino, 1971). This may be more appropriate for the case of L-band where volume scattering is weak (Barber et al., 1998). The calculated dielectric constants can then be combined with radiative transfer models to integrate over the vertical variations (Johnsen, 1998; Burke et al., 1979) such as in the Microwave Emission Model of Layered Snowpack (MEMLS) (Wiesmann and Maetzler, 1999).

If it is assumed that the sea-ice is homogeneous, specularly reflecting and much thicker than the penetration depth, then the Fresnel equations provide a simple and useful emissivity model (Hewison and English, 1999; Naoki et al., 2008). These are derived by imposing continuity of the fields of a plane wave in three dimensions along a plane boundary between two media with differing refractive indices. They return reflection coefficients for vertically and horizontally polarised waves:

$$R_v = \left| \frac{n\cos\theta - \cos\theta_t}{n\cos\theta + \cos\theta_t} \right|^2 \tag{2.1}$$

$$R_h = \left| \frac{\cos\theta - n\cos\theta_t}{\cos\theta + n\cos\theta_t} \right|^2, \tag{2.2}$$

where R_v and R_h are the reflection coefficients at vertical and horizontal polarisations, respectively, which are defined in terms of the interface. θ and θ_t are the angle of incidence and angle of transmission, which can be found by Snell's law. It is straightforward to calculate reflection from emission: see equation (2.12).

At the next level of sophistication are models that integrate these or similar equations across two or more layers. At L-band, the penetration depth in ice can be quite large, from between 10 cm and 2 m for saline ice, more for freshwater ice (Tonboe et al., 2006a). Therefore, for thin ice types the ice-water interface must be included at the very least. A "three-layer dielectric slabÂt′Ât′ model, for instance, has been found to give useful results for L-band. As its name implies, it integrates an ocean layer, an ice layer and an air layer, each having uniform dielectric properties (Menashi et al., 1993). Since sea ice is rarely flat, simple specular reflection does not always provide an adequate description. Small scale irregularities will cause diffuse reflection (or scattering) while large scale irregularities mean that over a large footprint, emissions must be averaged over the slope distribution for different incidence angles.

It is apparent that emissivity models for sea ice are not at the same level of maturity as atmospheric radiative transfer models because of the high level of complexity and variability of the system being simulated, the difficulty in accurately measuring and characterising the relevant physical variables. To drive the point home, consider the following quote from a recent paper:

> Significant differences among the brightness temperatures and the extinction coefficients simulated with the four models in the cases of the six classes of snow are observed. Moreover, no particular model is found to be able to systematically reproduce all of the experimental data. The results highlight the need to more closely examine the relationships relating mean grain size and correlation length, introduce multiple layers in each model and to perform controlled laboratory measurements on materials with well-known electromagnetic properties in order to improve the understanding of the causes of the observed differences and to improve model performance (Tedesco et al., 2006).

The paper deals with modelling of layered snowpack, however the basic challenges are the same and many of the same models are used, in this case strong fluctuation theory, MEMLS (Microwave Emission Model of Layered Snowpacks) (Wiesmann and Maetzler, 1999), dense-medium radiative-transfer (Winebrenner et al., 1992) and the Helsinki University of Technology snow emission model.

2.2.3 Emissivity Measurements

Many field studies have been performed to gather microwave emission measurements of sea ice at frequencies other than L-band. While at this point there is a long record of satellite data, the smaller footprint of ground-based and aircraft measurements means that there will be less heterogenity of surface types contributing to the final signature which can then be paired more definitely with a distinct ice type. This section covers only those observations made at frequencies other than L-band: for L-band, see section 2.5.

Several generalisations can be made. First, ice in the process of formation tends to be cooler radiometrically than consolidated pack ice, with brightness temperatures somewhere between that and open water. It will also have a stronger polarisation at off-nadir incidence angles. with anisotropy in the crystal structure as well as water contributing to the polarisation signal (Maetzler, 1982). For lower frequencies where the penetration depth is larger, emissions will still contain some influence from the water signal for the thinnest consolidated new ice types. These effects will tend to be cancelled out by the increase in heat exchange with decreasing thickness, making the surface of new ice warmer. Even for new ice types, the relationships seem quite complex (Maetzler, 1982).

Emissions from multi-year ice tend to be both colder and more variable within a given floe than those of first-year (Eppler et al., 1992). An interesting feature of multi-year ice, which occurs primarily in the Arctic Ocean, is that its microwave brightness temperature increases with latitute, which is not seen in first-year ice (Eppler et al., 1992). Increases in salinity will make the ice more opaque by increasing conductivity and will also increase the strength of the signal, which at least partially explains the cooler signatures of multi-year ice. This may also explain why re-frozen melt ponds tend to be warmer radiometrically.

The presence of snow can considerably alter the microwave signature, with effects increasing with both frequency, and water content (Barber et al., 1998). Grain size will also have an effect and the relationships appear again to be quite complex, although it is less of an issue issue at L-band because snow tends to be relatively transparent and scattering at this frequency is weak. For dry snow, the penetration depth at L-band can be hundreds of metres (Maetzler, 2001).

For a comprehensive review of the subject, please see Eppler et al. (1992), while results from specific field campaigns are contained in Grenfell et al. (1998), Shokr (1998), Hwang et al. (2007), Stogryn (1986), Naoki et al. (2008) and Hewison and English (1999). A major gap in the literature is the lack of campaign data providing detailed ice-core analyses matched with emissivity measurements. This makes it difficult to properly validate emissivity models that attempt to account for the internal snow and ice structure.

2.3 Passive Microwave Remote Sensing of Sea Ice Properties

2.3.1 Ice type and concentration

Most ice concentration algorithms are predicated on the dual obervation that: 1. different surface types have different, strongly clustered, radiometric signatures and 2. the final radiometric signature at the instrument head is a simple linear combination of that of the surface types found in the footprint, with weighting factors taking on the values of the relative concentrations. If we form a vector-space from the measurements in which the signatures of the different surface types are assumed invariant and all but one are linearly independent, then it becomes a straightforward matter to derive the relative ice concentrations.

To illustrate the general principal, suppose we have measurements at a given but unspecified microwave frequency at horizontal (T_h) and vertical (T_v) polarisations. Then:

$$T_v = CT_{vi} + (1 - C)T_{vw} \tag{2.3}$$
$$T_h = CT_{hi} + (1 - C)T_{hw}, \tag{2.4}$$

where the i and w subscripts denote ice and open water, respectively, and C is the relative ice concentration. The polarisation is defined:

$$P = \frac{T_v - T_h}{T_v + T_h}, \tag{2.5}$$

The polarisation of ice and water differ markedly in the microwave range, with that of water being much higher than ice. Here we assume that they are both roughly constant at P_i and P_w for ice and water respectively. In ice covered regions of the ocean, we would expect the surface temperature of the water to be roughly constant, thus the emission temperature should be constant as well. Some arithmetic shows:

$$1 - C = \frac{(P - P_i)(T_v + T_h)}{(P_w - P_i)(T_{vw} + T_{hw})}. \tag{2.6}$$

Most of the current operational ice concentration algorithms use some variation of this technique. The Comiso "Bootstrap" algorithm uses the SSMI/AMSR-E 37 GHz horizontally and vertically polarized channels to detect total ice concentration in the Arctic and the 37 GHz and 18/19 GHz (both vertically polarized) to detect the same in the Antarctic. By contrast, the NASA Team (NT) algorithm uses the polarisation at 19 GHz and the so-called spectral gradient ratio, GR(37V, 19V),

$$GR(\nu_1, \nu_2) = \frac{T_b(\nu_1) - T_b(\nu_2)}{T_b(\nu_1) + T_b(\nu_2)}, \tag{2.7}$$

between the 37 and 19 GHz vertically polarised channels, where $T_b(\nu)$ is the brightness temperature at ν. By using normalised ratios instead of raw brightness temperatures, the designers of this algorithm hope to reduce errors produced by variable surface temperatures (Comiso et al., 1997). In the Arctic, Team is able to discriminate between first and multi-year ice. The ARTIST Sea Ice (ASI) algorithm uses the contrast in polarisation difference between ice and water at near 90 GHz to detect sea ice concentration (Spreen et al., 2008; Svendsen et al., 1987). The smaller footprint and higher sampling rate of this frequency will result in more detailed maps at the expense of greater sensitivity to weather effects. The ASI algorithm takes account of this by assuming only that the weather effects over ice will be different than those over water and determine these empirically, with effects varying smoothly to the third power for fractional concentrations.

Another algorithm to take advantage of the higher resolution of the near 90 GHz channels is the NASA Team II (NT2) algorithm which implicitly takes account of the atmospheric state using the radiometric signature itself: a look-up table of brightness temperatures are simulated for all ice concentrations from 0% to 100% in 1% increments and for twelve different, representative atmospheric states (Cavalieri, 1994; Markus and Cavalieri, 2000).

Of particular interest are attempts to automate the process of categorizing ice types and determining concentration by using neural networks or other forms of advanced, multivariate statistics. Grenfell et al. (1994) and Wensnahan et al. (1993) both use principal component decomposition of measured brightness temperatures to distinquish between different ice types. If the resulting vectors correspond to actual ice types, then it is trivial to solve for their relative concentrations as described above: this is the approach taken by Wensnahan et. al., although, as they point out, the derived types may not correspond to accepted definitions. They test such an algorithm on SSM/I satellite data and find that it is better able to distinguish areas of thin, new ice from open water than the original Team algorithm.

Belchansky et al. (2004) use a neural network algorithm trained with SAR image data to estimate multi-year ice concentration in the Arctic and derive a 26-year time series from SMMR and SSMI data (Belchansky et al., 2005) using three channels: 18/19 GHz, both polarisations and 37 GHz, vertical polarisation.

Comparison studies between the different ice concentration algorithms and against other sources of ice data such as SAR, optical and infrared sensors and in situ measurements often turn up surprisingly large discrepensies (Comiso et al., 1997; Andersen et al., 2007; Comiso and Parkinson, 2008; Heygster et al., 2008). These stem from a variety of sources such as variability in the emissivities of pack ice and open water. Over pack ice, this could be caused by snow cover and the formation of melt ponds, while over open water by wind-induced surface roughness . Thin and newly formed ice in particular will frequently have a signature close to that of open water, especially at lower frequencies where the penetration depth is larger. Variations in surface temperature of pack ice will also have an effect, especially in algorithms such as Bootstrap that do not attempt to correct for this. Influence from weather effects can also reduce estimate accuracies, especially at higher frequencies and where the ice concentration is low. On average, errors in ice concentration retrievals are typically less than 5 %.

These difficulties highlight the need for more research into the issue. The potential for improvement could come from techniques that are routine in many other areas of geophysical remote sensing, for example:

1. assimilation methods that combine dynamic models with remote sensing data (Kwok and

Cunningham, 2002),

2. combined use of different sensors such as active and passive (Grandell et al., 1999; Remund et al., 2000),

3. automated statistical methods such as neural networks, classification algorithms and other forms of machine learning (Remund et al., 2000),

4. application of radiative transfer models to filter out weather effects (Andersen et al., 2006),

5. inverse methods that iterate to a solution using forward model calculations (Golden et al., 1998b,a; Heygster and Melsheimer, 2008),

The first item is a challenging problem because of the extreme nonlinearity of ice when considered as a moving fluid: motion, especially in convergence zones, will be strongly affected by the mechanical properties of the ice (Maykut et al., 1992). The last item is hampered by the difficulty of reliably modelling sea ice emissions.

2.3.2 Thickness and other variables

Several studies report a relationship between microwave signatures and the thickness of thin ice. In particular, Martin et al. (2004) use the ratio between vertical and horizontal polarisations at 37 GHz,

$$R_{37} = \frac{T_v(37\text{GHz})}{T_h(37\text{GHz})}, \tag{2.8}$$

to derive ice thickness. Note that this value can be converted to polarisation, P, as follows:

$$P(37\text{GHz}) = \frac{R_{37} - 1}{R_{37} + 1}. \tag{2.9}$$

By fitting the following curve,

$$h = e^{1/(\alpha R_{37})} - \gamma, \tag{2.10}$$

they are able to retrieve ice thickness, h, up to about 20 cm with an estimated accuracy of 1 cm for ice of thicknesses between 0.5 and 5 cm and 2 cm for thickness up to 12 cm (Martin et al., 2005). Hwang et al. (2007), however, find that the relationship is considerably shifted for snow-covered ice.

Similarly, Naoki et al. (2008) find that both brightness temperature and emissivity increase up to the same thickness in both polarisations within the frequency range of 10 to 37 GHz. They postulate that this is not a direct relationship since the penetration depth at these frequencies is very shallow (Mathew, 2007), but is rather due to decreases in near-surface salinity of the growing ice sheet (Ehn et al., 2007).

Kwok et al. (2007) study the response of ice concentration retrievals to thin ice sheets and polynyas in the Ross Sea and find that areas of low ice concentration generated by both the NT2 and the bootstrap algorithm could just as well signal the presence of thin ice, suggesting that the two quantities cannot yet be separated in current microwave radiometry practice. Indeed, this is apparent from the above discussion: the original Team algorithm uses two variables to

derive two parameters; it would be impossible to derive a third, unrelated quantity from one of those two variables, as equations (2.9) and (2.10) attempt.

Other parameters that have been derived from passive microwave sensors include snow thickness (Comiso et al., 2003), winter snow water equivalent (Langlois et al., 2007) and solar albedo (Hwang et al., 2006). All of these use some subset of the same channels used to derive ice concentration, so without some understanding of how these quantities co-vary, both in nature and in the resulting microwave signatures, they should be treated with caution. Dry snow is more transparent at lower frequencies (Barber et al., 1998; Maetzler, 2001), another benefit of the L-band receiver. Thus it can supply knowledge of the underlying ice type, while the higher frequencies are sensitive to the snow cover.

2.3.3 Emissivity of sea water

It is easy to understand that all forms of sea ice retrieval require accurate knowledge of the emission properties of sea water. This is required for deriving ice concentration, but also for determining any other ice properties in the case of fractional concentrations as the water contribution must be removed first. Since sea water emissivity is already covered by the other two uses of the SMOS instrument (Reul and Chapron, 2001), only the basics will be covered here.

Like sea ice, the Fresnel equations provide a useful means of modelling the emissions and in the case of still water are quite accurate. As its name implies, one purpose of SMOS is to monitor surface salinity, so the dielectric constant as a function of salinity must be accurately determined. This variation is stronger at L-band than at higher frequencies and is usually determined by some sort of Debye relaxation curve (Maetzler, 2006).

Successive refinements in the estimates are accomplished by accounting for roughness at various scales, again, much as with sea ice. Surface roughness will tend to produce a decrease in the polarisation of the signal while causing overall emissivity to increase (Maetzler, 2006). Small scale surface variations are caused by wind roughening and increase the amount of scattering effects. These are more important at large wavelengths such as L-band than for higher frequencies and can be accounted for by empirical modifications to the Fresnel equations (Liu et al., 1998). Large scale variations are caused by both wind effects and non-locally from gravity waves, which require input from numerical wave models. These are treated geometrically by integrating over the slope distribution. Multiple scattering events can also be accounted for (Liu et al., 1998). At higher wind speeds, the appearance of foam and whitecaps has a significant effect on the emissivity, necessitating an additional layer in the model. As they are added, the preceding describes, respectively, one-, two- and three-scale models.

A significant challenge for SMOS will be modelling the third and fourth Stokes components. This necessitates accounting for horizontal anisotropy in the surface variations. Thus, it is not just wind speed that must be known, but also its direction; not just the power or frequency spectrum of the waves, but also the associated directional spectrum (Maetzler, 2006). These must then be translated into emission calculations.

2.4 Remote detection of sea ice from other instruments

The relevance of other remote sensing sea ice retrievals to the present study can be demonstrated in two ways. First, they supply a secondary source with which to validate existing algorithms as well as develop new ones. Second, the potential exists to extrapolate methods

from other domains, for instance different frequency bands, to the one of interest, that is L-band passive microwave.

2.4.1 Inferring ice thickness from observables using physical models

Ice thickness is frequently diagnosed from combined knowledge of the surface temperatures and surface heat flux. The total heat flux is given by the sum of longwave, shortwave, sensible and latent heat fluxes. Longwave fluxes can be approximated based strictly on the temperature gradient between surface and air while latent and sensible heat flux over open ocean requires the surface wind-speed in addition. Shortwave heat flux (insolation) requires latitude, the time of day and year, cloud cover and the (shortwave) surface albedo, or simply upwelling shortwave radiation and albedo. All of these can be derived from satellite measurements. If the ice is not too thick and the air temperature is varying slowly, ice thickness is calculated by assuming thermal equilibrium in combination with a constant (freezing) water temperature. Drucker et al. (Drucker et al., 2003) use two AVHRR (Advanced, Very-High-Resolution Radiometer) channels to derive surface temperature and assimilation data for air temperature. Surface winds are calculated using the geostrophic approximation. Insolation is neglected by excluding measurements at mid-day. A similar procedure is described in Yu and Lindsay (2003).

It is possible to derive surface temperatures from microwave measurements, although this requires knowledge of the surface emissivities. Emissivities in the microwave range are more variable than at infrared, and it is this variability that both makes sea ice detection difficult but also makes possible the distinction between different ice types. Emissivities at different frequencies are not constant, although they are often correlated (Mathew, 2007), thus, microwave spectra contain at least indirect knowledge of ice thickness in calm conditions. Surface temperature has been extracted from the 6.9 GHz channel in an enhanced Bootstrap algorithm (Comiso et al., 2003) by simply assuming constant emissivities (deviations are less than 0.01, empirically) for both ice and water. Ice concentration estimates are then derived from calculated emissivities rather than brightness temperatures.

Ice thickness may also be derived from prognostic models that take into account motion and growth (Yu and Lindsay, 2003). Ice motion can be derived through correlation of equivalent features in a time sequence of SAR (Synthetic Aperture Radar) or other images, (Thomas et al., 2008) while ice growth is approximated from air temperature. Again, these are quantities deriveable from passive microwave measurements.

2.4.2 SAR applications to ice remote sensing

Synthetic Aperture Radar is a popular method for conducting remote sensing of sea ice and other surface features. Like microwave radiometry, it can operate in most weather conditions, but provides a much higher horizontal resolution. SAR images are frequently used to validate ice retrievals from passive microwave measurements (Comiso et al., 1997; Kwok et al., 2007; Andersen et al., 2007). While ice concentration per se is difficult to estimate, distinct classes of surface cover can be derived either from individual pixel brightness or from texture analysis, while the high horizontal resolution makes it easy to convert these to concentrations for the much larger radiometer footprint sizes.

Operational instruments exist that use L-band (Dierking and Busche, 2006), however a radar senses back-scattered rather than emitted radiation. The amount of back-scattered ra-

diation will be given by some sort of scattering phase function $\gamma(\theta, \phi, p, \theta', \phi', p')$, where θ, ϕ and p are, respectively, the azimuth angle, zenith angle and polarization of the incoming radiation, while θ' and ϕ' are the same for the outgoing radiation. The absorption coefficients are given by integrating over the outgoing directions and polarisations:

$$\alpha(\theta, \phi, p) = 1 - \sum_{p'} \int \int_{4\pi} \gamma(\theta', \phi', p', \theta, \phi, p) d\theta' d\phi', \tag{2.11}$$

while the emission coefficients are given by integrating over the incoming directions:

$$\xi(\theta, \phi, p) = 1 - \sum_{p'} \int \int_{4\pi} \gamma(\theta, \phi, p, \theta', \phi', p') d\theta' d\phi', \tag{2.12}$$

Unless the scattering function is strongly peaked at $\theta = \theta'$ and $\phi = \phi'$, knowledge of backscatter coefficients will not translate into knowledge of emissivities. Fortunately, this is frequently the case, especially at nadir, and it is known that backscatter coefficients and emissivities are negatively correlated in multi-year ice, although the two are positively correlated in first-year ice (Maykut et al., 1992).

2.5 Existing L-band sea ice observations

The new SMOS instrument has several key advantages over previous microwave instruments used for ice detection. First, the atmosphere is almost completely transparent at 1.4 GHz. Second, sea ice is also somewhat translucent at this frequency: this, combined with full polarimetric data, promises at least some knowledge of the internal structure of the ice, such as thickness and bulk salinity. These variables are needed to fully model interactions with the ocean and atmosphere. Sea-ice is mentioned in the original SMOS proposal (Kerr, 1998) and a brief review of the subject is contained in Maetzler (2001) and in Kerr (1998) , including model results.

2.5.1 Skylab

Currently, the only passive L-band measurements from space come from early Skylab experiments conducted between 1973 and 1974 (Eagleman and Lin, 1976; Jackson et al., 2002). The 1.4 GHz non-polarized radiometer aboard Skylab had a nadir looking geometry with a 3 degree FOV and measured at 2.5 second intervals. With the 435 km orbit, this translates to a footprint diameter of roughly 110 km and a measurement spacing of about 3 km. The available overpasses are summarized in Figure 2.1.

The fifty-degree orbit inclination of the space station limits the possibilities of finding ice to lakes and estuaries during wintertime. There is one winter overpass that traverses the Great Lakes and the Gulf of St. Lawrence on 11 January 1974. Ice charts show the St. Lawrence Seaway to be relatively free from ice at that time (Figure 2.2), however the brightness temperature measurements themselves suggest that the Gulf has at least some ice since its minimum signature is much higher, both absolutely and relative to measurements taken in the Atlantic, when compared to an earlier overpass taken in September: see Figure 2.3.

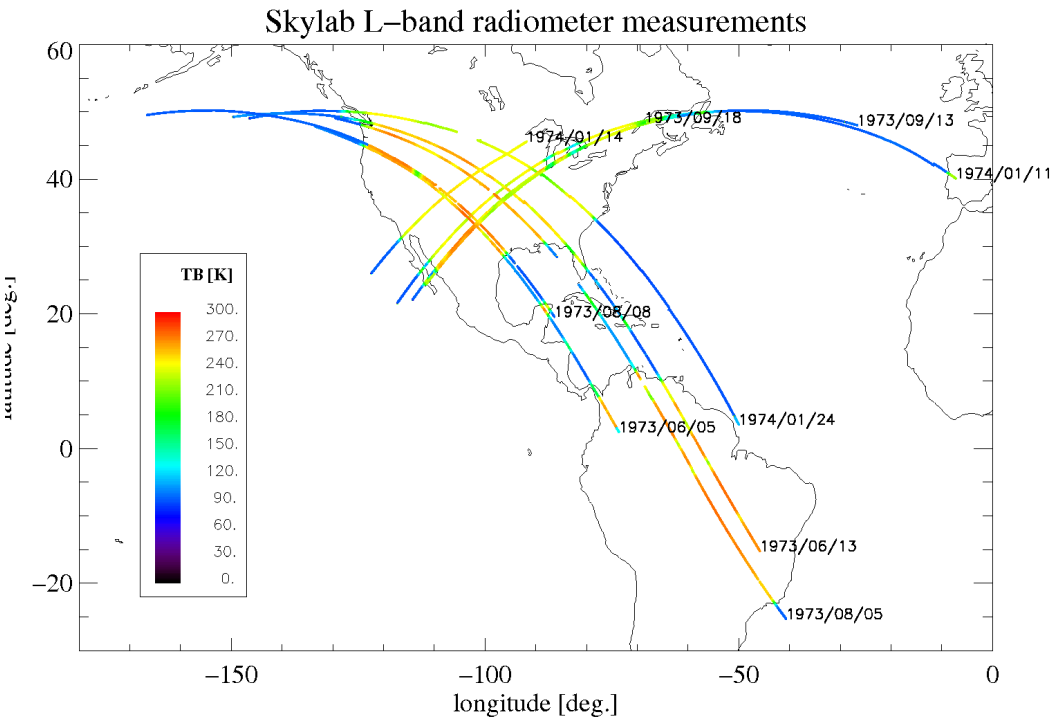

Figure 2.1: Summary of L-band measurements collected by Skylab

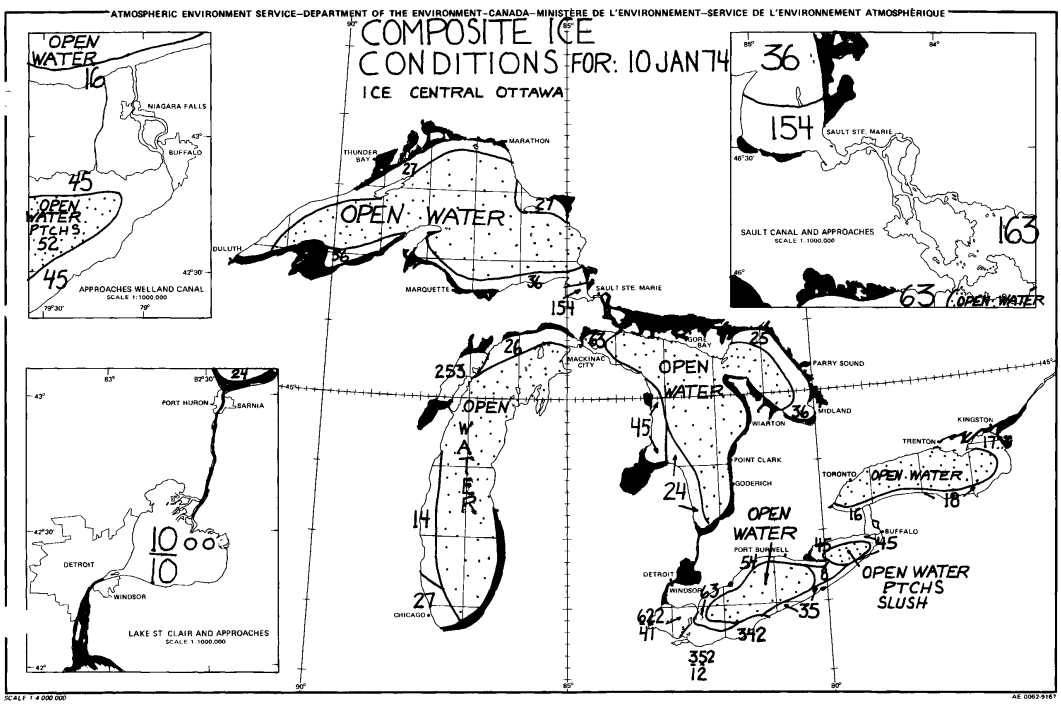

Figure 2.2: Ice conditions on the St. Lawrence Seaway for 10 January 1974 (courtesy of Roger DeAbreu, Atmospheric Enviromental Service, Canada)

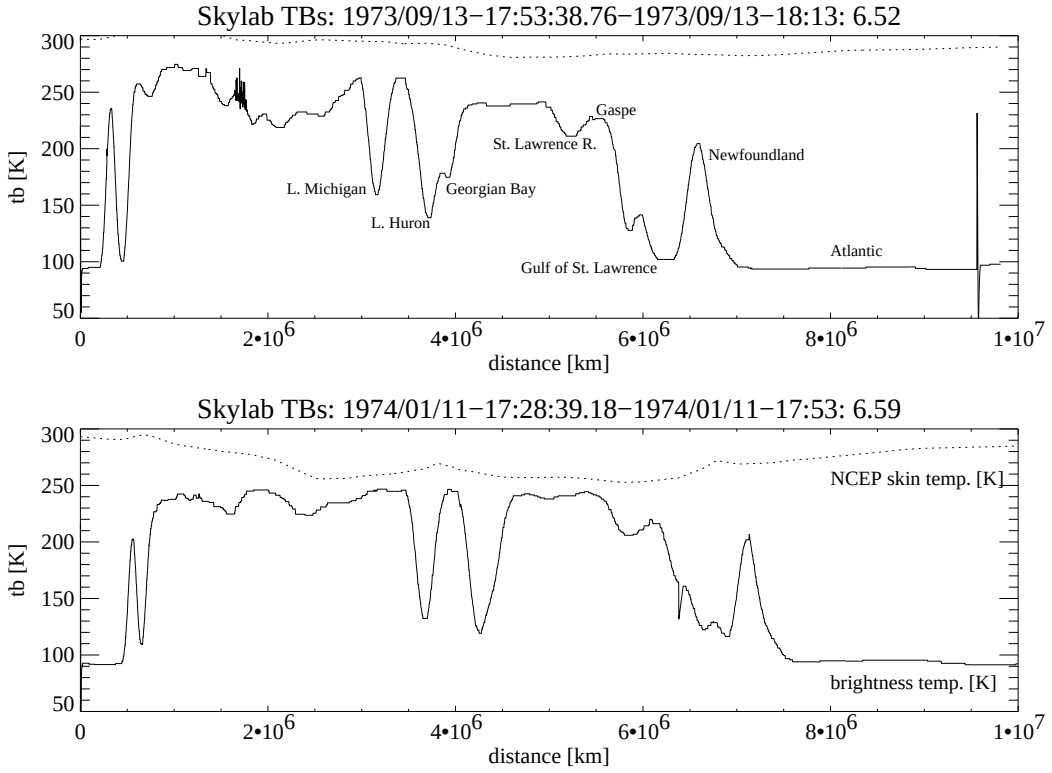

Figure 2.3: Skylab L-band measurements relevant to sea-ice remote sensing

2.5.2 Meltpond 2000

A second source of measurement data is from the Meltpond 2000 campaign conducted in the Canadian Arctic Archipelago in June and July 2000. This included five eight-hour flights of a P-3 aircraft carrying several C-band radiometers in addition to one for L-band called Scanning Low Frequency Microwave Radiometer (SLFMR). The latter consisted of a vertically polarised, cross-track scanning receiver with eight scan positions, four on each side of the aircraft, with incidence angles ranging between 6 and 47 degrees. Due to a failure in the electronics, only the four outermost beams at 36 and 47 degrees were available. Flight altitudes ranged from 1400 m to 6400 m, providing horizontal resolutions of between 800 and 3600 m (Klein et al., 2001; Klein, 2002). It has turned out that the radiometer gain was not stable during the flights. Therefore, data of the Meltpond 2000 campaign has not been considered during this study.

2.5.3 Pol-Ice 2007

The most promising experimental data so far comes from a campaign conducted in the Baltic Sea in March 2007 called Pol-Ice. This had two components: point-to-point and circular fly-overs with a single frequency but fully polarimetric radiometer and point-to-point overflights with an E-M Bird ice thickness detection instrument. The E-M Bird instrument detects the ice-water transition using inductance variations in a pair of electromagnetic coils (similar to a metal-detector) while the ice surface height is measured with a laser altimeter (Hendricks and Haas, 2008). Figure 2.4 summarizes a selection of radiometer flights while Figure 2.5 summa-

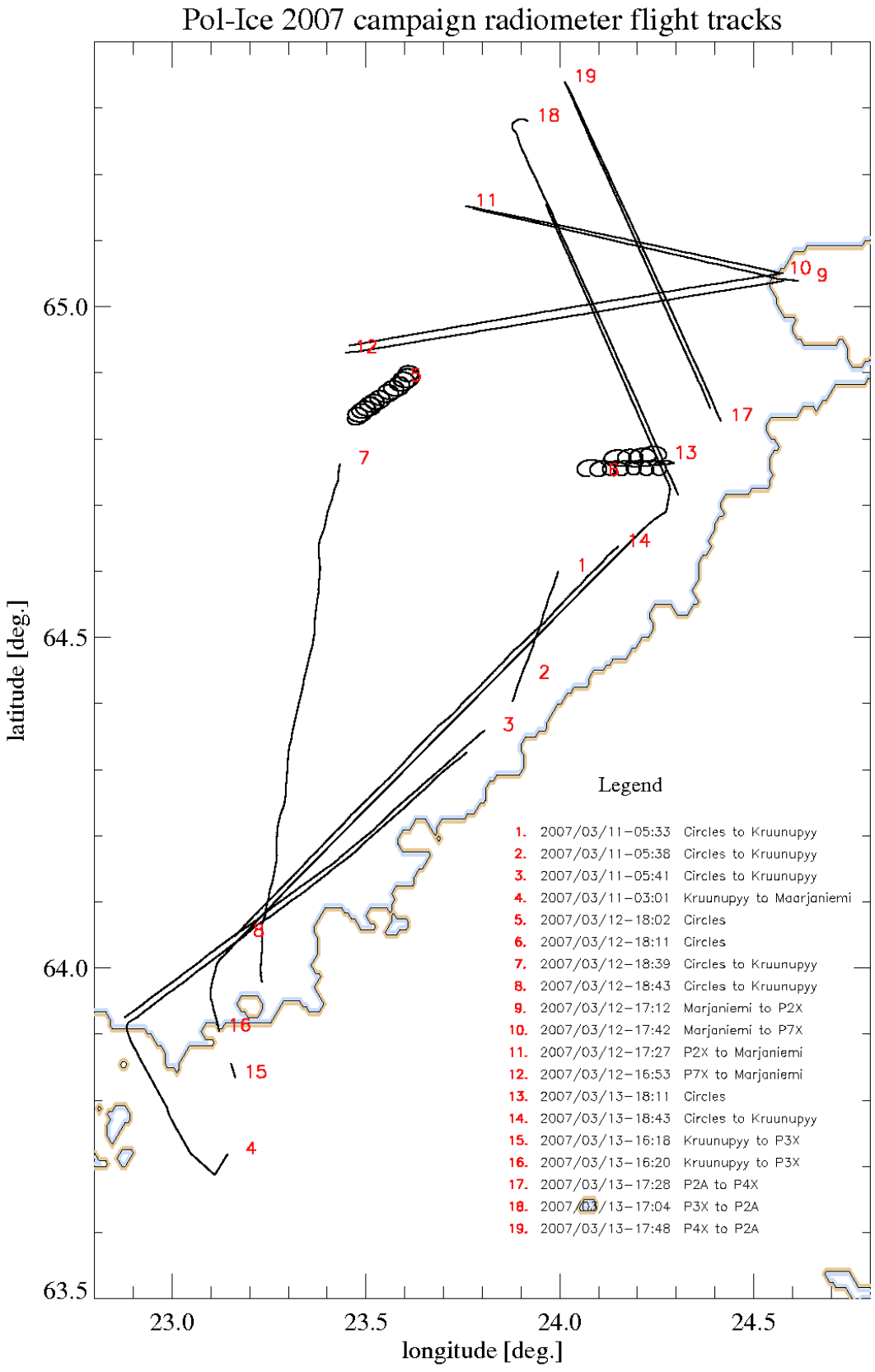

Figure 2.4: Summary of Pol-Ice campaign radiometer flights

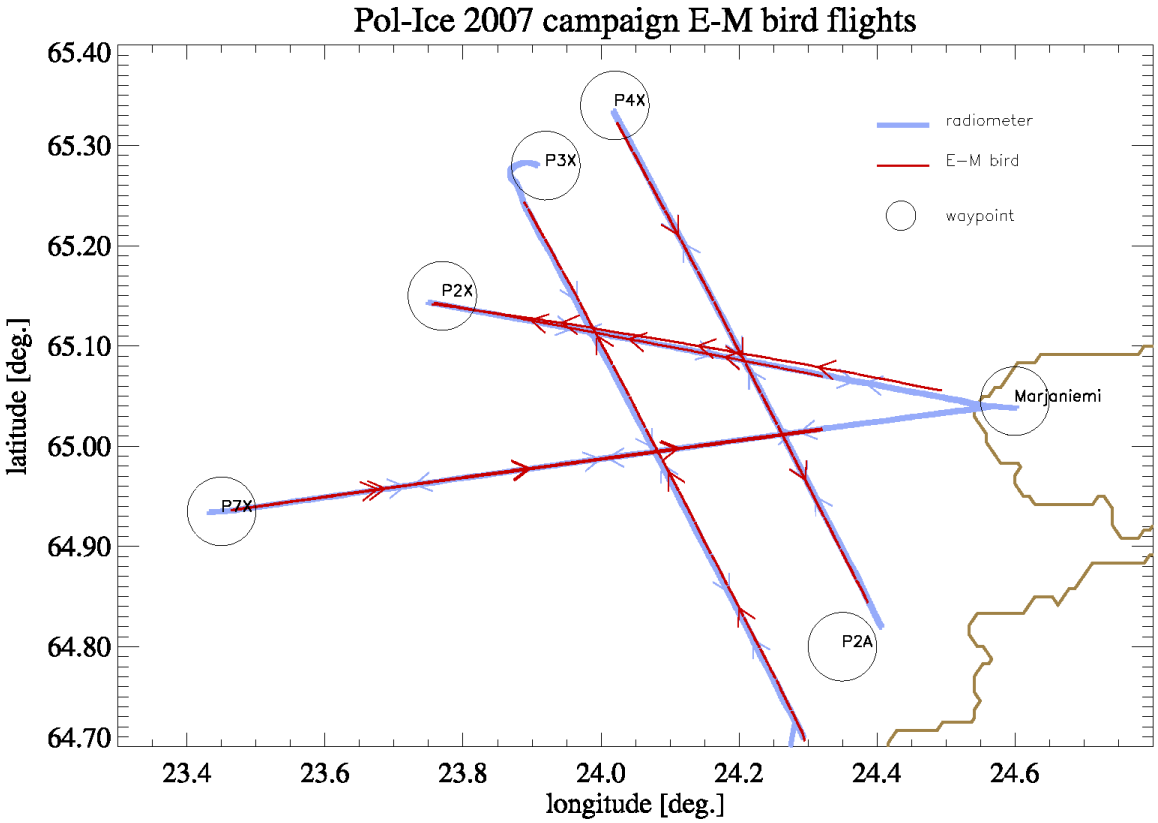

Figure 2.5: Summary of Pol-Ice campaign E-M bird flights

rizes the E-M bird flights along with coincident radiometer flights.

One issue with this campaign is the significantly lower salinities found in the Baltic, especially the Northern Baltic (Bay of Bothnia). Salinity in the Baltic varies between 9 psu in the South and less than 1 psu in the Northernmost part and in river estuaries, while the sea ice will typically have bulk salinities of less than 2 psu. So long as the surface salinity is greater than 0.6 psu, ice in the Baltic structurally resembles that of more saline bodies of water with preferred crystal orientations and brine inclusions. All sea ice found in the Baltic is first year, however it usually lacks the 'C'-shaped salinity profiles of that in polar regions; rather profiles tend to decrease with depth (Granskog et al., 2006). Since both bulk salinity and brine volume have a significant impact on microwave emission, extrapolating results to the more saline polar oceans will present the greatest challenge in applying this data to operational retrievals.

2.6 Conclusion

A cursory review of recent literature on the physical properties of sea ice and their retrieval from spaceborne observations provides a plethora of possibilities for adding the L band passive microwave to the current repertoire of tools. To this end, the 1.4 GHz channel used by SMOS would seem best fit to supplement existing radiometer data, rather than supplying new products. Pure ice types could be distinguished via supervised or unsupervised machine learning algorithms such statistical classification. If unsupervised techniques are used, then the resultant ice types may not correspond to accepted definitions but only be relevant to microwave

remote sensing work. Maps of the probability density functions of each category would help provide accurate bounds on concentration estimates. The procedure could be done first for L-band, then later for a composite of all available frequencies.

Some scientists may object to such a strictly statistical description of the data and desire a more physical understanding. However, a statistical model can often shed light on unknown or poorly understood physical relationships. Until emissivity models for sea ice reach a higher level of maturity, however, this appears to be a good way to proceed. Since campaign data samples only a tiny fraction of conditions encountered by the operational instrument, some theoretical considerations will no doubt be necessary to extrapolate to all areas. For this, more limited models that merely capture the functional forms would seem preferable to highly involved models like multi-layer SFT.

One issue with passive microwave measurements from space is that ice conditions within a single footprint are often highly heterogeneous. This of course is already addressed in concentration retrievals, in which a fundamentally discrete quantity is converted into a continuous one. With quantities like snow depth that are already continuous, the retrieval must by necessity be of an ensemble or average value. The challenge here is that in situ measurements representative of an entire footprint do not exist. This is where other, higher resolution, active, optical and infrared instruments can be of considerable service.

Chapter 3

WP 2.2: POL-ICE campaign: Ice thickness observations

Stefan Hendricks

Alfred Wegener Institute for Polar and Marine Research
Bremerhaven, Germany

Christian Haas
University of Alberta
Edmonton, Canada

3.1 Introduction

Based at the Bothnian Bay Research Station in Marjaniemi on the island Hailuoto in Finland, several helicopter-borne sea ice thickness surveys were conducted within the POL-ICE field campaign in March 2007. To measure sea ice thickness the Alfred Wegener Institute (AWI) utilize an airborne electromagnetic probe, the EM-Bird. The goal of the field campaign was to sample sea ice properties for the validation of operational sea ice monitoring with RADARSAT-2 SAR images. In addition, ice thickness data was gathered for the SMOS validation campaign ((Kerr, 1998)).

of the European Space Agency (ESA). The validation activities included coincident data sampling of sea ice thickness together with L-Band radiometry by a TKK[1] Short Skyvan research aircraft over various types of sea ice in the Baltic Sea. The validation activities took place at March 12. and 13. over sea ice west of Hailuoto (see figure 3.1).

Weather conditions were very warm during the field campaign, with air temperatures above 0°on most of the measurement days. Due to fog formation and low cloud covers waypoints of several flights had to be changed while being already airborne. As the result a EM-Bird profiles over thin ice south of Hailuoto had to be canceled because of poor visibility conditions.

[1]Helsinki University of Technology

The brackish water of the Baltic Sea with its low conductivity and thin sea ice marks a challenge for airborne EM measurements, which are dependent on a high conductivity contrast between sea ice and water. Additionally, ice thickness data was collected were the EM signals are biased by shallow waters and local changes in the sea water conductivity due to river runoff. The magnitude of these biases are estimated and have to be considered in further data analysis since the error mentionend are not considered in the standard data processing.

This report gives a brief overview of the ice thickness data delivered to the SMOS validation community (Deliverable WP 2.2). It addresses the processing steps as well as data format and file naming conventions.

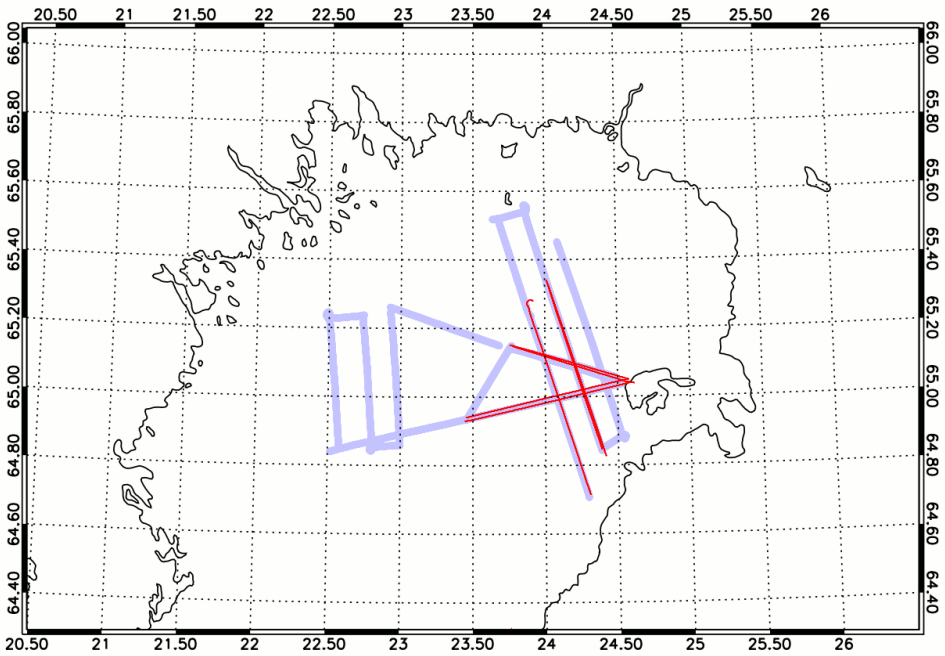

Figure 3.1: Coincident helicopter and aircraft flight tracks on March 12. and March 13. 2007 in the Bay of Bothnia. Helicopter flight tracks are marked by thicker lines, aircraft tracks by thinner lines.

Figure 3.2: Typical sea ice conditions during the field campaign: First year ice floes mixed with thin ice. Due to warm temperatures fog fields where common which formed a limitation for helicopter navigation.

3.2 EM Data Processing

3.2.1 EM Principle

EM sea ice thickness sounding is based on the conductivity contrast between snow and sea ice which neglegible electrical conductivity on the one side and the saline ocean water on the other side. In the northern Baltic Sea the conductivity of the sea water is small ($\approx$ 300 mS/m) compared to the Arctic Ocean ($\approx$ 2400 mS/m). Nevertheless, the EM system has been proven to be operable in the Bay of Bothnia for many field campaigns. For the data processing a value of 300 mS/m is assumed to be valid for all profils.
The EM-Bird contains a system of transmitter and receiver coils as well as a laser altimeter which is sampling the altitude of the coils above the sea ice. The transmitter coils emitts a harmonic (primary) electromagnetic field which induces eletrical eddy currents in the conductive sea water. These currents are the source of a weaker (secondary) electromagnetic field, which is detected together with the primary field in the receiver coil. The basic quantity of the EM technique is the strength of the secondary field relative to the primary field. The ratio is represented by the Inphase and Quadrature component, the real and imaginary part of the complex signal. The response of the Inphase and Quadrature channels can be modeled by a 1D layered earth forward model dependening on the height of the instrument over the water level.

Since the conductivity of snow and sea ice is small compared to the sea water, the EM problem is solved by means of model which consists of a homogenous halfspace with 0 mS/m for air, snow and water and 300 mS/m representing sea water. Sea ice thickness can be obtained

by this 1D approach for each channel independently. The Quadrature channel gives a stronger signal than Inphase throughout the typical range of altitude variation of the helicopter yielding better SNR, therefore it is used for the final data product. The basic idea of EM sea ice thickness sounding is to estimate the distance of the instrument to the water-ice interface by using the inverted model function and substract the laser range to get ice plus snow (total) thickness.

3.2.2 Sampling

EM data is recorded with a frequency of 10 Hz yielding a datapoint spacing of 3 to 4 meters for typical speed of the helicopters. This datapoints are oversampled by the laser altimeter by a factor of 10 (100 Hz). For the data processing the laser datapoints are averaged to match the EM footprint.

3.2.3 Limitations of the EM technique

Drill hole measurements have shown that the general accuracy over level ice lies in the range of $\pm$ 10 centimeters. Over deformed ice in particular over ridges the EM can underestimate the real ice thickness by about 50 %. One reason is possible saline water intrusion in unconsolidated ridges, which yields in significant conductivity values of the sea ice. A second effect is the footprint of the EM system, caused by the diffuse nature of the electromagnetic field. The footprint is defined as a box in which 90% of the induction process take place and has a size of about 4 time the height of the instrument. For normal measurement operations the footprint varies between 40 and 60 meters. Sea ice topography features smaller than the footprint are smoothed out and underestimated in peak thickness.

3.2.4 Thickness Bias

In the Baltic Sea several factors have an impact on the retrieved ice thickness value. On the one side the EM field can see in shallow water areas the sea floor, because the low conductivity of the sea water lead to a deep penetration of the EM field. On the other hand, river runoff can change the sea water significantly in the coastal areas.
Both effects are not accounted for in the standard processing. Due to a possible superposition this can only be solved by a formal layered earth inversion.
But treated separatly, the thickness bias introduced by shallow waters and lower conductivity can be quantified by means of the *apparent ice thickness*, which is the result of the standard processing without considering the pertubations described above.

Water depth

The influence of the sea floor as an additional layer in the EM problem with significant lower conductivity than the water itself cannot be described by simple relation. In an ideal conductor with infinite conductivity all the electrical currents would be induced in ice water boundary layer only and would be independent from water depth. Since even the more saline sea water in the Arctic Ocean does not fulfill this requirement there are always contributions from the volume of the water column to the EM signal. For the Baltic Sea the so called skin depth, which defines the penetration depth at which the EM signal has been faded by the factor $1/e$ amounts

to roughly 15 meters. Measurements taken in waters which are shallower than this values must be considered biased by the seafloor.

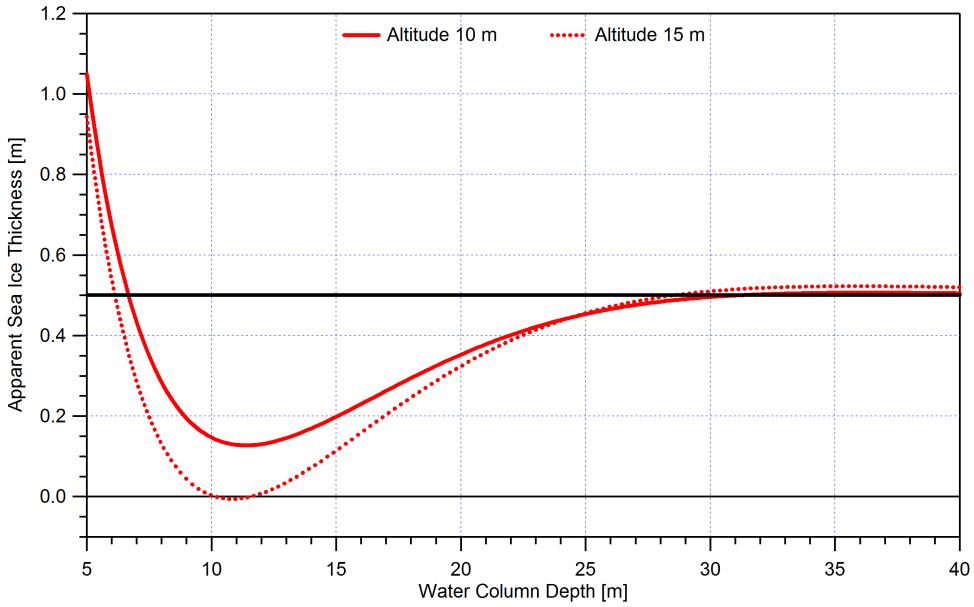

Figure 3.3: Apparent sea ice thickness depending on the depth of the water column

For a numerical sensitivity study (figure 3.3) a seafloor layer with a conductivity of 0 mS/m is added to the model with varying depth of the water column. The choice of a non-conductive layer reflects an upper limit to the expected error in the retrieved thickness. This bias also depends on the instrument height, therefore the study is repeated for two typical heights of the instrument.
The influence of the seafloor can be seen until water depth of at least twice the skin depth. In a range of 7 to 30 meters the error is consistently scales down the apparent ice thickness, while the contribution to the thickness value gets smaller than the system noise ($\pm$ 10cm) for areas deeper than 25 meters.
For convenience of the end user of the sea ice thickness data product, a quality flag is raised in areas of shallow waters. Since no high resolution bathymetry map was available, areas of biased thickness data were marked manually. The identification of such areas is based on the offset between the result of the Inphase and Quadrature channels (see figure 3.4, 3.5).

Fresh Water Entry

Local changes in the sea water conductivity are directly associated with the bias in the retrieved ice thickness. As a rule of thumb overestimation of the conductivity leads to overestimation of ice thickness and vice versa (see figure 3.6).

A single conductivity measurement of the water directly beneath the fast ice showed a conductivity value of roughly 240 mS/m, which is only 80 % of the default value of 300 mS/m used in the data processing. Such an error in the used conductivity would result in an ice thickness misinterpretation of more than 100% (1.1m instead of 0.5 m thick ice), but an expected increase of the conductivity with depth would lessen the thickness bias, since the EM fields

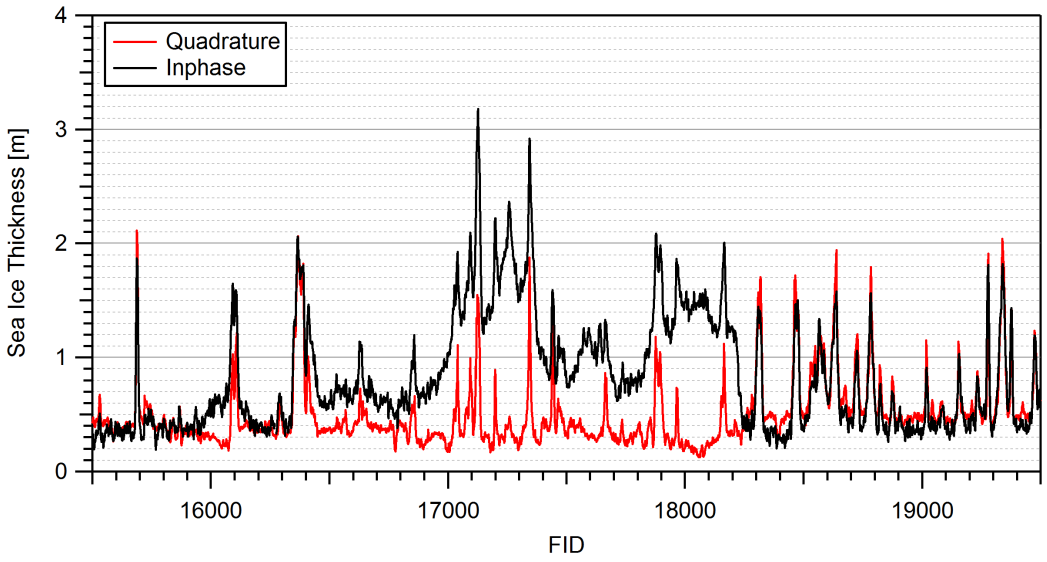

Figure 3.4: Influence of bathymetrie on sea ice thickness

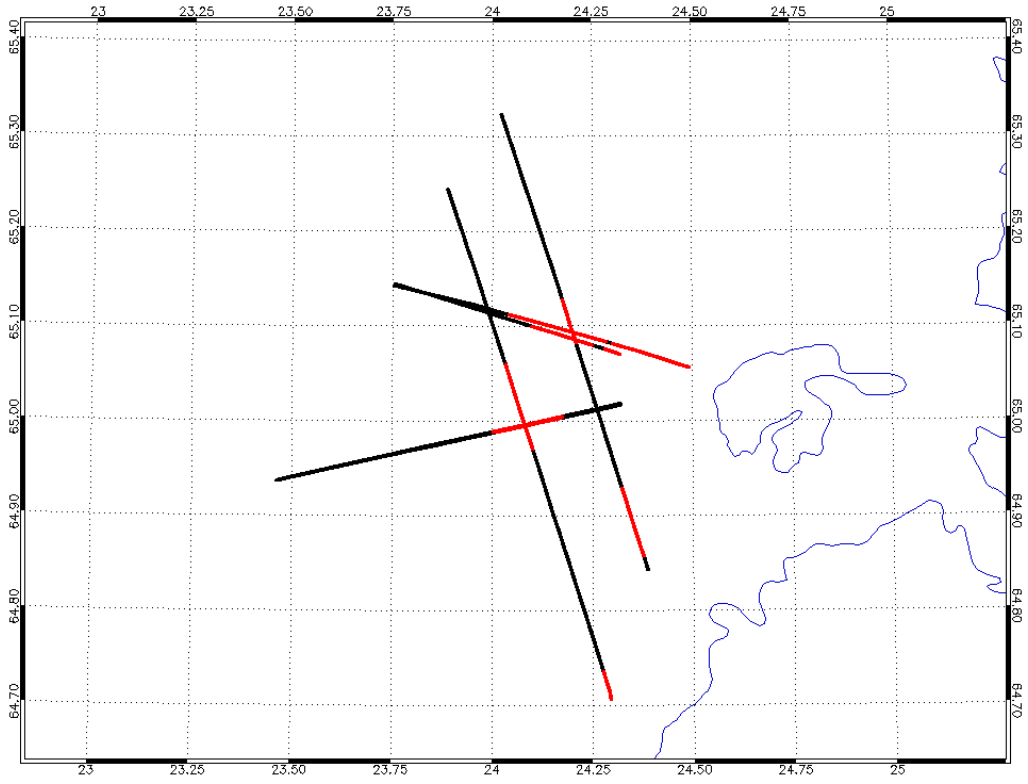

Figure 3.5: Geographical positions (red) where quality flag is raised due to the influence of the bathymetry on the sea ice thickness

have a large penetration depth in the brackish waters. Therefore the thickness bias in figure 3.6 represent a worst case scenario.

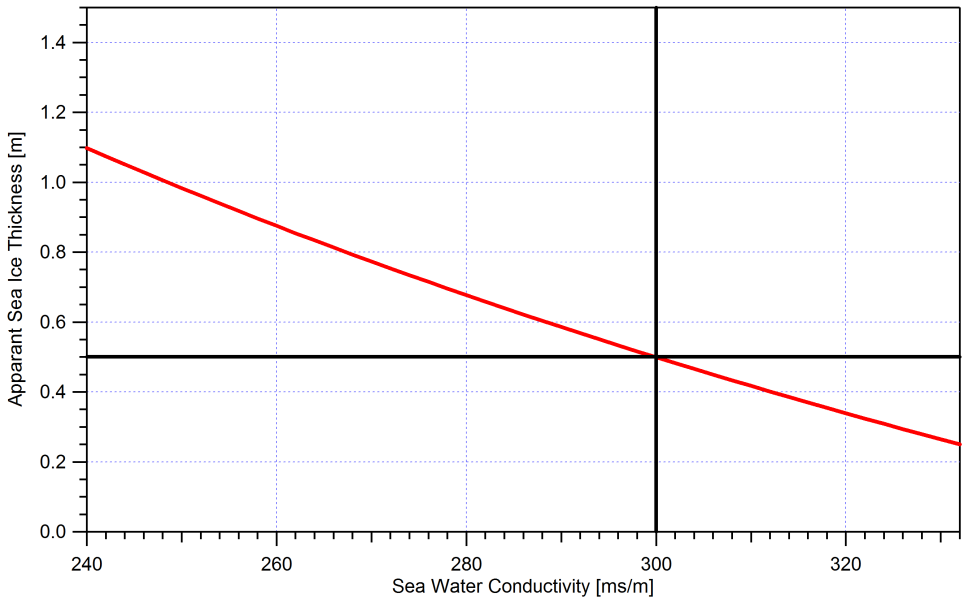

Figure 3.6: Apparent sea ice thickness depending on the real conductivity of the sea water

3.2.5 Filtering

Several system constraints can have a negative effect the retrieved ice thickness. Data sampled under these conditions is removed from the data product.

Instrument Altitude : A good compromise between measurement quality and aviation safety is a instrument height of 10 to 12 meters above the ice. Normally, pilots are able to limit the height variations to a few meter. But sometimes short ascends are necessary which decrease the SNR of the EM response significantly. To maintain a accuracy of $\pm$ 10 cm all data points with a laser range > 20 m are removed.

Instrument Roll : The EM bird is towed on a 20 to 30 meter long cable, depending on the helicopter type. Higher roll angle give wrong laser altimeter heights and the assumption of horizontal layers is not longer valid for the EM processing. Since no inertial navigation system is installed in the bird, which could give actual roll angles, the change of GPS heading from successive datapoints is used as a proxy for bird roll. All datapoints with a turnrate of more than 5°/sec are removed.

3.3 Deliverable

3.3.1 EM data files

One ice thickness data file is delivered for each section with coincident L-band radiometer measurements.

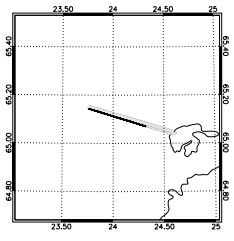

`20070312_MRJN_P2X_morning.dat`
Date : 2007/03/12
Length: 27.6 km

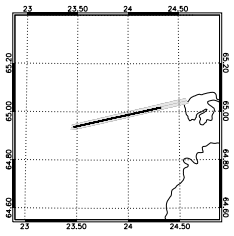

`20070312_P7X_MRJN_morning.dat`
Date : 2007/03/12
Length : 41.3 km

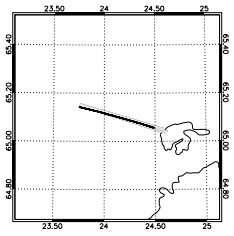

`20070312_MRJN_P2X_afternoon.dat`
Date : 2007/03/12
Length : 36.0 km

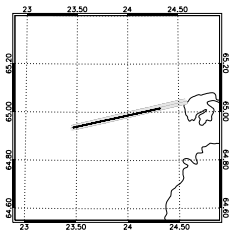

`20070312_P7X_MRJN_afternoon.dat`
Date : 2007/03/12
Length : 41.3 km

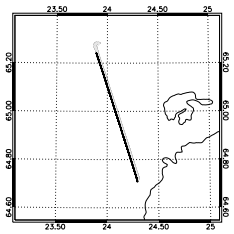

`20070313_P3X_P2A.dat.dat`
Date : 2007/03/13
Length : 62.7 km

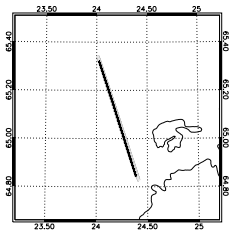

`20070313_P2A_P4X.dat.dat`
Date : 2007/03/13
Length : 56.0 km

3.3.2 Data Format

The EM data is delivered in blank separated ASCII data format described in table 3.1. All time tags are standard UTC time.

Column	*Description*	*Format*	*Unit*
1	Year	I4	UTC
2	Month	I2	UTC
3	Day	I2	UTC
4	Hour	I2	UTC
4	Minute	I2	UTC
4	Second	F5.2	UTC
6	Longitude	F12.7	degree
7	Latitude	F12.7	degree
9	Thickness	F5.2	m
10	Quality Flag	I1	–

Table 3.1: File format for EM data files

3.4 Navigational accuracy

Waypoints for the coincident data sampling of helicopter and aircraft were calculated prior to each flight and distributed to the flight crews. This section gives a brief overview of the distance between the ice thickness data and the ground track (nadir point) of the aircraft gps antenna. All calculated distances for each ice thickness dataset are based on the longitude/latitude positions of the helicopter and the aircraft, the dynamics of the sea ice is not taken into account.

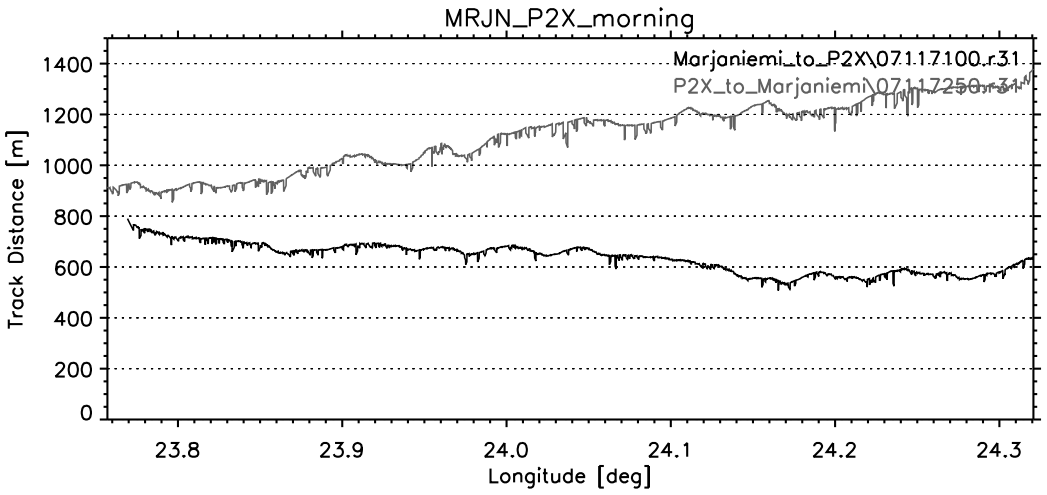

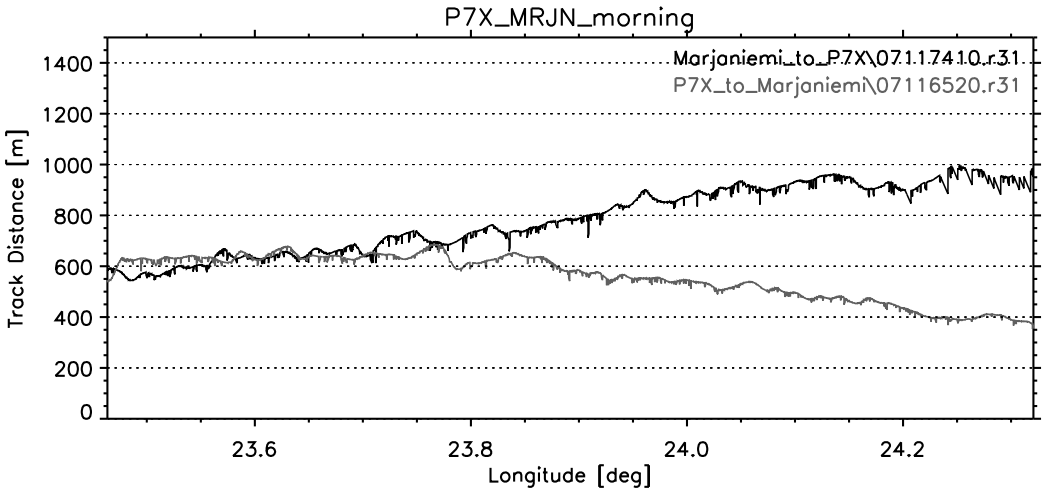
P7X_MRJN_morning
Marjaniemi_to_P7X\07117410.r31
P7X_to_Marjaniemi\07116520.r31
Track Distance [m]
1400
1200
1000
800
600
400
200
0
23.6
23.8
24.0
24.2
Longitude [deg]

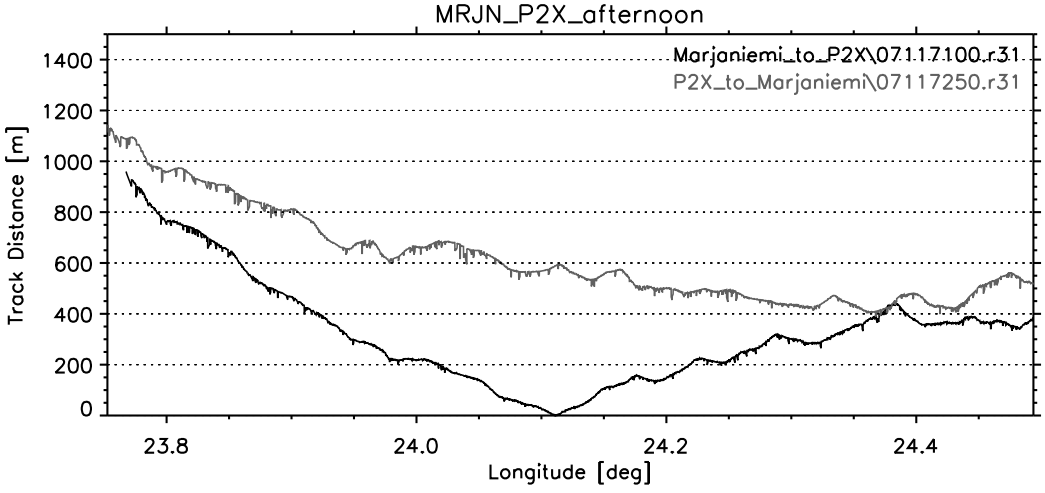
MRJN_P2X_afternoon
Marjaniemi_to_P2X\07117100.r31
P2X_to_Marjaniemi\07117250.r31
Track Distance [m]
1400
1200
1000
800
600
400
200
0
23.8
24.0
24.2
24.4
Longitude [deg]

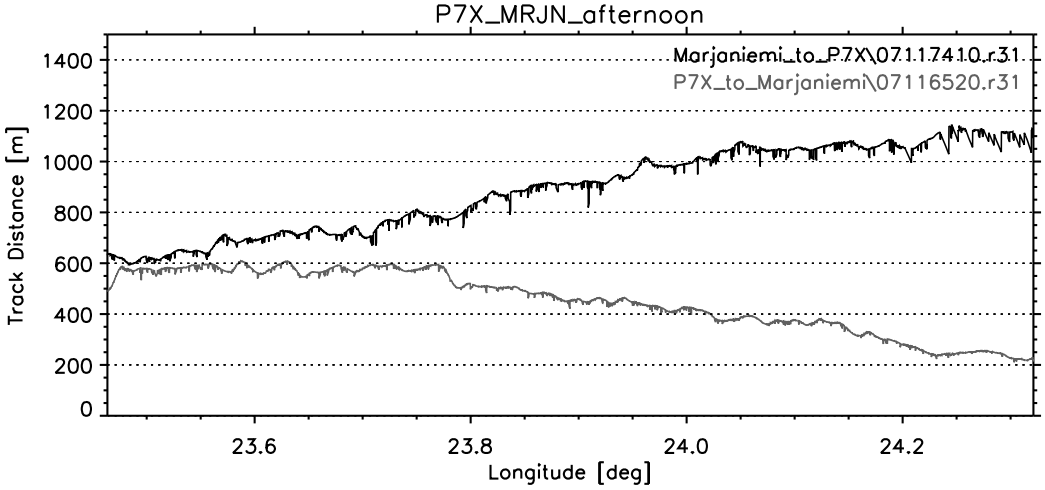
P7X_MRJN_afternoon
Marjaniemi_to_P7X\07117410.r31
P7X_to_Marjaniemi\07116520.r31
Track Distance [m]
1400
1200
1000
800
600
400
200
0
23.6
23.8
24.0
24.2
Longitude [deg]

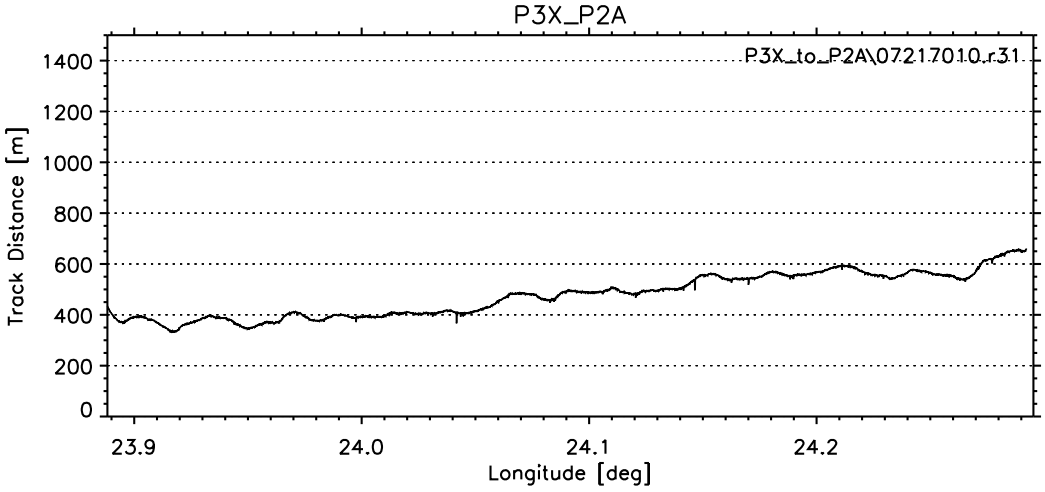
P3X_P2A
P3X_to_P2A\07217010.r31
Track Distance [m]
1400
1200
1000
800
600
400
200
0
23.9
24.0
24.1
24.2
Longitude [deg]

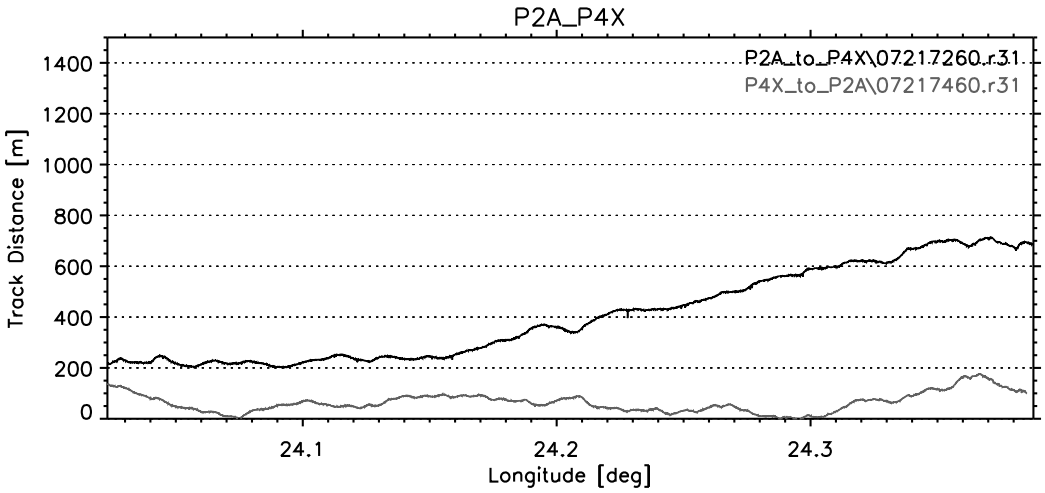
P2A_P4X
P2A_to_P4X\07217260.r31
P4X_to_P2A\07217460.r31
Track Distance [m]
1400
1200
1000
800
600
400
200
0
24.1
24.2
24.3
Longitude [deg]

Chapter 4

WP 2.1: Campaign data analysis; WP 2.5: Ice concentration vs. ice thickness

Lars Kaleschke, Nina Maaß

Institute of Oceanography, University of Hamburg

4.1 Abstract

Soil Moisture and Ocean Salinity (SMOS) is an earth observation mission developed by the European Space Agency to be launched in 2009. The main objective is to provide global measurements of soil moisture over land and sea surface salinity over ocean from L-band (1.4 GHz) radiometric observations. An exciting spin-off is the retrieval of sea ice thickness which we demonstrate to be possible due to the large penetration depth at L-band. SMOS will provide sea ice thickness information complementary to those from altimeters because of the expected sensitivity for thin ice thickness variations. Moreover, SMOS will provide data with an almost global coverage every second day.

A three layer (ocean-ice-atmosphere) dielectric slab model is used to calculate the brightness temperature as a function of ice thickness and the dielectric properties. The dielectric properties depend on the relative brine volume as a function of bulk salinity and temperature. A model for the brightness temperature of a mixture of open water and sea ice reveals that the parameters ice concentration and thickness can hardly be retrieved both simultaneously. With the assumption of a closed ice cover the retrieval of ice thickness is feasible. The model calculations suggest a thickness sensitivity of up to 150 cm for low salinity (multi year or brackish) sea ice at low temperatures. At temperatures approaching the melting point the thickness sensitivity reduces to a few centimeters. For first year ice the modeled thickness sensitivity is roughly half a meter.

The brightness temperature at 1.4 GHz (L-band) was measured in the Bothnian Bay in March 2007 as part of the SMOS Sea-Ice campaign. The research aircraft was equipped with the Technical University of Denmark (TUD) Electromagnetics Institute Radiometer (EMIRAD). The EMIRAD measurements were coordinated with helicopter EM ice thickness measurements.

The campaign was conducted under non-favourable conditions with temperatures around the melting point and there was only a relatively small overlap of EMIRAD and EM data. However, these measurements agree in general very well with the model results. The ice thickness from the L-band radiometer is in good agreement with the EM ice thickness in the range of 20 cm to 150 cm. The retrieval failed for a region of ice with a melted surface.

4.2 Model description

4.2.1 Brightness temperature

The total radiance emitted by the earth's surface is made up of the radiance emitted both by the water surface and the ice surface, depending on their relative proportions to each other. Accordingly the brightness temperature observed at the surface depends on the temperatures of water and ice, their emissivities and the ice concentration, C:

$$T_{\text{obs}} = (1 - C)e_{\text{water}}T_{\text{water}} + Ce_{\text{ice}}T_{\text{ice}} \tag{4.1}$$

The measured brightness temperatures also include the atmospheric contribution, ionospheric effects, solar system and galactic radiation (Reul et al., 2008; Tenerelli et al., 2008). We neglect these effects in the following.

4.2.2 Water emissivity

The emissivity of a specular reflecting water surface in thermal equilibrium can be derived from the Fresnel equations (Swift, 1980)

$$e_{\text{water}}(H,\theta) = 1 - \left| \frac{\cos\theta - \sqrt{\epsilon_{\text{water}} - \sin^2\theta}}{\cos\theta + \sqrt{\epsilon_{\text{water}} - \sin^2\theta}} \right|^2 \tag{4.2}$$

$$e_{\text{water}}(V,\theta) = 1 - \left| \frac{\epsilon_{\text{water}}\cos\theta - \sqrt{\epsilon_{\text{water}} - \sin^2\theta}}{\epsilon_{\text{water}}\cos\theta + \sqrt{\epsilon_{\text{water}} - \sin^2\theta}} \right|^2 \tag{4.3}$$

where θ is the angle of incidence and ϵ_{water} is the complex dielectric constant of sea water. The indices V and H denote vertical and horizontal polarisation, respectively.

Dielectric constant of sea water

There is only one model for the dielectric constant of natural sea water that is based on measurements at 1.4 GHz, the one of Klein and Swift (1976). The dielectric constant of sea water is calculated with the standard Debye expression

$$\epsilon_{\text{water}} = \epsilon_\infty + \frac{\epsilon_s - \epsilon_\infty}{1 + (i\omega\tau)} - i\frac{\sigma}{\omega\epsilon_0} \tag{4.4}$$

where $\omega = 2\pi\nu$ is the angular frequency, $\epsilon_\infty = 4.9$ ($\pm 20\%$) is the dielectric constant at infinite frequency, ϵ_s is the static dielectric constant, τ is the relaxation time, σ is the ionic conductivity and $\epsilon_0 = 8.854 \cdot 10^{-12}$F/m is the permittivity of free space. ϵ_s, τ, σ are all functions of

water salinity and temperature and have been fitted to experimental data with the following formulations. Temperature T has to be inserted in degrees centigrade and salinity S in ‰.

$$\epsilon_s(T,S) = \epsilon_s(T)a(S,T)$$

where

$$\begin{aligned} \epsilon_s(T) &= 87.134 - 1.949\cdot 10^{-1}T - 1.276\cdot 10^{-2}T^2 + 2.491\cdot 10^{-4}T^3 \\ a(S,T) &= 1.000 + 1.613\cdot 10^{-5}ST - 3.656\cdot 10^{-3}S + 3.210\cdot 10^{-5}S^2 \\ &\quad -4.232\cdot 10^{-7}S^3 \end{aligned}$$

$$\tau(T,S) = \tau(T,0)b(S,T)$$

where

$$\begin{aligned} \tau(T,0) &= 1.768\cdot 10^{-11} - 6.086\cdot 10^{-13}T + 1.104\cdot 10^{-14}T^2 - 8.111\cdot 10^{-17}T^3 \\ b(S,T) &= 1 + 2.282\cdot 10^{-5}ST - 7.638\cdot 10^{-4}S - 7.760\cdot 10^{-6}S^2 \\ &\quad +1.105\cdot 10^{-8}S^3 \end{aligned}$$

$$\sigma(T,S) = \sigma(25,S)\exp(-\Delta\beta)$$

where

$$\begin{aligned} \Delta &= 25 - T \\ \beta &= 2.033\cdot 10^{-2} + 1.266\cdot 10^{-4}\Delta + 2.464\cdot 10^{-6}\Delta^2 \\ &\quad -S(1.849\cdot 10^{-5} - 2.551\cdot 10^{-7}\Delta + 2.551\cdot 10^{-8}\Delta^2) \\ \sigma(25,S) &= S(0.182521 - 1.46192\cdot 10^{-3}S + 2.09324\cdot 10^{-5}S^2 - \\ &\quad 1.28205\cdot 10^{-7}S^3). \end{aligned}$$

Klein and Swift (1976) claim accuracies of 0.2% and 0.4% on the real and imaginary part of ϵ respectively but the measurements suffered from a bias and thus these accuracies may be optimistic (Dinnat and Boutin, 2003).

Brightness temperature of the polar ocean

The brightness temperature at normal incidence calculated according to the model described above is shown for a range of sea surface temperatures and salinities in Fig. 4.1. The brightness temperature of the ocean surface is about 92 K for typical polar conditions of S=34‰ and close to the freezing point of seawater of $T = -1.9°$C. A variability of less than one Kelvin is expected for the marginal ice zone (MIZ) as the sensitvities to temperature and salinity are both small. The brackish water of the Baltic sea emits a brightness temperature of about 96 K and a small variability of less than one Kelvin for typical wintertime conditions is expected.

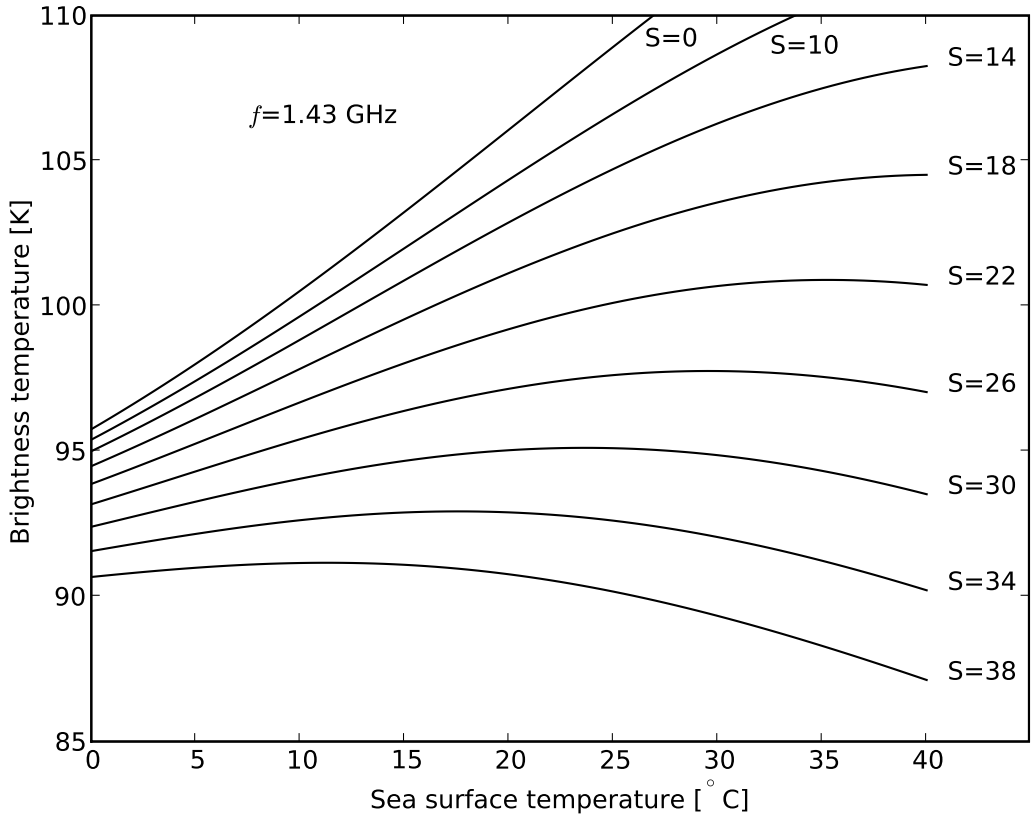

Figure 4.1: Brightness temperature at normal incidence according to Klein and Swift (1976)

4.2.3 Sea ice emissivity

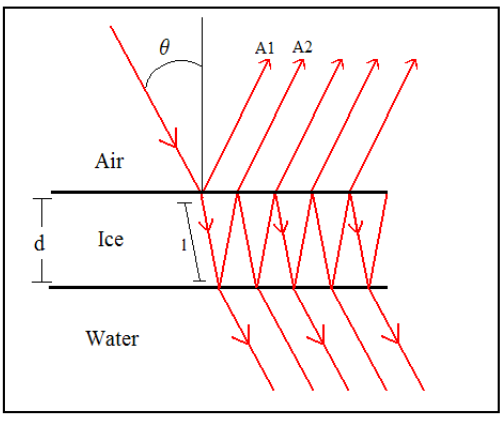

Figure 4.2: Dielectric slab model

The emissivity of ice follows from considering reflection at a dielectric slab of ice over water (Fig. 4.2).

The reflection coefficient of an ice slab over an infinite half plane can be expressed as a function of the reflection coefficients R_1 and R_2, describing reflection at the upper and lower boundary of the slab (Ulaby et al., 1981):

$$R = \frac{R_1 + R_2 e^{-2ik_{i,z}h}}{1 + R_1 R_2 e^{-2ik_{i,z}h}} \tag{4.5}$$

where h is ice thickness and $k_{i,z}$ is the z-component of the propagation vector in ice $\vec{k_i}$, when the z-axis is perpendicular to the slab. The z-component of vector $\vec{k_i}$ with magnitude k_i is (Ulaby et al., 1981):

$$\begin{aligned} k_{i,z} &= k_i \cos\theta_i && (4.6)\\ &= \omega\sqrt{\mu\epsilon}\cos\theta_i && (4.7)\\ &= \omega\sqrt{\mu_0\mu_i\epsilon_0\epsilon_i}\cos\theta_i && (4.8)\\ &= \frac{\omega}{c_0}\sqrt{\epsilon_i}\cos\theta_i && (4.9) \end{aligned}$$

where
ϵ_0 / μ_0: electric / magnetic constant
ϵ_i / $\mu_i = 1$: relative permittivity / permeability of ice
$c_0 = 1/\sqrt{\mu_0\epsilon_0}$: speed of light in vacuum
$\omega = 2\pi\nu$: angular frequency.

The expression for $k_{i,z}$ can be separated into its real part β, which is called the phase constant, and its imaginary part α, which is referred to as the attenuation coefficient: $k_{i,z} = \beta - i\alpha$. Accordingly, the expressions for α and β are:

$$\beta = \frac{\omega}{c_0}\cos\theta_i \,\mathrm{Re}\,\sqrt{\epsilon_i} \tag{4.10}$$

$$\alpha = \frac{\omega}{c_0}\cos\theta_i |\,\mathrm{Im}\,\sqrt{\epsilon_i}| \tag{4.11}$$

Ice emissivity can then be computed from $e_{ice} = 1 - r = 1 - R\overline{R}$, where r is reflectivity and $\overline{R}$ is the conjugate-complex of the reflection coefficient R. Assuming that no scattering takes place and that the power reflection coefficients are real the following expression for ice emissivity can be derived (Menashi et al., 1993):

$$e_{ice} = \frac{(1 - R_{ia})(1 - AR_{wi})}{1 + AR_{ia}R_{wi} + 2\sqrt{AR_{ia}R_{wi}}\cos(2\beta l)} \tag{4.12}$$

where R_{ia} is the reflectivity of air to ice, R_{wi} is the reflectivity of ice to water and $A = \mathrm{e}^{-4\alpha h}$.
The above equation is a coherent solution describing ice emissivity as a periodic function of ice thickness. If the rms thickness variation of the ice slab is sufficiently large, i.e. more than a quarter of the used electromagnetic wavelength over the illumination footprint, the periodicity averages out and an incoherent solution can be introduced instead.
The emissivity of ice averaged over a variety of ice thicknesses, which can be considered as the ice roughness is derived by (Menashi et al., 1993) and can be expressed as follows:

$$e_{ice} = \frac{(1 - R_{ia})(1 - AR_{wi})}{1 - AR_{ia}R_{wi}} \left[\frac{1 - \sqrt{AR_{ia}R_{wi}}\mathrm{e}^{-\beta\sigma_h}}{1 + \sqrt{AR_{ia}R_{wi}}\mathrm{e}^{-\beta\sigma_h}}\right] \tag{4.13}$$

where σ_h is rms thickness variation (roughness).
The equations presented in (Menashi et al., 1993) contain optical pathlength l and its variation σ_l instead of ice thickness h and thickness variation σ_h in (4.13). This is contradictory to the theoretical considerations of reflection at a dielectric slab of certain thickness over an infinite half-plane (Ulaby et al., 1981). The expressions for the attenuation coefficient α and the phase coefficient β used in (Menashi et al., 1993) do not take into account the cosine term, that originates from considering the z-component of the propagation vector only (Eqs. 4.11,4.10). However, the general pattern of the coherent equation does not change even when inserting the slightly different expressions for α, β and pathlength in ice. The derivation of an incoherent expression for ice emissivity remains the same. The coherent solution is therefore used with the modified expressions for the above mentioned components.

Reflection at air-ice-boundary

$$R_{ia}(H, \theta > 0^\circ) = \frac{\sin^2(\theta - \varphi_1)}{\sin^2(\theta + \varphi_1)} \tag{4.14}$$

$$R_{ia}(V, \theta > 0^\circ) = \frac{\tan^2(\theta - \varphi_1)}{\tan^2(\theta + \varphi_1)} \tag{4.15}$$

$$R_{ia}(H, \theta = 0^\circ) = R_{ia}(V, \theta = 0^\circ) = \left(\frac{\sqrt{\frac{\epsilon_{\text{ice}}}{\epsilon_{\text{air}}}} - 1}{\sqrt{\frac{\epsilon_{\text{ice}}}{\epsilon_{\text{air}}}} + 1} \right)^2 \tag{4.16}$$

with $\varphi_1 = \arcsin(\sqrt{\frac{\epsilon_{\text{air}}}{\epsilon_{\text{ice}}}} \sin\theta)$.

Reflection at ice-water-boundary

$$R_{wi}(H, \theta > 0^\circ) = \frac{\sin^2(\theta - \varphi_2)}{\sin^2(\theta + \varphi_2)} \tag{4.17}$$

$$R_{wi}(V, \theta > 0^\circ) = \frac{\tan^2(\theta - \varphi_2)}{\tan^2(\theta + \varphi_2)} \tag{4.18}$$

$$R_{wi}(H, \theta = 0^\circ) = R_{wi}(V, \theta = 0^\circ) = \left(\frac{\sqrt{\frac{\epsilon_{\text{water}}}{\epsilon_{\text{ice}}}} - 1}{\sqrt{\frac{\epsilon_{\text{water}}}{\epsilon_{\text{ice}}}} + 1} \right)^2 \tag{4.19}$$

with $\varphi_2 = \arcsin(\sqrt{\frac{\epsilon_{\text{ice}}}{\epsilon_{\text{water}}}} \sin\theta)$.

Sea ice dielectric constant

The expressions for the power reflection coefficients contain the dielectric constants of air, water and ice. The dielectric constant of air is assumed to be $\epsilon_{\text{air}} = 1$.

Vant et al. (1978) proposed an empirical relationship for the dielectric constant of ice depending on the relative brine volume:

$$\epsilon_{\text{ice}} = a_1 + a_2 V_b + i(a_3 + a_4 V_b) \tag{4.20}$$

Hallikainen and Winebrenner (1992) provides the following coefficients for first year ice:

$$a_1 = 3.12,\ a_2 = 0.0090,\ a_3 = 0.039,\ a_4 = 0.00504 \quad \text{for } f\text{=1GHz}$$
$$a_1 = 3.07,\ a_2 = 0.0076,\ a_3 = 0.034,\ a_4 = 0.00356 \quad \text{for } f\text{=2GHz}$$

and for multi year ice with different imaginary coefficients

$$a_3 = -0.004,\ a_4 = 0.00436 \quad \text{for } f\text{=1GHz}$$
$$a_3 = \ 0.013,\ a_4 = 0.00435 \quad \text{for } f\text{=2GHz}$$

In this study a linear combination of the coefficients valid for 1 and 2 GHz is used as an approximate value for 1.4 GHz. Brine volume fraction has to be inserted in ‰. The coefficients are valid for relative brine volumes $V_b < 70‰$.

Brine volume

The relative brine volume is defined as

$$V_b = \frac{S_{\text{ice}}}{S_b} \tag{4.21}$$

where S_{ice} is the total ice salinity and S_b is the salinity of the brine entrappments.

Cox and Weeks (1974) examined cold sea ice samples collected from Arctic and sub-Arctic locations. The empirical relationship between ice salinity S and ice thickness h they found can be used as constraint for the retrieval of ice thickness

$$S[‰] = \begin{cases} 14.24 - 19.39h & \text{for } h \leq 0.4m \\ 7.88 - 1.59h & \text{for } h > 0.4m \end{cases} \tag{4.22}$$

The freezing temperature of a saline solution depends on the solution's salinity. Correspondingly the brine salinity in thermodynamic equilibrium is a function of ice temperature. The polynomial approximations for this dependency developed by Vant et al. (1978) are used here:

$$S_b[‰] = \begin{cases} 1.725 - 18.756T - 0.3964T^2 & \text{for } -8.2 \leq T \leq -2°\text{C} \\ 57.041 - 9.929T - 0.16204T^2 - 0.002396T^3 & \text{for } -22.9 \leq T \leq -8.2°\text{C} \\ 242.94 + 1.5299T + 0.0429T^2 & \text{for } -36.8 \leq T \leq -22.9°\text{C} \\ 508.18 + 14.535T + 0.2018T^2 & \text{for } -43.2 \leq T \leq -36.8°\text{C} \end{cases} \tag{4.23}$$

Baltic Sea conditions The empirical relationship between the bulk ice salinity and ice thickness is not valid for ice conditions like in the Baltic Sea. Salinity of Baltic Sea water is much lower than in the Arctic Sea. The salinity of northern Baltic Sea water lies between 2 and 7 psu in the surface layer. Despite these low salinity values the ice shows typical sea ice features. Winter bulk ice salinity averaged over samples collected at landfast sea ice in the Gulf of Finland in 1999-2001 is 0.65 ± 0.33 (Granskog et al., 2004).

Cox and Weeks (1983) developed an equation for determining the brine volume fraction in sea ice for temperatures in the range of -2 to $-30°C$:

$$V_b = \frac{\rho S}{F_1(T)}$$

where

ρ: ice density

S: bulk ice salinity

$F_1(T) = \alpha_0 + \alpha_1 T + \alpha_2 T^2 + \alpha_3 T^3$ with

$$\left.\begin{aligned} \alpha_0 &= -4.732 \\ \alpha_1 &= -2.245 \cdot 10 \\ \alpha_2 &= -6.397 \cdot 10^{-1} \\ \alpha_3 &= -1.074 \cdot 10^{-2} \end{aligned}\right\} \text{ for } -2 \geq T \geq -22.9°C$$

$$\left.\begin{aligned} \alpha_0 &= 9.899 \cdot 10^3 \\ \alpha_1 &= 1.309 \cdot 10^3 \\ \alpha_2 &= 5.527 \cdot 10 \\ \alpha_3 &= 7.160 \cdot 10^{-1} \end{aligned}\right\} \text{ for } -22.9 \geq T \geq -30°C$$

Ice density ρ is expressed by density of pure ice (subscript i) and brine solution (subscript b) and the relative brine volume. The gas content of ice is neglected in this simplified treatment.

$$\rho = \rho_i(1 - V_b) + \rho_b V_b$$

It follows that brine volume fraction can be expressed as

$$V_b = \frac{S\rho_i}{F_1(T) + S\rho_i - S\rho_b} \tag{4.24}$$

Density of pure ice can be calculated from ρ_i [g/m^3] = $0.917 - 1.403 \cdot 10^{-4}\ T[°C]$.
Brine density can be approximated by ρ_b [g/m^3] $= 1 + 0.0008 S_b$ [‰].
Brine salinity is calculated from Equation (4.23).
Leppäranta and Manninen (1988) derived equations for determining relative brine content for temperatures between $-2°C$ and $0°C$.

$$V_b = \frac{\rho_i S}{F_1(T) - \rho_i S F_2(T)} \tag{4.25}$$

where

$$F_1(T) = \alpha_0 + \alpha_1 T + \alpha_2 T^2 + \alpha_3 T^3 \text{ with } \begin{aligned} \alpha_0 &= -4.1221 \cdot 10^{-2} \\ \alpha_1 &= -1.8407 \cdot 10 \\ \alpha_2 &= 5.8402 \cdot 10^{-1} \\ \alpha_3 &= 2.1454 \cdot 10^{-1} \end{aligned}$$

$$F_2(T) = \beta_0 + \beta_1 T + \beta_2 T^2 + \beta_3 T^3 \text{ with } \begin{array}{l} \beta_0 = 9.0312 \cdot 10^{-2} \\ \beta_1 = -1.6111 \cdot 10^{-2} \\ \beta_2 = 1.2291 \cdot 10^{-4} \\ \beta_3 = 1.3603 \cdot 10^{-4} \end{array}$$

Sea ice roughness

The parameter σ_h is the sea ice thickness roughness and is related to the pathlength variation σ_l. It is not obvious how to choose the σ_d because it should depict the specific L-band electromagnetic roughness. The choice of σ_d influences the asymptotic behaviour of the emissivity model towards zero ice thickness. For a decreasing ice thickness the modeled emissivity should converge to the emissivity of open water. One assumption about the roughness is that it is large enough to enable incoherent reflection. On the other hand, only a vanishing roughness for zero ice thickness leads to the convergence of the ice emissivity to those of open water.

A sensitivity study for different parameterizations of σ_d is shown in Fig. 4.3. The coherent solution for the emissivity of a plane-parallel ice slab over an infinite half plane reduces to the emissivity of open water for a vanishing ice thickness. The incoherent form (Eq. 4.13) with a parameterization of σ_d as a fixed percentage of ice thickness also approaches the emissivity of open water. The incoherent solution for a constant positive σ_d does not converge to the emissivity of open water. For roughnesses greater than a quarter of the electromagnetic wavelength, which is about 5 cm, the incoherent solutions do not differ significantly for different σ_d. For a smooth surface $\sigma_d < \frac{\lambda}{32\cos(\theta)}$ (Fraunhofer criterion), the validity for the incoherent solution is not anymore fulfilled.

4.3 Data

The brightness temperature at 1.4 GHz (L-band) was measured in the Bothnian Bay in March 2007 as part of the SMOS Sea-Ice campaign. The Helsinki University of Technology (HUT) SkyVan research aircraft was equipped with the Technical University of Denmark (TUD) Electromagnetics Institute Radiometer (EMIRAD). The EMIRAD measurements were coordinated with helicopter EM ice thickness measurements. These measurements were also part of the POL-ICE field campaign with the aim to investigate multipolarization SAR for operational sea ice monitoring. The helicopter was based at the Bothnian Bay Research Station in Marjaniemi on the island Hailuoto and the airplane was based at Kokkola in Finland, respectively.

The L-band radiometer measures the fully polarimetric state of the electromagnetic emission(Rotboll et al., 2003). In the following its data have been analysed only for the vertically and horizontally polarized channels. The radiation was measured with two antennas, one with a nadir beam and the other with an aft looking beam with an angle of incidence of 40°. The non-imaging radiometer thus provides only a profile along the flight track of the aircraft. The footprint of the nadir measurement at a flight level of 1000m is about 300m. The radiometer data have been provided with a sampling rate of 125 Hz. The signal was integrated over 200 samples. This leads to a slightly oversampled footprint spacing of approximately 90-100m for the following data analysis.

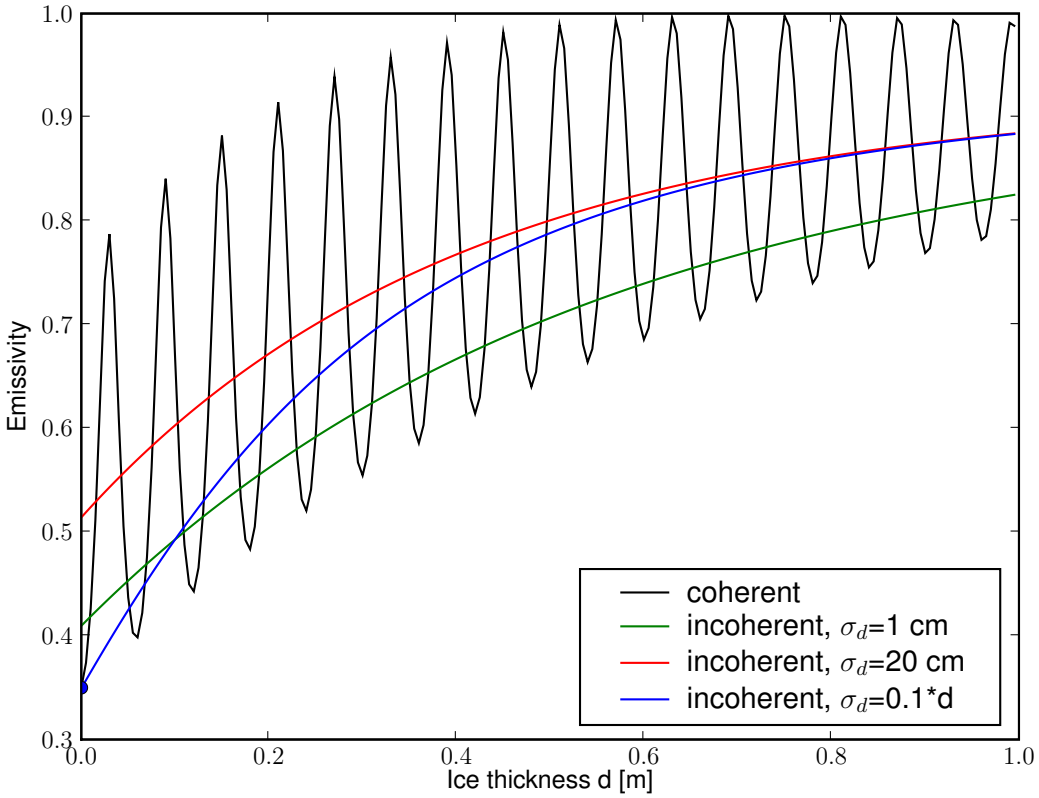

Figure 4.3: Emissivity of a slab of Baltic sea ice (S=0.65, T=-2 °C) for nadir incidence. The coherent and incoherent solution are shown for different parameterizations of the thickness roughness σ_d. The open water emissivity is indicated with the blue filled circle.

The radiometer measurements was seen to be affected by unstable behaviour due to erratic behaviour of the power supply. This caused deviations from the nominal performance of the radiometer and introduced spikes and jumps in the data. The brightness temperature signals have been carefully investigated and obviously degraded sections have been excepted from the analysis.

The EM ice thickness measurement is based on a system of a transmitter and receiver coil to obtain the conductivity of the underlying scene. Together with the altitude information from a laser altimeter it is possible to retrieve the ice thickness from the conductivity contrast of ice and water. The footprint diameter of a measurement is about 40m recorded at 10 Hz. With an averaging over 100 samples the resulting spacing is approximately 30-40m. The general accuracy over level ice is $\pm$ 10 cm. Over ridged areas the error can increase to about 50% of ice thickness.

An overview about the brightness temperature measurements of the 12th and 13th March is shown in Fig. 4.4 together with a MODIS image. The MODIS image was taken on the 14th March because of the cloud coverage on the previous days.

The helicopter EM ice thickness averaged in 3 km boxes is shown in Fig. 4.6. The EM

data shown here have not been corrected for the influence of the bathymetry, the according quality flags have been ignored, and all flights from 11th to 14th March have been taken into account. In the following analysis only data of 12th and 13th March are included because of the coordinated flights of the helicopter and the SkyVan aircraft on these two days.

The air temperature measured at Hailuoto is shown in Fig. 4.5. The temperature increased from an average of -6 °C on the 5th to an average above 0 °C on the 12th and 13th March.

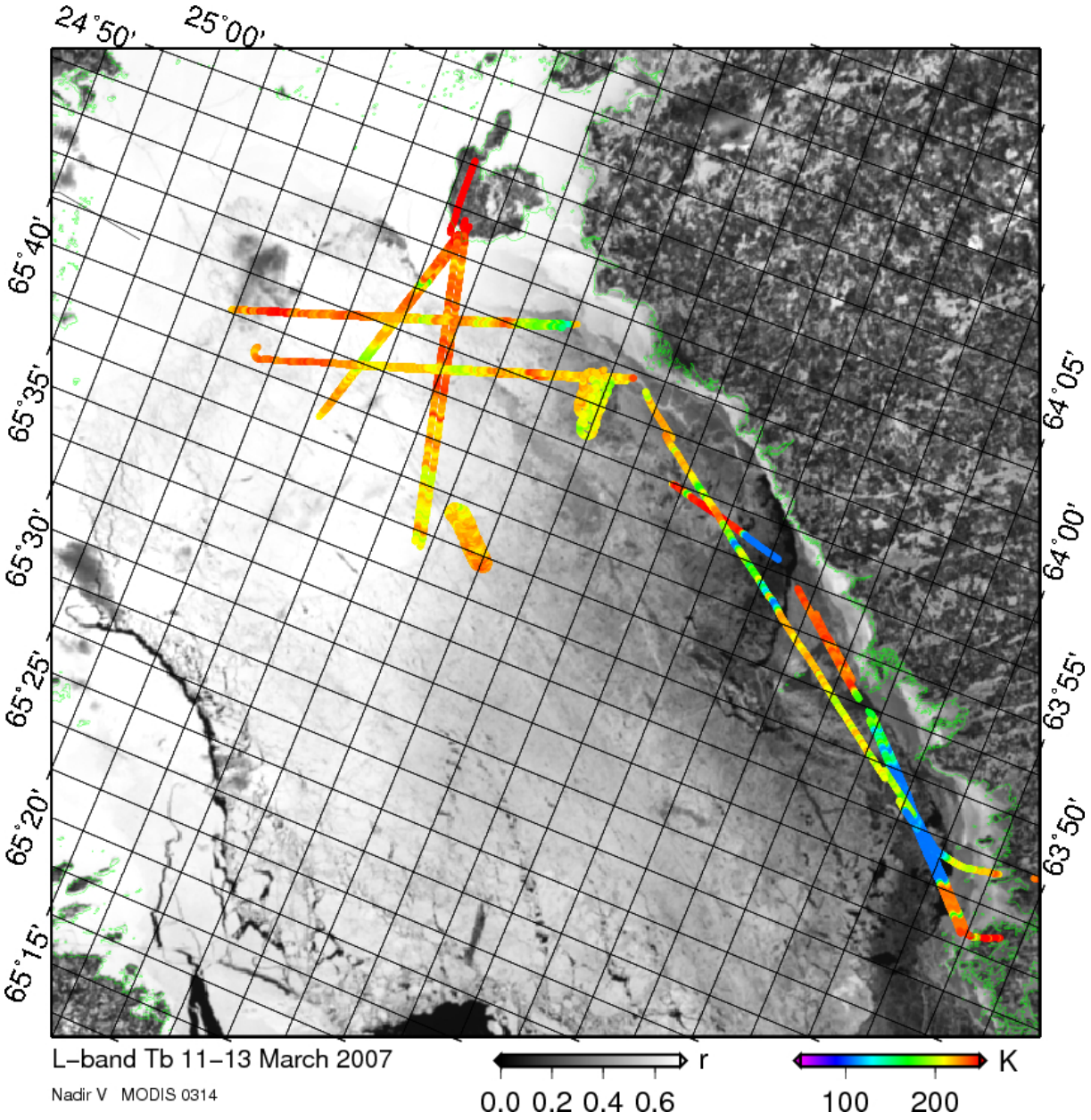

Figure 4.4: MODIS reflectivity (λ=645 nm) of 14 March and vertical polarized nadir brightness temperature measured during field campaign of 12-13 March 2007.

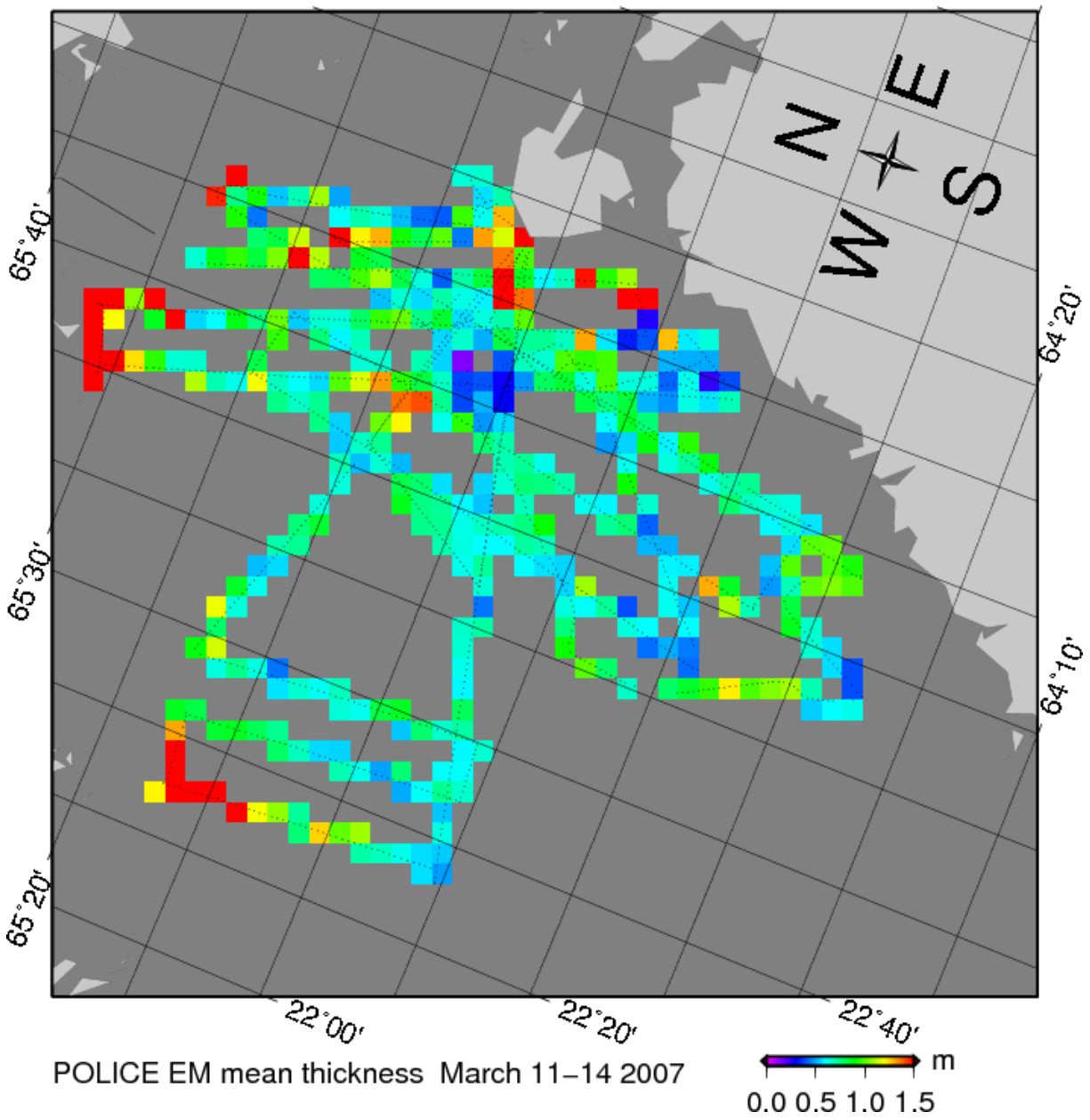

Figure 4.5: Helicopter EM ice thickness averaged in 3×3 km^2 grid boxes from the field campaign of 11-14 March 2007.

4.4 Results

Homogeneous sections from the helicopter EM thickness and EMIRAD radiometer brightness temperature have been selected and co-located to the best possible extent. In general there was no overlap of both datasets with an exception of one single track with some overlap. Due to the different spatial resolution of both sensors the integrated area was different. Therefore, with co-location is meant only the closest distance of a section of one dataset to the other.

The radiometer data have not been accurately calibrated. Therefore it seems to be reasonable to adjust for a possible bias by adding a constant. The constants have been chosen in a

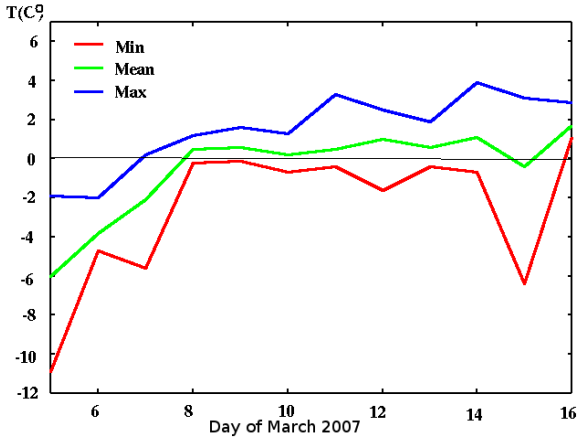

Figure 4.6: Air temperature measured at Hailuoto. Courtesy of Juha Karvonen (FIMR).

way that they minimize the difference between the model and the observation as decribed below. This step may mask possible shortcomings of our emissivity model but it introduces no limitations for the assesment of the retrieval sensitivities as the addition of a constant does not change the variability.

The influence of the ice concentration on the brightness temperature is investigated in a region of open water which was only partly covered with ice. A nearly coincident ASAR image is available for this case study. As it is problematic to derive ice concentrations from synthetic aperture radar data, the image can only serve as a means to select a suitable part of the radiometer track. The variation of the brightness temperature is simulated with the model for a range of ice concentration and thicknesses and compared to the selected part of the measured data.

4.4.1 Thickness

Sections of relatively constant ice thickness have been manually selected and co-located to the brightness temperature (see Appendix 4.7). An average difference between the measured and modeled brightness temperature has been calculated and substracted as a bias correction. For this we assumed a constant ice temperature of -2 °C, salinity of $S = 0.5$ and rms roughness $\sigma_d = 0.1$m. The resulting offset for the four channels are -15.8K, -8.8K, -14.6K, -0.9K for the nadir looking vertical, the nadir looking horizontal, the aft looking vertical and the aft looking horizontal component, respectively.

The modeled and measured brightness temperature is shown in Fig. 4.7 for temperatures of -2 °C and -0.5 °C. The results are in relatively good agreement and at least support the validity of the model and assumptions as a very reasonable first approximation. The remaining scatter can easily be explained by the non-overlapping measurements. The nadir brightness temperature varies between 206 K for 40 cm level ice and 240 K for ice of 180 cm thickness, respectively. The curve for a temperature of -0.5 °C demonstrates the effect of melting which leads to a saturation thickness of less than 40 cm.

The one flight track with the best spatial overlap of EM and EMIRAD data is shown in Fig. 4.9. There is a general good agreement for most of the track with the exception of an area with a large overestimation of the radiometric ice thickness. The area stands out by its low albedo

and shape in the MODIS image. We assume that the low albedo is caused by melting at the ice surface. A photograph (Fig 4.10) taken close to this area reveals the existence of features that look like a very wet snow surface or even like ponded ice. This interpretation is consistent with the overestimation of the radiometric ice thickness.

4.4.2 Concentration

The measurement of 11th March over ice and open water is investigated for the effect of a varying ice concentration on the brightness temperature. The ASAR APP image shows an area of open water enclosed by fast ice at the coast and drift ice. The color coded brightness temperature along the flight track in Fig. 4.11 shows higher temperatures for the thicker fast ice and lower temperatures for the thinner drift ice, as well as a large contrast between ice and open water. The vertical and horizontal signal is shown in Fig. 4.12 together with modeled brightness temperatures for different thicknesses and the ice concentrations. The variation of the model parameters should lead to a coverage of all parts of the possibly observed data space. It can be seen that the range of measured brightness temperatures is in very good agreement with the range of the modeled values. It is again remarked that ice concentration has not been measured and that the comparison just shows the range of both the modeled and observed data space.

The model captures well the high variability of the brightness temperature as a function of ice concentration. This is not surprising because of the large emissivity contrast of ice and water. The brightness temperature for a variety of ice concentrations and thicknesses covers rather a line than a two dimensional part of the data space. Therefore, it seems not to be possible or highly uncertain that both quantities could be retrieved simultaneously from the vertically and horizontally polarised brightness temperature at an incidence angle of 40°. Furthermore, the model results indicate (not shown here) that any other SMOS polarization and incidence angle combination does not provide this orthogonality which would be necessary for simultaneous retrieval of ice concentration and thickness.

4.4.3 Arctic simulation using a thermodynamic sea ice model

We used the results of a thermodynamic sea ice model which was driven by reanalysis data as input to the emissivity model. The thermodynamic model and setup is described in the SMOSIce work package of DMI (Rasmus Tonboe). From the modeled sea ice profiles we calculated bulk values of salinity and temperature. The resulting time series of brightness temperature are shown in Fig. 4.13 to Fig. 4.15. From these results it can be concluded that retrieval of ice thickness seems to be feasible for first year ice thicknesses of up to half a meter. It will probably be difficult to measure changes of multi year ice thickness because of the simultaneous influence of temperature and salinity.

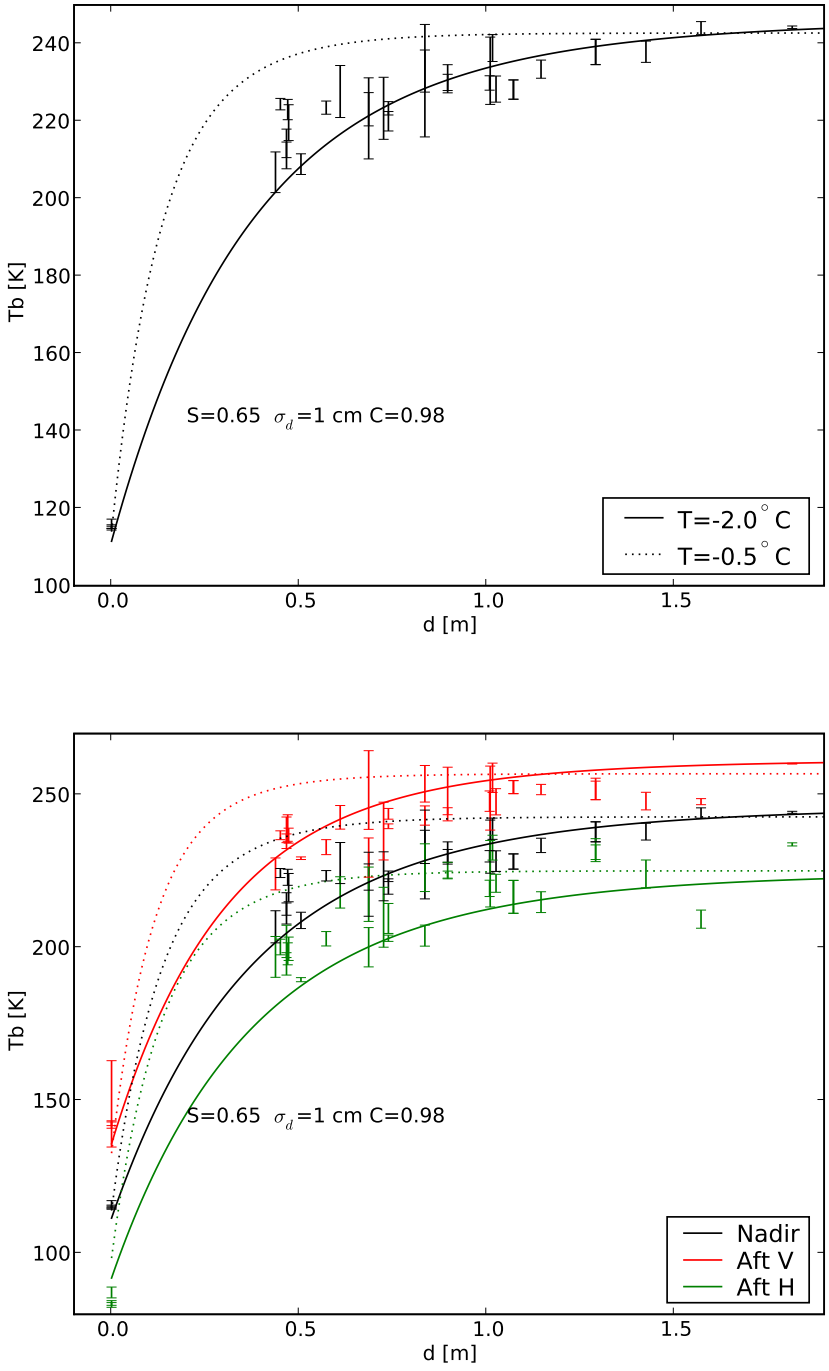

Figure 4.7: Modeled and observed brightness temperature. The upper graph is only nadir view, the lower figure contains also the data of the aft looking beam. The error bars represent the standard deviation of the brightness temperature for the according section of homogeneous thickness. The standard deviation of the difference of modeld and observed brightness temperature is about 7 K for all four channels. The solid (dotted) line is the modeled brightness temperature for -2 (-0.5) °C, respectively.

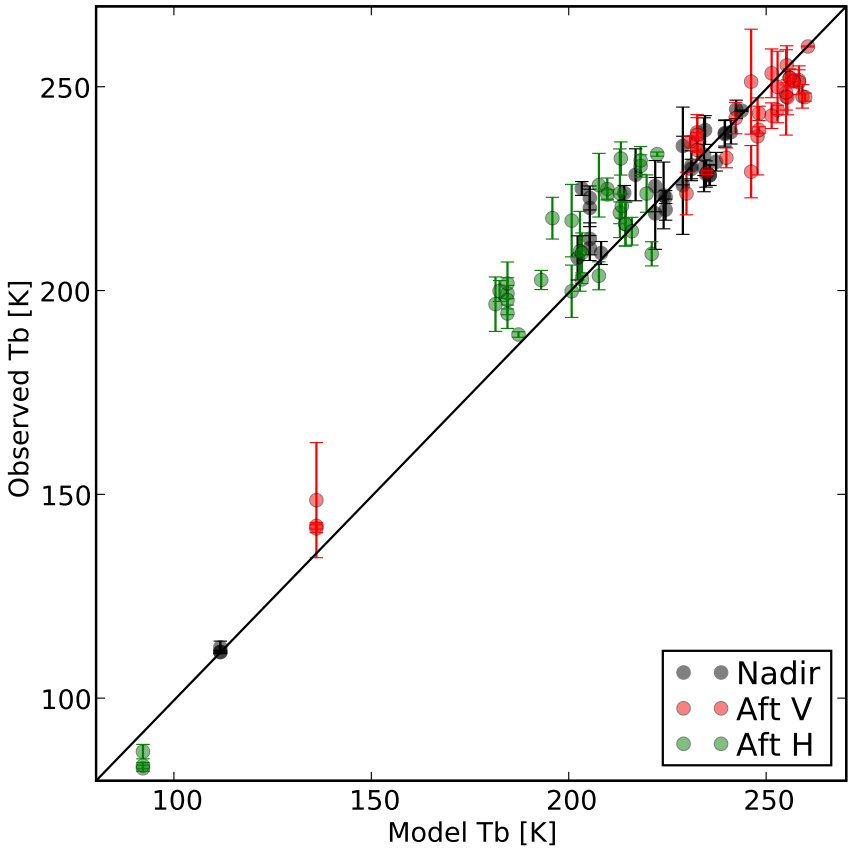

Figure 4.8: Modeled and observed brightness temperature. The error bars represent the standard deviation of the brightness temperature for the according section of homogeneous thickness. The standard deviation of the difference of modeld and observed brightness temperature is about 7 K for all four channels. The correlation of model and observation is 0.98.

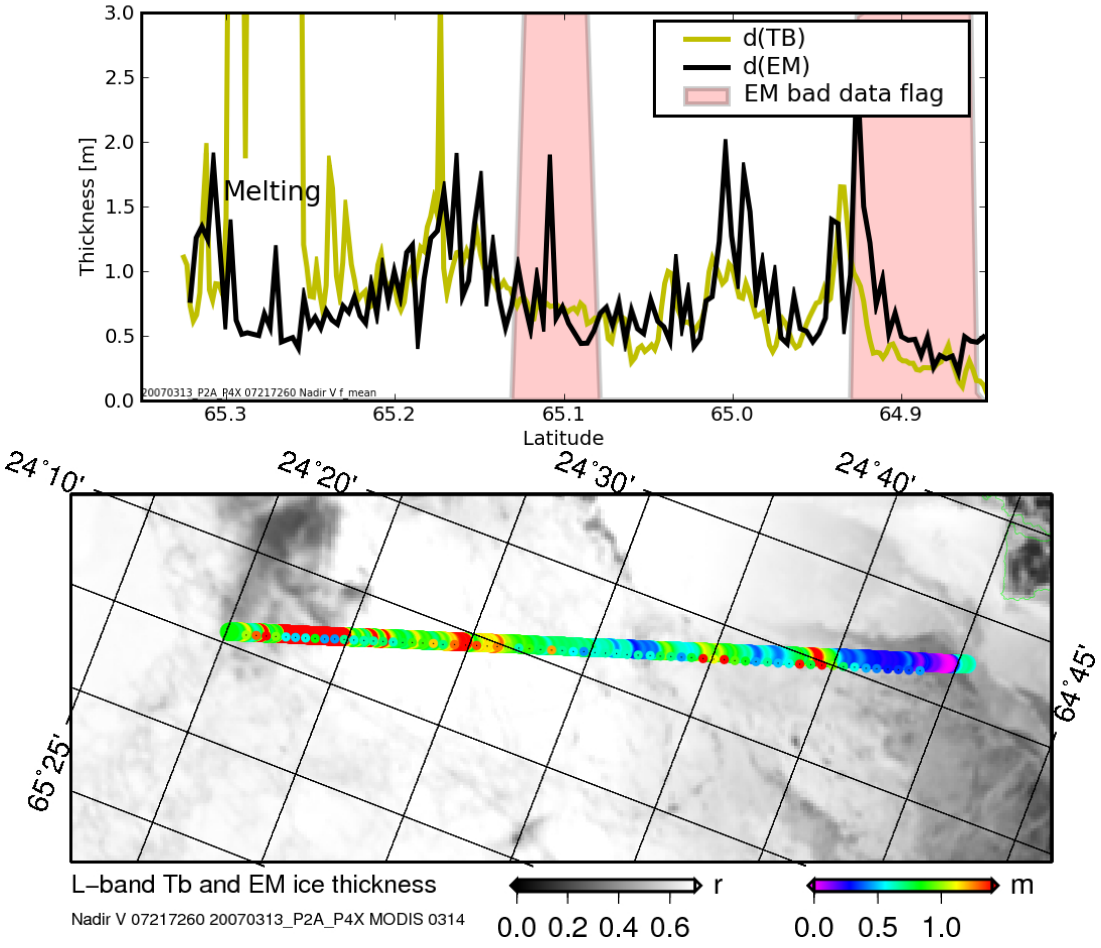

Figure 4.9: Thickness from Radiometer and EM from the flight of 13th March 2007. The upper graph shows the EM thickness with the thickness derived from the brightness temperature. The possible influence of the bathymetry is indicated with the red boxes. The lower graph shows the flight track and the color coded thickness overlaid on a MODIS image of 14th March 2007. The smaller dots indicate the helicopter EM and the larger dots the SkyVan EMIRAD measurements. The size of the footprints are not in scale. The EMIRAD and EM data was averaged over 200 and 100 samples, respectively.

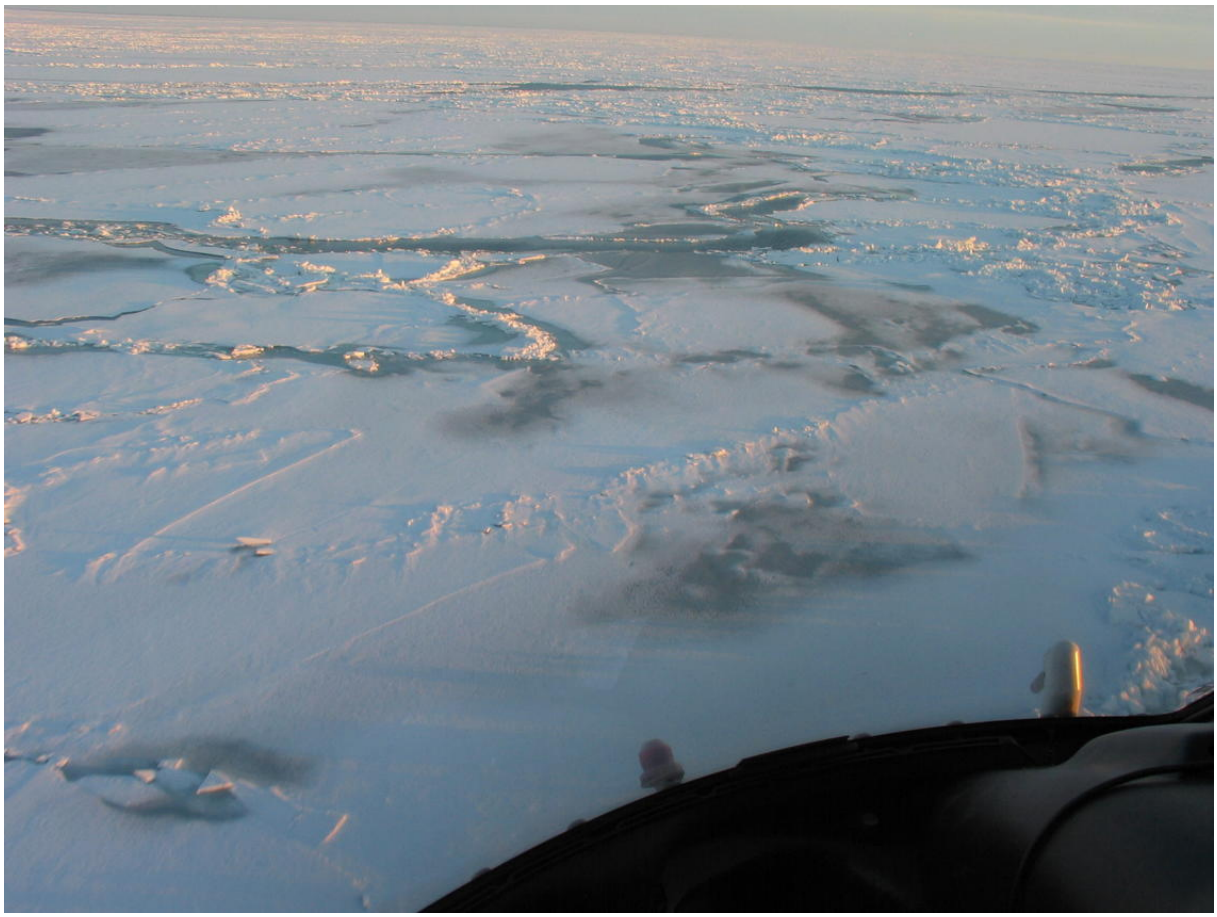

Figure 4.10: Melt ponds on the flight of 13 March 2007. Photograph courtesy of Juha Karvonen (FIMR).

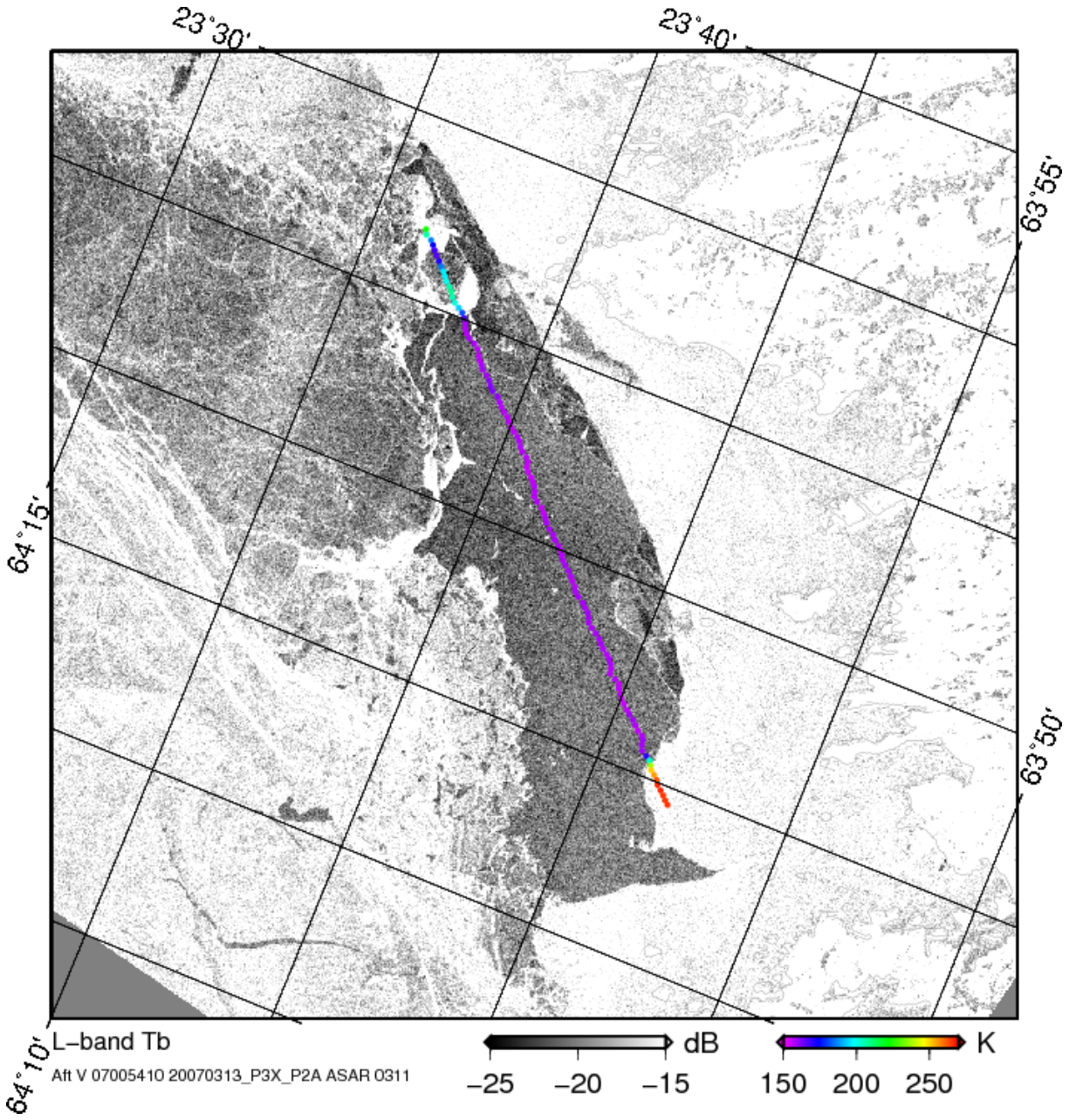

Figure 4.11: ASAR APP HH image of sea ice and open water 11 March

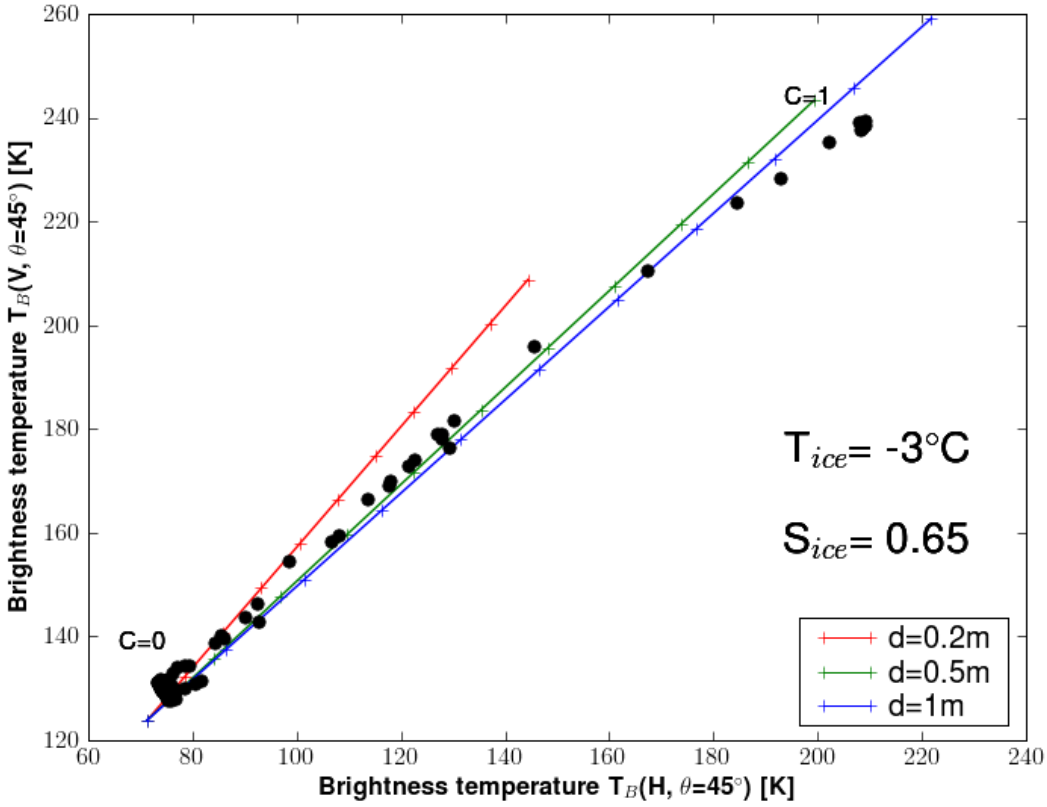

Figure 4.12: Covariance of ice thickness and concentration. The black circles indicate the aft beam measurements on 11 March over a partly ice covered area as shown in Fig. 4.11. The coloured lines are model results for different ice thicknesses d and different ice concentrations in 10 % steps as indicated with the crosses.

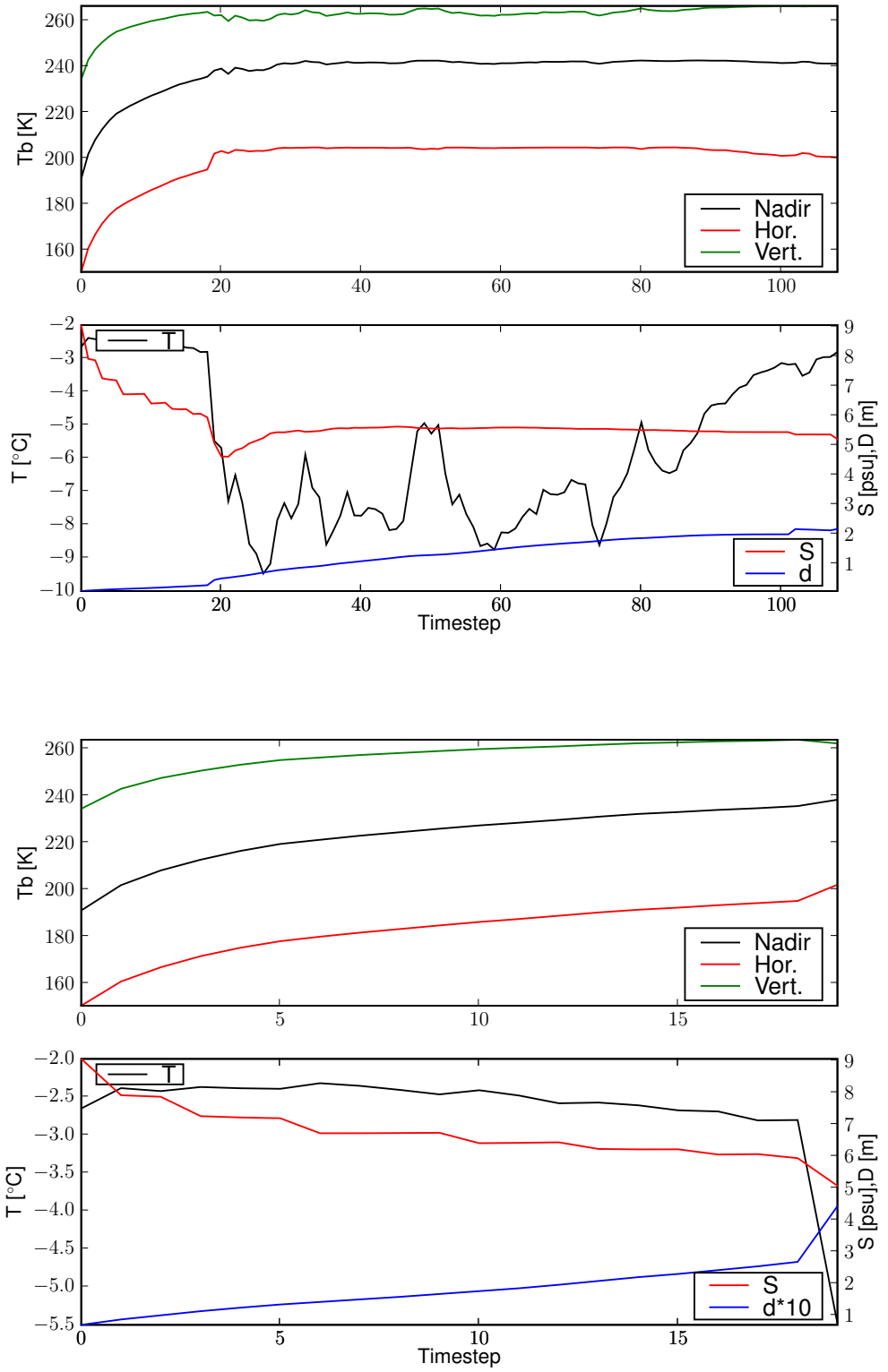

Figure 4.13: First year ice case 1. The simulation run started in January.

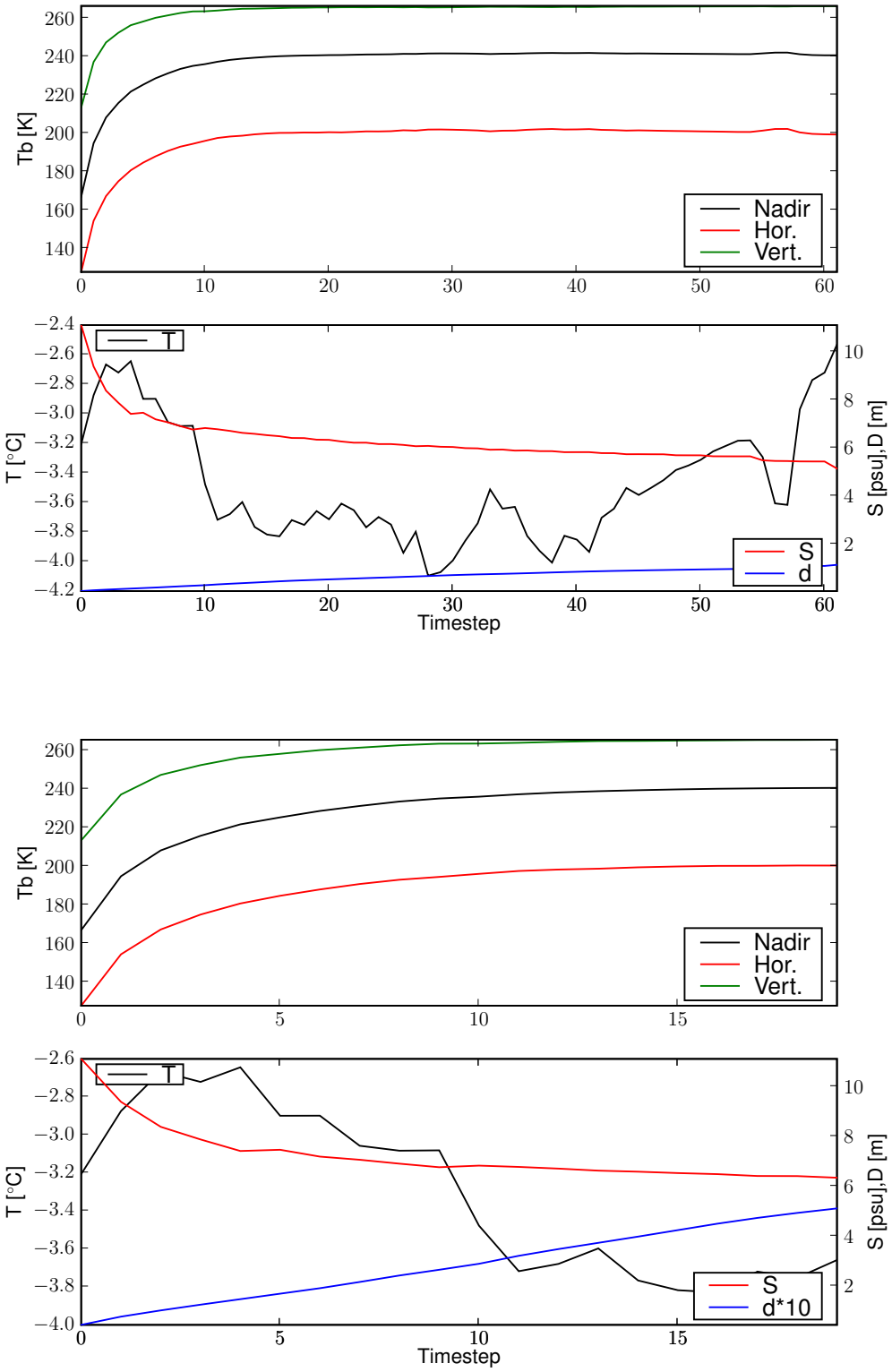

Figure 4.14: First year ice case 2. The simulation run started in September.

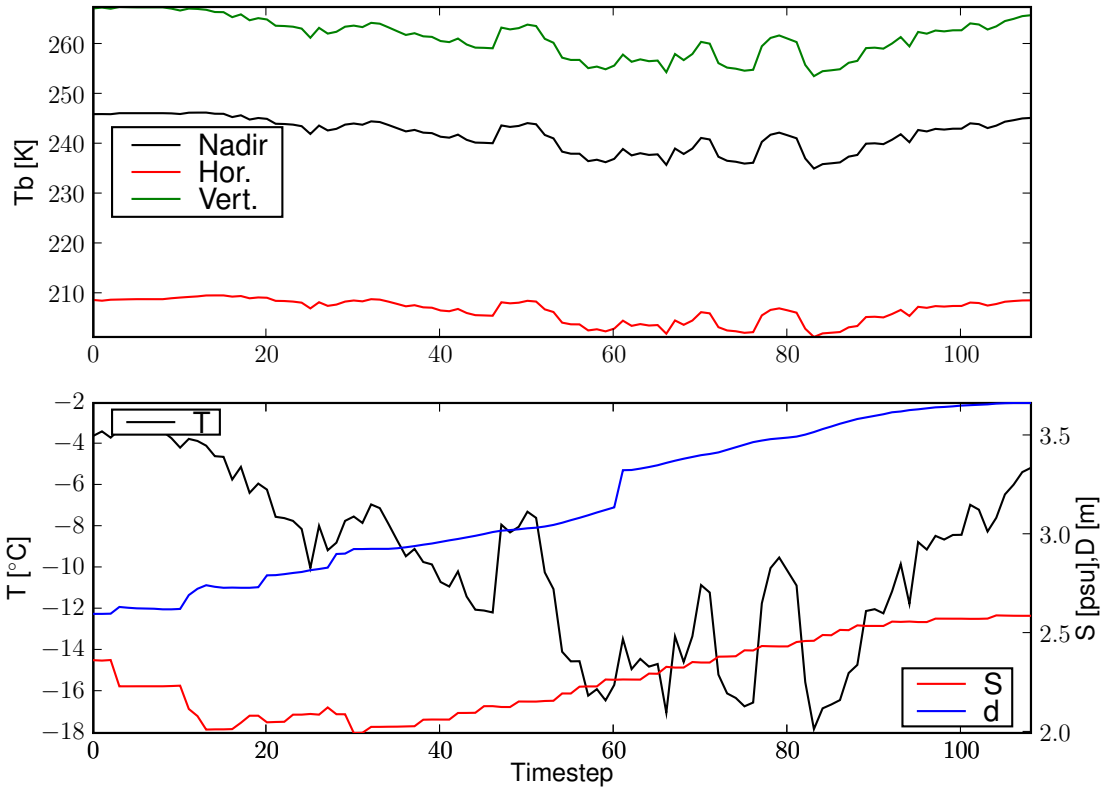

Figure 4.15: Multiyear ice

4.5 Errors of the thickness retrieval

The incoherent solution (Fig. 4.3) shows a monotonic increase of brightness temperature for increasing ice thickness. This allows to calculate the sea ice thickness from the measured brightness temperature with some further assumptions about the ice temperature T, ice bulk salinity S, ice surface roughness σ_d and ice concentration C. The latter set of parameters is in the following simply called ice parameters. The retrieval function is shown in Fig. 4.16 together with the resulting retrieval error for a $\pm 5\%$ uncertainty of the brightness temperature. The error is asymmetric for a symmetric error in brightness temperature. It should be noted that towards larger ice thickness the error becomes infinitely large. The thickness that corresponds to the sharp increasse of the upper errorbar is henceforth called the saturation thickness.

The superposition principle is the assumption for the model (eq. 4.1). This principle results in a mixture equation for the two surface types ice and water. For constant ice parameters the brightness temperature is a linear function of the ice concentration. Thus, errors of the ice concentration propagate linearly in the ice thickness retrieval error. The retrieval error for the ice concentration is in the order of 5% for high ice concentrations (Andersen et al., 2007). With this relation one can state that the retrieval error for ice thickness is in the same order of magnitude for thin ice but increases sharply as the thickness approaches the saturation level.

A model assumption is on the one hand a pure thermodynamic ice thickness distribution which means that the ice cover has a spatial uniform thickness. On the other hand, some extent of ice thickness variability (or roughness) is needed for the incoherent assumption. A sea ice cover that is grown in a divergent condition may well fullfill both assumptions. Under convergent conditions the thickness distribution has a long tail caused by the dynamic ice thickness redistribution (e.g. ridging). Thus, the model assumptions are not anymore fullfilled.

Consider the following Gedankenexperiment: The ocean surface is totally ice covered (100% ice concentration). 90% of the surface has a thickness of 10cm and 10% has a thickness of 10m. The saturation thickness is 50 cm. The actual mean ice thickness is 1.09m but the retrieved ice thickness would be only 14cm because the sensors sees only 50 cm of the 10m ice.

The conclusion is that the retrieval should only be interpreted in terms of the thermodynamic (modal) ice thickness or as a lower boundary of the ice volume. The actual mean ice thickness or ice volume could be much larger.

4.6 Discussion and conclusions

We described a model for the L-band emissivity of sea ice and open water that could be used for the interpretation of the data. The model is a suitable candidate for the retrieval of ice thickness because of the low model complexity.

The model degrees of freedom are limited and the needed information could be obtained from other sources. The most important model parameters beside incidence angle, ice thickness, and ice concentration are the ice surface roughness, the ice bulk temperature and the ice bulk salinity.

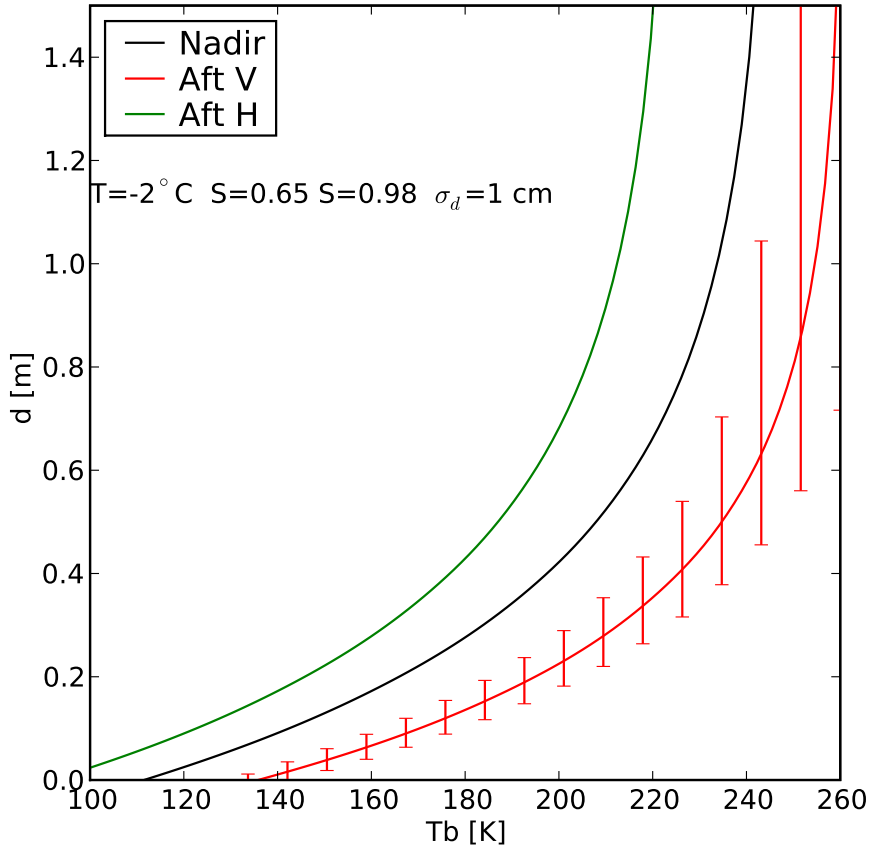

Figure 4.16: Inversion of the emissivity model to calculate thickness from brightness temperature. The error bars indicate the deviation in ice thickness for a brighntess temperature change of $\pm$ 5%.

4.6.1 Ice concentration

Ice concentration can be measured from independent sensors such as SSM/I or AMSR-E. Or it can be assumed that the ice concentration is almost 100% for ice within the ice edge in Arctic Winter.

4.6.2 Ice temperature

The ice surface temperature could be obtained from IR data, or better, the ice interior temperature at a frequency of 7 GHz from AMSR-like instruments. The bulk temperature can be calculated from the surface temperature with knowledge about the snow cover. The sensitivity of the emissivity to changes of the ice temperature decreases with decreasing temperature and is greatest close to the melting point. Although the measurements described here were conducted under non-favourable conditions at temperatures close to 0°, the results obtained under these circumstances seem to be very promising for the possibility of sea ice thickness retrieval using SMOS.

4.6.3 Ice salinity

As it seems to be not feasible to retrieve ice thickness and salinity simultaneaously, the salinity has to be prescribed or parameterized. The bulk salinity of sea ice can be parameterized as a function of thickness in the case of arctic sea ice. New measurements would be of advantage since the usual coring method leads to a significant underestimation of the bulk salinity due to drainage from the lower parts of the cores (Notz et al., 2005).

4.6.4 Ice roughness

The influence of the surface roughness σ_d deserves further investigations but the sensitivity seems to be small, at least for larger ice thicknesses. The transition of open water to a very thin ice cover falls outside the assumptions for the incoherent solution. A parameterization of the sea ice roughness as a percentage of ice thickness seems to be a promising approach since this leads to a meaningful asymptotic behavior towards vanishing ice thickness. However, measurements over thin ice (0-40cm) would be necessary for the investigation of the validity of this parameterization.

4.6.5 Ice thickness distribution and ice volume

The retrieval model assumes only two surfaces, open water and ice with a uniform ice thickness. The resulting retrieved thickness should be interpreted as the modal ice thickness and not the mean. Moreover, the resulting ice volume should not be interpreted as the mean volume but as a lower boundary estimate because of the asymetric retrieval error.

4.6.6 Conclusion

Salinity and roughness variations are probably very difficult to be retrieved from SMOS data. Therefore, these parameters have to be accounted for as a priori information and their sensitivity has to be studied. More ice thickness measurements in both Arctic and Antarctic are essential for the validation of a SMOS ice thickness algorithm. The timing and position of the thickness measurement is uncritical because of the good spatial and temporal coverage of the SMOS data which is of great advantage as compared to altimeters.

Overall, the results are quite promising that SMOS will have some potential for ice thickness or the lower boundary of ice volume retrieval. The sensitivity for Arctic ice thickness retrieval of up to half a meter is complementary to the capabilities of altimeter instruments. The thin ice plays an important role for heat exchange between the ocean and the atmosphere. Therefore, a SMOS based ice thickness product will be certainly useful for sea ice applications in climate research, meteorology, and perhaps even for operational services for the assistance of ship navigation in polar waters.

Acknowledgement

We thank Juha Karvonen and Markku Similä (FIMR) for meteorological informations and photographs, Sebastian Bathiany (Stud. Meteorology, University of Hamburg) for the coding of an early version of the emissivity model and the drawing of Fig. 4.2. We thank Christian Mätzler for revealing the errors in the equations of Menashi et al. (1993).

4.7 Appendix A - Selected homogeneous regions

The following table includes all brightness temperatures and nearby ice thickness measurements that have been plotted in Figure 4.7. Please note that the brightness temperatures listed in the table have been filtered (see below) but are not absolutely calibrated.

V	H	V	H	thickness [m]	track	samples
Nadir beam [K]		Aft beam [K]				
94.5 ± 1.5	104.6 ± 1.4	136.7 ± 14.1	78.4 ± 1.8	0.00 ± 0.00	07216200	11000 - 15000
93.3 ± 0.2	103.9 ± 0.3	130.3 ± 0.8	74.3 ± 0.8	0.00 ± 0.00	07005380	0 - 3159
93.4 ± 0.4	104.1 ± 0.5	129.7 ± 1.0	74.9 ± 0.8	0.00 ± 0.00	07005410	30000 - 40000
202.3 ± 4.6	208.4 ± 4.6	224.4 ± 2.4	190.8 ± 3.8	0.47 ± 0.25	07216200	33678 - 38825
220.9 ± 2.9	226.7 ± 2.8	235.7 ± 2.9	215.3 ± 4.6	1.42 ± 0.18	07216200	39878 - 40903
210.4 ± 6.4	216.5 ± 6.7	230.4 ± 3.9	209.2 ± 5.1	0.61 ± 0.10	07216200	46009 - 48069
207.1 ± 1.7	213.2 ± 1.5	224.6 ± 1.4	191.4 ± 2.6	0.45 ± 0.05	07216200	36794 - 37799
190.1 ± 5.4	195.6 ± 5.3	211.9 ± 5.2	188.1 ± 6.7	0.44 ± 0.04	07216200	50028 - 51961
212.2 ± 1.9	218.7 ± 1.9	235.7 ± 3.3	210.6 ± 2.7	1.01 ± 0.11	07216200	68178 - 70238
221.4 ± 3.5	227.7 ± 3.5	243.3 ± 4.8	223.9 ± 4.1	1.02 ± 0.10	07217010	5573 - 13319
210.6 ± 3.2	217.1 ± 3.4	235.5 ± 4.3	212.2 ± 2.9	1.03 ± 0.12	07217010	13319 - 17383
215.4 ± 9.1	221.8 ± 8.7	236.7 ± 10.5	215.4 ± 10.9	1.01 ± 0.12	07217010	42377 - 45470
205.4 ± 8.2	212.1 ± 8.0	225.9 ± 9.5	201.1 ± 9.8	0.73 ± 0.10	07217010	34624 - 39778
204.8 ± 2.9	211.8 ± 2.6	226.9 ± 4.3	189.1 ± 3.6	0.47 ± 0.06	07217010	50111 - 53117
206.0 ± 1.8	212.3 ± 1.7	220.7 ± 2.5	194.1 ± 2.4	0.57 ± 0.05	07217010	45961 - 47046
220.7 ± 3.2	226.7 ± 3.3	239.7 ± 3.5	222.0 ± 2.7	1.29 ± 0.20	07217260	32090 - 35176
212.7 ± 3.7	219.8 ± 3.6	238.0 ± 8.8	216.4 ± 2.7	0.90 ± 0.13	07217260	36160 - 37174
207.7 ± 6.3	213.8 ± 6.2	239.3 ± 12.9	208.6 ± 8.9	0.69 ± 0.10	07217260	10990 - 12974
220.4 ± 3.3	226.6 ± 3.3	239.2 ± 3.0	223.4 ± 3.4	1.29 ± 0.20	07217460	16170 - 19236
211.9 ± 2.4	218.8 ± 2.1	232.4 ± 1.1	215.1 ± 1.2	0.90 ± 0.13	07217460	14115 - 15133
201.0 ± 8.8	207.6 ± 8.6	217.3 ± 6.4	191.3 ± 6.4	0.69 ± 0.10	07217460	38178 - 40177
210.3 ± 2.5	217.0 ± 2.5	240.3 ± 2.1	207.8 ± 5.4	1.07 ± 0.09	07117250	2557 - 4602
191.3 ± 2.8	197.7 ± 2.7	217.0 ± 0.4	180.7 ± 0.7	0.50 ± 0.02	07117250	12986 - 13416
194.7 ± 3.9	203.1 ± 3.7	226.3 ± 4.2	193.2 ± 5.3	0.47 ± 0.03	07117410	42149 - 44764
205.0 ± 1.6	212.1 ± 1.7	231.6 ± 1.8	200.7 ± 4.9	0.74 ± 0.09	07117410	41082 - 41891
217.5 ± 9.5	225.0 ± 8.7	241.4 ± 6.0	217.3 ± 7.8	0.84 ± 0.13	07117410	28258 - 29347
192.5 ± 3.1	200.0 ± 3.5	222.6 ± 2.4	185.9 ± 3.7	0.47 ± 0.03	07116520	3540 - 6017
201.9 ± 2.6	208.8 ± 2.5	227.5 ± 0.8	194.2 ± 1.0	0.74 ± 0.09	07116520	6223 - 7094
207.9 ± 12.0	216.0 ± 11.2	231.0 ± 3.1	195.1 ± 3.4	0.84 ± 0.13	07116520	17658 - 18639
213.6 ± 2.3	222.2 ± 2.3	239.5 ± 1.7	206.0 ± 3.4	1.15 ± 0.11	07116520	14761 - 15159
226.5 ± 2.3	232.8 ± 1.7	235.5 ± 1.0	200.5 ± 3.0	1.57 ± 0.09	07116520	18443 - 18639
226.2 ± 0.2	233.1 ± 0.3	248.0 ± 0.1	224.9 ± 0.5	1.81 ± 0.19	07116520	23350 - 23567

4.8 Appendix B - EMIRAD tracks

This section gives an overview of the EMIRAD data that has been analysed. The following table summarises the tracks and their quality after processing with a despiking filter.

Useful EMIRAD tracks. Brackets mean limited quality

Track	Aft Beam	Nadir Beam
07002550	V, H	V, H
07116520	V, (H)	V, H
07117100	V, (H)	V, H
07117250	V, (H)	V, (H)
07117410	(V), H	V, H
07216160	V, H	V, H
07216200	(V), (H)	V, H
07217010	H	V, H
07217260	H	V, H
07217460	H	V, H
07307590	(V), (H)	(V), H
07308110	(V), (H)	(V), (H)

4.9 Appendix C - Source codes

4.9.1 Despiking filter code

A Sobel operator detects the high frequency noise (spikes). The absolute value is smoothed using a Gaussian filter with a width of 5 samples. This yields a signal S that is large for spiky data and small for a regular signal. The reciprocal of S is used for a weighted least-squares B-spline interpolation of the brightness temperature signal T. The resulting interpolation has therefore a large weight on the regular signal and ignores sporadic spikes. The filter used for the despiking of the brightness temperature signal T was developed using Scientific Python (`http://www.scipy.org`).

```
def peakedness_filter(T):
    S=ndimage.gaussian_filter(abs(ndimage.sobel(T)),5)
    t=arange(T.shape[0])
    tck=interpolate.splrep(t,T,w=1.0/S)
    return interpolate.splev(t,tck)
```

```
splrep(x, y, w=None,..)
    Find the B-spline representation of 1-D curve.

    Description:

      Given the set of data points (x[i], y[i]) determine a smooth spline
      approximation of degree k on the interval xb <= x <= xe.  The coefficients,
      c, and the knot points, t, are returned.  Uses the FORTRAN routine
      curfit from FITPACK.

    Inputs:

      x, y -- The data points defining a curve y = f(x).
      w -- Strictly positive rank-1 array of weights the same length as x and y.
           The weights are used in computing the weighted least-squares spline
           fit. If the errors in the y values have standard-deviation given by the
           vector d, then w should be 1/d. Default is ones(len(x)).
```

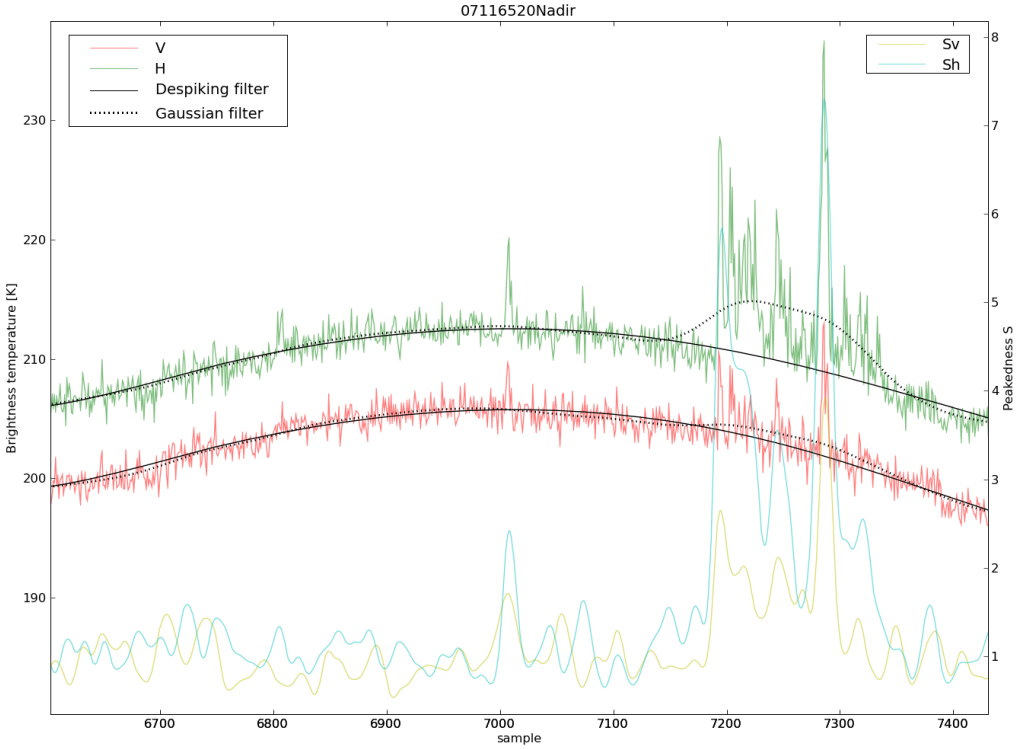

Figure 4.17: RFI despiking filter. Sv and Sh denotes the peakedness or spikedness S for the vertical and horizontal component, respectively.

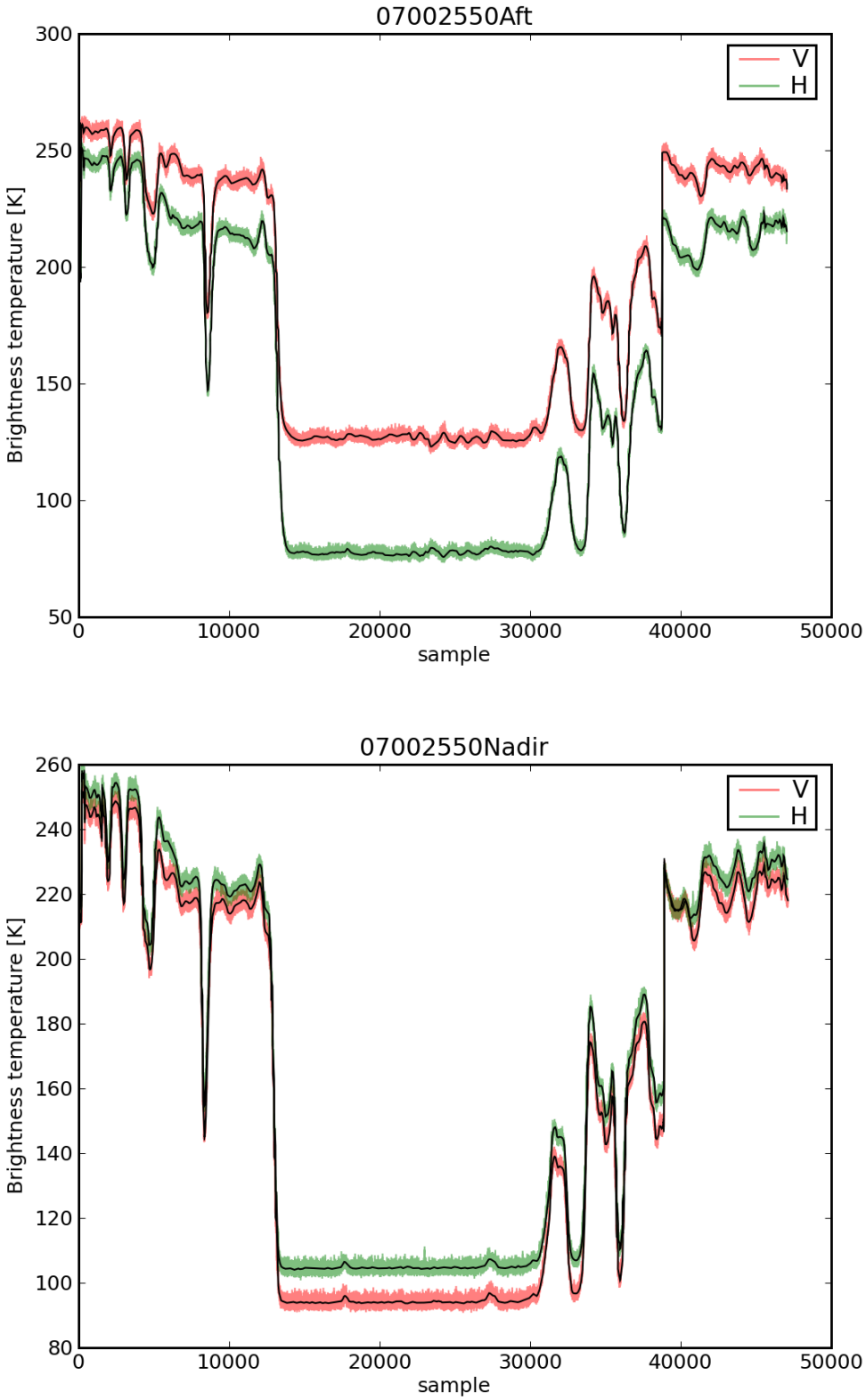

Figure 4.18: Track 07002550

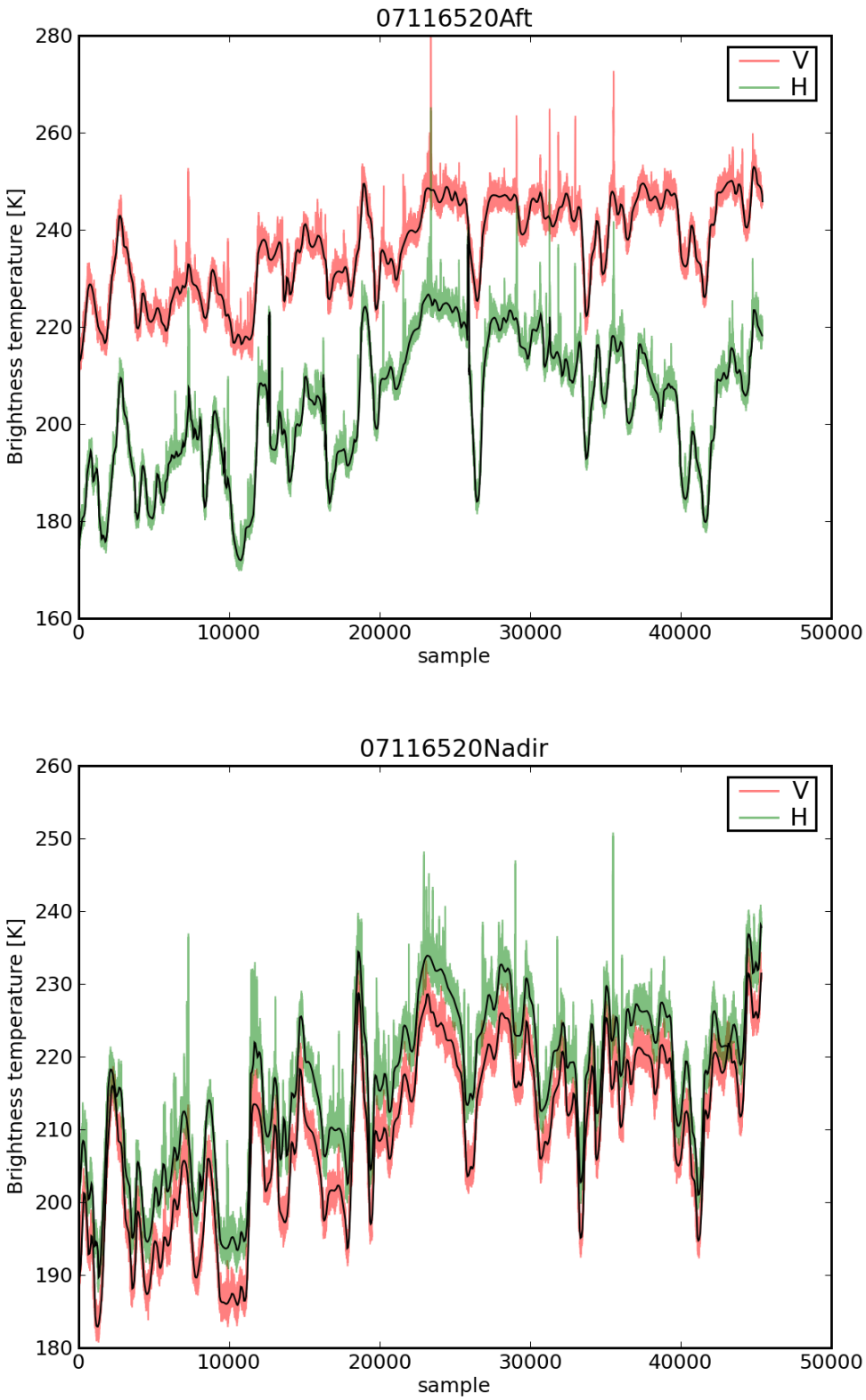

Figure 4.19: Track 07116520

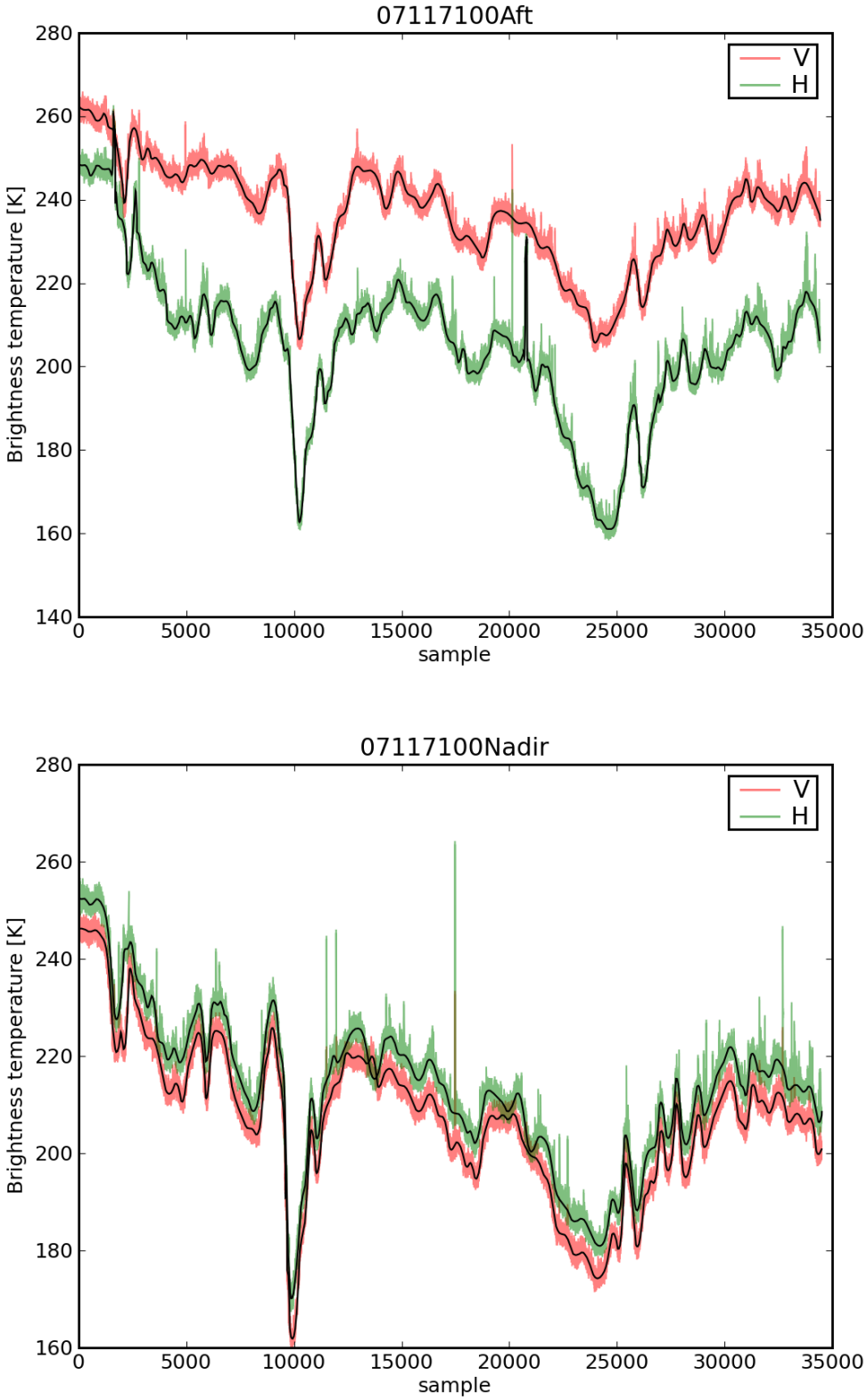

Figure 4.20: Track 07117100

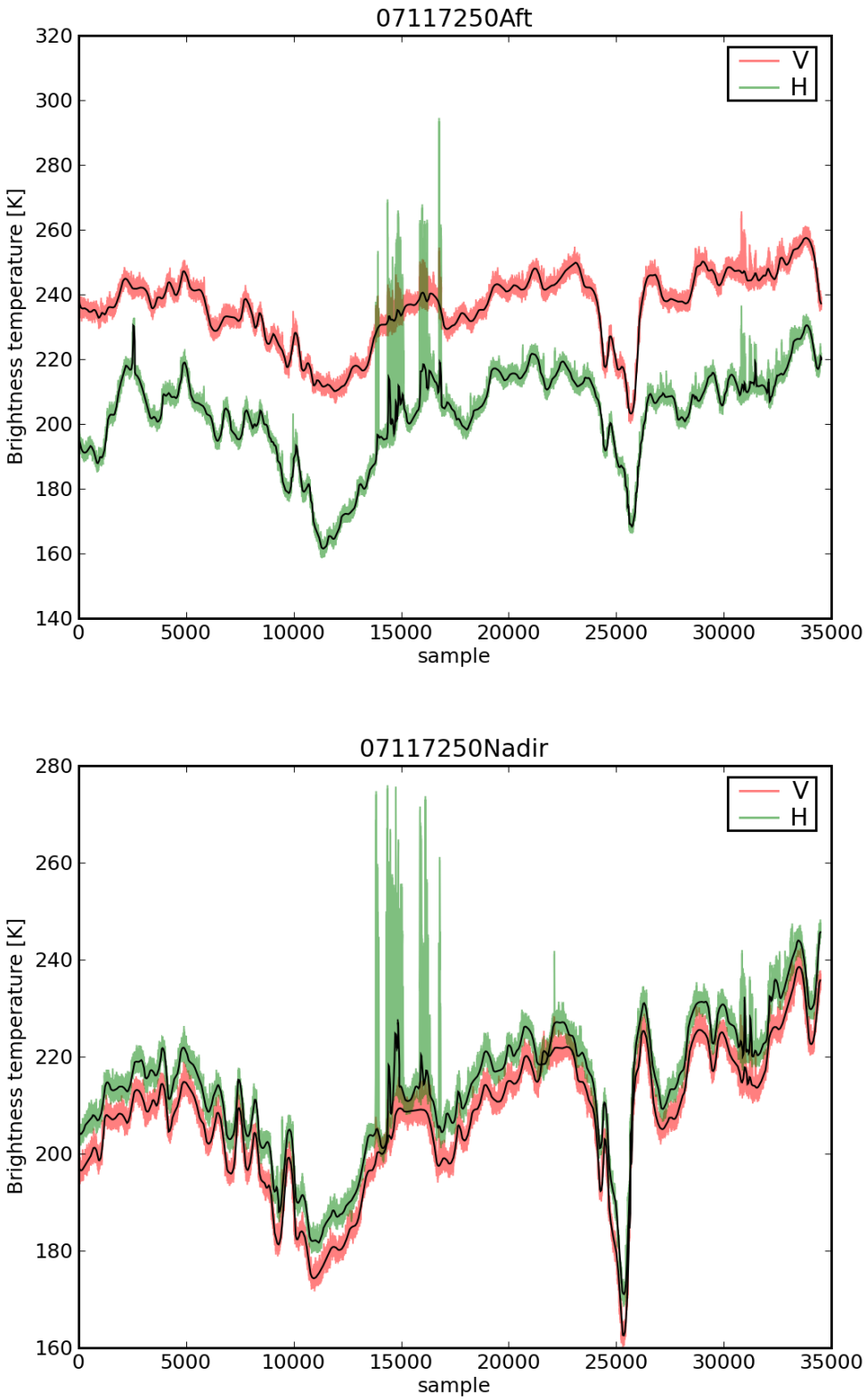

Figure 4.21: Track 07117250

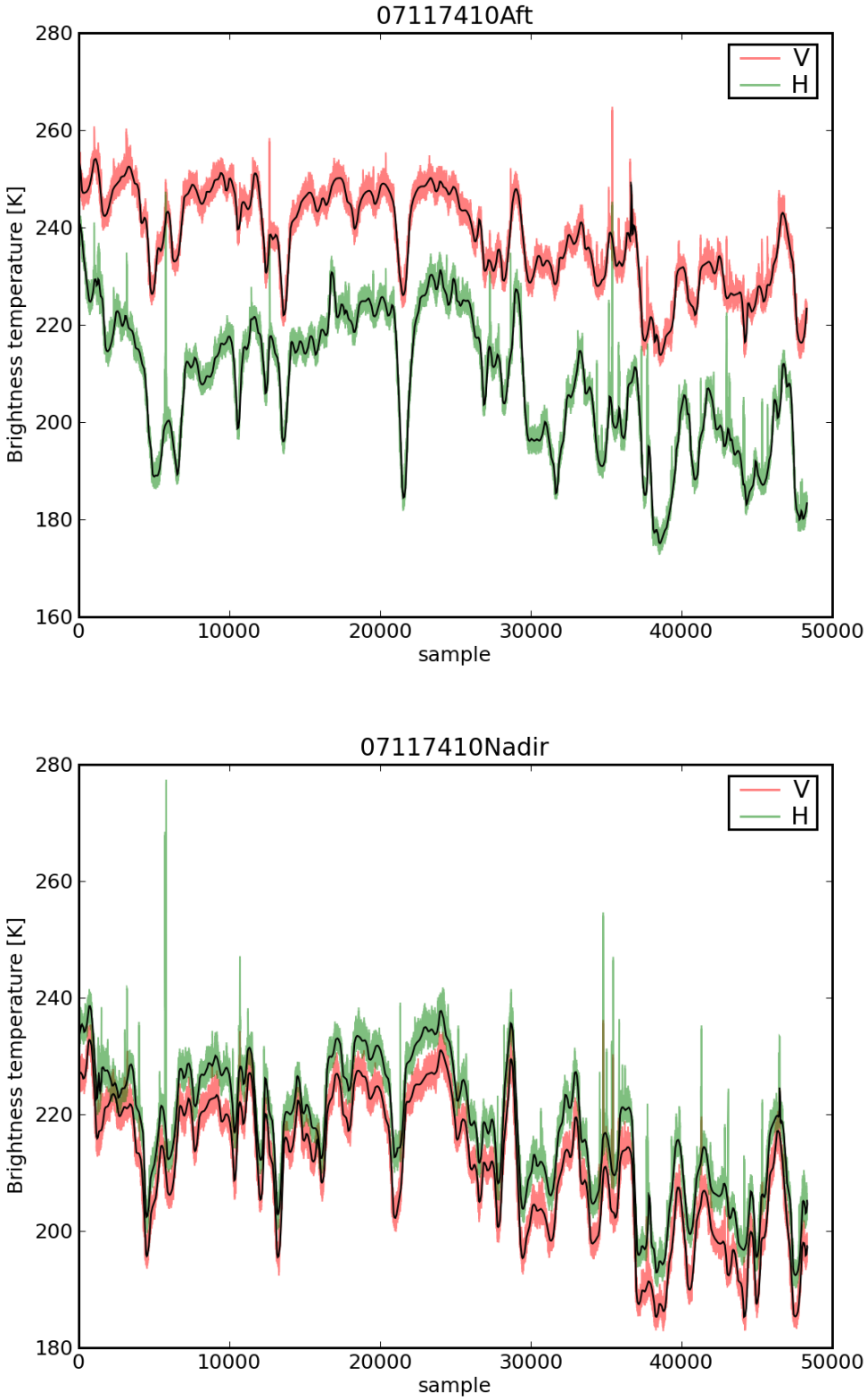

Figure 4.22: Track 07117410

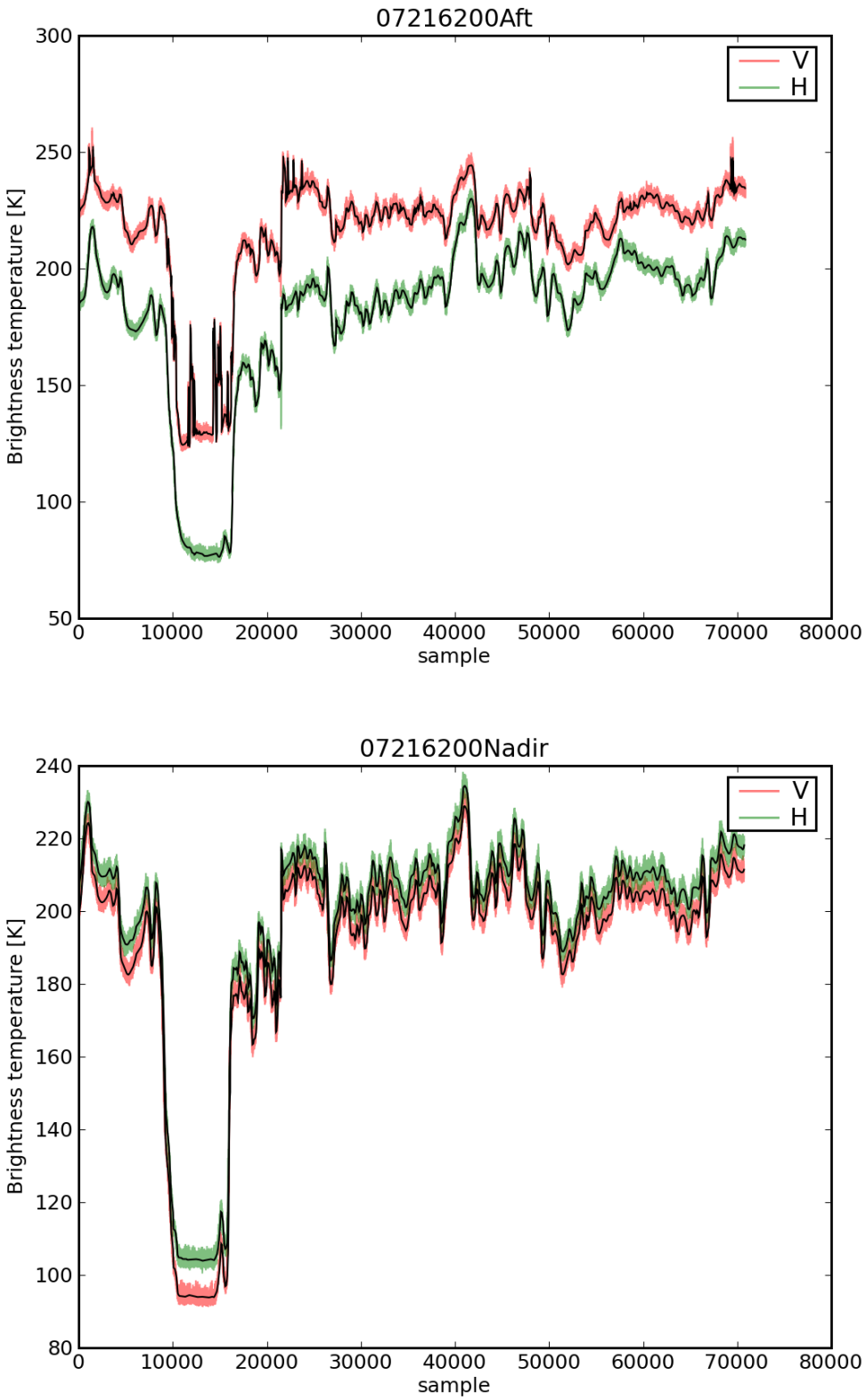

Figure 4.23: Track 07216200

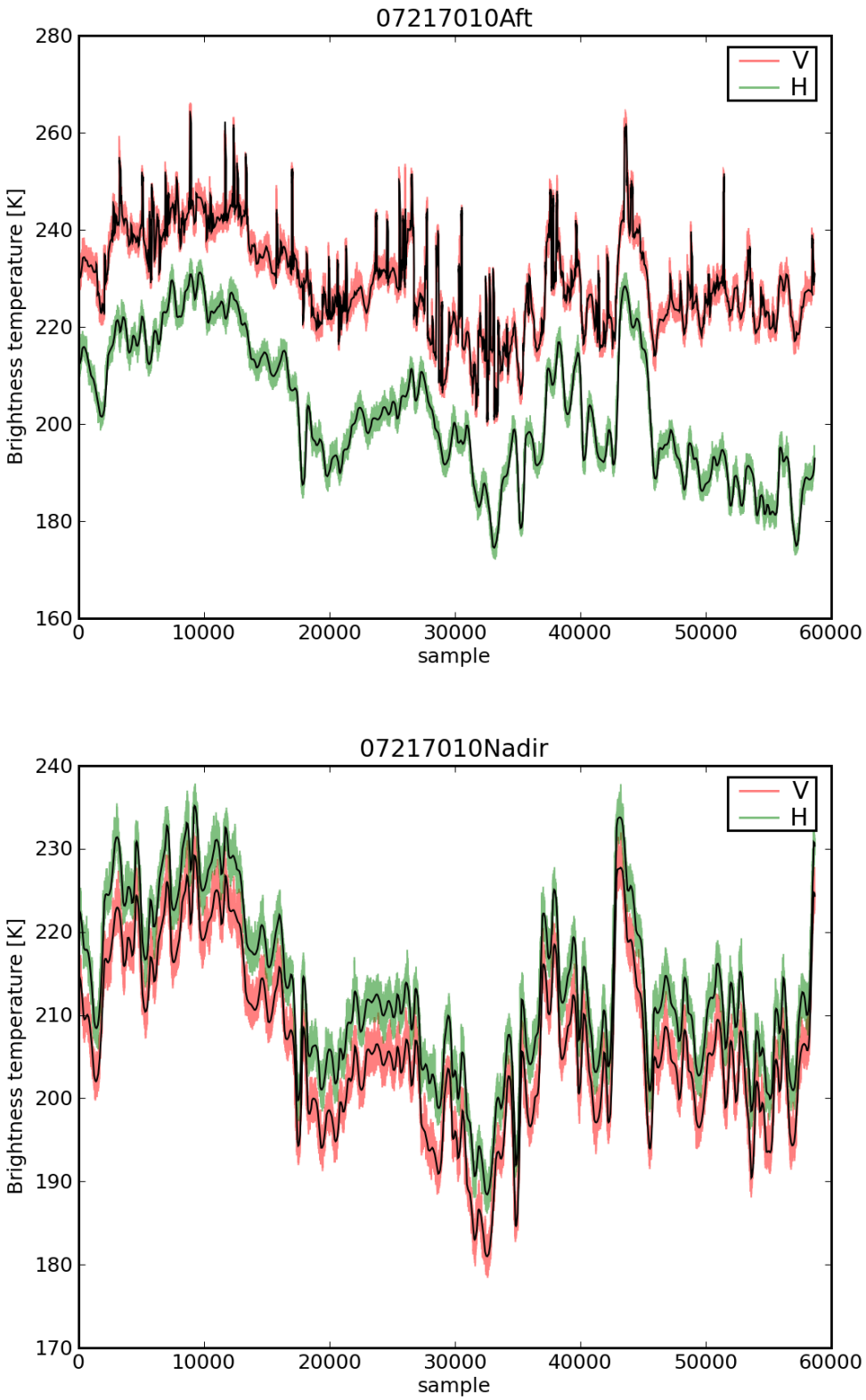

Figure 4.24: Track 07217010

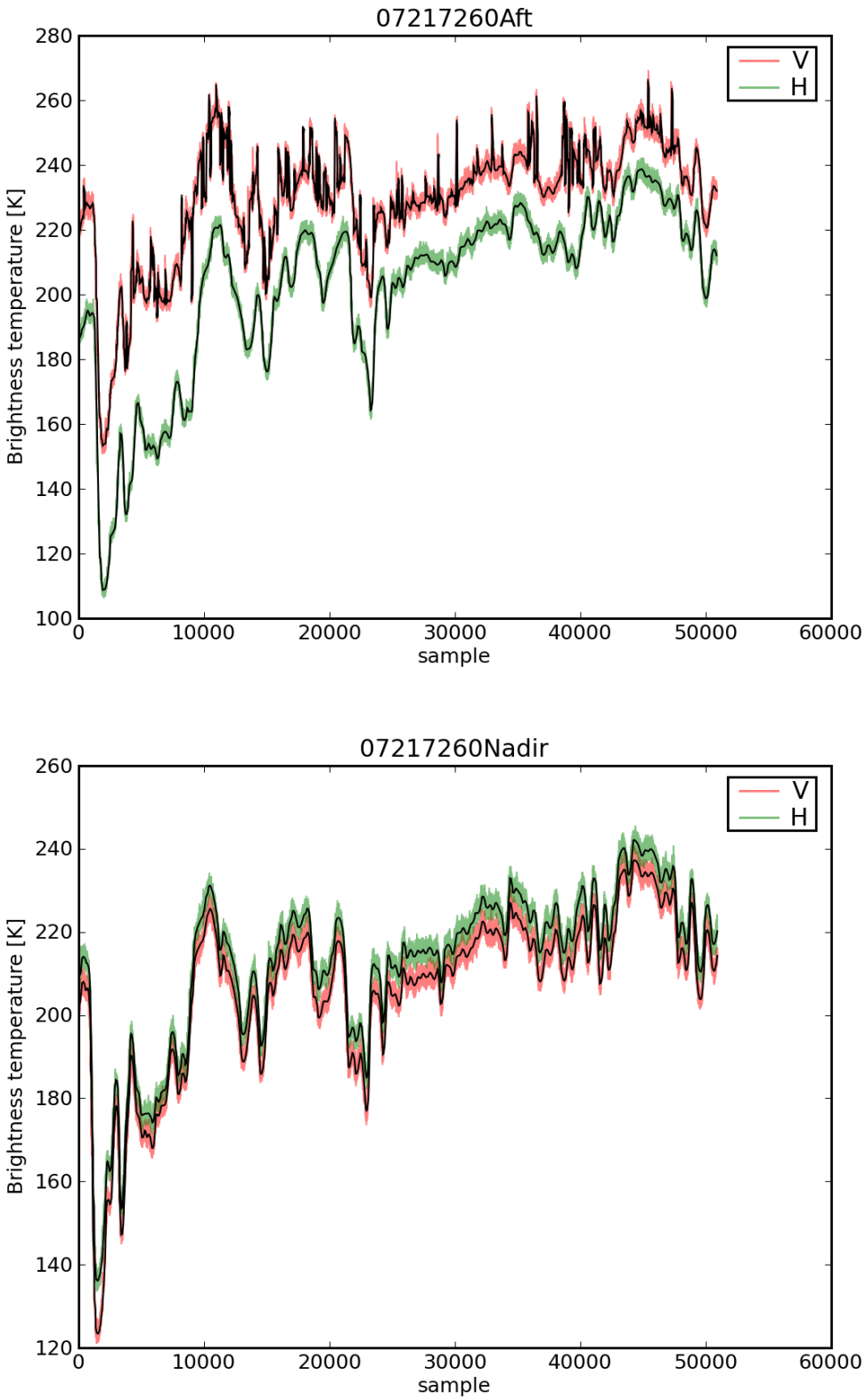

Figure 4.25: Track 07217260

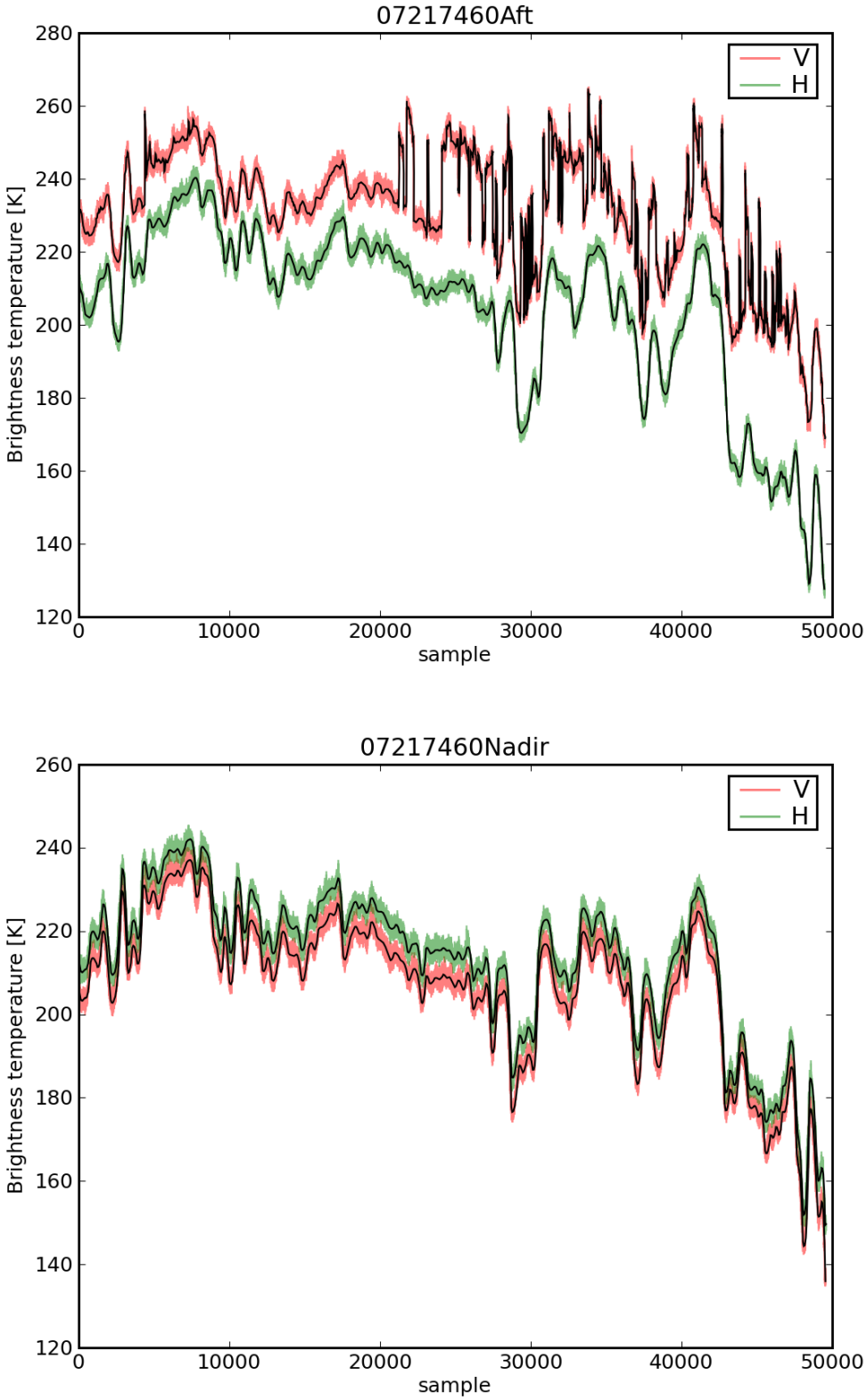

Figure 4.26: Track 07217460

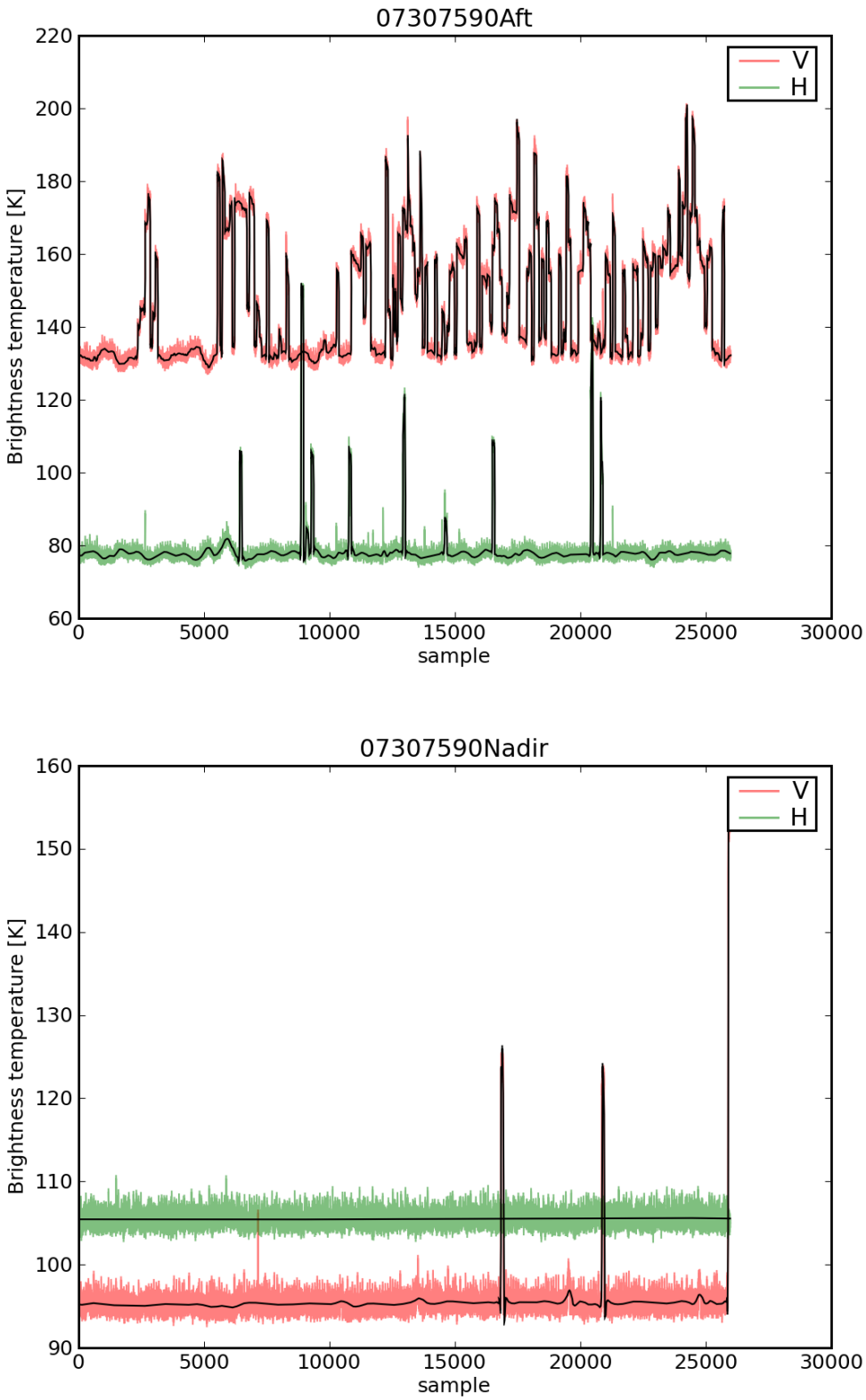

Figure 4.27: Track 07307590

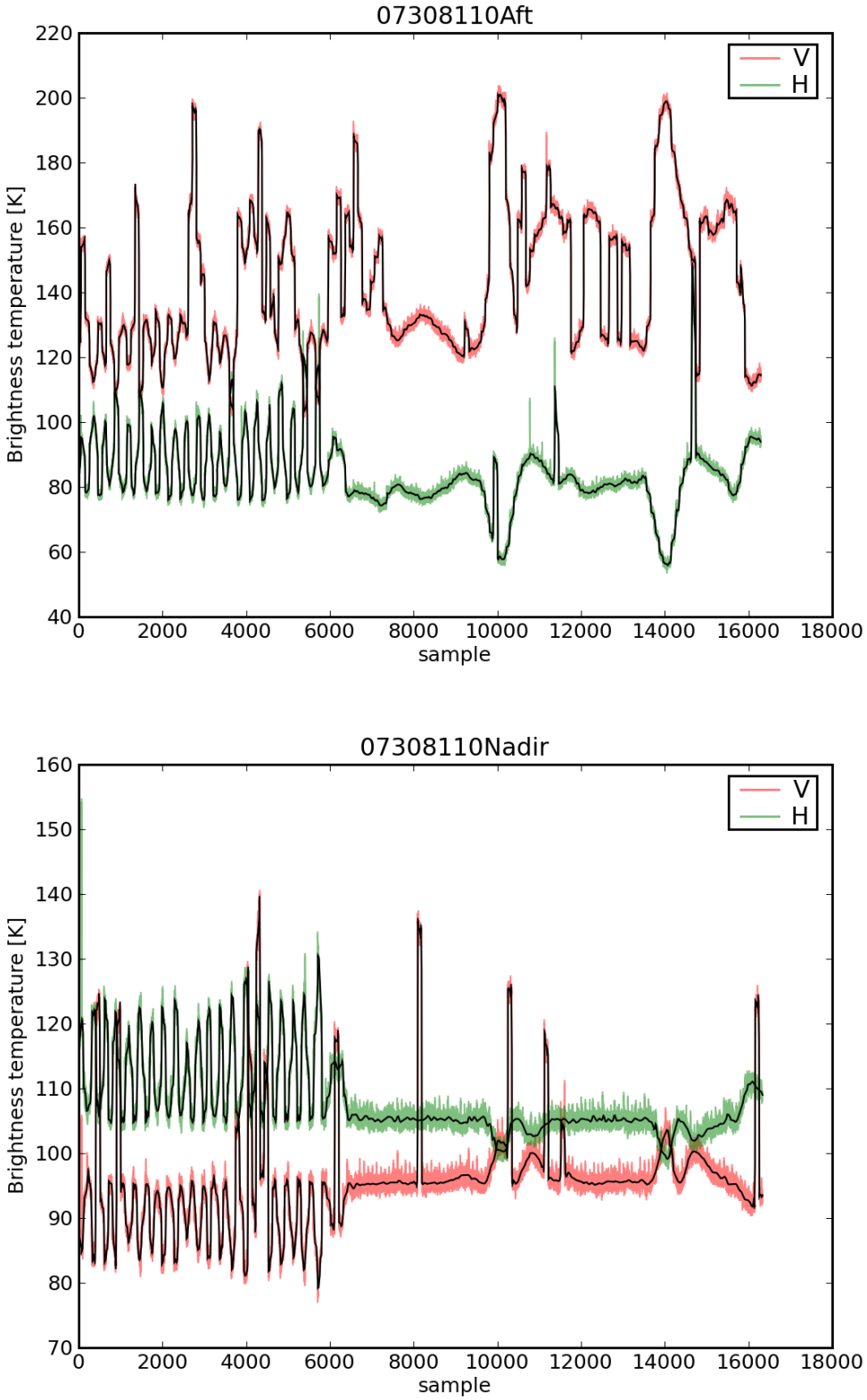

Figure 4.28: Track 07308110

Appendix D: Model sourcecode

4.9.2 Module: emissivity model

The following code is the implementation of the emissivity model as described in the report. An example main program can be found in the next section.

```
#radiation_model.py
from scipy import pi,linspace,arange,empty,zeros,mat,sin,cos,tan,sqrt,exp,arcsin,derivative,linalg,mean,std,array
from brine_volume import *

def brightness_temp(salinity,icetype,c0,f,T_water,S_water,T_ice,S_ice,theta,c,d,sigma_d):
    """Calculates brightness temperature for an slab of ice over water.
        Returns an array containing brightness temperature for horizontally and vertically polarised radiation
        at incidence angle theta and frequency f: array([TB_horizontal,TB_vertical]).
        Uses functions em_ice and em_water.
        Input parameters related to ice are ice thickness d and its variation sigma_d, concentration c, temperature
        T_ice, salinity S_ice (if known) and icetype (icetype = firstyear or multiyear). If ice salinity is not known
        an empirical relationship between ice thickness and ice salinity valid for Arctic conditions can be used
        (salinity = known or empirical).
        Required water parameters are temperature T_water and salinity S_water."""

    Tice=em_ice(salinity,icetype,c0,f,T_water,S_water,T_ice,S_ice,theta,d,sigma_d)*T_ice
    Twater=em_water(f,T_water,S_water,theta)*T_water
    TB=(1.-c)*Twater+c*Tice
    return TB

def theta_vec(theta):
    theta_vec=array([theta,theta])
    if theta==0.:
        N=array([1.,1.])
        H=array([0.,0.])
        V=array([0.,0.])
    else:
        N=array([0.,0.])
        H=array([1.,0.])
        V=array([0.,1.])
    return theta_vec,N,H,V

def em_ice(salinity,icetype,c0,f,T_water,S_water,T_ice,S_ice,theta,d,sigma_d):
    """Calculates emissivity of slab of ice over water using an incoherent approximation valid for a variety of ice
        thicknesses developed by Menashi et al. (1993). Menashi's equation has been corrected for an error concerning
        the product of wavenumber and pathlength.
        Returns an array containing ice emissivity for horizontally and vertically polarised radiation
        at incidence angle theta and frequency f: array([em_horizontal,em_vertical]).
        Uses functions eps_ice, eps_water and ref_coeff.
        Input parameters related to ice are ice thickness d and its variation sigma_d, temperature T_ice, salinity S_ice
        (if known) and icetype (icetype = firstyear or multiyear). If ice salinity is not known an empirical relationship
        between ice thickness and ice salinity valid for Arctic conditions can be used (salinity = known or empirical).
        Required water parameters are temperature T_water and salinity S_water."""

    thetavec=theta_vec(theta)[0]
    eps_w=eps_water(f,T_water,S_water)
    eps_i=eps_ice(d,T_ice,S_ice,icetype,salinity)
    ri,rw=ref_coeff(salinity,icetype,f,T_water,S_water,T_ice,S_ice,theta,d)
    theta_ice=arcsin(sin(thetavec)/sqrt(eps_i))
    k=2.*pi*f/c0
    alpha = k*cos(theta_ice)*abs(sqrt(eps_i).imag)
    beta = k*cos(theta_ice)*sqrt(eps_i).real
    A=exp(-4.*alpha*d)

    em_ice=(1.-ri)*(1.-A*rw)/(1.-A*ri*rw)*((1.-sqrt(A*ri*rw)*exp(-beta*sigma_d))/(1.+sqrt(A*ri*rw)*exp(-beta*sigma_d)))
    return em_ice

def ref_coeff(salinity,icetype,f,T_water,S_water,T_ice,S_ice,theta,d):
    """Calculates reflectivities of boundaries air-ice and ice-water using Fresnel equations.
        Returns reflectivity of boundary air-ice, reflectivity of boundary ice-water for incidence angle theta.
        Uses functions eps_ice and eps_water.
        Input parameters related to ice are ice thickness d, temperature T_ice, salinity S_ice (if known) and icetype
        (icetype = firstyear or multiyear). If ice salinity is not known an empirical relationship between ice thickness
        and ice salinity valid for Arctic conditions can be used (salinity = known or empirical).
        Required water parameters are temperature T_water and salinity S_water."""

    thetavec,N,H,V=theta_vec(theta)
    eps_w=eps_water(f,T_water,S_water)
    eps_i=eps_ice(d,T_ice,S_ice,icetype,salinity)
    thet1=N+arcsin(sqrt(1./eps_w)*sin(thetavec))
    thet2=N+arcsin(sqrt(1./eps_i)*sin(thetavec))
    ####
    ri=N*abs(((sqrt(eps_i)-1.)/(sqrt(eps_i)+1.)))**2 #nadir view
    rw=N*abs(((sqrt(eps_w/eps_i)-1.)/(sqrt(eps_w/eps_i)+1.)))**2  #nadir view
    ####
    ri=ri+H*abs((sin(thetavec-thet2)/sin(thetavec+thet2)))**2  #horizontal polarisation
    rw=rw+H*abs((sin(thet2-thet1)/sin(thet2+thet1)))**2  #horizontal polarisation
    ####
    ri=ri+V*abs((tan(thetavec-thet2)/tan(thetavec+thet2)))**2  #vertical polarisation
    rw=rw+V*abs((tan(thet2-thet1)/tan(thet2+thet1)))**2  #vertical polarisation
    return ri,rw
```

```
def eps_ice(d,T_ice,S_ice,icetype,salinity):
    """Calculates permittivity (dielectric constant) of ice for a frequency of 1.4 GHz.  The coefficients describing ice
       permittivity as a function of brine volume fraction introduced by Carsey for frequencies of 1 and 2 GHz are linearly
       interpolated.
       Returns complex ice permittivity.
       Uses functions Vb_empirical and Vb_known.
       Ice input parameters are thickness d, temperature T_ice, salinity S_ice (if known) and icetype (icetype = firstyear
       or multiyear). If ice salinity is not known an empirical relationship between ice thickness and ice salinity valid
       for Arctic conditions can be used (salinity = known or empirical)."""

    aa = 3.12-0.4*(3.12-3.07)          #value(1.4GHz)=value(1GHz)-0.4*(value(1GHz)-value(2GHz))
    bb = 0.009-0.4*(0.009-0.0076)
    if icetype=='firstyear':
        cc = 0.039-0.4*(0.039-0.034)
        dd = 0.00504-0.4*(0.00504-0.00356)
    elif icetype=='multiyear':
        cc = -0.004-0.4*(-0.004-0.013)
        dd = 0.00436-0.4*(0.00436-0.00435)
    if salinity=='empirical':
        constants2(T_ice)
        eps_ice = aa+bb*Vb_empirical(d,T_ice)+(cc+dd*Vb_empirical(d,T_ice))*1j
    elif salinity=='known':
        eps_ice = aa+bb*Vb_known(T_ice,S_ice)+(cc+dd*Vb_known(T_ice,S_ice))*1j
    return eps_ice

def eps_water(f,T_ice,S_ice):
    """Calculates permittivity (dielectric constant) of water using an empirical relationship described
       by Klein and Swift (1976).
       Returns complex water permittivity for a frequency f.
       Water input parameters are temperature T_water and salinity S_water."""
    T=T_ice-273.15
    S=S_ice
    omega=2*pi*f
    eps_0=8.854*10**(-12)
    eps_inf=4.9
    ####
    eps_s_T=87.134-1.949*10**(-1)*T-1.276*10**(-2)*T**2+2.491*10**(-4)*T**3
    a_ST=1.+1.613*10**(-5)*S*T-3.656*10**(-3)*S+3.210*10**(-5)*S**2-4.232*10**(-7)*S**3
    eps_s=eps_s_T*a_ST
    ####
    tau_T0=1.768*10**(-11)-6.086*10**(-13)*T+1.104*10**(-14)*T**2-8.111*10**(-17)*T**3
    b_ST=1.+2.282*10**(-5)*S*T-7.638*10**(-4)*S-7.760*10**(-6)*S**2+1.105*10**(-8)*S**3
    tau=tau_T0*b_ST
    ####
    delta=25-T
    beta=2.0333*10**(-2)+1.266*10**(-4)*delta+2.464*10**(-6)*delta**2-S*(1.849*10**(-5)-2.551*10**(-7)*delta+2.551*10**(-8)*delta**2)
    sigma_25S=S*(0.182521-1.46192*10**(-3)*S+2.09324*10**(-5)*S**2-1.28205*10**(-7)*S**3)
    sigma=sigma_25S*exp(-delta*beta)
    ####
    eps_water=eps_inf+(eps_s-eps_inf)/(1+1j*omega*tau)-1j*sigma/(omega*eps_0)
    #eps_water=77.9-81.5*1j
    return eps_water

def em_water(f,T_water,S_water,theta):
    """Calculates water emissivity using Fresnel equations.
       Returns an array containing water emissivity for horizontally and vertically polarised radiation
       at incidence angle theta and frequency f: array([em_horizontal,em_vertical]).
       Water input parameters are temperature T_water and salinity S_water."""
    thetavec,N,H,V=theta_vec(theta)
    eps_w=eps_water(f,T_water,S_water)
    em_waterH= (1.-abs((cos(thetavec)-sqrt(eps_w-sin(thetavec)**2))/(cos(thetavec)+sqrt(eps_w-sin(thetavec)**2)))**2)#horizontal
    em_waterV= (1.-abs((eps_w*cos(thetavec)-sqrt(eps_w-sin(thetavec)**2))/(eps_w*cos(thetavec)+sqrt(eps_w-sin(thetavec)**2)))**2)#vertical
    em_water=em_waterH*H+em_waterV*V+em_waterV*N
    return em_water
```

4.9.3 Module: Brine volume

```
#brine_volume.py
from scipy import pi,linspace,arange,empty,zeros,ones,mat,sin,cos,tan,sqrt,exp,arcsin,derivative,linalg,mean,std
from scipy.interpolate import *

#Computing relative brine volume of ice

#############################################################################################
#salinity='empirical'

def Vb_dis(d,T_ice):
    # computing S_brine:
    T = T_ice - 273.15     #polynomial approximations for dependency brine salinity - ice temperature (Vant et al.)
    if (T < -36.8):
       S_brine = 508.18 + 14.535*T + 0.2018*T**2.
    elif (T < -22.9):
       S_brine = 242.94 + 1.5299*T + 0.0429*T**2.
    elif (T < -8.2):
       S_brine = 57.041 - 9.929*T-0.16204*T**2.-0.002396*T**3.
```

```
    elif (T < -2.):
        S_brine = 1.725 -18.756*T-0.3964*T**2.
    if (T >= -2. or T < -43.2):
        print "Ice temperature lies outside permitted range"
    #computing S_ice:
    ee = 14.24     #empirical relationship ice salinity - ice thickness (Cox and Weeks)
    ff = -19.39
    gg = 7.88
    hh = -1.59
    ii = 0.4
    if d <= ii:
        S_ice = ee + ff*d
    else:
        S_ice = gg + hh*d
    #
    Vb_dis=(S_ice/S_brine)*1000.
    return Vb_dis

def Vb_empirical(d,T_ice):
    #fitting empirical relationship of Cox and Weeks to remove discontinuity:
    d_lower,d_upper = 0.,4.
    gridpoints=100

    d_emp = linspace(d_lower, d_upper, gridpoints)
    Vb_emp = empty([len(d_emp)])
    for i in range(len(d_emp)):
        Vb_emp[i] = Vb_dis(d_emp[i],T_ice)

    fit=splrep(d_emp,Vb_emp,s=5.)

    Vb = splev(d, fit)
    return Vb

#############################################################################################################
#salinity='known'

def Polynom(T,a0,a1,a2,a3):
    Polynom=a0+a1*T+a2*T**2+a3*T**3
    return Polynom

def Vb_known(T_ice,S_ice):
    T=T_ice - 273.15
    S=S_ice
    if T < -2. :
        #T1=-54.11
        #Sb=T/(T1+T)*1000. gilt nur bis etwa -8 grad C
        if (T < -22.9) and (T >= -30.):
            Sb = 242.94 + 1.5299*T + 0.0429*T**2.
        elif (T < -8.2):
            Sb = 57.041 - 9.929*T-0.16204*T**2.-0.002396*T**3.
        elif (T < -2.):
            Sb = 1.725 -18.756*T-0.3964*T**2.
        else:
            print 'Ice temperature outside permitted range'
        rho_brine=1+0.0008*Sb
        rho_ice=0.917-1.403*10**(-4)*T
        if T >= -22.9:
            a0=-4.732
            a1=-2.245*10
            a2=-6.397*10**(-1)
            a3=-1.074*10**(-2)
        else:
            a0=9.899*10**3
            a1=1.309*10**3
            a2=5.527*10
            a3=7.160*10**(-1)
        F1=Polynom(T,a0,a1,a2,a3)

        Vb=1000.*S*rho_ice/(F1+S*rho_ice-S*rho_brine)

    elif T >= -2. :
        rho_ice=0.917-1.403*10**(-4)*T
        a0=-4.1221*10**(-2)
        a1=-1.8407*10
        a2=5.8402*10**(-1)
        a3=2.1454*10**(-1)
        b0=9.0312*10**(-2)
        b1=-1.6111*10**(-2)
        b2=1.2291*10**(-4)
        b3=1.3603*10**(-4)
        F1=Polynom(T,a0,a1,a2,a3)
        F2=Polynom(T,b0,b1,b2,b3)

        Vb=1000.*rho_ice*S/(F1-rho_ice*S*F2)

    return Vb
```

4.9.4 Main: model test

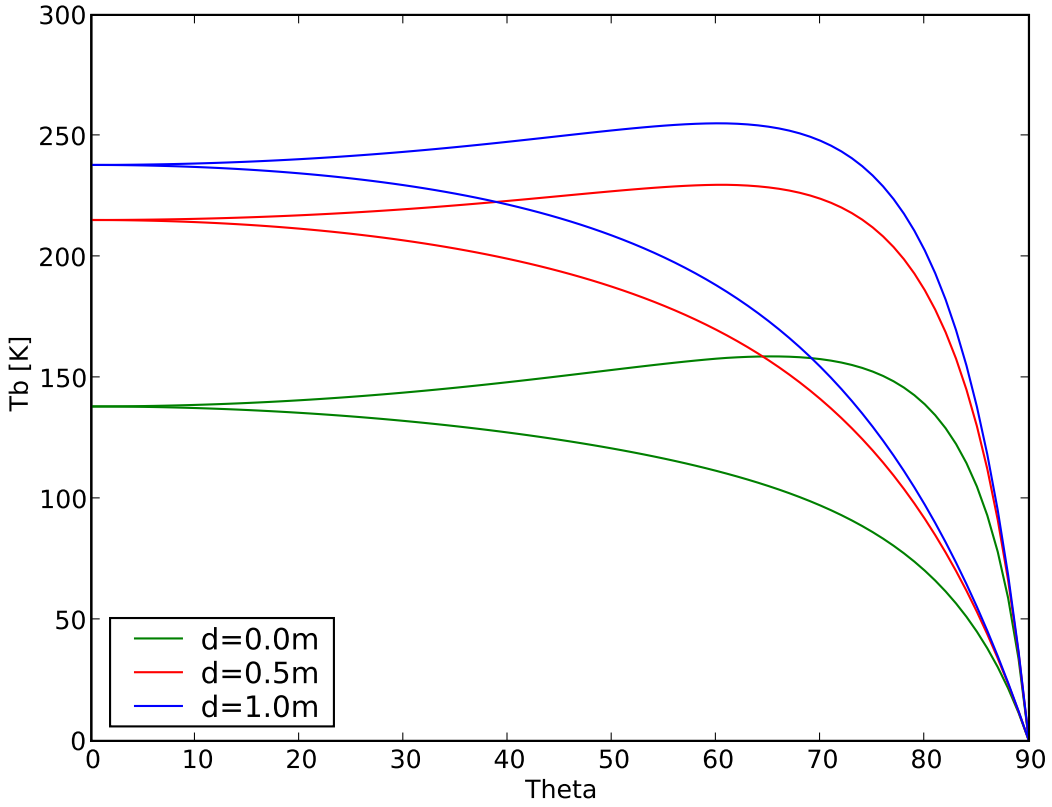

Figure 4.29: Brightness temperature calculated with the main script.

The following script calculates the brightness temperatures for a range of thicknesses as a function of incidence angle as shown in Fig. 4.29.

```
#
from pylab import *
from radiation_model import *

#lab.rc('text', usetex=True)
# c0                    speed of light in vacuum [m/s]
# T_water               water temperature [K]
# S_water               water salinity [psu]
# T_ice                 ice temperature [K]
# S_ice                 ice salinity [psu] (if known)
# f                     frequency [Hz]
# theta                 angle of incidence / observation
# c                     fraction of ice cover / ice concentration
# d                     ice thickness [m]
# sigma_d               ice thickness variation (roughness) [m]
# eps_water             complex rel. dielectric constant of water
# ri                    power reflection coefficient of boundary air to ice
# rw                    power reflection coefficient of boundary ice to water
# alpha                 attenuation coefficient in ice
# beta                  phase constant
# eps_ice               complex rel. dielectric constant of ice
# em_ice                emissivity of ice
# em_water              emissivity of open water
# Vb                    relative brine volume in ice / volume fraction of brine pockets [parts per thousand]

#########################################################################################################

##### Constants:
salinity='known' # Choose 'known' when ice salinity values are provided, use 'empirical' if not (empirical relationship
                 # between ice thickness and ice salinity, valid for cold ice in arctic regions, is used then)
icetype='firstyear'  #Choose 'multiyear' or 'firstyear'
c0 = 299792458.
```

```
f   = 1.4E09
T_water = -0.+ 273.15
S_water=5.
T_ice = -4. + 273.15  # <- must be < -2 degrees celsius for empirical approach
S_ice=0.65            # <- only used when salinity is set to 'known'
theta=40.*pi/180.
c=1.0
d=0.5
sigma_d=0.1


dn=91
theta_space=linspace(0.0,pi/2,dn)
D_space=linspace(0.0,1.0,3)

Tb_h=zeros((theta_space.size,D_space.size))
Tb_v=zeros((theta_space.size,D_space.size))

for di,dd in enumerate(D_space):
    for ti,tt in enumerate(theta_space):
        Tb_h[ti,di],Tb_v[ti,di]=brightness_temp(salinity,icetype,c0,f,T_water,S_water,T_ice,S_ice,theta_space[ti],c,D_space[di],sigma_d)


figure()
st=['g-','r-','b-','y-','k-']
for di,dd in enumerate(D_space):
    plot(theta_space*180/pi,Tb_v[:,di],st[di],label='d='+str(dd)+'m')
    plot(theta_space*180/pi,Tb_h[:,di],st[di])

xlabel('Theta')
ylabel('Tb [K]')
legend(loc=3)
show()
savefig('test_model.pdf')
```

Chapter 5

WP 2.3a Stokes components Tv, Th from combining thermodynamic and emissivity models

Rasmus T. Tonboe

Danish Meteorological Institute

5.1 Introduction

ESA's Earth explorer programme will launch the Soil Moisture and Ocean Salinity (SMOS) L-band radiometer satellite in 2009. It will measure the soil moisture and ocean surface salinity. However, in this project its potential application for sea ice is investigated using a sea ice emission model. Sea ice emission models relate physical snow and ice properties such as density, temperature, snow crystal and brine inclusion size to microwave thermal emission. The model used here is a sea ice version of Microwave Emission Model for Layered Snow-packs (MEMLS) (Wiesmann and Mätzler, 1999) described in Tonboe et al. (2006b) and hereafter called the emission model. The emission model is used to simulate the sea ice brightness temperature (T_b), emissivity where the subscript v or h and number denote the polarisation, e.g. ev for the emissivity at vertical polarisation, effective thermometric temperature where only Teff for vertical polarisation is given, and penetration depth. All simulations are at 0 to 54deg incidence angle at increments of 6deg. Here, the penetration depth is defined as the depth where the intensity just above the surface has decreased beneath the surface to 1/e (0.37) of its initial value. This includes the transmission loss at the surface and at layer interfaces. This definition differs from Hallikainen and Winebrenner (1992) where transmission loss is not included.

In order to produce input to the emissivity model a one dimensional snow/ice thermodynamic model has been developed. The thermodynamic model is fed with ECMWF ERA40 data input. In return the thermodynamic model produces detailed snow and ice profiles which are input to the emission model. The intension is to give a picture of significant emission processes and the brightness temperature variability in level sea ice even though the one di-

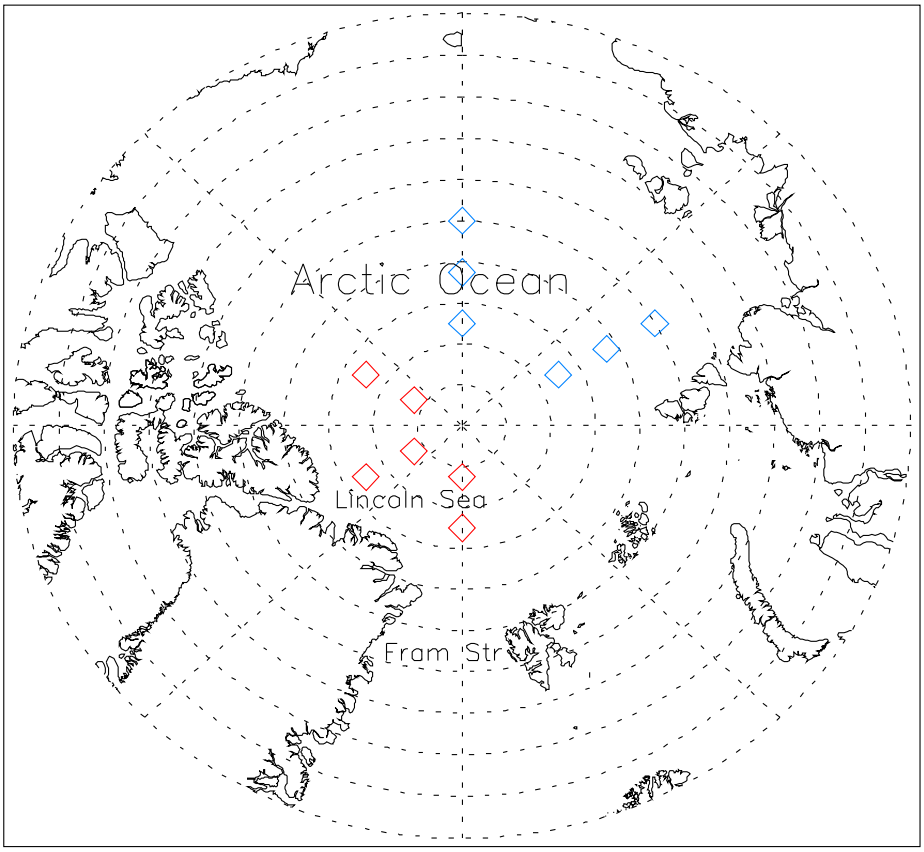

Figure 5.1: Multiyear ice profiles in red and first-year ice profiles in blue.

mensional thermodynamic model is not capturing the spatial variability of the sea ice cover (convergence/deformation, divergence/new-ice formation, wind redistribution of the snow cover). It does not have a hydrological module and cannot simulate melt processes in the snow and ice. The thermodynamic model is further described in Tonboe (2005). The simulated snow depths during winter are comparable to climatology (Warren et al., 1999). Further, the salinity profile and ice thickness produced by the model are comparable to campaign measurements of these quantities.

Both multiyear ice and first-year ice is simulated. The simulations begin on September 1. at 6 different geographical multiyear ice positions and the first-year ice simulations begin on September 1. and January 1. also at 6 different geographical positions. The positions are shown in figure 5.1. The initial multiyear ice profile is an isothermal 2.5m stack of layers with salinity between 1 at top and 2.5psu further down. The fist-year ice simulations begin with a 1cm 15psu layer and an underlying 3cm layer where the salinity is determined by initial growth rate. For all profiles the salinity of additional layers (3cm thick) is determined by ice growth rate and ocean salinity (Nakawo and Sinha, 1981). Snow precipitation is accumulated on top according to the meteorological input. New-snow density is a function of air temperature and wind speed and deposited snow layers later compact to higher density as part of the snow metamorphosis.

5.2 Microwave emission from sea ice

The microwave brightness temperature of a lossy half-space such as snow and sea ice is the product of the effective temperature and the emissivity. The effective temperature is the integrated emitting layer thermometric temperature. Usually during winter when the atmosphere is colder than the ocean the surface temperature is also lower than the effective temperature. The emissivity at a certain polarisation, frequency and incidence angle is a function of subsurface extinction and reflections between layers with different permittivity. The microwave penetration for frequencies higher than 89GHz is usually confined to the snow cover due to significant extinction in the snow. The ice is saline which leads to a high absorption coefficient thus limiting penetration. Eppler et al. (1992) noted that during winter at frequencies around 19GHz, the level first-year ice microwave signatures change primarily due to snow cover related processes. At these relatively high frequencies compared to L-band snow cover is very important for the signature variability of all sea ice types including multiyear ice and new/young ice (Eppler et al., 1992). Snow cover does also affect the emission at L-band mostly by moderating the reflection coefficient at the surface and the incidence angle. The effect is seen in cases with or without snow cover. Scattering from snow grains, brine pockets and air bubbles is insignificant at L-band but is included in the computation anyway.

5.3 Sensitivity study

An ice profile is constructed to compute the emissivity sensitivity to ice salinity and thickness. The profile consists of 10 layers with a uniform temperature profile at 267K. There is no snow on top. The thickness and salinity of each layer is increased in a for-loop so that the total thickness varies between 1 and 300cm and the salinity between 0.2 and 20psu. The results are shown in figures 5.2 and 5.3.

The figures show to what extent the emission is affected by the ice water interface. It also shows an emissivity ambiguity between thin highly saline ice and thick less saline ice. The ice is no longer transparent at 8ppt when it is about one meter thick as seen in Figure 5.2. When the salinity increase the ice becomes less transparent seen in figure 5.3. When it is opaque (1m, 8ppt) the increased salinity increase the surface reflectivity and the emissivity is then decreasing. For natural first-year ice the salinity is within a much more narrow range than indicated in Figures 5.2 to 5.3. The bulk salinity during winter in Baltic sea ice is 15 to 25% of the surface water salinity which is about 6psu (Granskog et al., 2004). The average salinity in Arctic first-year ice is in the order of 6-8psu in winter (Eppler et al., 1992). Thin ice and the top of the ice sheet may have higher salinities (Weeks and Ackley, 1985). In order to study the emission variability within a more realistic natural range we use the thermodynamic model to produce the profiles in the next section.

5.4 The combined thermodynamic and emission model

Combined thermodynamic and emissivity models have the potential to build long snow/sea ice/microwave time-series that can be used for statistical analysis of radiometer sea ice data sensitivities. However, Wiesmann et al. (2000) show that 1-D thermodynamic models for snow and frozen ground including microphysical parameters and a vertical stack of layers,

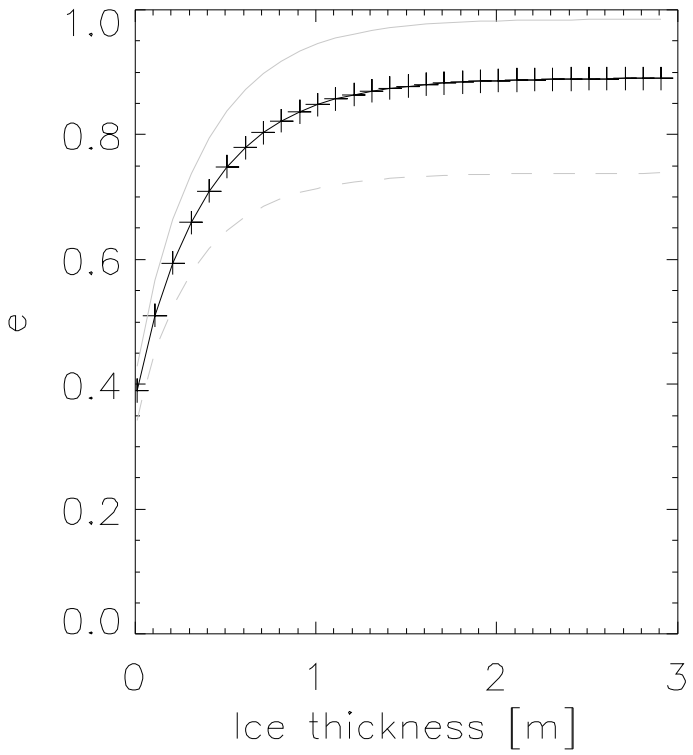

Figure 5.2: The emissivity as a function of ice thickness. enadir is marked with (+), the ev and eh at 54deg are the grey full and dashed line respectively. The salinity is 8ppt and the ice surface temperature is 267K.

e.g. SNTHERM (Jordan, 1991) and Crocus (Brun et al., 1989), underestimate the formation of thin crusts or weak layers in the snow pack. Comparison to snow pit measurements showed that the density of thin layers is underestimated in Crocus and thin layers are not represented properly in SNTHERM. Further, when the thermodynamic model output is used as input to a microwave emission model this leads to underestimation of the simulated polarisation difference. These models were developed for other applications. The thermodynamic model used here treats layers from individual precipitation events and retains all layers even when thin (1mm) in an attempt to alleviate earlier problems in microwave modelling applications. Snow is accumulated for each major precipitation event. However, to ensure reasonable initial snow layer thickness precipitation events less than 1 kg/m^2 are retained and later released when the next precipitation event exceeds the 1 kg/m^2 threshold. While this may not be totally realistic it does produce simulated snow depths which are comparable to climatology (Warren et al., 1999). At L-band it is particularly important that the thermodynamic model can reproduce realistic temperature, ice salinity profiles and ice thickness. These simulated parameters are comparable to measurements although actual climatology does not exist for all these parameters.

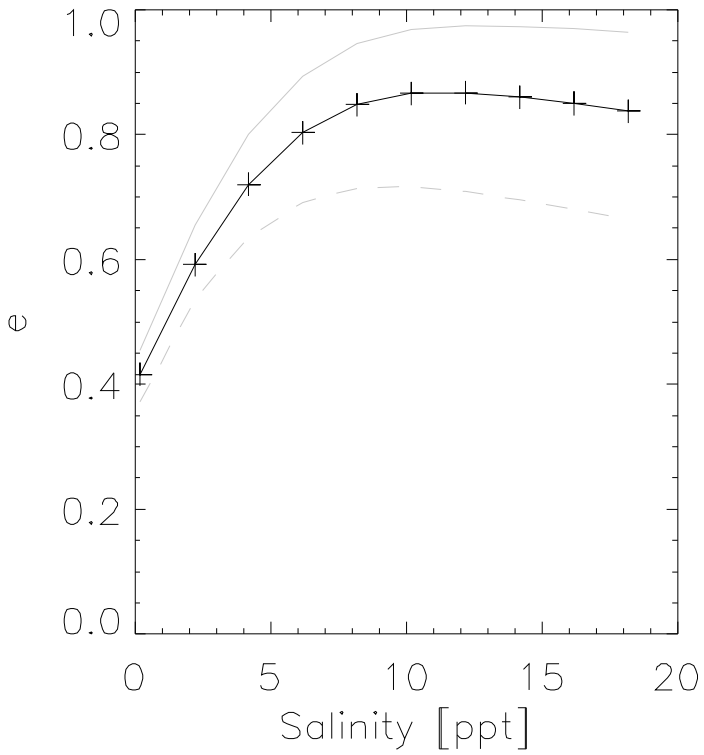

Figure 5.3: The emissivity as a function of bulk salinity. enadir is marked with +, the ev and eh at 54deg are the grey full and dashed line respectively. The thickness is 1m and the ice surface temperature is 267K.

5.5 The interface between the thermodynamic and the emission models

Snow grain size is a parameter used in the thermodynamic model to compute the shortwave extinction in the snow and it is further related to microwave scattering magnitude (Maetzler, 1998). Maetzler (1997) analyses different relationships between the snow structure, grain size (D_0) and the correlation length (p_{ec}). The grain size is used in the thermodynamic model and the correlation length is used in the emission model. Do is related to p_{ec} for rounded grains (Maetzler, 1997), i.e.

$$p_{ec} = FD_0 \tag{5.1}$$

where F is 0.16 for snow grain sizes modelled with SNTHERM, 0.3-0.4 for Crocus grain sizes and types, and 0.16 for fine grained snow and 0.25 for medium grained snow using a one dimensional scattering model.

There is no snow metamorphosis relationships in terms of p_{ec} so the conversion between terms is needed thus assuming that grain size and p_{ec} evolve similarly during metamorphosis and our grain size growth model is not dependent on initial grain size. Therefore the conversion factor F is not critical. We use $F = 0.4$ and p_{ec} of new snow deposits is set to 0.06mm which

is typical for new snow (Wiesmann et al., 1998). Other microphysical parameters in the profile such as physical temperature, density, salinity are used directly in the emission model The thermodynamic model has the following prognostic parameters for each layer: thermometric temperature, density, thickness, snow grain size and type, ice salinity and snow liquid water content. Snow layering is very important for the microwave signatures therefore it treats snow layers related to individual precipitation events. For sea ice it has a growth rate dependent salinity profile. The sea ice salinity as a function of growth rate and water salinity is (Nakawo and Sinha, 1981), i.e.

$$S = 0.12 S_w / \{0.12 + 0.88 \exp(-4.2 \times 10^4 u)\} \tag{5.2}$$

where S_w is the water salinity (here 32psu for the Arctic and 6psu for the Baltic) and u is the growth rate in cm/day.

5.6 Combined thermodynamic and emissivity model simulation results

Fig. 5.4 shows the simulated temperature profile in first-year ice in the central Arctic Ocean during the 1999/2000 winter season using ECMWF reanalysis data (ERA40) as input to the thermodynamic model. The geographic positions of the simulated profiles for both first- and multiyear ice are shown in figure 5.1. These are processed in the same way as the profile shown in figure 5.4 and comprise the total simulated dataset.

The simulations begin with a bare ice surface on 1 Sep., which is approximately the end of the melt season. First-year ice profiles are also initiated on January 1. The multiyear ice simulations begin with a 2.5m ice profile which gradually grows to about 3.3m and the first-year ice profiles grows from 0.01m to about 1.5-2m. The first-year ice profiles which are stared later grow to about 1m. The profiles started on January 1. should simulate different growth rates and snow-cover situations. Most of the waters with seasonal ice cover in the Arctic freeze-up during autumn (October), but due to dynamics, leads and parts of the ice cover freeze up later.

The permittivity of snow and first-year ice sea ice is shown in figure 5.12. The permittivity of snow is primarily a function of snow density. The permittivity of sea ice is primarily a function of salinity and temperature.

The simulated average emissivity as a function of incidence angle is shown in figure 5.14. The thin (thickness<0.5 and transmissivity >0) first-year ice emissivity is low since it is affected significantly by the ice-water interface. When the first-year ice is optically thick (thickness >0.5 and transmissivity =0) then the emissivity is not a function of thickness anymore. The multiyear ice emissivity is greater than the thick first-year ice emissivity because its surface reflectivity (r) is smaller (e=1-r).

The first-year ice simulations, ice thickness vs. brightness temperature (Tv) are shown in figure 5.15.

5.7 Conclusions

A sea ice version of microwave emission model for layered snow-packs (MEMLS) has been used to simulate the sea ice brightness temperature at L-Band. The brightness temperature

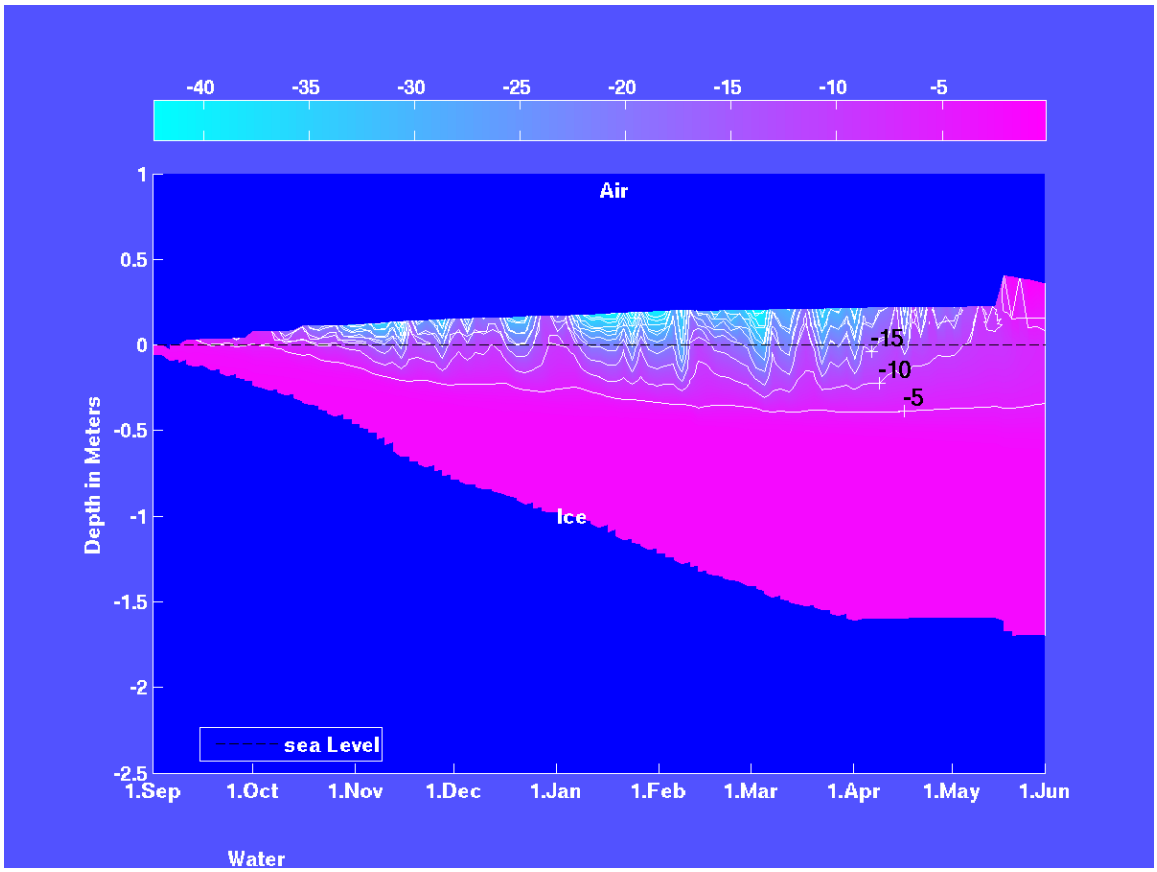

Figure 5.4: The temperature of first-year ice during winter at 85N 180E.

sensitivity to central parameters such as ice thickness, ice salinity and temperature has been investigated. Further, a thermodynamic model has been used to produce sea ice profiles for multiyear ice, first-year ice and Baltic sea ice. Using these simulated profiles as input to the emissivity model it has been found that:

1. Penetration in multiyear ice is about 2.5m
2. Penetration in first-year ice is about 0.5m
3. Multiyear ice emissivity is greater than first-year ice emissivity because multiyear ice has lower reflectivity (e=1-r).
4. Surface density (or the reflectivity) is more important for enadir and e54h than e54v.
5. The brightness temperature is a function of ice thickness when the ice is optically thin (thickness<0.5m). This information would be complimentary to CryoSat.

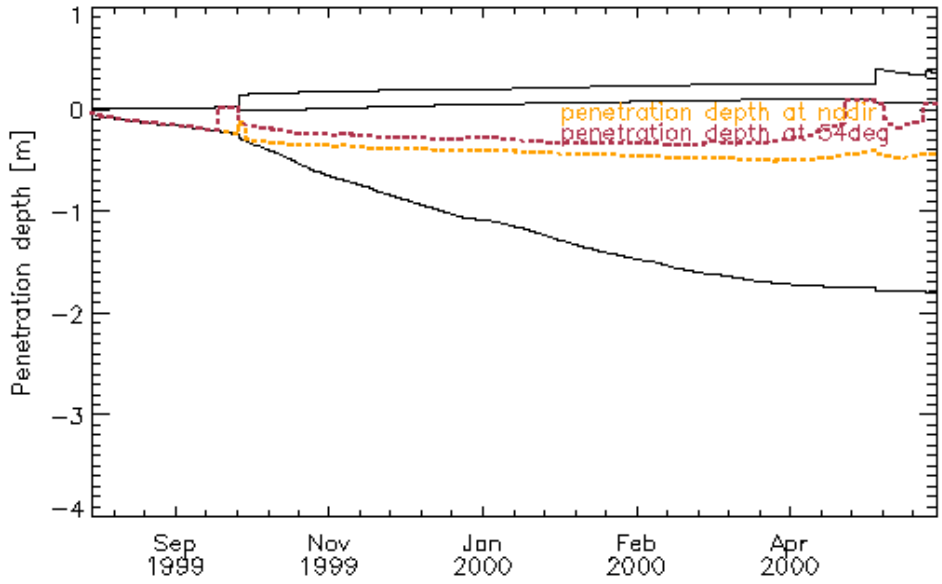

Figure 5.5: The simulated first-year ice penetration depth at 85N 180E. The black curves show the air/snow, snow/ice, and ice/water interface respectively. The dashed red and yellow curves show the penetration depth at 54deg and nadir respectively. Penetration is about 0.5m in first-year ice.

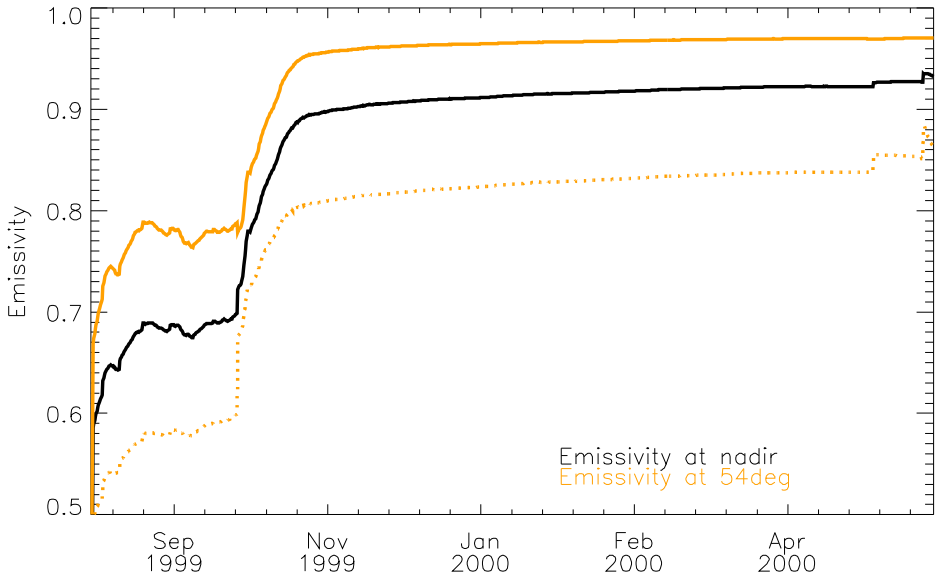

Figure 5.6: The simulated first-year ice emissivity at 85N 180E. The orange full line is the vertical polarisation the dashed line is the horizontal polarisation. The black full line is the vertical and horizontal polarisation at nadir.

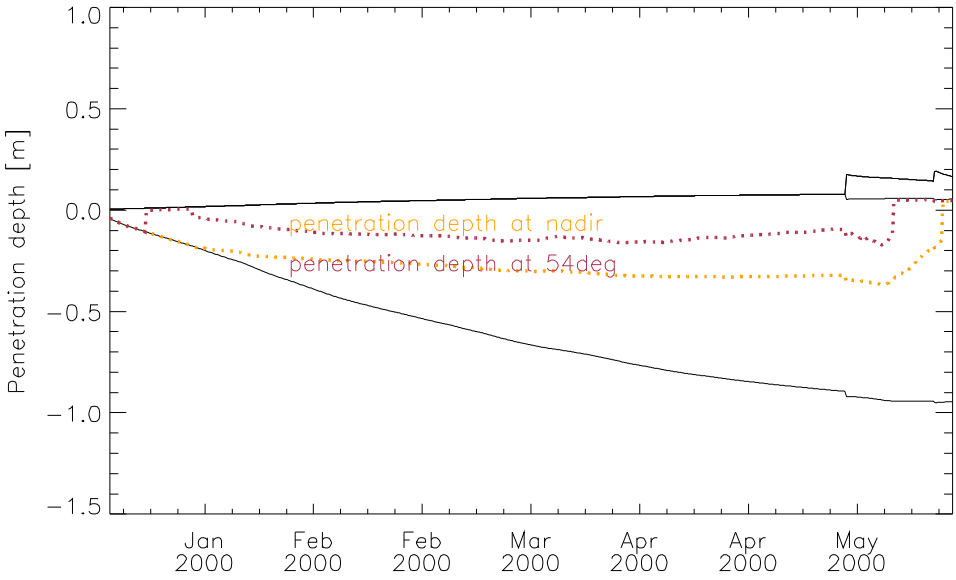

Figure 5.7: The simulated first-year ice penetration depth at 85N 180E starting at new-year. The black curves show the air/snow, snow/ice, and ice/water interface respectively. The dashed red and yellow curves show the penetration depth at 54deg and nadir respectively. Penetration is down to 0.5m in first-year ice

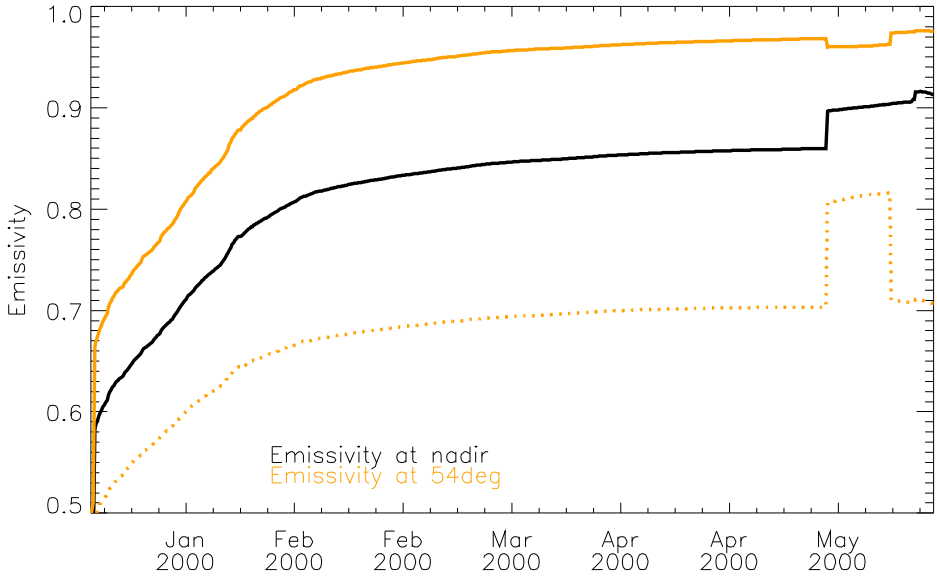

Figure 5.8: The simulated first-year ice emissivity at 85N 180E starting at new-year. The orange full line is the vertical polarisation and dashed line is the horisontal polarisation. The black line is the vertical and horizontal polarisation at nadir. The snow fall event in May has a significant impact on the horizontally polarised emissivity at 54deg because of the transition from bare ice to snow covered ice.

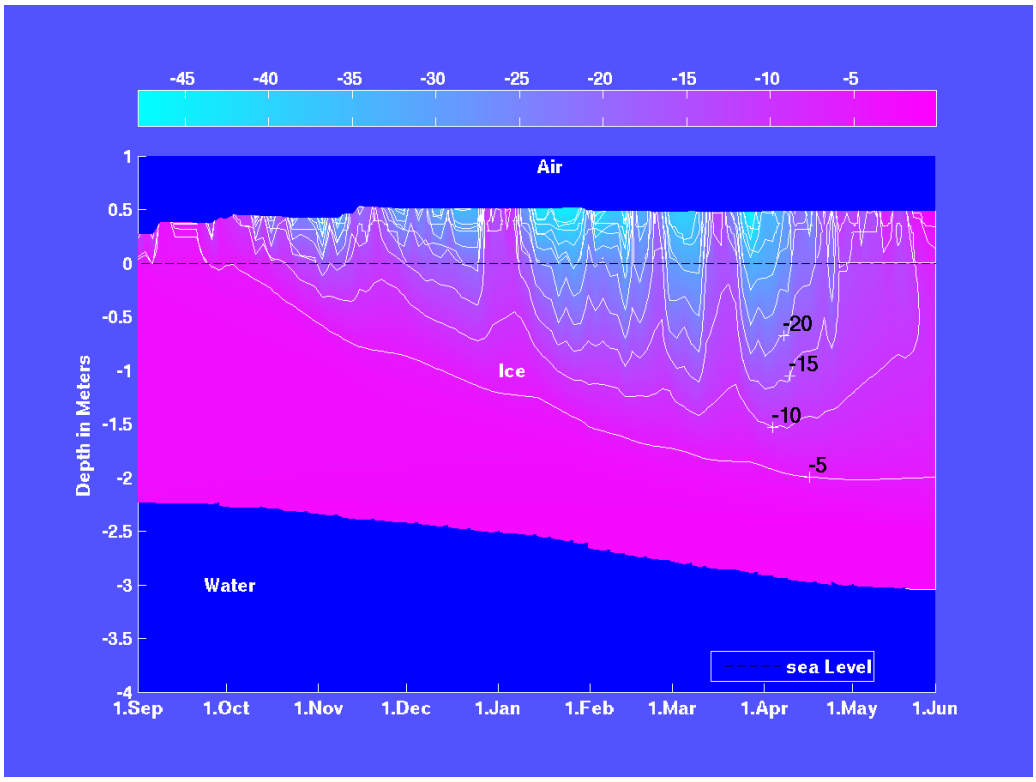

Figure 5.9: The temperature in multiyear ice at 87.5N 300E during winter.

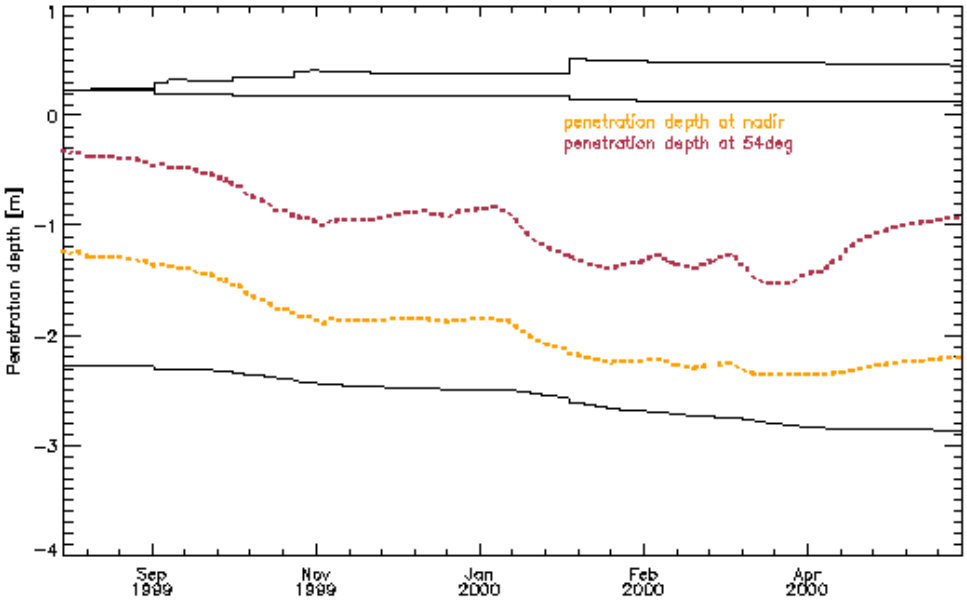

Figure 5.10: The simulated multiyear ice penetration depth at 87.5N 300E. The black curves show the air/snow, snow/ice, and ice/water interface respectively. The dashed red and yellow curves show the penetration depth at 54deg and nadir respectively. Penetration is about 2.5m in multiyear ice to the old (September) ice/water interface.

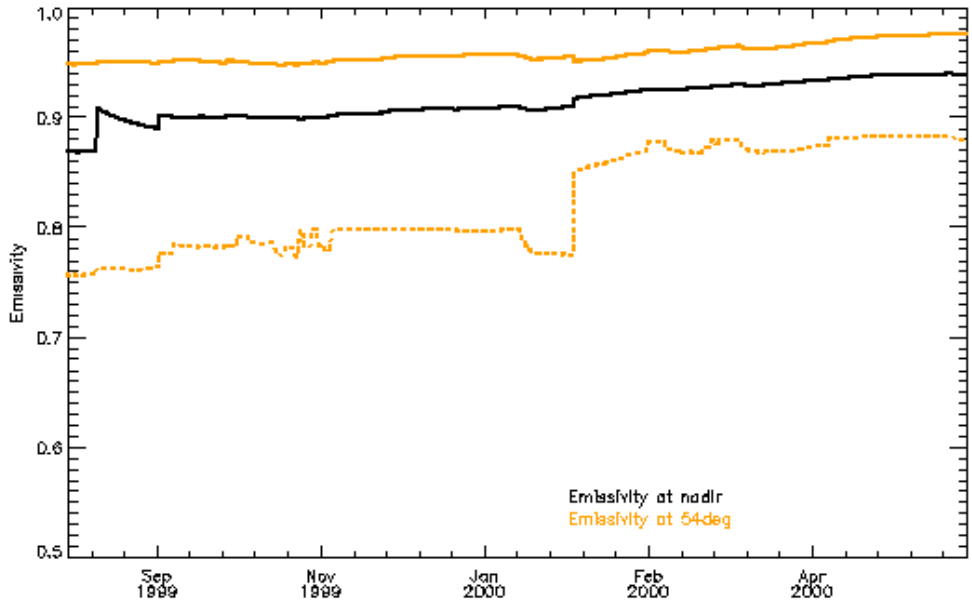

Figure 5.11: The simulated multiyear ice emissivity at 87.5N 300E. The orange full line is the vertical polarisation and dashed line is the horizontal polarisation. The black line is the vertical and horizontal polarisation at nadir.

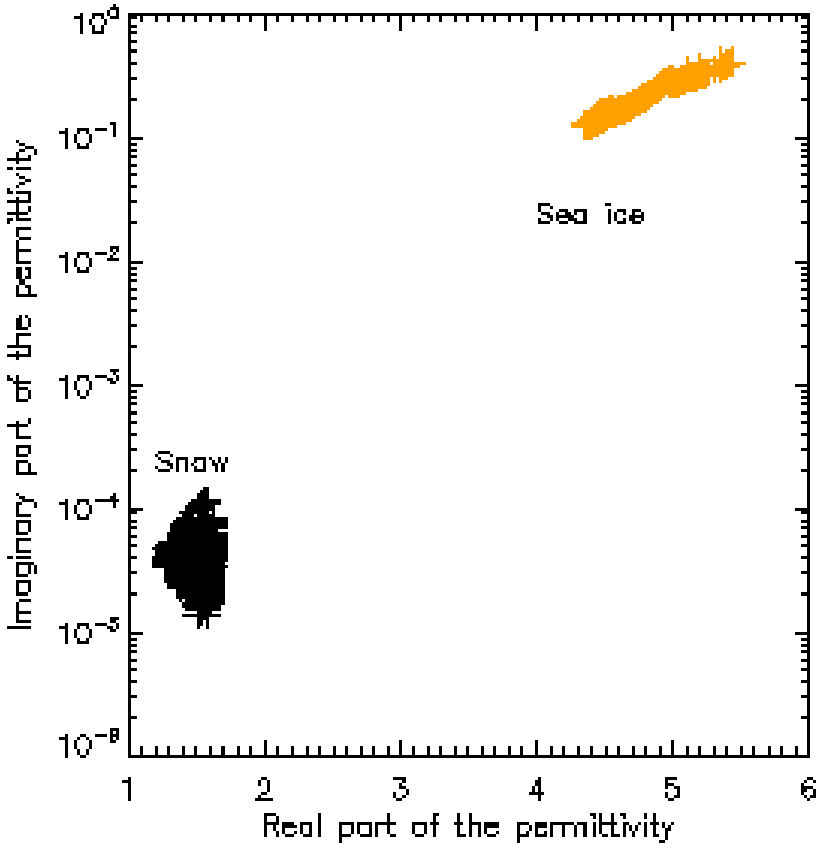

Figure 5.12: The winter permittivity of snow and first-year ice The simulated first-year ice thickness vs. the bulk salinity is shown in figure 5.13. An almost similar figure based on measurements is found in Weeks and Ackley (1985), p. 93, fig 64.

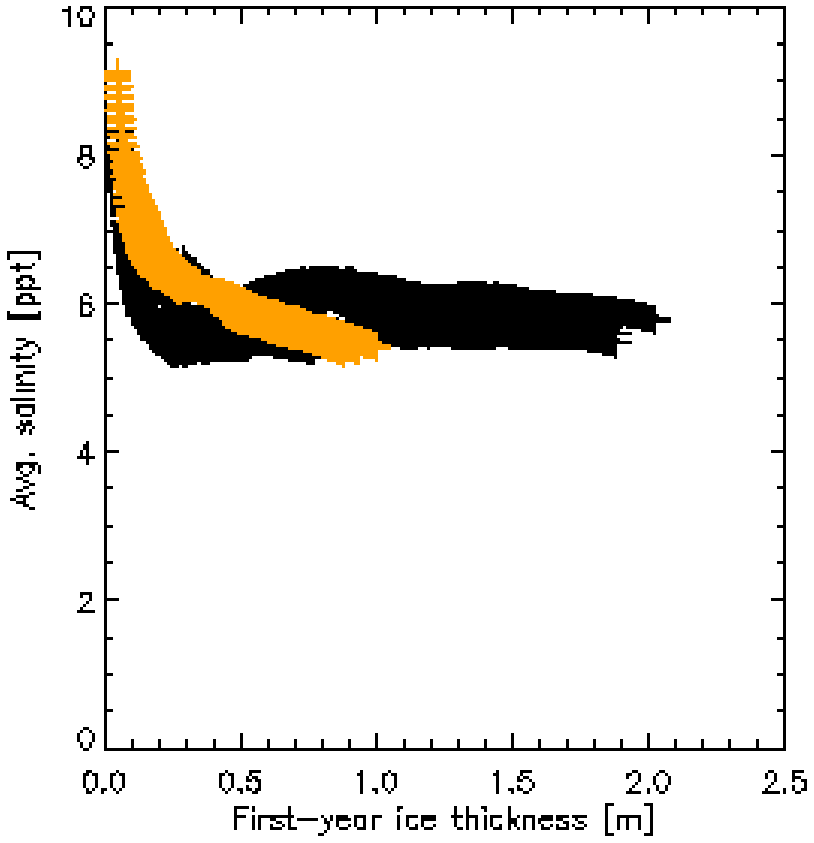

Figure 5.13: The bulk first-year ice salinity as a function of ice thickness in the Arctic. The black points show the simulations starting on September 1. and the yellow points show the simulations starting on January 1. Both series end on May 31.

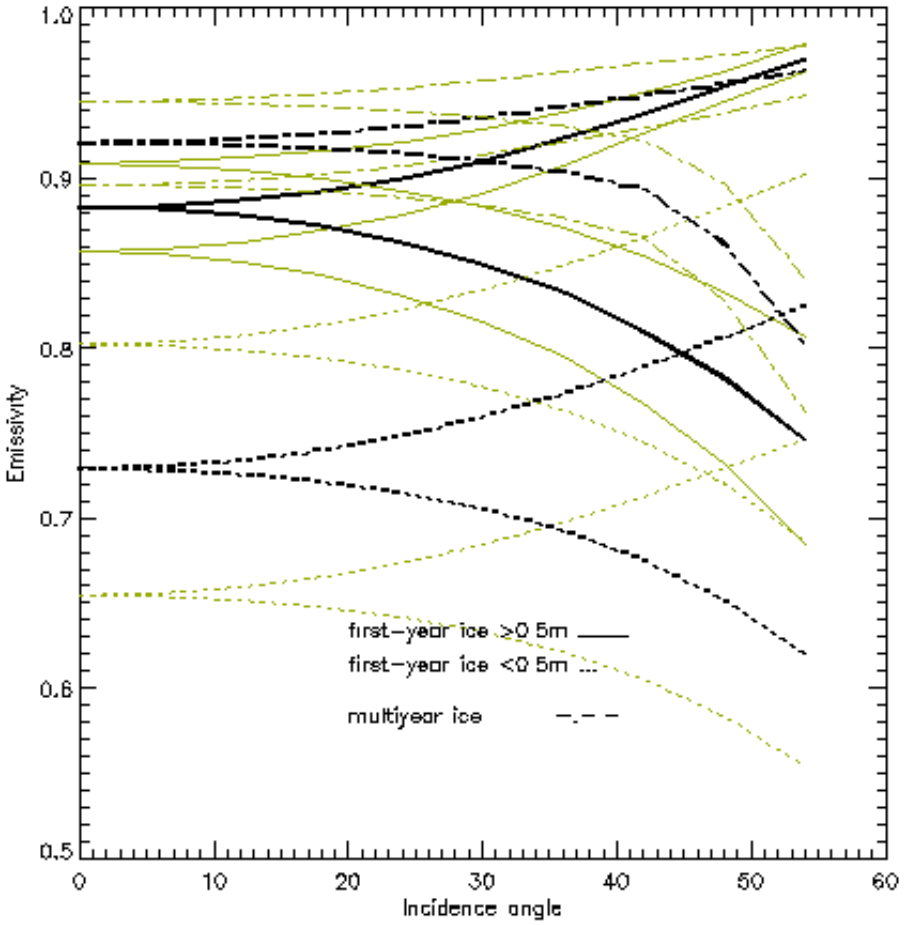

Figure 5.14: The mean emissivity for the simulated profiles as a function of incidence angle. Only the first-year ice simulations starting on September 1. are included. Standard deviation (mean+/-std) is indicated with green curves

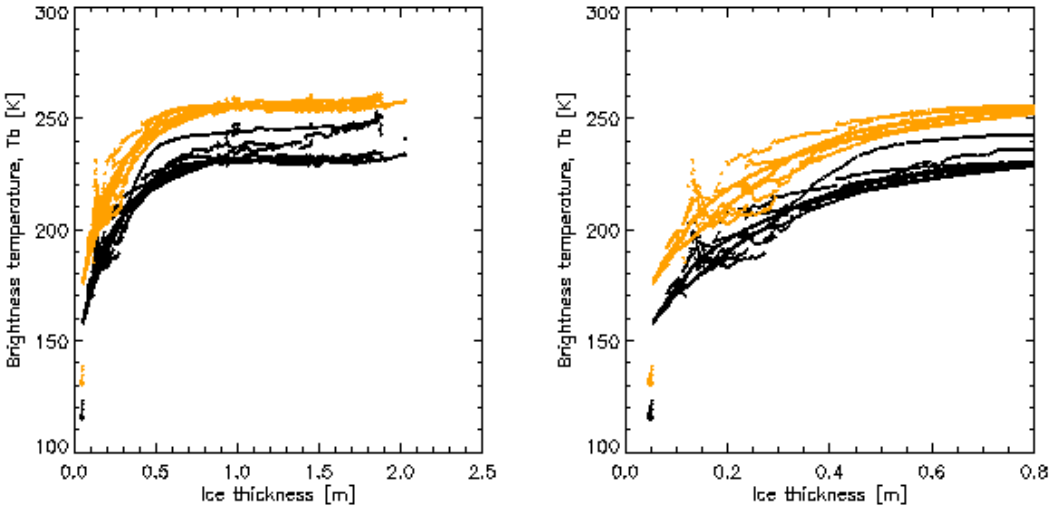

Figure 5.15: The T_bv as a function of ice thickness for the simulated first-year ice profiles starting at September 1. and January 1. The black dots are the brightness temperature at nadir and the yellow dots are at 48deg. incidence angle. The profiles starting on September 1. typically reach thicknesses of 1.5-2m before May 31. The profile starting on January 1. reach about 1m before May 31. The left figure has different axis scaling.

Chapter 6

WP 2.3b: Foward modelling of the first two Stokes components using Combined Strong Fluctuation Theory (CSFT)

Peter Mills and Georg Heygster

Institute for Environmental Physics, University of Bremen, Otto-Hahn-Allee 1, 28359 Bremen, Germany

6.1 Introduction

SMOS (Soil Moisture and Ocean Salinity) is a proposed new satellite that will measure microwave radiation in all four Stokes components at 1.4 GHz which is in the L-band frequency range. SMOS will also provide valuable information about the cryosphere. In particular, because of the deep penetration depth at this frequency, it may be possible to infer knowledge about sea-ice thickness and other quantities relating to its internal structure, such as bulk salinity. Several layered, plane-parallel ice models have been described in the literature, including Strong Fluctuation Theory (SFT) (Stogryn, 1985), Microwave Emission of Layered SnowPack (MEMLS) (Wiesmann and Maetzler, 1999) and various types of radiative transfer models (Winebrenner et al., 1992). While these have some experimental support in C-band (Hwang et al., 2007; Winebrenner et al., 1992), they have yet to be tested at lower frequencies. Since relatively few campaign measurements of L-band emissions over sea-ice exist, a model of this type will be required to design the algorithms, and to extrapolate radiometer observations taken over the brackish waters of the Baltic to the more saline oceans in the Arctic and Antarctic.

The goal of this report is to compare forward model calculations of sea-ice for the first two Stokes components using four ice emissivity models: a modified version of SFT called Combined Strong Fluctuation Theory (CSFT) (Johnsen, 1998), the mixture model (described

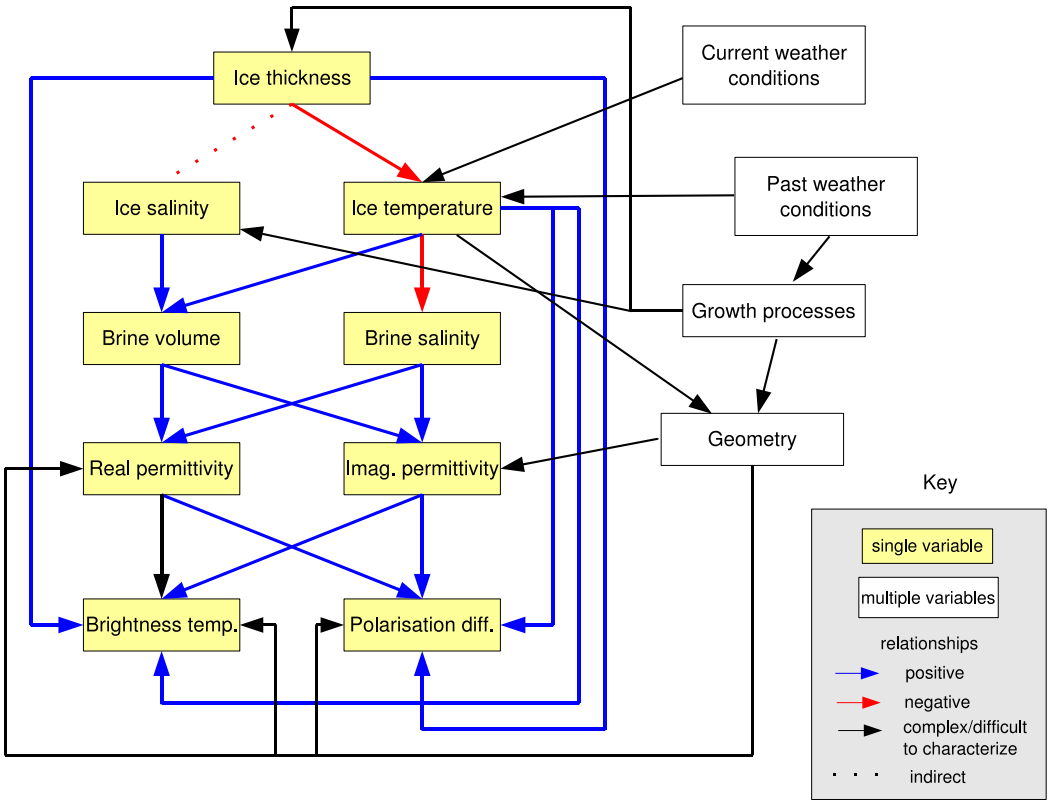

Figure 6.1: Diagram showing the inter-dependencies of the different quantities determining the final, measured brightness temperature of sea ice. Blue arrows indicate direct, positive, monotonic relationships. Red arrows are direct, inverse, monotonic relationships. Black arrows are more complex relationships. Dotted lines are indirect relationships.

later in this report), MEMLS and the three-layer dielectric slab model. (Menashi et al., 1993) In the first section we will briefly describe this model. The second section will focus on four different model ice types, while the third will show results from a series of profiles generated from an ice-growth model. These are meant for intercomparison with similar results from the Microwave Emissivity of Multi-Layer Snowpack (MEMLS) (Wiesmann and Maetzler, 1999) from Chapter 5.

6.2 Theory

6.2.1 Strong Fluctuation Theory

The SFT is a mean field theorem that attempts to find an approximate solution to Maxwell's equations for a medium with a randomly fluctuating dielectric constant. The equation:

$$\nabla \times \nabla \times E = \frac{\epsilon \omega^2}{c_0^2} E \tag{6.1}$$

can be reduced from Maxwell's equations and describes the electric field component of a wave of constant frequency in a conducting but non-magnetic medium. E is the electric field, c_0 is the speed of light, $\epsilon = \epsilon' + \epsilon''$ is the relative permittivity and ω is the angular frequency of the wave. Both the electric field and the permittivity are assumed to be composed of a mean component and a randomly fluctuating one:

$$E = < E > + E_r \tag{6.2}$$

$$\epsilon = < \epsilon > + \epsilon_r \tag{6.3}$$

where the r subscript denotes the random component and the angular brackets denote the mean. To describe the statistical variations in permittivity of a multi-component medium, the correlation length is used, which can be related to the average size and shape of individual inclusions in a manner such as in Maetzler (1997). In the many-layer strong fluctuation theory, the procedure has been generalized sufficiently to allow for variations in correlation length along a single axis–that is, in depth. However, because we are solving a wave equation, the solution is a coherent one: the pronounced oscillations seen in Figure 6.6 are the result of interference effects.

According to Kirchoff's law, there are two components to the solution which contribute to the resulting emissivity:

$$\xi_p(\mathbf{k_0}) = 1 - R_p(\mathbf{k}_0) - S_p(\mathbf{k}_0) \tag{6.4}$$

where $\xi_p(\mathbf{k_0})$ is the emissivity at polarisation p (v or h) and viewing angle $\mathbf{k_0}$, R_p are the reflection coefficients and S_p are the volume scattering coefficients. The scattering contribution is determined by integrating the bi-static scattering coefficients, γ_{ph} and γ_{pv} (Johnsen, 1998):

$$S_p(\mathbf{k_0}) = \frac{1}{4\pi} \int \left[\gamma_{ph}(\mathbf{k_0}, \mathbf{k}) + \gamma_{pv}(\mathbf{k_0}, \mathbf{k})\right] \sin\theta d\theta d\phi \tag{6.5}$$

where θ and ϕ are the zenith and azimuthal components of the angle, respectively.

6.2.2 Combined Strong Fluctuation Theory

The combined strong fluctuation theory (CSFT) was introduced by Johnsen (1998) and combines the SFT with the radiative transfer (RT) model described in Burke et al. (1979). The latter model, however, was found to be both erroneous and incomplete: in particular, only emissions in the upward direction contribute to the final, emitted radiances. Therefore, the full derivation of an improved RT model that takes into account multiple reflections across all layers will be presented here.

In the CSFT, the reflection coefficients are replaced with a radiative transfer model. SFT will return a set of effective permittivities:

$$\epsilon_{eff} < E > = < \epsilon E > \tag{6.6}$$

describing the dielectric properties of each layer. Transmission and emission within each layer is treated by standard radiative transfer while transmission across the boundaries is treated as in the Fresnel equations by assuming continuity of the electric and magnetic fields of the wave, but with no coherency effects from one boundary to the next.

Suppose we have an ice sheet with m discontinuous layers each with thickness Δz_i and complex permittivity ϵ_i as shown in Figure 6.2. In order to determine the emitted radiation, the

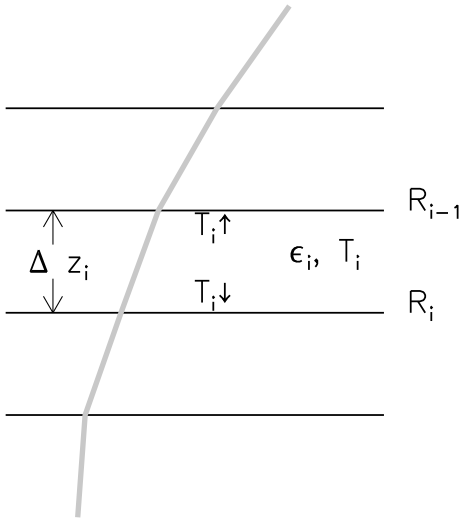

Figure 6.2: Geometry of radiative transfer model for layered, discontinuous, plane-parallel media.

first step is to calculate the refraction angle at each layer using Snell's law:

$$n_i \sin\theta_i = n_{i-1} \sin\theta_{i-1} \tag{6.7}$$

where $n_i = \sqrt{\epsilon_i}$ is the refractive index of the ith layer. The transmission coefficient of the ith layer is given by:

$$\tau_i = \exp\left(-\frac{\alpha_i \Delta z}{\cos\theta_i}\right) \tag{6.8}$$

where

$$\alpha_i = \frac{4\pi\nu}{c_0} \text{imag} n_i \tag{6.9}$$

is the attenuation coefficient within the ith layer, ν is the frequency and c_0 is the speed of light. If perfect plane-parallel geometry is assumed, then the angles of all reflecting rays will be the same and we can solve for the upwelling and downwelling radiation in each layer by summing the components of each contribution:

$$T_i \uparrow - \tau_i(1 - R_i)T_{i+1} \uparrow - \tau_i R_i T_i \downarrow \;=\; (1 - \tau_i)T_i \tag{6.10}$$

$$T_i \downarrow - \tau_i(1 - R_{i-1})T_{i-1} \downarrow - \tau_i R_{i-1} T_i \uparrow \;=\; (1 - \tau_i)T_i \tag{6.11}$$

where $T_i \uparrow$ and $T_i \downarrow$ are, respectively, the brightness temperatures the upwelling and downwelling radiation at the top and bottom of the ith layer, T_i is the physical temperature of the ith layer and R_i is the reflection coefficient of the interface between the ith and $(i+1)$th layer. For continuous media, these can be set to zero and the equations reduce to a discrete integral

of the radiative transfer equation. This could be useful in the case of modelling dark nilas or other new ice types which will have a pronounced variation of salinity with depth, but with only one distinct ice layer.

For the boundary conditions, we set $\epsilon_1 = 1$, $T_1 \downarrow = T_{sky}$ and $T_m \uparrow = T_m$ where T_{sky} is the emission temperature of the sky and T_m is the physical temperature of the lowermost layer, normally water. In other words, the top layer is the open air and the bottom layer is assumed to be infinitely optically thick.

The rate of transmission of a plane wave across a discontinuous, plane boundary between two dielectrics is computed via the Fresnel equations:

$$R_{vi} = \left[\frac{n_{i+1}\cos\theta_i - n_i\cos\theta_{i+1}}{n_{i+1}\cos\theta_i + n_i\cos\theta_{i+1}}\right]^2 \tag{6.12}$$

$$R_{hi} = \left[\frac{n_i\cos\theta_i - n_{i+1}\cos\theta_{i+1}}{n_i\cos\theta_i + n_{i+1}\cos\theta_{i+1}}\right]^2 \tag{6.13}$$

where R_{vi} and R_{hi} are the reflection coefficients for vertical and horizontal polarisations respectively, θ_i and θ_{i+1} are the incident and transmission angles respectively, calculated via Snell's law (6.7).

6.2.3 Coherent solution

Coherency effects have been observed in thin ice sheets of uniform thickness (St. Germain et al., 1993). The radiative transfer model treated in the previous section can easily be converted to a coherent solution simply by leaving in the phase terms in both the transmission coefficients (6.8) and the reflection coefficients ((6.12) and (6.13)). Thus, Equation (6.8) becomes:

$$\tau_i = \exp\left(-\frac{4\pi \mathrm{i}\nu n_i \Delta z}{c_0\cos\theta_i}\right) \tag{6.14}$$

where θ_1 is the angle of incidence. Such a formulation will be useful in the calculation of the third and fourth Stoke's components which result from some kind of anisotropy in either the surface characteristics or the bulk electromagnetic properties. That is, a change in the complex permittivity at different angles will produce a phase shift between waves at different (linear) polarisation directions, i.e., horizontal and vertical polarisation, that will be detected in the third and fourth components of the Stokes vector:

$$\begin{bmatrix} I \\ Q \\ U \\ V \end{bmatrix} = \begin{bmatrix} |E_v|^2 + |E_h|^2 \\ |E_v|^2 - |E_h|^2 \\ 2\mathrm{Re} < E_v E_h^* > \\ 2\mathrm{Im} < E_v E_h^* > \end{bmatrix}. \tag{6.15}$$

This effect will be treated in more detail in Chapter 7.

6.2.4 Mixture models of effective permittivity

The weak link in emissivity models of this type appears to be the calculation of effective permittivity. Because volume scattering is weak at L-band due to the small size of the scatterers, mixture models based on the low-frequency limit would appear to be more appropriate than more involved models such SFT. Two types of mixture models may be distinguished: those

that take as input only the brine volume, and those that require calculation of brine permittivity. In the former case, we have the empirical formulae of Vant et al. (1978) in which the effective permittivity is linearly related to brine volume:

$$\epsilon^* = mV_b + k, \tag{6.16}$$

where ϵ^* is real or imaginary permittivity, V_b is brine volume and m and k are constants. Another example is the following formula for real permittivity:

$$\epsilon' = \frac{\epsilon_{pi}}{1 - 3V_b}, \tag{6.17}$$

found in Hoekstra and Cappillino (1971). Here, ϵ_{pi} is the permittivity of pure ice.

More involved formulae require knowledge of the permittivity of the inclusion material (in this case brine). Representative formulae can be found in Sihvola and au Kong (1988) and Shokr (1998), for instance. Once we admit brine permittivity, the functional dependencies become quite complex, as illustrated in Figure 6.1. Because the brine is always at or near its freezing point, brine salinity is a function of temperature only. We use the empirical, piecewise-continuous polynomial relationship given in Ulaby et al. (1986), Appendix E-5.1, to calculate brine salinity. So long as the ice is not too porous, brine volume can be approximated from brine salinity:

$$V_b \approx \frac{s_b(T)}{s}, \tag{6.18}$$

where s is ice salinity and s_b is the brine salinity.

That leaves the dielectric constant of the brine. This is a complex function of frequency, temperature and salinity, a formula for which can also be found in Ulaby et al. (1986) and will not be repeated here. The same formula, or a similar one, will also be needed to calculate the permittivity of sea water for the lowest layer of the emissivity model.

The difficulty with mixture formulae is that there are many different ones that produce widely divergent results as will be discussed in more detail in Section 6.5. They also require at least some knowledge of inclusion geometry, which is generally lacking. Golden (1995) shows a method of generating rigorous bounds on the effective permittivity for a two-component dielectric medium through analytic continuation (Golden and Papanicolaou, 1983). The geometry of the mixture is represented by a measure, μ, which is then expanded in terms of its moments, thus limited knowledge of the mixture properties, such as relative volume or statistical isotropy, may be used to determine permissible values for the effective permittivity.

By the analytic continuation method, the bounds on effective permittivity, ϵ^*, are represented by two arcs. The first is given by:

$$\epsilon_2(1 - V) - (\epsilon_2 - \epsilon^*)z = (\epsilon_2 - \epsilon^*)s, \tag{6.19}$$

where z is a parameter between 1 and $1 - V$. The second is given by:

$$\frac{\epsilon_1}{\epsilon^*} = 1 - \frac{V_b}{s - z} \tag{6.20}$$

Here, z is a parameter between 1 and V. V is the volume of inclusion material (typically brine), ϵ_1 is the permittivity of the host material (ice), ϵ_2 is the permittivity of the inclusion material (brine), and $s = 1/(1 - \epsilon_1/\epsilon_2)$.

6.3 Special models

6.3.1 Ridged Monte Carlo model

Most ice emissivity models assume plane-parallel geometry, with permittivity variations solely along depth. Yet in ocean emissivity modelling, it is well understood how both small-scale and large- scale roughness affects the emitted radiation (Liu et al., 1998). Like the ocean, sea ice will also have rough interfaces, not only with the air, but also with the water. Ridging in particular will affect the signal by changing the effective viewing angle.

To account for this effect, a simple, two-dimensional, ray-tracing Monte Carlo model was designed. The E-M bird thickness meter is described in Chapter 3. Since it actually comprises two instruments, an inductance meter to determine the ice-water interface, and a laser altimeter to measure the surface topography, we have knowledge of both interfaces along a linear cross-section. The inductance meter samples at a rate of 10 Hz which translates to a datapoint-spacing of between 2 and 4 m while the laser altimeter samples at ten times the rate. The footprint size of the inductance meter is estimated at around 40 m. Because of attenuation of the radiation as it travels through the ice, the highly-resolved top surface should be most important in determining the emitted radiance.

Both top and bottom altitude profiles are interpolated using a cubic spline (Press et al., 1992). To best understand the procedure, a flow-diagram describing the procedure for tracing a single ray through the ice sheet is shown in Figure 6.3, while a plot of an actual simulation is shown in Figure 6.4. The ray is traced backwards, from the instrument head to the ice sheet. When it encounters an interface (either ice-air or water-ice) it is either reflected back or refracted into the new material with the probability equal to the reflection coefficient as determined by the Fresnel equations. Once the ray encounters no further interfaces it is initialized with the temperature of its current material – either ice, air or water – and a radiative transfer calculation performed in the opposite direction:

$$\frac{dI(s)}{ds} = \alpha(s)\left[T(s) - I(s)\right], \tag{6.21}$$

where I is the brightness temperature of the radiation along the path, s, α is atttenuation coefficient and T is the physical temperature. Note that the reflection terms are not included in this integration; they are implicitly accounted for through the random direction on encountering an interface. The final brightness temperature at the instrument head is estimated by tracing many rays and averaging the results with the standard deviation providing a rough bounds on the accuracy of the estimate (Press et al., 1992).

A plane parallel model with only one ice layer, or three layers total (see Section 6.3.2) is a limiting case of the Monte Carlo model and the two were validated one against the other. Generally, they agree to within four Kelvin for virtually all cases. For more specific cases, the agreement will be closer.

6.3.2 Three-layer models

As is the case for measurements from the Pol-Ice campaign, we may have no knowledge of the internal structure of the sea ice. By assuming uniform properties within the ice sheet, we arrive at the following, closed-form solution to the system of equations in (6.10) and (6.11):

$$T_b = (R_{ia} - 1)\frac{(R_{wi} - 1)\tau T_{water} + (R_{ia} - 1)R_{wi}\tau^2 T_{sky} + \left[R_{wi}\tau^2 + (1 - R_{wi})\tau - 1\right] T_{ice}}{R_{ia}R_{wi}\tau^2 - 1}, \tag{6.22}$$

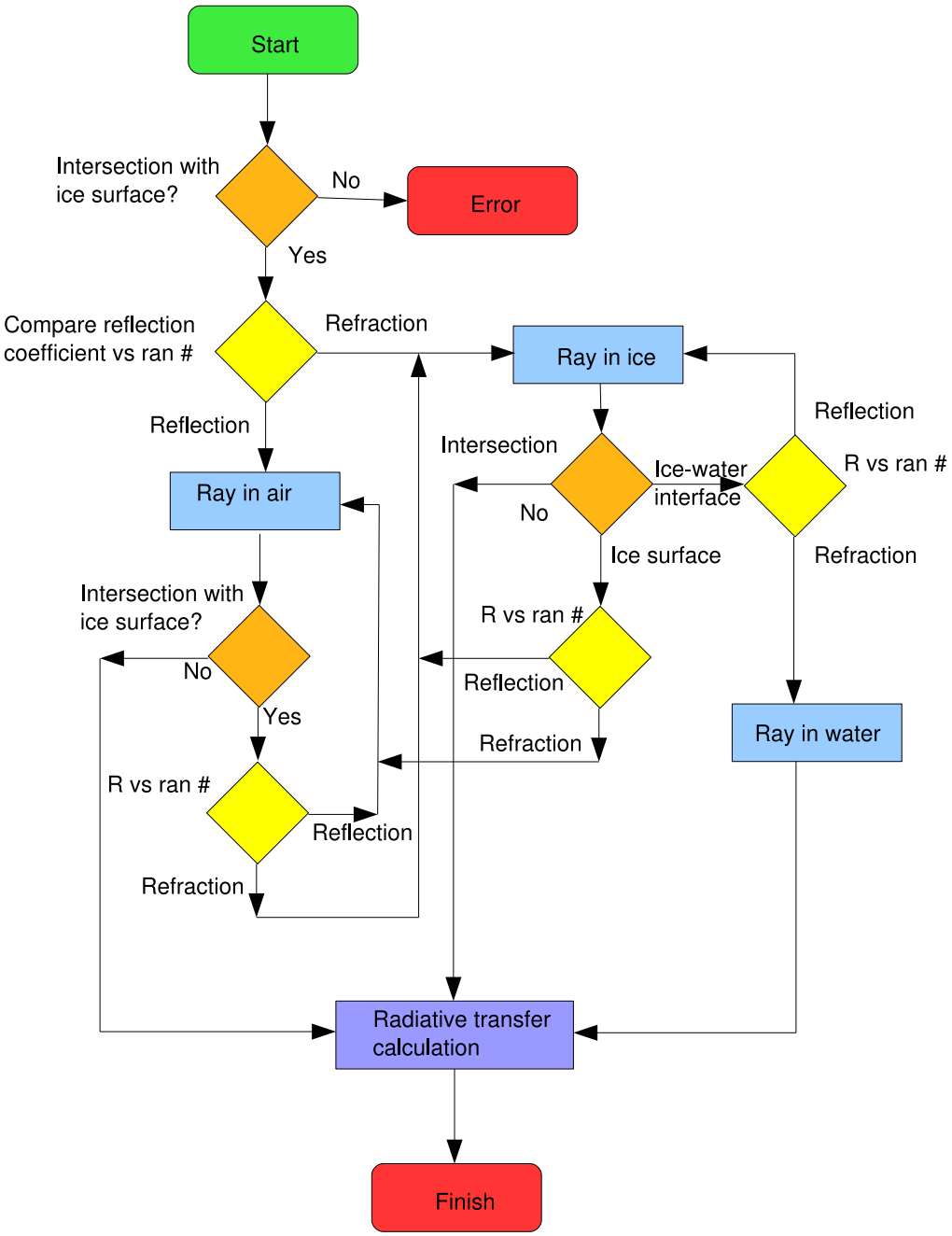

Figure 6.3: Flow diagram describing Monte Carlo ray-tracing algorithm.

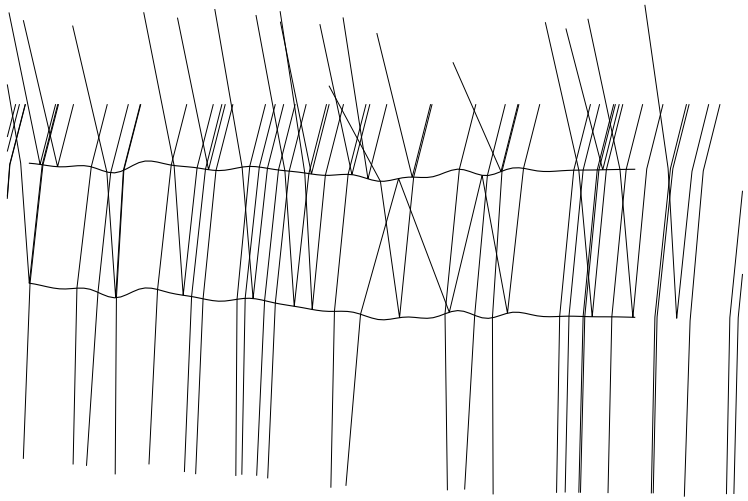

Figure 6.4: An example of a single ray-tracing simulation.

where T_b is the measured brightness temperature, R_{ia} is the reflection coefficient at the ice-air interface, R_{wi} is the reflection coefficient at the water-ice interface, T_{ice} is the ice temperature and T_{water} is the water temperature.

Compare this with the three-layer, "dielectric slab" model presented in Menashi et al. (1993) and applied in Chapter 4:

$$e = \frac{(R_{ia}-1)(R_{wi}\tau^2-1)}{(R_{ia}R_{wi}\tau^2-1)}\left[\frac{\delta\tau\sqrt{R_{ia}R_{wi}}-1}{\delta\tau\sqrt{R_{ia}R_{wi}}+1}\right], \tag{6.23}$$

where δ is a term used to account for variations in thickness:

$$\delta = \exp\left(-\frac{2\pi\nu}{n_{ice}c}\sigma_l\right), \tag{6.24}$$

where σ_l is the optical pathlength variation:

$$\sigma_l = \frac{\sigma_h}{\sqrt{1-\sin^2\theta_1/\epsilon_{ice}}}, \tag{6.25}$$

where θ_1 is the incidence angle and σ_h is the standard deviation of ice thickness or "roughness parameter."

While the Menashi model converges to the open water values as ice thickness approaches zero, it does not account for differences in ice and water temperature, nor does it account for the sky temperature. The two may be combined in an ad hoc manner by taking the second

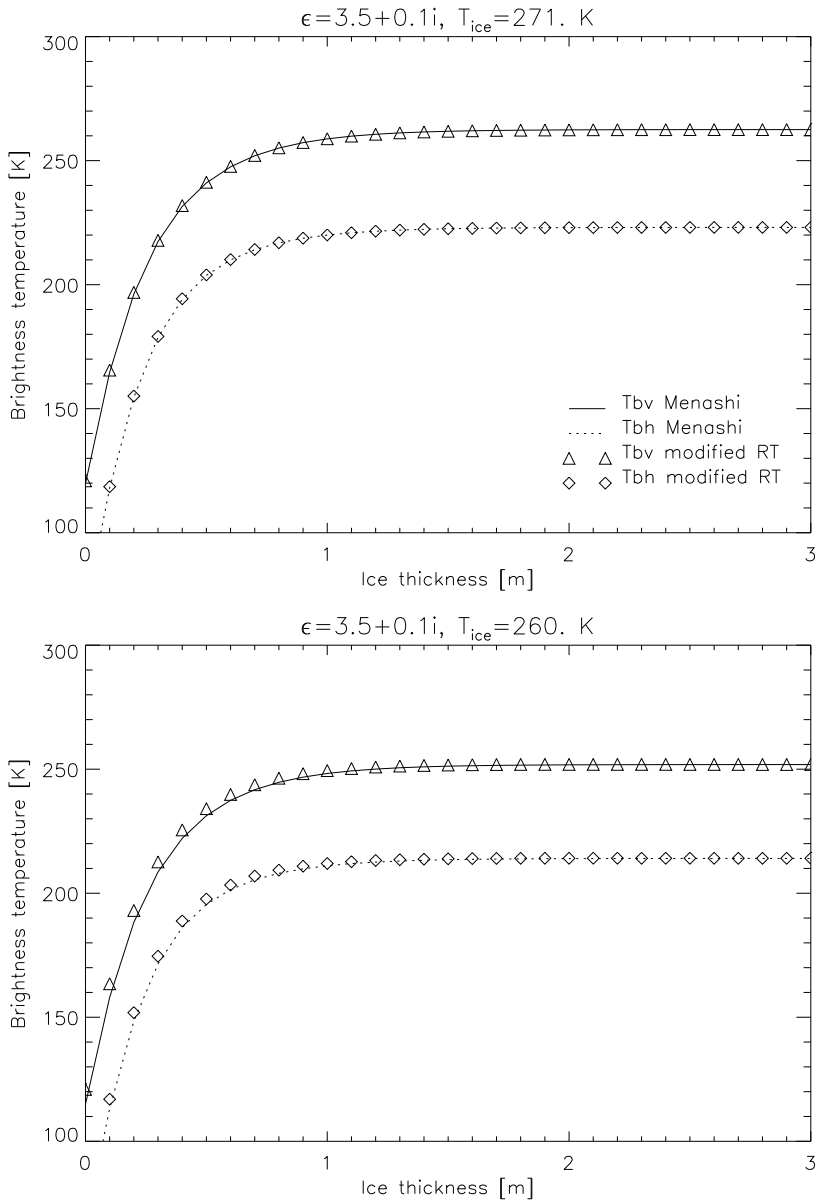

Figure 6.5: Comparison of Menashi versus modified radiative transfer three-layer, dielectric-slab models.

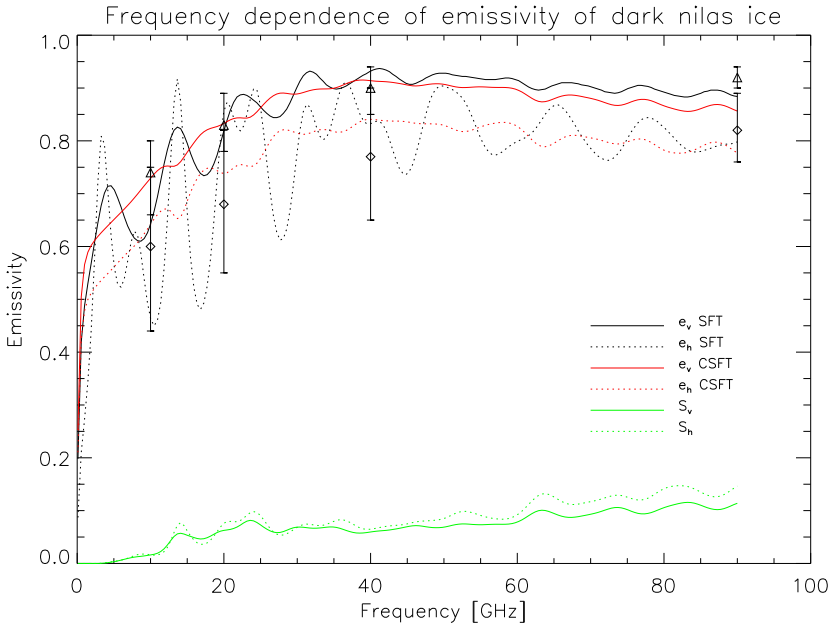

Figure 6.6: Modelled emissivity and scattering of dark nilas model ice profile (Table 6.1). S_v and S_h are the scattering contributions. Triangles and diamonds indicate averaged measured values for vertical and horizontal polarization,respectively, with error bars giving the range.

factor in Equation (6.23) and placing it alongside Equation (6.22):

$$T_b = (R_{ia}-1)\frac{(R_{wi}-1)\tau T_{water} + (R_{ia}-1)R_{wi}\tau^2 T_{sky} + \left[R_{wi}\tau^2 + (1-R_{wi})\tau - 1\right] T_{ice}}{R_{ia}R_{wi}\tau^2 - 1} \left[\frac{\delta\tau\sqrt{R_{ia}R_{wi}} - 1}{\delta\tau\sqrt{R_{ia}R_{wi}} + 1}\right]. \tag{6.26}$$

This will generate equivalent results when the ice and water temperatures are the same, but higher brightness temperatures for thin ice when the ice temperature is lower than the water temperature as Figure 6.5 shows (although the differences are small and it will be rare for thin ice to manifest such a large difference in temperature between that of the water.)

6.4 Frequency dependence for model ice profiles

6.4.1 Standard profiles

Results for three standard ice types for a 50 degree viewing angle are shown in Figures 6.6, 6.7 and 6.8. These are dark nilas, first-year and multiyear ice respectively, and the profile specifications are shown in Tables 6.1, 6.2 and 6.3 respectively (Johnsen, 1998; Fuhrhop et al., 1997).

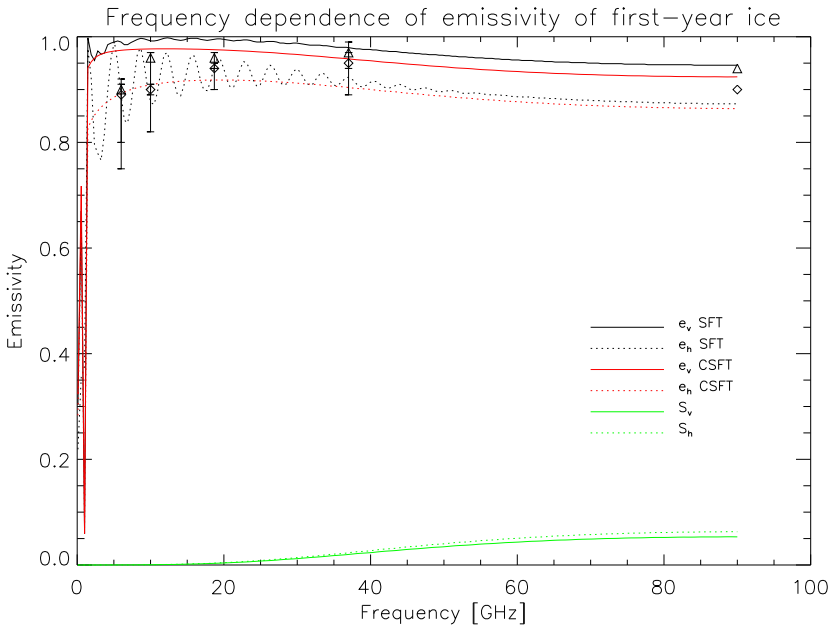

Figure 6.7: Modelled emissivity and scattering of first-year model ice profile (Table 6.2). Triangles and diamonds indicate averaged measured values for vertical and horizontal polarization,respectively, with error bars giving the range.

Table 6.1: Standard profile for dark nilas. Table columns are: depth, temperature T, density ρ, free-water content fwc, grain size d_i, bubble diameter d_{bub}, salinity S, brine-pocket angle θ_{br} and brine-pocket aspect ratio r_{br}.

z [m]	T [K]	ρ [g/cm^3]	d_{snow} [mm]	fwc	d_i [mm]	d_{bub} [mm]	S [$^\circ/_{\circ\circ}$]	θ_{br} [$^\circ$]	r_{br}
-9.00	271.4	1.0	0.0	1.0	0.0	0.0	32.0	0.0	0.0
-0.01	265.0	0.80	0.0	0.0	10.0	1.2	10.0	54.7	1.0
0.00	260.0	0.34	1.00	0.0	0.0	1.2	3.0	54.7	1.0

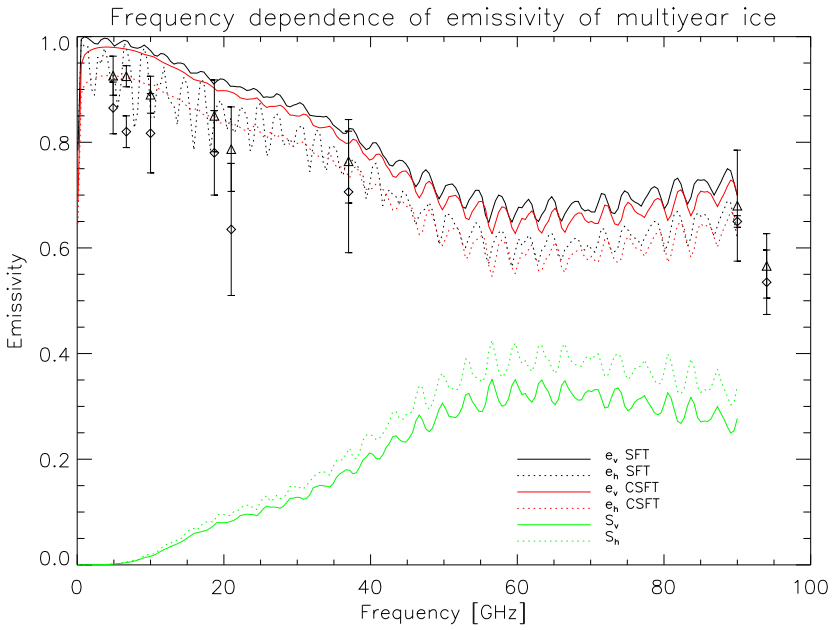

Figure 6.8: Modelled emissivity and scattering of multi-year model ice profile (Table 6.3). Triangles and diamonds indicate averaged measured values for vertical and horizontal polarization,respectively, with error bars giving the range.

Table 6.2: Standard profile for first year ice. For column descriptions, see Table 6.2.

z [m]	T [K]	ρ [[g/cm^3]	d_{snow} [mm]	fwc	d_i [mm]	d_{bub} [mm]	S [°/₀₀]	θ_{br} [°]	r_{br}
-0.68	271.0	1.00	0.0	1.00	0.0	1.2	35.0	4.0	0.25e-4
-0.59	271.0	0.92	0.0	0.138	1.2	1.2	5.6	4.0	0.25e-4
-0.49	270.0	0.92	0.0	0.141	1.2	1.2	6.9	4.0	0.25e-4
-0.29	269.0	0.92	0.0	0.131	1.2	1.2	9.4	4.0	0.25e-4
-0.19	268.0	0.92	0.0	0.100	1.2	1.2	10.0	4.0	0.25e-4
-0.09	266.0	0.92	0.0	0.131	1.2	1.2	17.5	4.0	1.0
-0.08	266.0	0.92	0.0	0.131	1.2	1.2	17.5	4.0	1.0
-0.04	263.0	0.34	1.0	0.028	0.0	1.2	5.9	4.0	1.0

Table 6.3: Standard profile for multi year ice. For column descriptions, see Table 6.3.

z [m]	T [K]	ρ [[g/cm^3]	d_{snow} [mm]	fwc	d_i [mm]	d_{bub} [mm]	S [$^\circ/_{\circ\circ}$]	θ_{br} [$^\circ$]	r_{br}
-2.50	269.9	1.0	0.0	1.0	0.0	0.0	32.0	0.0	0.0
-1.58	266.1	0.870	0.0	0.0	10.0	1.2	3.0	24.0	0.25e-4
-1.02	265.7	0.870	0.0	0.0	10.0	1.2	2.4	24.0	0.25e-4
-0.97	265.4	0.890	0.0	0.0	10.0	1.2	1.9	24.0	0.25e-4
-0.87	265.1	0.890	0.0	0.0	10.0	1.2	1.4	24.0	0.25e-4
-0.77	264.8	0.890	0.0	0.0	10.0	1.2	1.2	24.0	0.25e-4
-0.63	264.5	0.895	0.0	0.0	10.0	1.2	0.7	24.0	0.25e-4
-0.46	264.1	0.895	0.0	0.0	10.0	1.2	0.3	24.0	0.25e-4
-0.38	263.7	0.728	0.0	0.0	10.0	1.2	0.1	24.0	0.25e-4
-0.20	263.5	0.728	0.8	0.0	0.0	3.0	0.0	54.7	1.0
-0.15	263.3	0.460	0.8	0.0	0.0	5.0	0.0	54.7	1.0
-0.10	263.1	0.100	0.8	0.0	0.0	1.2	0.0	0.0	1.0

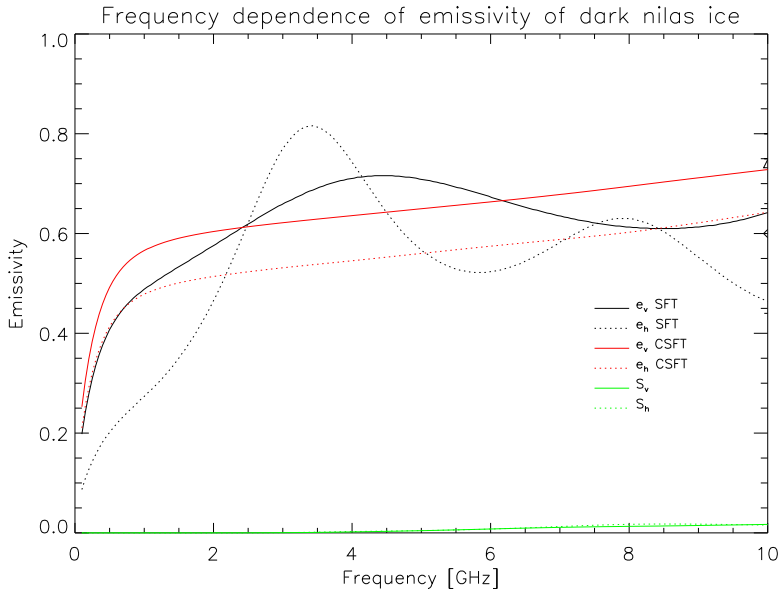

Figure 6.9: Modelled emissivity and scattering of dark nilas model ice profile (Table 6.1). Triangles and diamonds indicate averaged measured values for vertical and horizontal polarization,respectively, with error bars giving the range.

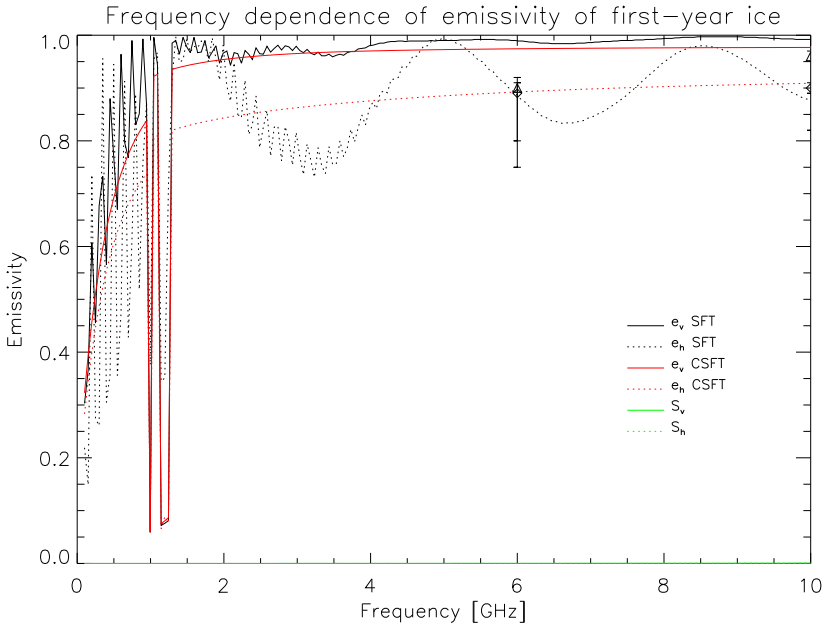

Figure 6.10: Modelled emissivity and scattering of first-year model ice profile (Table 6.2). Triangles and diamonds indicate averaged measured values for vertical and horizontal polarization,respectively, with error bars giving the range.

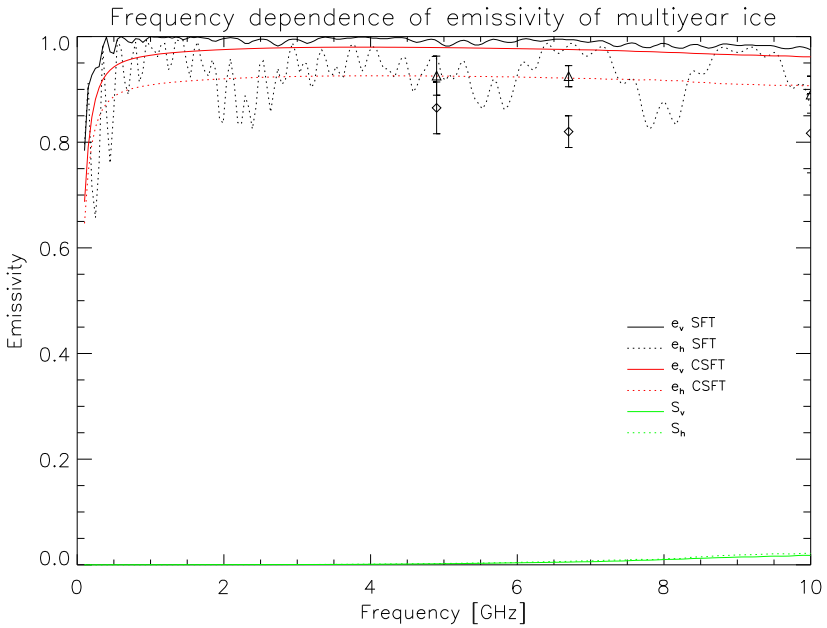

Figure 6.11: Modelled emissivity and scattering of multi-year model ice profile (Table 6.3). Triangles and diamonds indicate averaged measured values for vertical and horizontal polarization,respectively, with error bars giving the range.

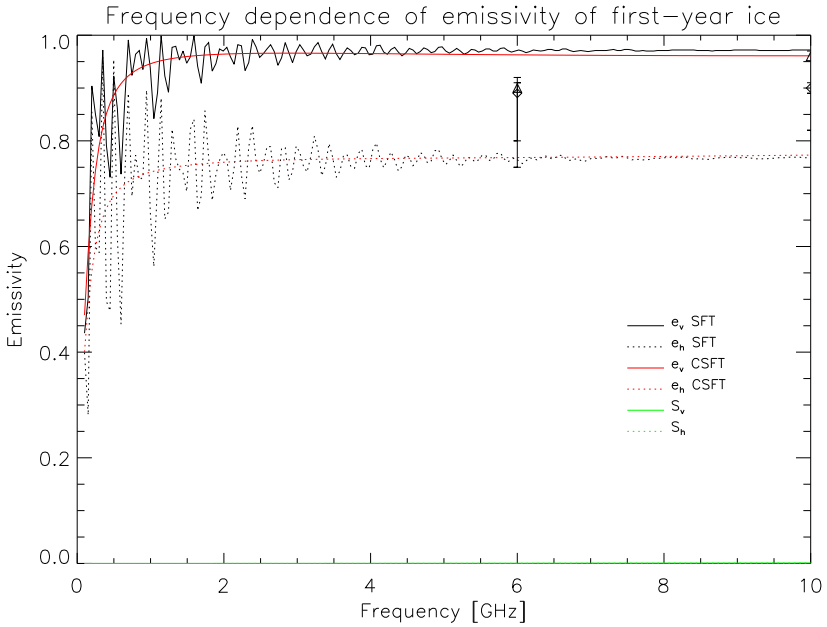

Figure 6.12: Modelled surface emissivity and scattering of "synthetic" ice profile: 'C'-shaped salinity profile, bulk salinity, $S_{ave} = 6$, and surface temperature, $T_s = 265$ K (Table 6.4). Triangles and diamonds indicate, averaged measured values for vertical and horizontal polarization,respectively, with error bars giving the range.

Horizontal lines divide the three major layers: water, ice and snow. In lieu of simple correlation lengths, the program for CSFT computation accepts five parameters for ice–density (ρ), grain size (d_i), bubble diameter (d_{bub}), brine pocket ratio (r) and brine pocket angle (θ_{br})– and four for snow–density, grain size (d_{sn}), free-water content (fwc) and bubble diameter (d_{bub}). The results are within the range of average in situ measurements which are indicated by vertical error bars. Blow-ups for lower frequencies are shown in Figures 6.9, 6.10 and 6.11. Unless otherwise stated, the viewing angle is always held fixed at 50°.

In addition to results for the SFT and CSFT calculations, scattering coefficients are also shown. For lower frequencies, these drop to almost zero so that volume scattering at L-band is completely negligible for all three ice types: scattering coefficients are of order 1×10^{-4} for multiyear ice. This is in agreement with the literature: see for instance Barber et al. (1998). Vant et al. (1978) estimate that scattering will only be significant above 1.5 GHz for multi-year ice and 24 GHz for first-year ice.

6.4.2 Parameterized model profiles

The SFT and CSFT emission models require a large number of parameters as input, which produces a difficult inversion problem. To reduce the number of free parameters, a set of synthetic

Table 6.4: Synthetic model ice profile with 'C'-shaped salinity profile, bulk salinity, $S_{ave} = 6$, and surface temperature, $T_s = 265K$. Table columns are: depth, temperature T, density ρ, free-water content fwc, grain size d_i, bubble diameter d_{bub}, salinity S, brine-pocket angle θ_{br} and brine-pocket aspect ratio r_{br}.

z [m]	T [K]	ρ [[g/cm^3]	d_{snow} [mm]	fwc	d_i [mm]	d_{bub} [mm]	S [$^\circ/_{\circ\circ}$]	θ_{br} [$^\circ$]	r_{br}
-0.7	271.0	1.0	0.0	1.0	0.0	0.0	34.00	0.0	0.0
-0.5	271.0	0.9	0.0	0.1	1.2	1.2	9.49	0.0	0.1
-0.4	269.5	0.9	0.0	0.1	1.2	1.2	4.42	0.0	0.1
-0.3	268.0	0.9	0.0	0.1	1.2	1.2	3.98	0.0	0.1
-0.2	266.5	0.9	0.0	0.1	1.2	1.2	6.57	0.0	0.1
-0.1	265.0	0.9	0.0	0.1	1.2	1.2	10.60	0.0	0.1
-0.0	265.0	0.9	0.0	0.1	1.2	1.2	10.60	0.0	0.1

model profiles has been developed that take as input a smaller set of bulk parameters, thus making the problem more tractable. These are: number of layers, thickness, salinity profile type, bulk salinity and surface temperature. If reasonable assumptions are made, we should be able to generate realistic ice profiles that might occur in nature and if the model is working properly, simulated emissivities should also resemble those found in nature.

Eicken (1992) has identified four major types of ice profiles whose shapes correspond roughly to the symbols 'C', '?', 'Z' and 'S'. These can be varied by simply shifting their relative magnitudes to correspond to a given given bulk salinity. A simple linear temperature profile, corresponding to thermodynamic equilibrium, is used:

$$T(z) = \frac{z(T_{water} - T_s)}{h} + T_s \tag{6.27}$$

where T is the ice temperature, z is depth from the surface, T_s is surface temperature, $T_{water} =$ 271 K is water temperature. All other parameters are held constant and the snow layer is omitted: dry snow at least is almost transparent at L-band (Maetzler, 2001). A sample such profile is shown in Table 6.4 and resultant emissivity calculations in Figure 6.12.

6.5 Detailed comparison of mixture formulae

An analysis of the different mixing formulae reveals quite surprising differences between them and between the resulting calculated brightness temperatures. Figure 6.13 shows modelled brightness temperatures for a series of ice cores taken from the Weddell sea. These are the same cores used in Section 9.4 and include temperature and salinity measurements as a function of depth. To get a maximal range of possible brightness temperatures, 100 runs of the radiative transfer model described in Section 6.2.2 (Equations (6.7) through (6.13)) using complex permittivities randomly chosen from along the bounds given by Equations (6.19) and (6.20). Averages are marked in Figure 6.13 by the stars while standard deviations are shown by the error bars.

The complex permittivity bounds used in the preceding analysis are constrained only by brine volume, with no consideration given to geometry, thus the results represent a maximal bound. Presumably, if geometry is more constrained, the bounds should be smaller. Figure 6.14 shows a similar plot to Figure 6.13 except this time applying three different mixture formulae and taking the averages and standard deviations. These are the empirical formulae, as

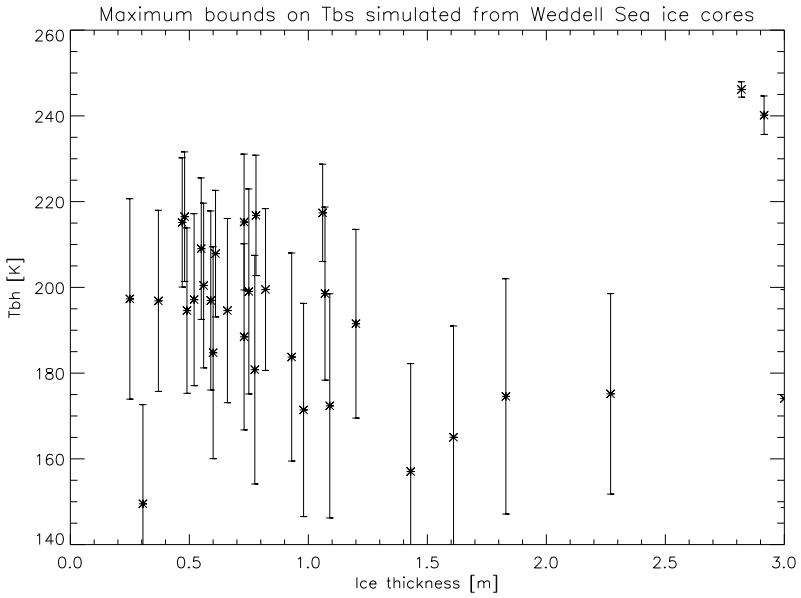

Figure 6.13: Bounds on brightness temperatures modelled from ice cores in the Weddell sea for arbitrary brine geometry.

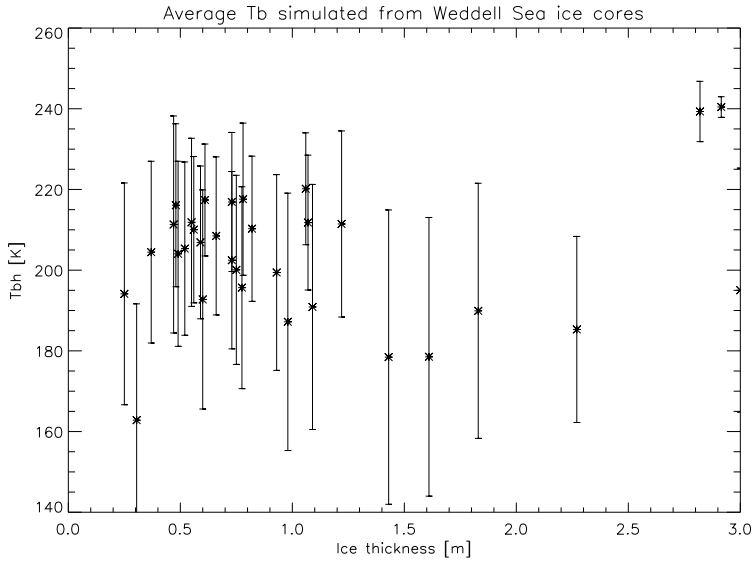

Figure 6.14: Bounds on brightness temperatures modelled from ice cores in the Weddell sea using three different mixture formulas.

in Equation (21) from Vant et al. (Vant et al., 1978), Equation (5) from Sihvola and au Kong (1988) for spherical inclusions:

$$\epsilon_{eff} = \epsilon_1 + \frac{3V(\epsilon_2 - \epsilon_1)\epsilon_2/(\epsilon_2 + 2\epsilon_1)}{1 - V(\epsilon_2 - \epsilon_1)/(\epsilon_2 + 2\epsilon_1)}, \tag{6.28}$$

and Equation (18) from Shokr (1998) for randomly oriented needles:

$$\epsilon_{eff} = \epsilon_1 + \frac{v(\epsilon_2 - \epsilon_1)}{3(\epsilon_2 + \epsilon^*)}(5\epsilon^* + \epsilon_2) \tag{6.29}$$

where $\epsilon^* = \epsilon_1$ for $V < 0.1$ and $\epsilon^* = \epsilon_{eff}$ for $V \geq 0.1$.

Even using only three different formulae, the results show a similar spread as using the maximally bounded analytic continuation method. More encouraging is the relatively good agreement between both the averages and the standard deviations, as seen in Figures 6.15 and 6.16.

To check the agreement between the different formulae, Figure 6.17 plots out the three different mixture models along with the analytic continuation bounds for several representative temperature and salinity conditions. An important point to note is that *none* of the mixture formula calculations for single values of complex permittivity fall within the bounds generated by analytic continuation. While absolute magnitudes vary broadly, once again the functional dependencies agree quite well as the cross-correlation matrices shown in Tables 6.5 and 6.6 demonstrate. These tables correlate the real and imaginary components of the permittivities calculated to produce Figures 6.13 and 6.14 plus Strong Fluctuation Theory. The tables show

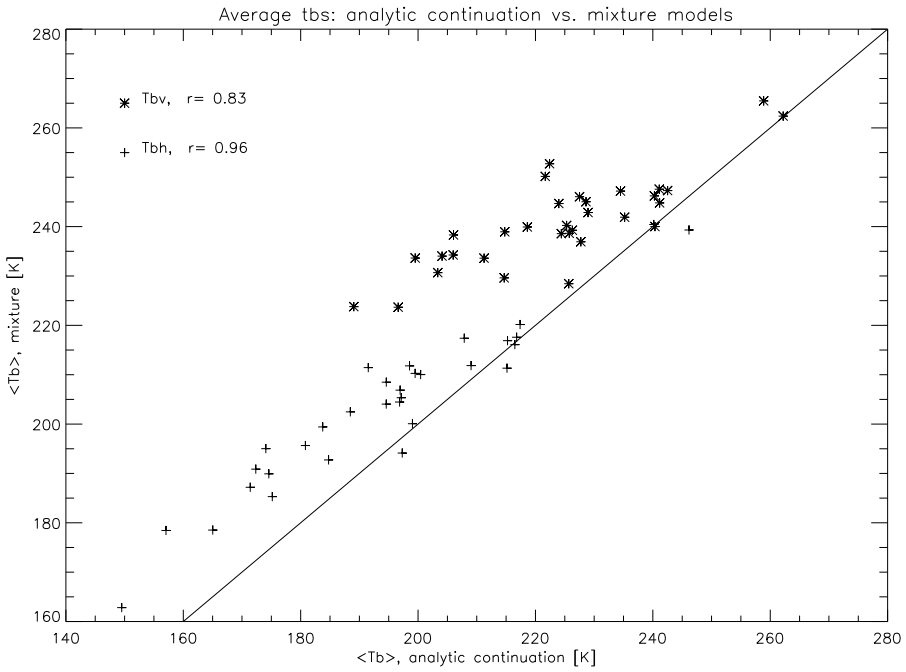

Figure 6.15: Comparison between average brightness temperatures for analytic continuation and mixture formulas.

Table 6.5: Cross-correlation matrix of real permittivities calculated from five different formulae.

	Vant	Sihvola	Shokr	Golden (mean)	SFT
Vant	1.00	0.998	0.979	0.753	0.723
Sihvola	0.998	1.00	0.983	0.754	0.730
Shokr	0.979	0.983	1.00	0.750	0.736
Golden (mean)	0.753	0.754	0.750	1.00	0.941
SFT	0.723	0.730	0.736	0.941	1.00

Table 6.6: Cross-correlation matrix of imaginary permittivities calculated from five different formulae.

	Vant	Sihvola	Shokr	Golden (mean)	SFT
Vant	1.00	0.971	0.924	0.530	0.658
Sihvola	0.971	1.00	0.985	0.617	0.676
Shokr	0.924	0.985	1.00	0.656	0.662
Golden (mean)	0.530	0.617	0.656	1.00	0.834
SFT	0.658	0.676	0.662	0.834	1.00

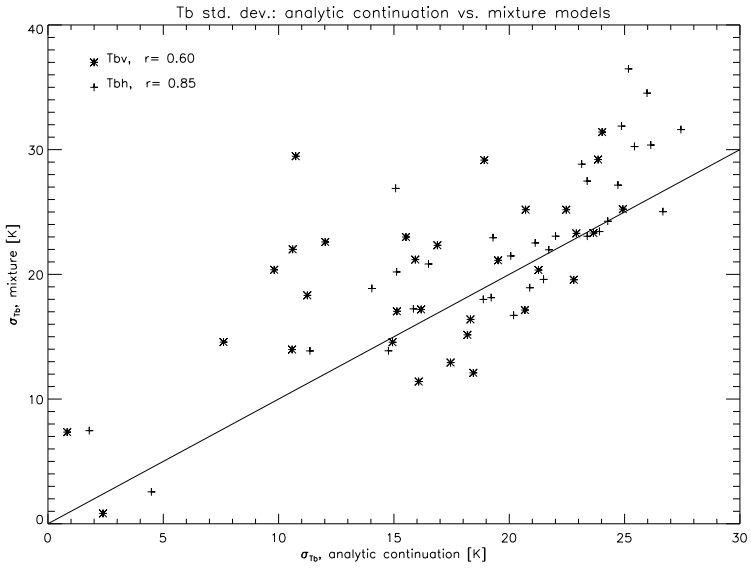

Figure 6.16: Comparison between brightness temperature standard deviations for analytic continuation and mixture formulas.

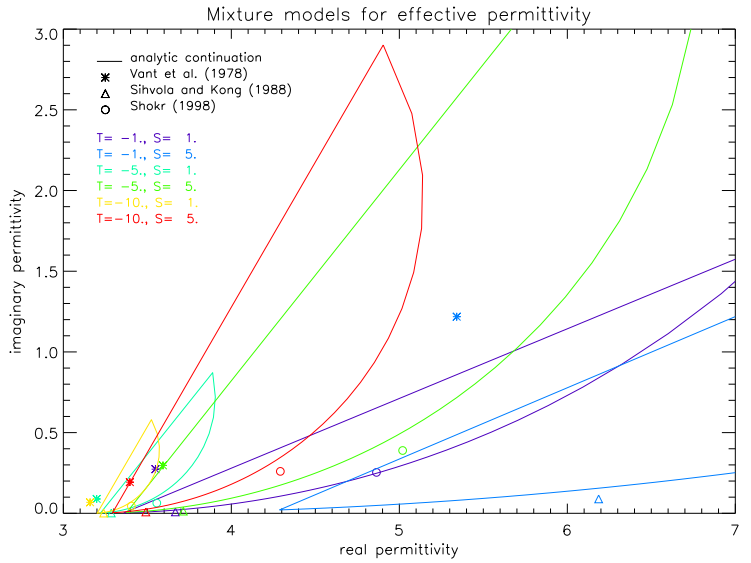

Figure 6.17: Comparison of different mixture formulas for representative temperatures and salinities.

that the five considered permittivity models can be subdivided into two groups of highly correlated permittivities. The first group comprises the models of Vant, Shivola and Shokr, the second group those of Golde an the SFT.

6.6 Intercomparison study

Chapter 5 describes a simple thermodynamic ice growth model that includes heat transfer but no brine drainage or expulsion. This is unlike the Cox and Weeks (1988) model that has just the opposite functionality. To test the validity of the revised RT model and to compare it with similar emissivity models such as MEMLS, brightness temperatures were calculated from three runs of this growth model using both CSFT and the mixture model. A sample for first-year ice is shown in Figure 6.18–compare with Figures 5.4 and 5.9 in Chapter 5 Unless otherwise stated, all simulations were done at a 47.2 degree viewing angle.

Figure 6.19 shows a plot of the imaginary versus real part of the permittivity for both the ice and snow component. The points are colour-coded by the different growth model runs and for the different permittivity models–SFT and mixture. The values are similar to those shown in Chapter 5 with a few key differences. The imaginary permittivities of ice tend to be lower and there is more variance in both values. Note that for the mixture model, the real and imaginary components for ice are directly related and fall along a curve. The values calculated from SFT fall close and also almost in a line; it is mainly the dependence on density that produces scatter. As previously mentioned, the imaginary permittivity of the snow is constant for the mixture model. Permittivities calculated from the mixture model are quite a lot higher than those generated by SFT, as can also be seen in Figure 6.17.

Figures 6.20, 6.21 and 6.22 show the brightness temperatures plotted with respect to ice thickness, surface temperature and bulk salinity. Compare with figure 5.15 in Chapter 5. The pronounced drop in emission temperature with increasing thickness (and time) seen in the first-year run started in January (blue points) is physical. Two events occur to produce this. First, there is a heavy snowfall. Second, the salinity of the top layer was fixed at a very high value of 15 and there is a sharp increase in air temperature: this will produce high values of the real permittivity. Both will serve to reflect more radiation from the sky, while less of the internally emitted radiation will come through. Note also in Figure 6.22 that if one follows the black points, the time series of salinity first decreases, then starts to increase before once again decreasing. While it is normal for older ice to be less saline than newer, one can see from the corresponding temperature profile in Figure 6.18 that the middle of the run encounters colder temperatures. This will produce faster ice growth (also clearly visible) and therefore higher salinity in the newly formed layers. Once a layer is formed, the salinity remains fixed throughout the run.

The CSFT and mixture models discussed in this report do not compare all that well seen in Figure 6.23. This is primarily because of the differences in calculated effective permittivities. Multiyear ice shows the least discrepency because the ice has become optically thick and because the lower density of multi-year ice, surprisingly, produces higher permittivity values as shown in Figure 6.19. In particular, CSFT shows a much larger sensitivity to ice thickness than mixture model results.

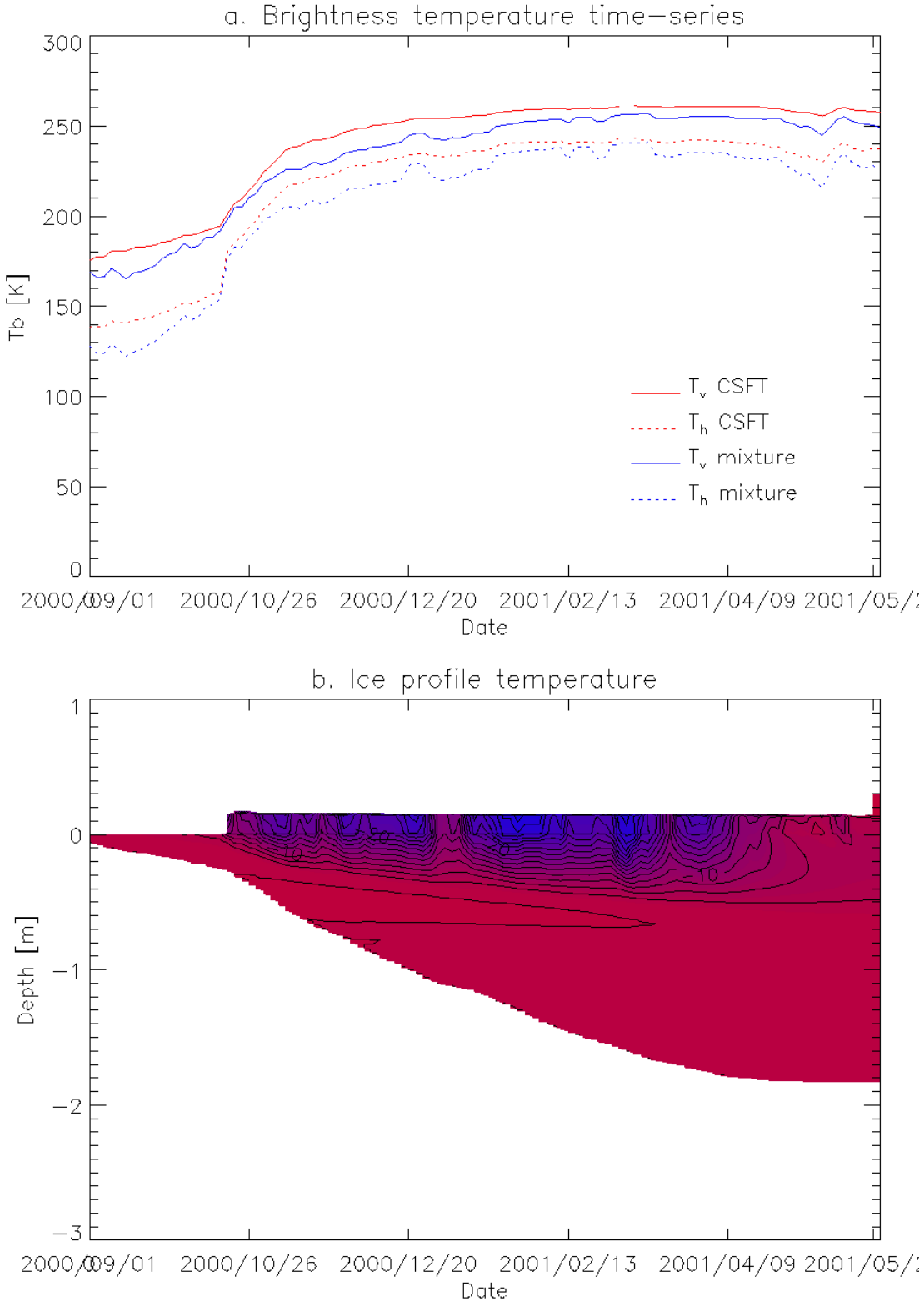

Figure 6.18: Time series of emitted brightness and physical temperatures modelled from growth and thermodynamics.

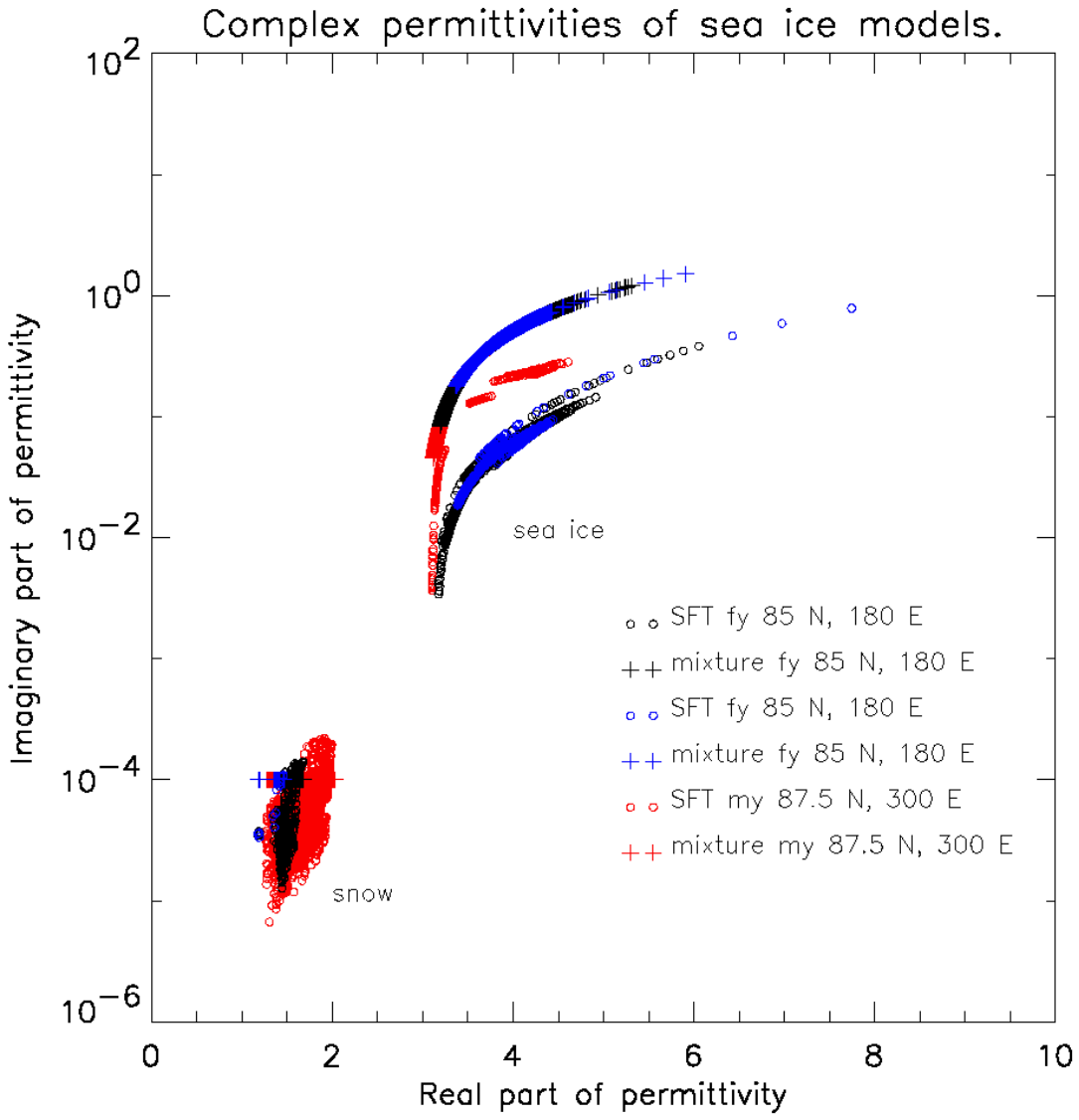

Figure 6.19: Permittivity values of snow and ice. Black is for first-year ice started in September, blue is first- year ice started in January and red is multiyear.

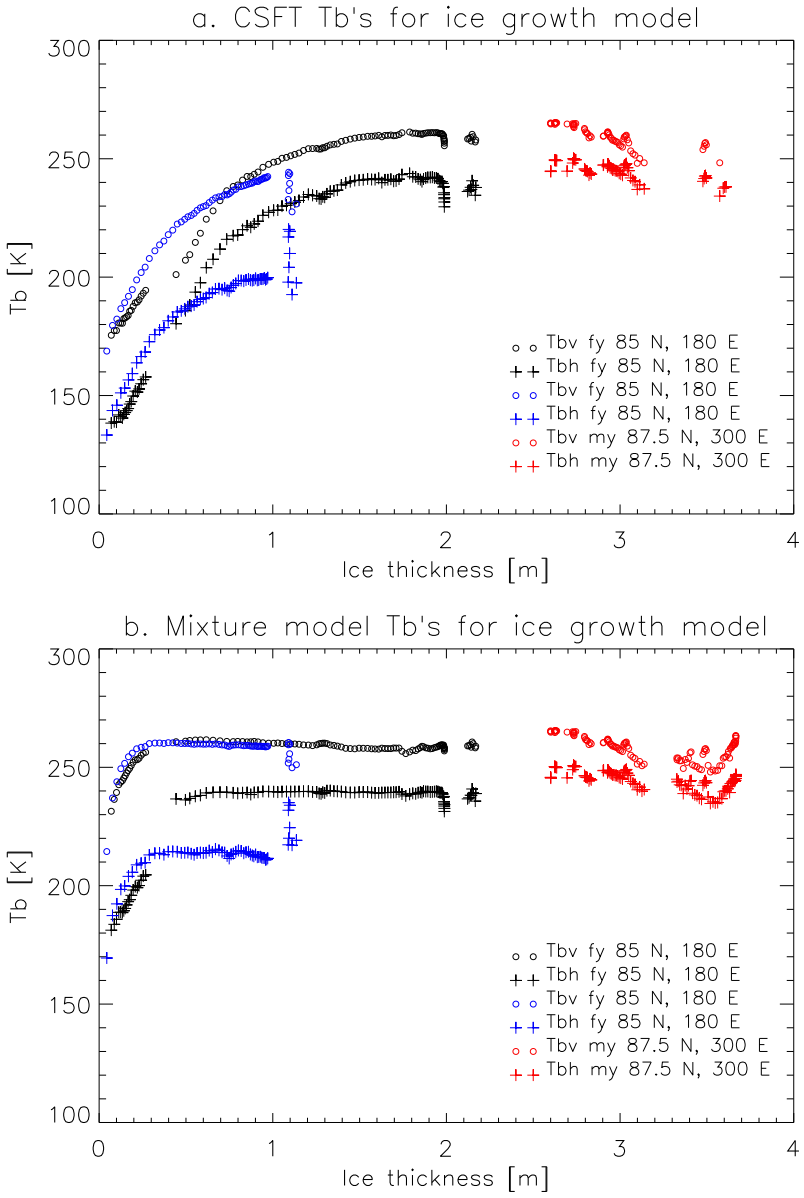

Figure 6.20: Brightness temperature as a function of ice thickness. Black is for first year ice started in September, blue is first year ice started in January and red is multi-year.

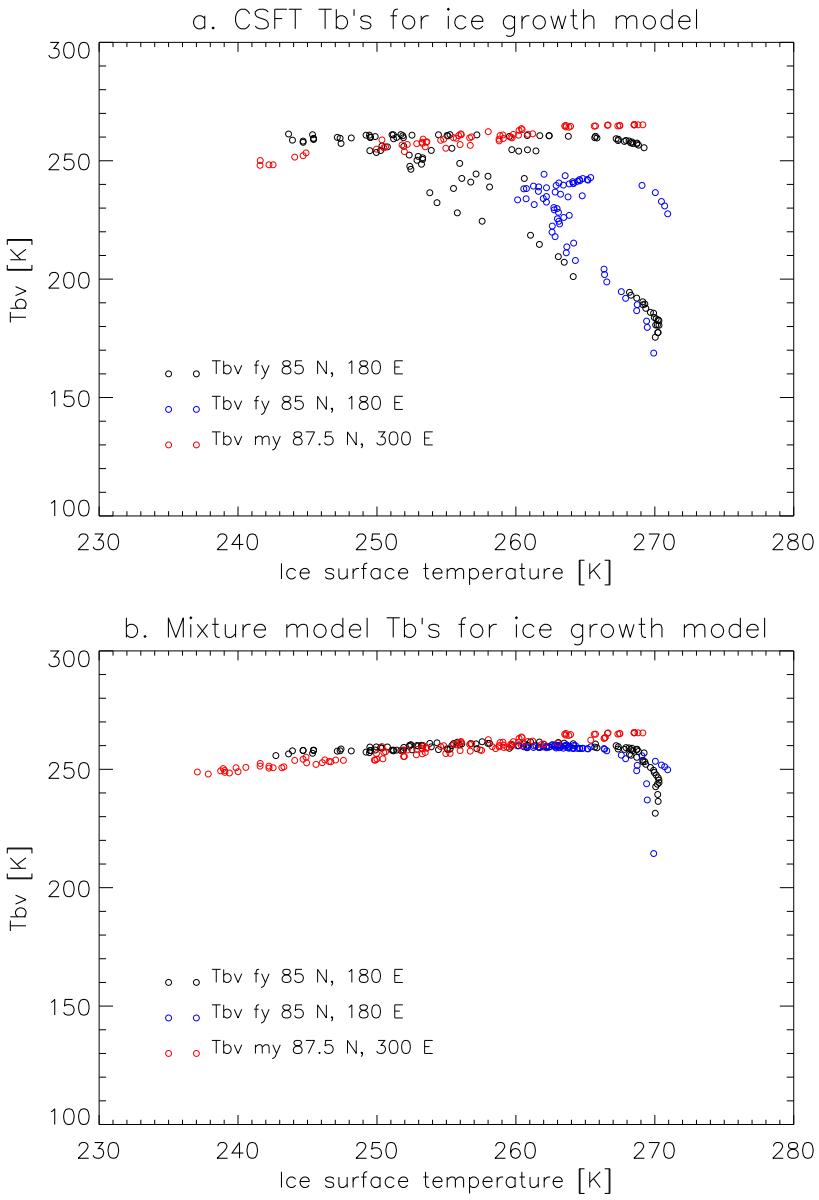

Figure 6.21: Brightness temperature as a function of ice surface temperature. Black is for first year ice started in September, blue is first year ice started in January and red is multi-year.

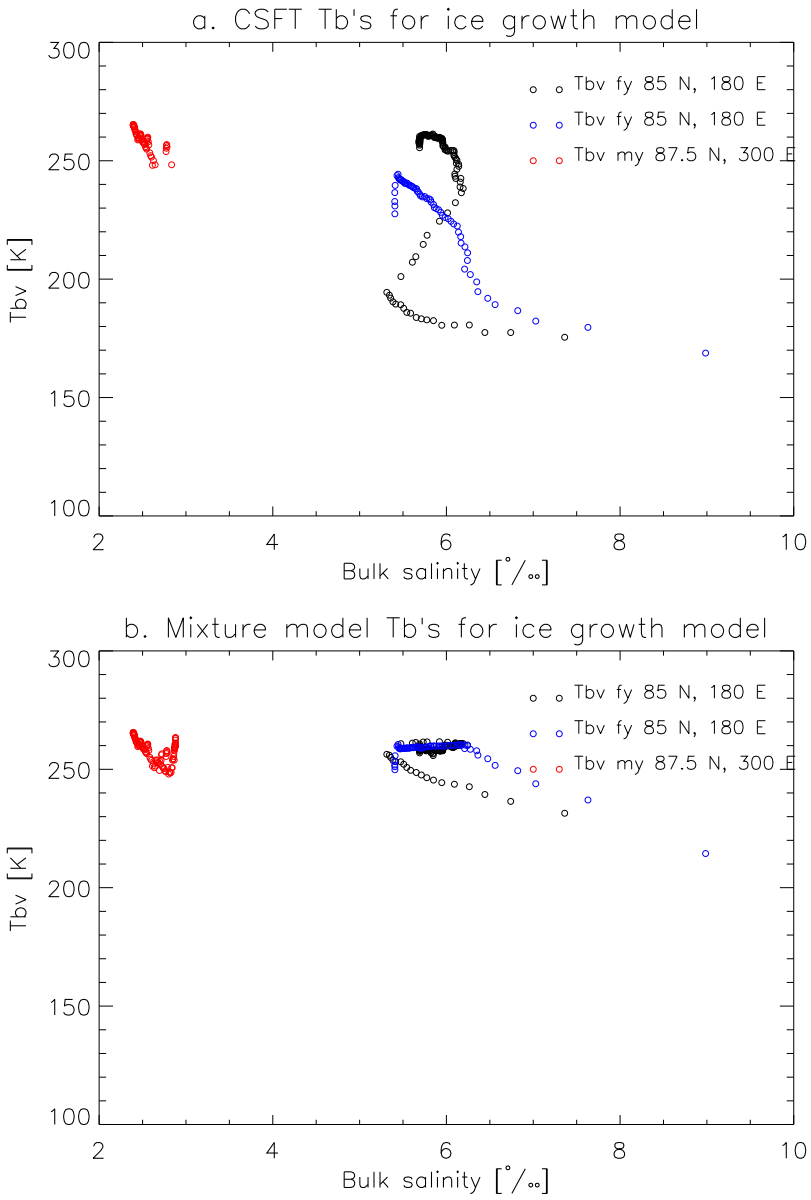

Figure 6.22: Brightness temperature as a function of bulk salinity. Black is for first year ice started in September, blue is first year ice started in January and red is multi-year.

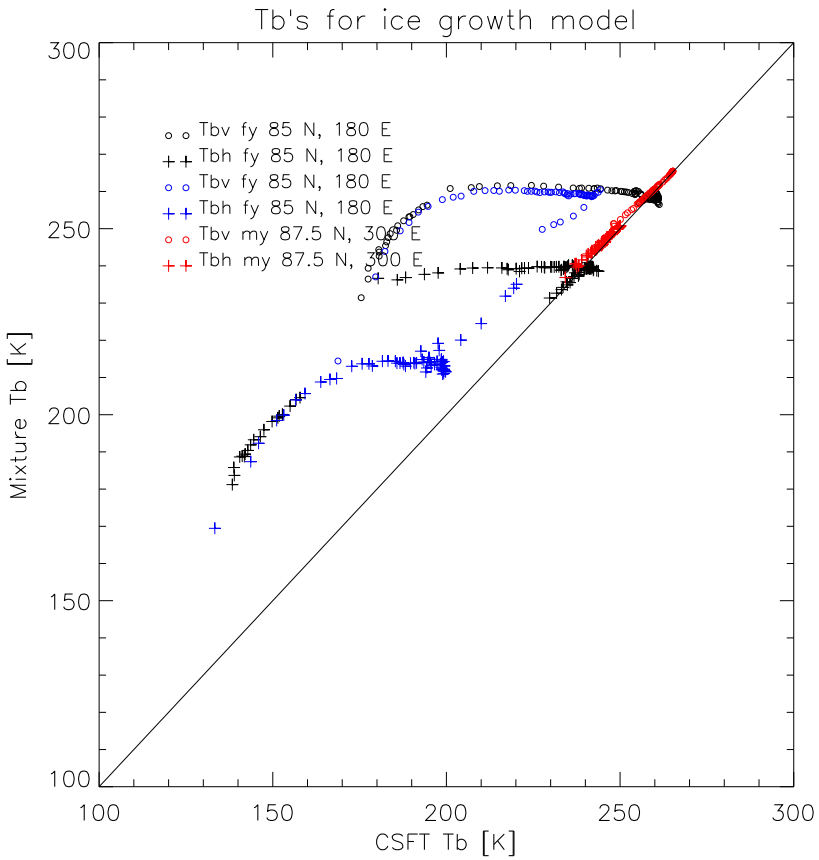

Figure 6.23: Comparison between CSFT and mixture models.

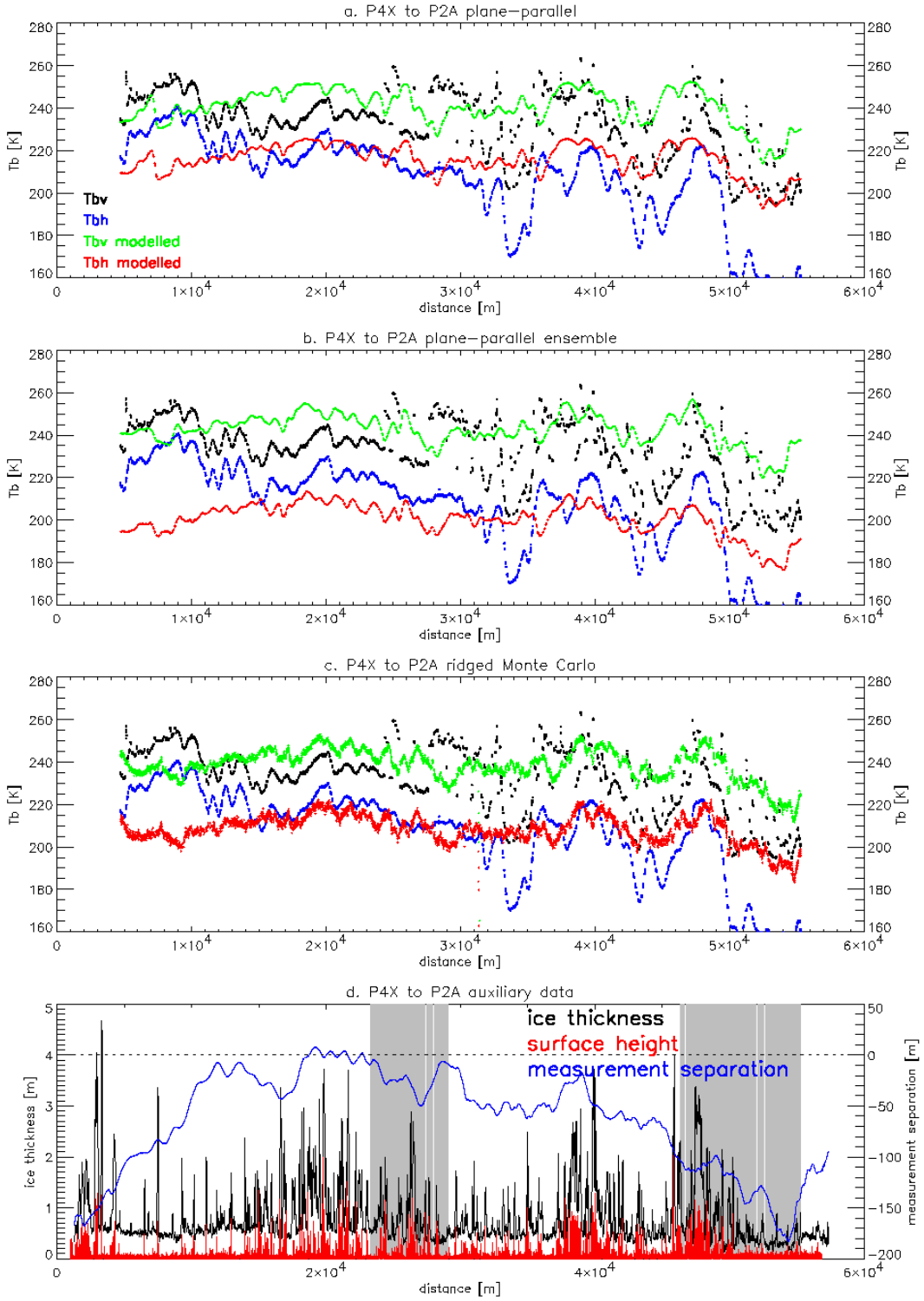

Figure 6.24: Time series showing model results versus measurements for one overflight (P4X to P2A). Three different models were used: a three-layer plane-parallel model, an ensemble of plane-parallel models averaged over the instrument footprint and a ridged Monte Carlo ray-tracing algorithm. A constant permittivity of $\epsilon = 4.0 + 0.1i$ was assumed.

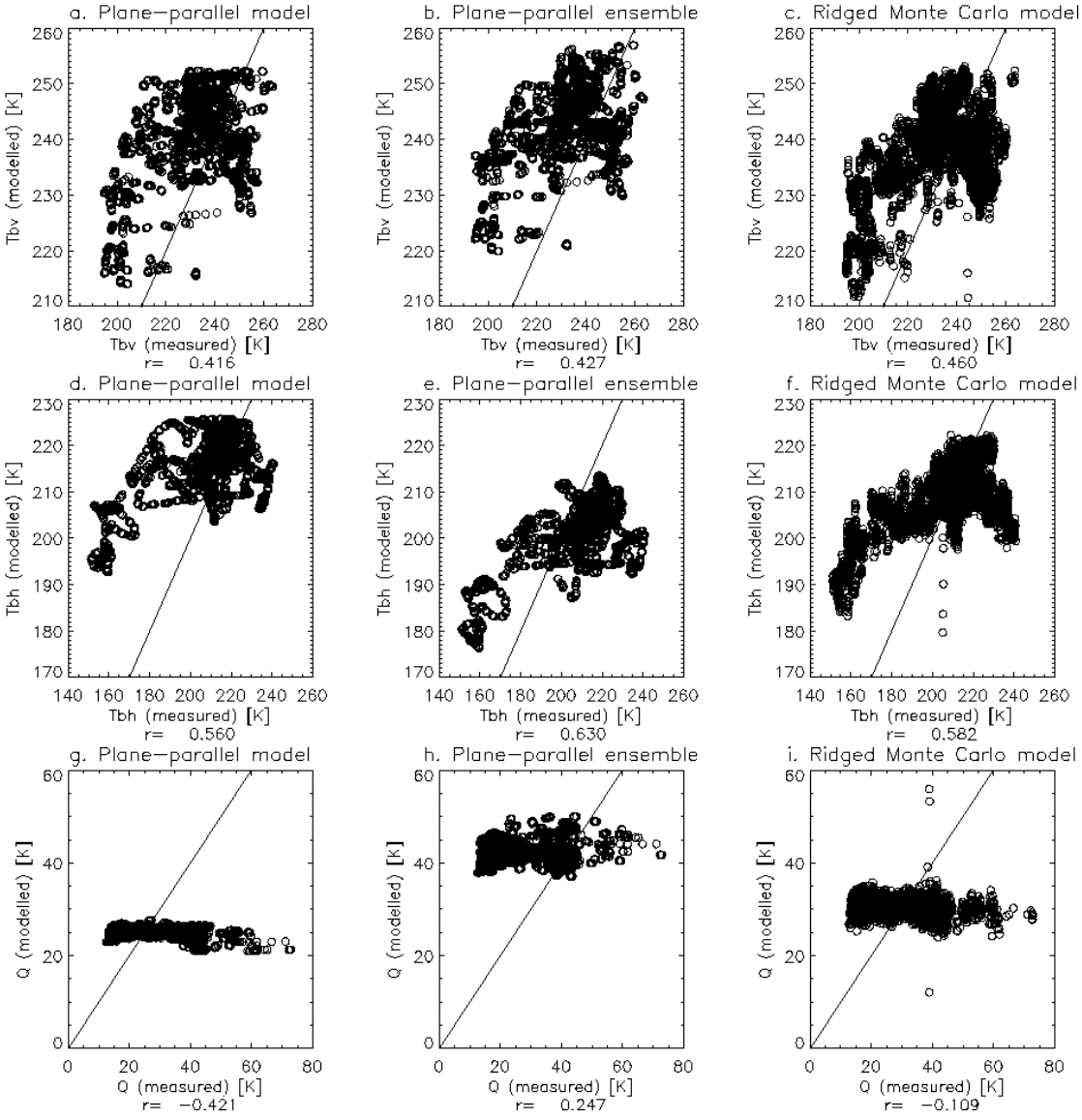

Figure 6.25: Scatter plots showing model results versus measurements for one overflight (P4X to P2A). Three different models were used: a three-layer plane-parallel model, an ensemble of plane-parallel models averaged over the instrument footprint and a ridged Monte Carlo ray-tracing algorithm. A constant permittivity of $\epsilon = 4.0 + 0.1i$ was assumed.

6.7 Forward modelling of Pol-Ice data

The ridged ice model was tested on the Pol-Ice 2007 campaign data for the flight track with the best coincidence between the radiometer and E-M bird overflights. Processing and collocation procedures for these measurements will be described in detail in Chapter 9. Forward model results as compared to measuremed values are shown in Figure 6.25 for three different models. The first model is the three-layer, plane-parallel model mentioned in the previous section. Input to the model is ice thickness averaged over the instrument footprint, an ice temperature of -1 degrees C and a constant permittivity of $\epsilon = 4.0 + 0.1i$. The second model, referenced ensemble model, is also a plane-parallel model, except instead of first averaging the parameters over the footprint, the model is run for each measurement point in the footprint. The final model is the ridged Monte Carlo model described in the first part of this section.

The results show that ice ridging accounts for a small but significant fraction of the measured variance. The Monte Carlo model has the best agreement in the vertical polarisation, while the ensemble model has the best agreement in the horizontal. Of particular note is the negative correlation between the measured and computed values of the polarisation difference in the single plane-parallel model. This is partially corrected for in the ensemble model, thus ice ridging accounts for a portion of the polarisation signal. A further explanation will be presented in Chapter 9.

6.8 Conclusion

Several forward ice emissivity models were described, including Strong Fluctuation Theory (SFT), a plane-parallel, radiative transfer (RT) model that can take as input permittivities from SFT or mixture formulae and a ridged Monte Carlo model. These models were tested on several scenarios. Perhaps the most revealing validation runs on field data from the Pol-Ice 2007 campaign. Several important conclusions can be drawn from this test. First, ice thickness explains some of the variance seen in ice radiance measurements at L-band. Second, a much smaller, but still significant, portion of the variance can be explained by ice ridging. In order to account for this ridging, the instrument receiver characteristics have to be properly modelled.

The most important link in the chain of dependencies determining the final brightness temperatures of sea ice is modelling the complex permittivities. It is also the most difficult, because it is not just the ice bulk properties that must be accounted for, it is also the microphysical properties which are notoriously difficult both to measure and to model. Several mixture formulas for effective permittivity were compared as well as model results from SFT. While their functional dependencies were quite close, their absolute magnitudes were found to differ broadly. The differences between SFT and mixture model effective permittivities were found to produce large discrepencies in modelled brightness temperature in the validation portion of this report. In particular, modelling permittivity with SFT is found to produce a much larger sensitivity to ice thickness than using the empirical mixture formulae from Vant et al. (1978).

Chapter 7

WP 2.4a: Forward modelling Stokes components U and V

Rasmus T. Tonboe

Danish Meteorological Institute

7.1 Introduction

SMOS will measure the complete brightness temperature polarisation state described by the Stokes vector. The components of the Stokes vector is the intensity, I, the polarisation Q, the tilt of the polarisation ellipse, U, and the left-right handedness, V. Here a simple model for the Stokes vector is presented which is also applicable at L-Band. Both an U and a V signal was produced by the model by changing the surface permittivity within reasonable limits. Fully polarimetric measurements from Space over sea ice were earlier acquired by Coriolis/ WindSat at 10, 18 and 37GHz (Narvekar et al., 2008). The U and V signal in WindSat data over sea ice was rather weak most of the time, however, during the onset of melt and during temporary surface melt a U sea ice signal was observed. The physical explanation for the observed U signal is not understood in detail but the model shows that a U signal is possible when the surface density is changing. If that is the case then a non-zero U signal is also expected over sea ice with SMOS.

7.2 The Stokes vector

The complete description of the polarisation state of electromagnetic radiation is given by the brightness Stokes vector (Schanda, 1987), i.e.

$$\hat{T}_B = \begin{pmatrix} I \\ Q \\ U \\ V \end{pmatrix} = \frac{\lambda^2}{kz} \begin{pmatrix} < E_v E_v^* > + < E_h E_h^* > \\ < E_v E_v^* > - < E_h E_h^* > \\ 2\mathrm{Re} < E_v E_h^* > \\ 2\mathrm{Im} < E_v E_h^* > \end{pmatrix} \tag{7.1}$$

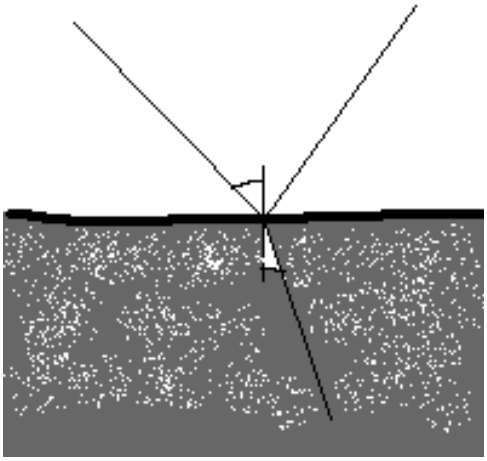

Figure 7.1: The reflected and transmitted ray across the interface.

where λ, k, and z are the wavelength, Stefan Bolzmanns constant and impedance respectively. E is the electric field and * denote the complex conjugate. I, is the intensity, Q, the polarisation, U, the tilt of the polarisation ellipse, and V, is the left or right handedness.

7.3 A simple model

A simple model which computes the reflection and transmission at an interface shown in fig. 7.1. The model uses the complex permittivity to compute the surface reflection and the normalised Stokes vector. Each of the three components Q, U, V are normalised to the intensity I. It is expected that the simulation results are applicable at L-Band.

For a wave travelling across a boundary between two different media we have (Schanda, 1987), i.e.

$$n_1(E_{1f} - E_{1r}) = n_2 E_{2f} \tag{7.2}$$

where E_{1f} is the forward electric field in media 1, E_{1r} is the reflected field at the boundary in media 1, E_{f2} is the forward field in media 2 and n_1 and n_2 the refractive index in media 1 and 2 respectively ($n = \sqrt{\epsilon}$). The reflection coefficient in terms of the reflected and forward field is (Schanda, 1987):

$$R_E = \frac{E_{1r}}{E_{1f}} \tag{7.3}$$

The reflection coefficient in terms of permittivity and incidence angle (Fung, 1994), i.e.

$$R_v = \frac{\epsilon_r \cos\theta - \sqrt{\mu_r\epsilon_r - \sin^2\theta}}{\epsilon_r \cos\theta + \sqrt{\mu_r\epsilon_r - \sin^2\theta}} \tag{7.4}$$

$$R_h = \frac{\mu_r \cos\theta - \sqrt{\mu_r\epsilon_r - \sin^2\theta}}{\mu_r \cos\theta - \sqrt{\mu_r\epsilon_r - \sin^2\theta}} \tag{7.5}$$

Now we set $E_{1f} = 1$ and we can compute the complex forward electric field across the bound-

ary for both vertical and horizontal polarisation and the Stokes vector.

7.4 Simulation results

The saline sea ice permittivity may be anisotropic due to vertically oriented elongated brine pockets. For example, expressions for the permittivity, ϵ, parallel and perpendicular to the brine pocket structure (Shokr, 1998):

$$\epsilon_{mx} = \epsilon_h + 2V_b\epsilon_{mx}\frac{\epsilon_i - \epsilon_h}{\epsilon_i + \epsilon_{mx}} \tag{7.6}$$

$$\epsilon_{mz} = \epsilon_h + V_b(\epsilon_i - \epsilon_h) \tag{7.7}$$

where the ϵ subscripts mx, h and i is mixture in x and z direction, host material and inclusion material respectively. V_b is the volume of brine. The fraction between the two directions permittivity is 1-1.4 for the real part and 10-20 for the imaginary part for realistic brine volumes between 1-20%. We expect a similar anisotropy between v and h polarisation is possible. We try to simulate this anisotropy by multiplying the imaginary part of the vertical component of the permittivity by an anisotropy factor. The anisotropy is primarily affecting the left-right hand polarisation, V, as shown in figure 7.2

The effect of the surface reflectivity to the normalized Stokes vector is simulated by increasing the permittivity (only the real part). In reality, this would be equivalent to snow cover densification. The simulation is shown in figure 7.3. As expected, this is primarily significant for the V and H polarisation difference, Q, but also U, the tilt of the polarisation ellipse.

7.5 WindSat polarimetric measurements at 10, 18 and 37 GHz

On November 17. 2004 a low pressure system is travelling through the Davis Strait over the relatively young ice cover in Baffin Bay. The air temperature goes from freezing to melt and back to freezing again. The event is probably associated with rain/snow precipitation. The U brightness temperatures for the three WindSat polarimetric channels and four different look or azimuth directions are shown in Figure 7.4. An U signal is seen for all three channels, but it is most clearly seen in the 180 to 270deg azimuth bin.

7.6 Conclusions

Using the simple model it was possible to produce both a non-zero U and a V signal by changing the surface permittivity. The U signal was produced by changing the real part of the complex permittivity. The V signal was produced by changing the media absorption anisotropy. These results are also applicable at L-Band.

In WindSat fully polarimetric data a non-zero U signal was observed in connection with temporary surface melt or onset of melt. The model results hint that the U signal could be related to surface densification, but this is yet speculative. Systematic non-zero V sea ice signals are not observed.

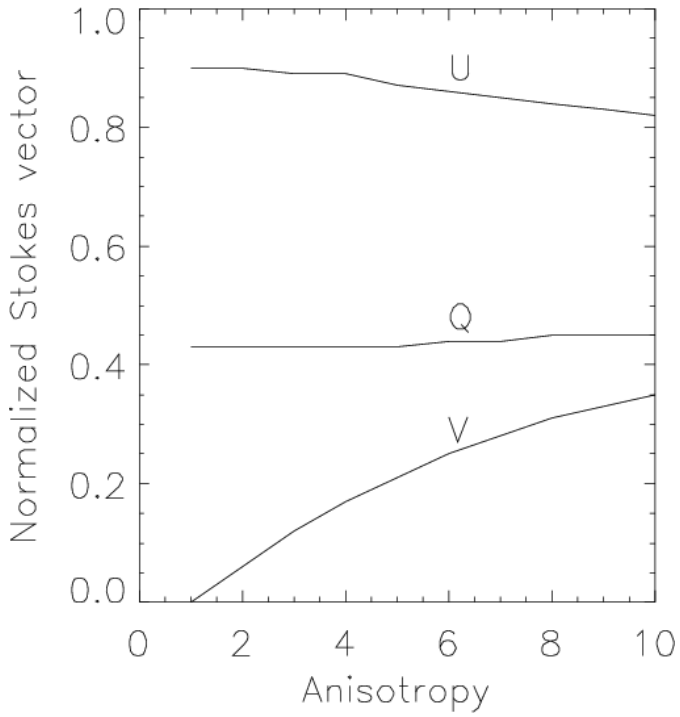

Figure 7.2: The normalised Stokes vector as a function of dielectric anisotropy. The imaginary part of the vertical component is multiplied by the anisotropy factor. The incidence angle is 50 degrees.

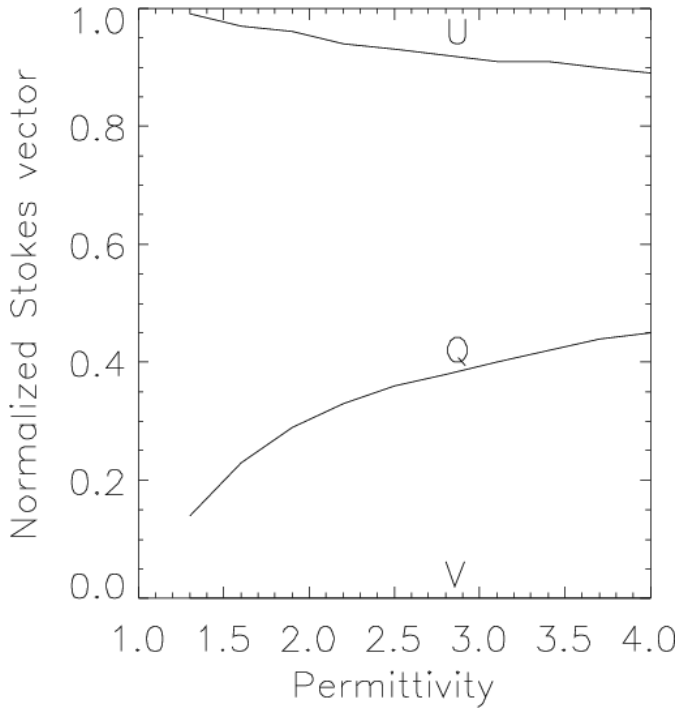

Figure 7.3: The normalized Stokes vector as a function of permittivity (the imaginary part is 0). The incidence angle is 50 degrees.

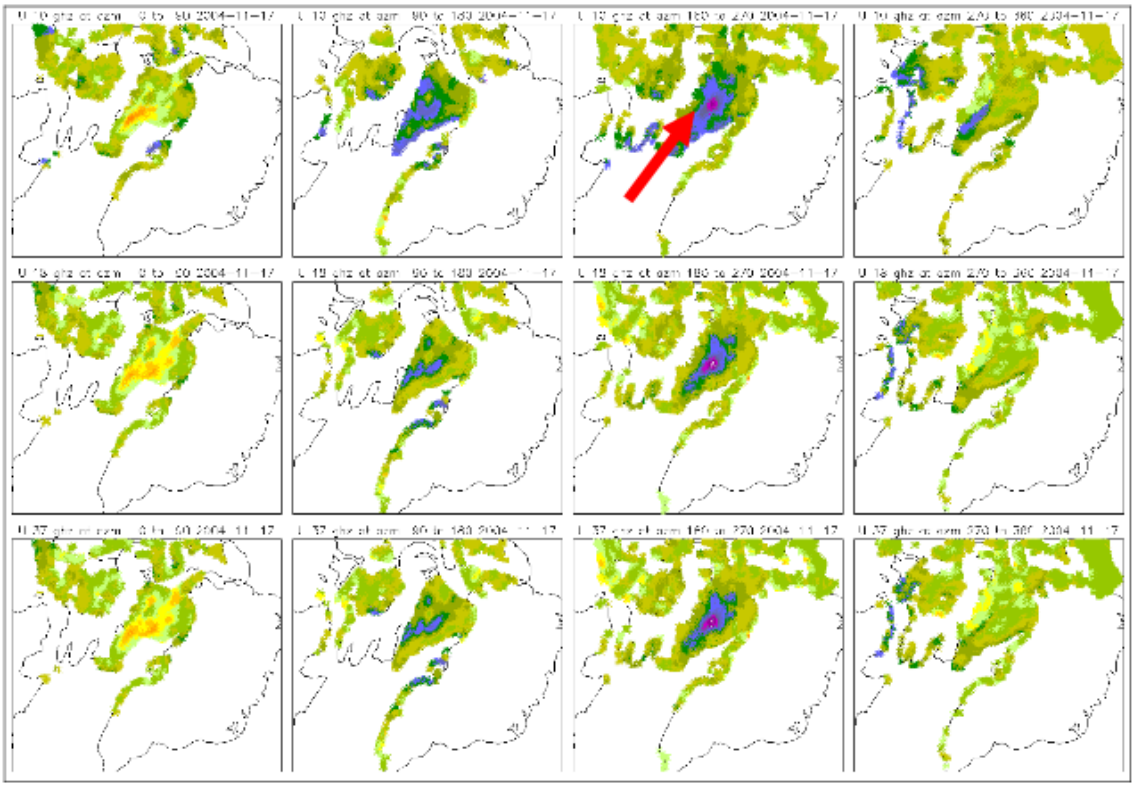

Figure 7.4: WindSat U brightness temperatures 17. November 2004, Baffin Bay. The U brightness temperatures are ordered in 4 different azimuth bins. The red arrow shows the direction of warm air advection.

Chapter 8

WP 2.4b: Modelling the third Stokes component from geometric considerations

Peter Mills and Georg Heygster

Institute for Environmental Physics, University of Bremen, Otto-Hahn-Allee 1, 28359 Bremen, Germany

8.1 Introduction

The Soil Moisture and Ocean Salinity (SMOS) instrument is a proposed new passive microwave radiometer operating in the L-band region (1.4 GHz). With the exception of Windsat, unlike previous surface- detecting microwave radiometers, SMOS will detect in all four Stokes components, providing full knowledge of the polarisation of the wave. While it is well understood how to model and extract sea ice information from the first two components of the Stokes vector, comprising waves in the horizontal and vertical polarisations, this is not the case for the higher order components. To help us understand how to extract information from these higher order polarisation signals, a forward model of some sort will be required since measurement and campaign data is sparse.

A complete polarimetric model of sea ice would be highly involved and is well beyond our scope here. One need only look at some of the vector radiative transfer models designed for atmospheric applications. These comprise either high-dimensional, discretely gridded models, such as DOIT (Emde, 2005) or Monte Carlo ray-tracing algorithms (Davis et al., 2005), both of which will be simpler than that required for ice since the atmosphere is a non-dense medium without discontinuous boundaries.

Simple geometric aspects can, however, give rise to a signal in the higher Stokes components. In the U, a sloping surface can cause a transfer of signal from the second component (polarisation difference, Q) to the third component, U. Horizontal anisotropy in the effective permittivity can also produce a signal in both U and V. The purpose of this report is to explore the signal created by only the first effect. The second will has been covered already in Chapter 7.

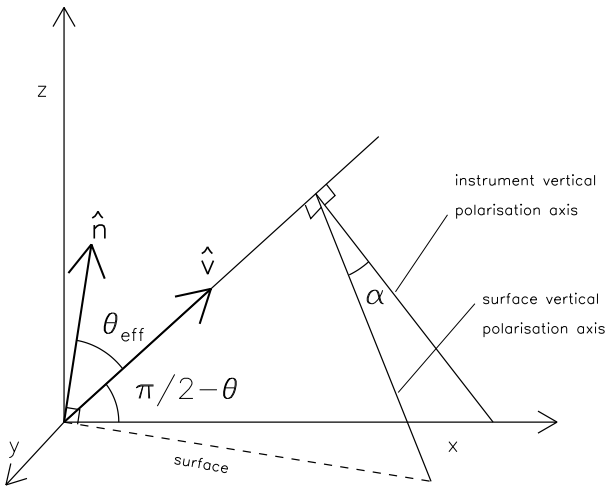

Figure 8.1: Geometry of surface-induced signal in the third Stokes component, U. $\hat{\mathbf{v}}$ is the instrument viewing direction, $\hat{\mathbf{n}}$ is the surface normal, θ is the instrument viewing angle wrt the z-axis (zenith angle), θ_{eff} is the instrument viewing angle wrt the surface normal, and α is the angle between the polarisation axes defined by the instrument and by the surface.

8.2 Theory

A microphysical foreward model for a nonzero U component of the Stokes vector requires scattering processes over a layered medium. Such a model has been developed by Xu et al. (2007) for the microwave range. However, a tilted surface or, equivalently, a deviation of the sensors attitude from the exact horizontal orientation may cause a crosstalk from the second to the third Stokes component. As at L-band scattering can be neglected (see Chapter 6), we concentrate here on the analysis of the geometric relationships between the second and third Stokes components. In any case, the influence of slope must first be compensated for before a microphysical analysis of the remaining signal can be undertaken.

The approach we will take here is geometric and algorithmic, taking advantage of the definitions the Stokes components and how they are formulated in the Fresnel equations. The

definition of the four Stokes component are, in a fixed basis:

$$\begin{bmatrix} I \\ Q \\ U \\ V \end{bmatrix} = \begin{bmatrix} |E_v|^2 + |E_h|^2 \\ |E_v|^2 - |E_h|^2 \\ 2\text{Re} < E_v E_h^* > \\ 2\text{Im} < E_v E_h^* > \end{bmatrix}, \tag{8.1}$$

where E_v and E_h are the electric field components in the vertical and horizontal directions respectively. The definitions of the coordinate bases are arbitrary and depend on the orientation of the instrument. In the case of the Fresnel equations, upon which our sea ice models are based, the bases are defined in terms of the surface, with the horizontal being parallel to the surface and the vertical in a plane perpendicular to the surface.

When the bases are rotated by 45 degrees around the viewing axis, the definition of the third Stokes component becomes equivalent to that of the second, that is the difference in field intensity between the horizontal and vertical polarizations. Thus, if the instrument is rotated out of plane from the surface upon which it is looking, this will give rise to a signal. The geometry is illustrated in Figure 8.1: θ is the instrument viewing angle with respect to nadir, θ_{eff} is the viewing angle with respect to the surface normal and α is the angle between the polarisation axes defined by the instrument and that defined by the Fresnel equations, i.e., the surface.

In most polarimetric radiometers, the polarisation axes are aligned with the Earth's surface, therefore we define the the instrument viewing direction using the following vector:

$$\hat{\mathbf{v}} = (\sin\theta,\ 0,\ \cos\theta). \tag{8.2}$$

We define the slope of the surface in terms of the normal vector, $\hat{\mathbf{n}}$, which can be calculated in a number of ways. Using angular slope and azimuth, it becomes:

$$\hat{\mathbf{n}} = (\cos\psi \sin\mu,\ \sin\psi \cos\mu,\ \cos\mu), \tag{8.3}$$

where μ is the slope and ψ is the azimuth relative to the instrument view. The effective viewing angle can be calculated via a dot product between the two vectors:

$$\theta_{eff} = \cos^{-1}(\hat{\mathbf{n}} \cdot \hat{\mathbf{v}}), \tag{8.4}$$

from which we compute the reflection coefficients, while the angle of the polarisation plane can be calculated with cross products:

$$\alpha = \text{sgn}(\hat{\mathbf{n}} \cdot \hat{\mathbf{j}}) \cos^{-1}\left(\frac{\hat{\mathbf{j}} \cdot \hat{\mathbf{n}} \times \hat{\mathbf{v}}}{|\hat{\mathbf{n}} \times \hat{\mathbf{v}}|}\right), \tag{8.5}$$

where $\hat{\mathbf{j}}$ is the unit vector defining the y-axis.

The U-component is calculated by projecting the polarization elipse, whose major and minor axes are defined by the horizontal and vertical components of the intensities, onto the rotated basis:

$$e_U = Q \sin(2\alpha) \tag{8.6}$$

where e_h and e_v are the emissivities calculated via the Fresnel or similar equations and e_U is the emissivity in U, that is, $U = e_U T$, where T is physical temperature.

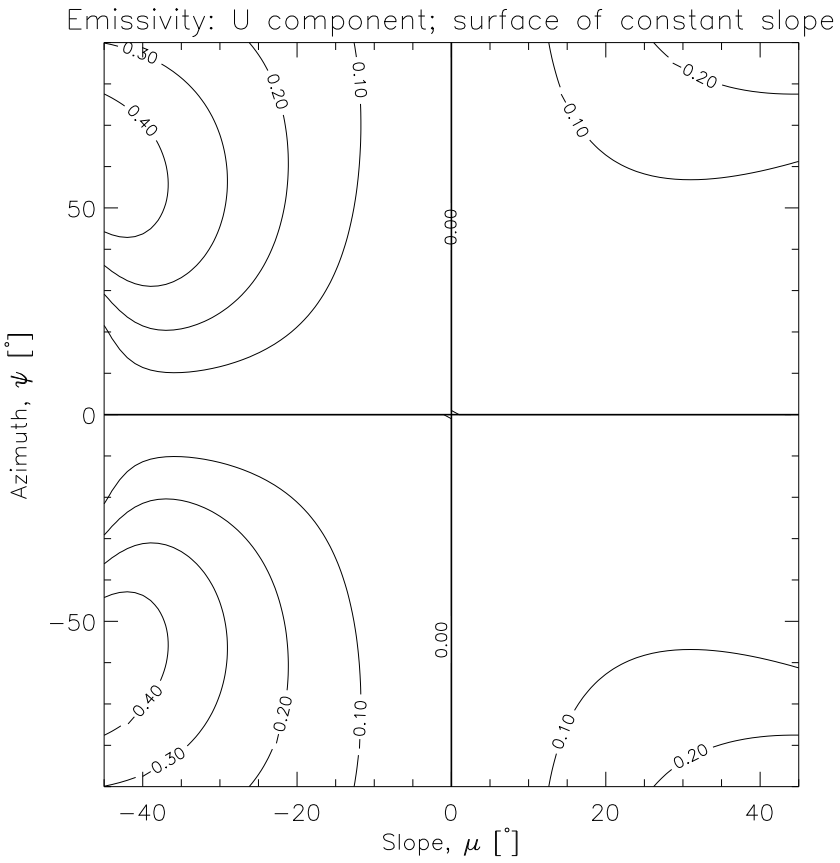

Figure 8.2: Emissivity of third Stokes component for a surface of constant slope and instrument looking angle of 45 degrees.

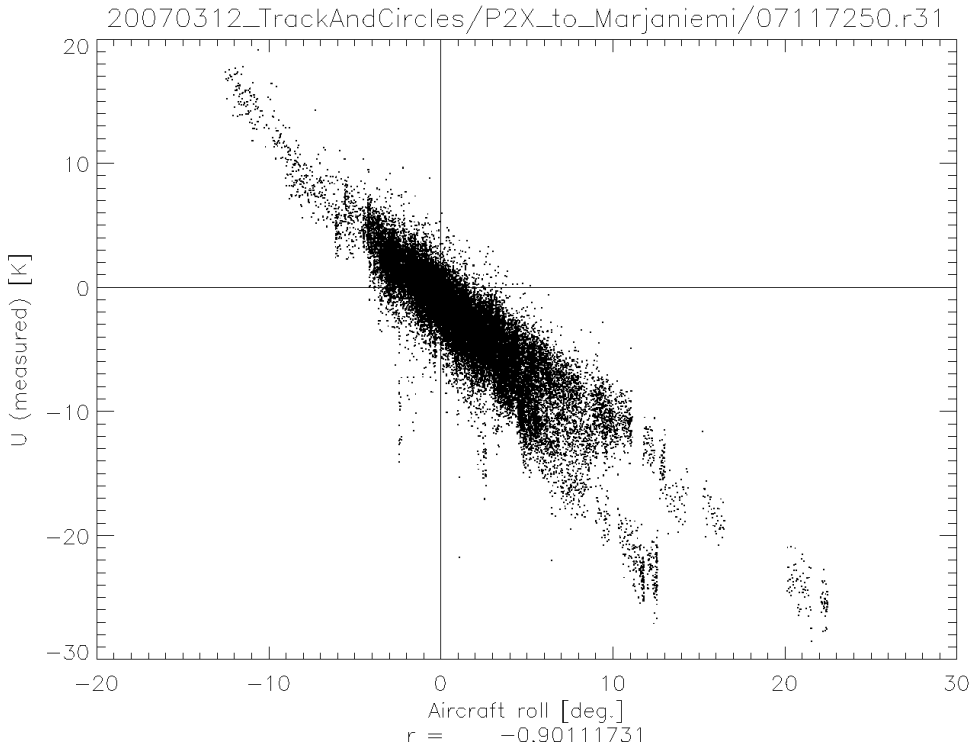

Figure 8.3: Third Stokes component vs. aircraft roll for one overflight.

A plot of the calculated emissivities for a surface of constant slope and an instrument zenith angle of 45 degrees is shown in Figure 8.2. As expected, the value is zero along both axes, that is, a non-sloping surface (μ=0) produces no signal in the U component, while a slope along the same axis as the instrument viewing (ψ=0) direction serves only to change the effective viewing angle and likewise produces no signal. Because of the larger effective viewing angle, negative slopes produce a larger signal than positive ones. For both slope and azimuth, a change in the sign of an angle produces a change in the sign of the emissivity. Finally, since an azimuth of 90 degrees is equivalent to an azimuth of -90 degrees with a slope of the same magnitude but opposite sign, we see that the top and bottom of the graph are the same, but reversed.

8.3 Experimental support: PolICE 2007

The PolICE campaign provides an excellent data-set on which to test the above theory because the fully polarimetric radiometer was rigidly mounted to the aircraft. Thus, out-of-plane shifts in the aircraft attitude, particularly aircraft roll (rotation about the longitudinal axis), will generate a signal in the third Stokes component. As a direct demonstration, consider the scatter-plot in Figure 8.3 which clearly shows a close, linear relationship between U versus aircraft roll for one overflight.

Figure 8.4 refines this somewhat by applying the geometric model to the full aircraft attitude data. The Fresnel equations are used to calculate initial (ground-referenced) emissivities using a real refractive index of 2, a typical value for sea ice. The imaginary part is ignored because it is normally much smaller than the real part. Since the air temperature during the campaign was above freezing, a physical temperature of 273 K was assumed. While the correlation is

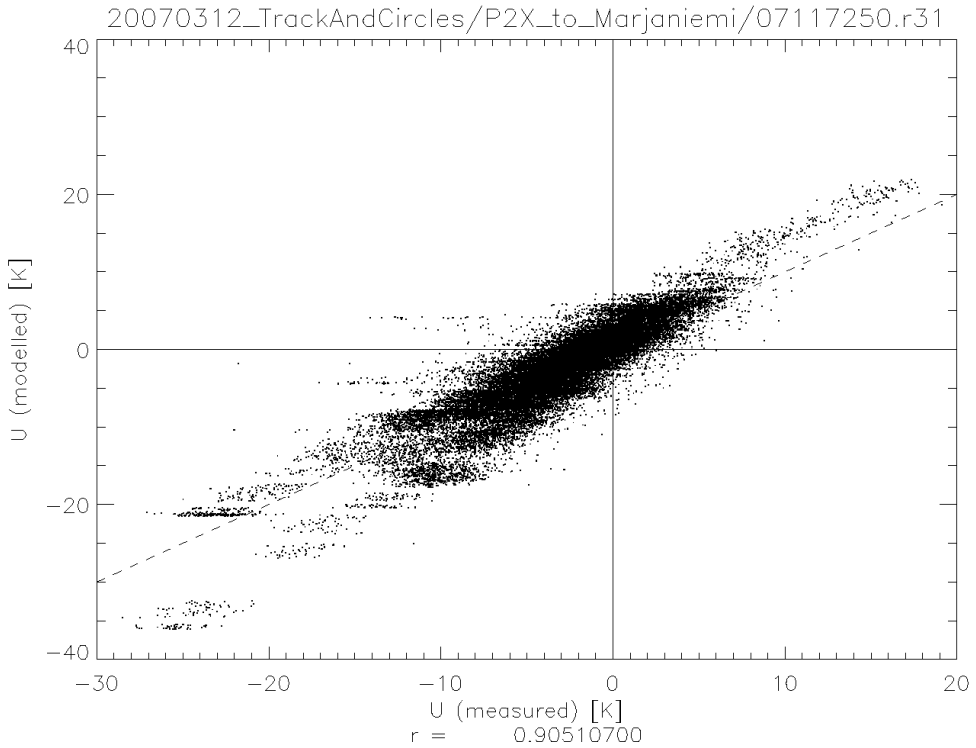

Figure 8.4: Third Stokes component for one overflight: modelled strictly from aircraft attitude vs. measured.

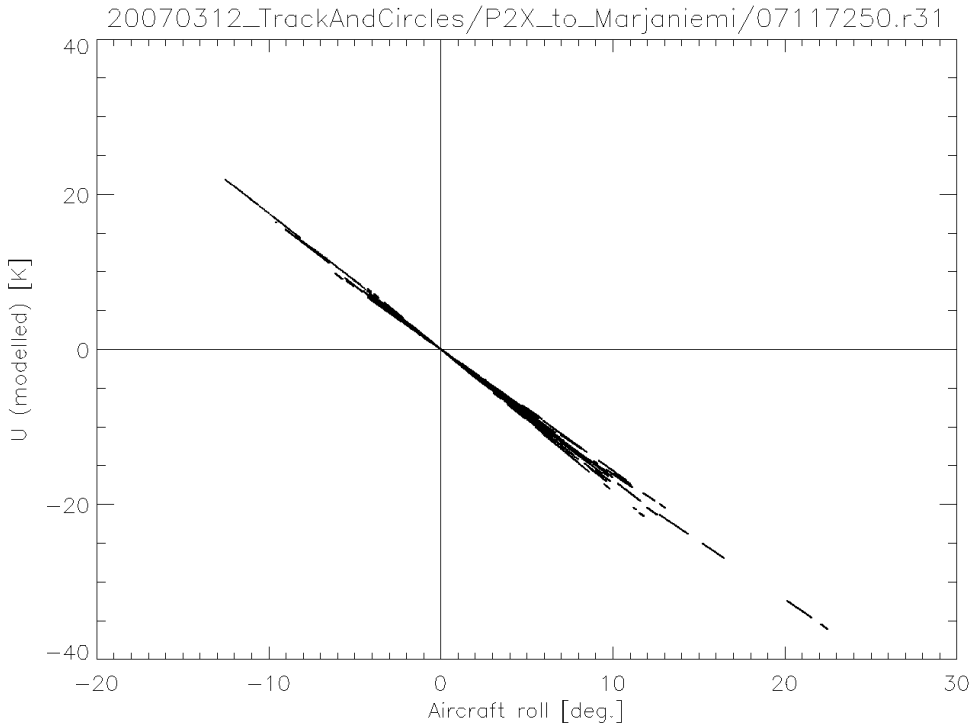

Figure 8.5: Third Stokes component modelled from aircraft attitude vs. aircraft roll for one overflight.

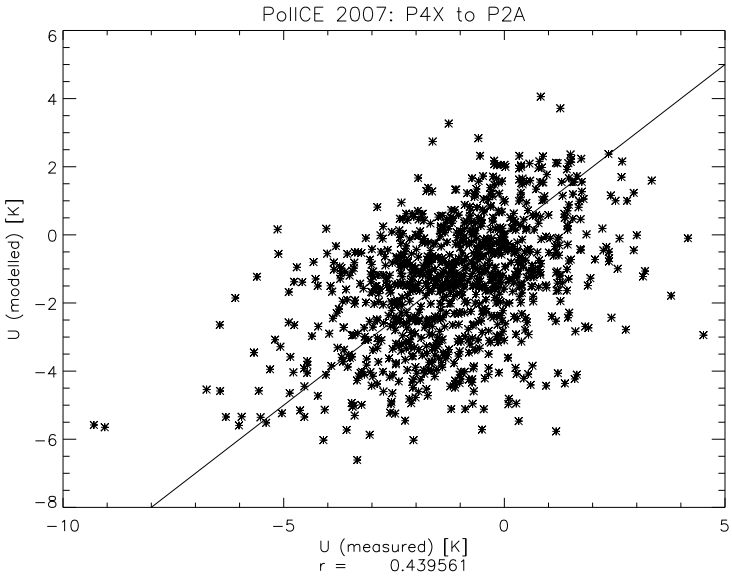

Figure 8.6: Third Stokes component estimated from coincident ice-thickness data using a plane-parallel RT model versus measured.

only slightly improved, there is little bias in the graph. The two plots, taken together, imply that the model is almost linear within the domain, a fact that is confirmed in Figure 8.5. This is also suggested by Figure 8.2: the scenario is roughly comparable to an azimuth angle of 90 degrees with the roll corresponding to the slope. The variation appears almost linear even for slopes of over 30 degrees.

Included in the PolICE campaign were coincident overflights of a helicopter carrying an ice thickness meter: the E-M bird instrument. From this data, more accurate estimates of the ice emissivity can be derived. Figure 8.6 shows modelled versus measured U for a different overflight, but this time using the plane-parallel ice emissivity model described in Section 6.3.2, Equation (6.22) instead of the Fresnel equations. A selection of 1000 points, randomly taken from the flight between the P4X and P2A waypoints, is used, ice thickness is taken from co-located E-M bird measurements and averaged over an instrument FOV of 15 degrees (flight altitudes were generally between 500 and 600 metres, translating to a footprint size of approximately 150 m), while the complex permittivies are varied with thickness using a procedure that will be described in Chapter 9. Agreement is poorer than seen in Figure 8.4, but this has nothing to do with the more sophisticated emissivity model, which still produces an essentially linear variation with aircraft roll (figure not shown here), as suggested in Figure 8.7. The explanation is simple: in the second example, the aircraft was more stable, tracing out only about 8 degrees between minimum and maximum roll angles (except for a few outliers), while in the first example it is more than 30 degrees.

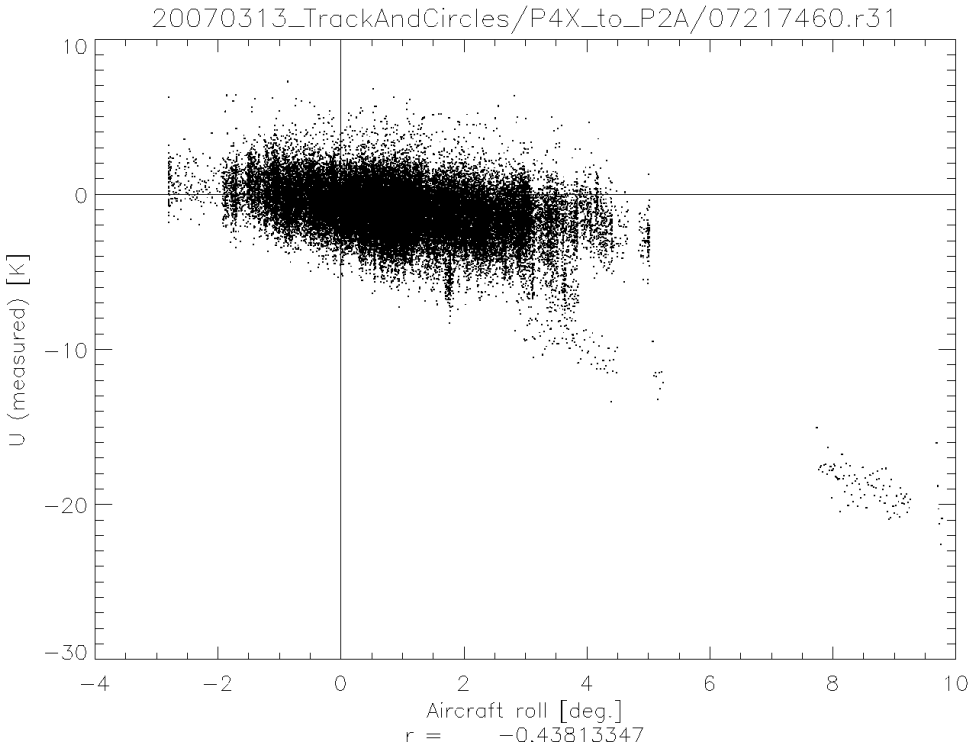

Figure 8.7: Third Stokes component versus aircraft roll for a different overflight

8.4 Ridged ice

As a simple conceptual model, consider a longitudinal ice ridge with a profile given by a half-wavelength of a harmonic function (sin or cos) illustrated by the mesh-diagram in Figure 8.8. An instrument azimuth of zero degrees is defined as parallel to the longitudinal axis of the ridge.

Neglecting coherency effects, the final signal will be given by integrating over all slopes. In contrast to a uniform slope, this will generate a periodic function that repeats at instrument azimuth angles of between -90 and 90 degrees rather than through the full range of 360 degrees. In addition, the signal is not even around the maxima, as seen in Figure 8.9. The signal will be zero at both the 0 and 90 degree incidence angles, but for different reasons. At ninety degrees, there is no slope that twists the surface polarisation axes relative to those of the instrument so the signal is zero at every point along the ridge, while at zero degrees, the signal from one side of the ridge will be opposite in sign from that on the other side thus the two will cancel.

Consider what happens when the contribution from an additional overall slope is removed from the signal: all that is left should be the result of anisotropy in the topography, assuming that contributions from scattering and direct emission are negligible. This appears to be what is seen in Figure 8.10 which shows both the overall signal from a circling overflight and the signal with the modelled components removed. Each 360 degree revolution of the aircraft is demarcated by the vertical lines. While there is no guarantee that they are produced strictly from topography, the same periodicity is apparent in the "reduced" U with, on average, two maxima and two minima per revolution. Absent the obvious bias, there would also be four zero-crossings. Qualitatively, this can be interpreted to be caused by pressure ridges of a prevailing azimuthal orientation since the signal generated from a conceptual model ridge shows

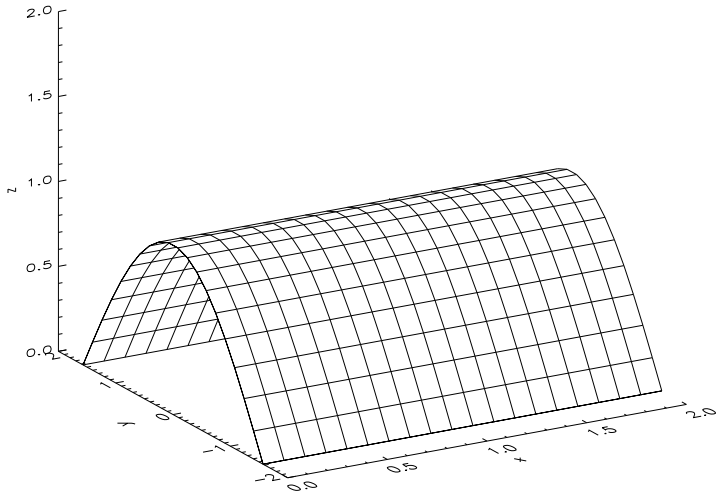

Figure 8.8: Mesh-diagram of the model ice ridge. X-axis corresponds to an instrument azimuth angle of 0 degrees.

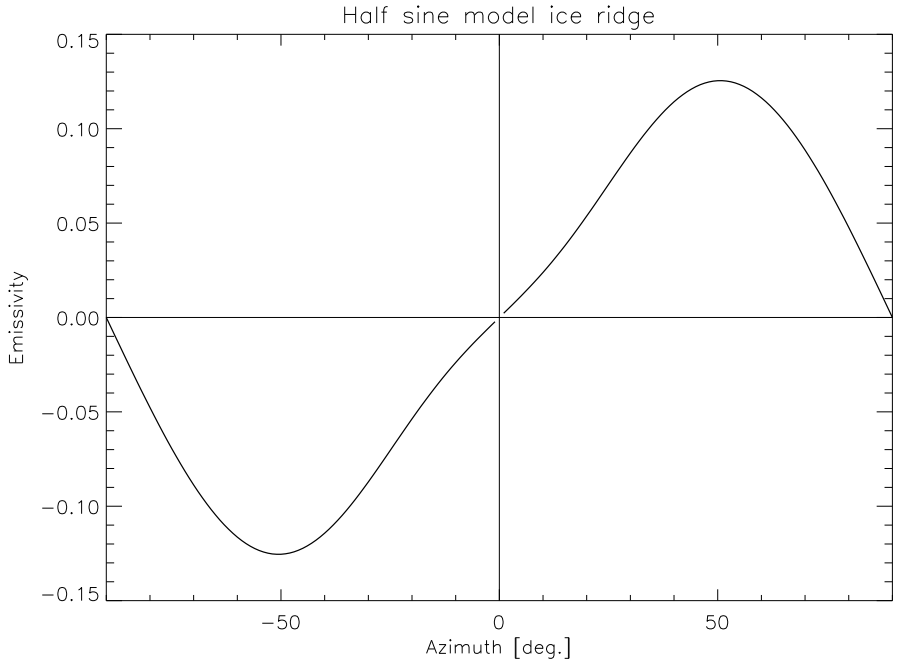

Figure 8.9: Emissivity of U for a model ice ridge comprised of a half sine wave with an aspect ratio of $1/\pi$.

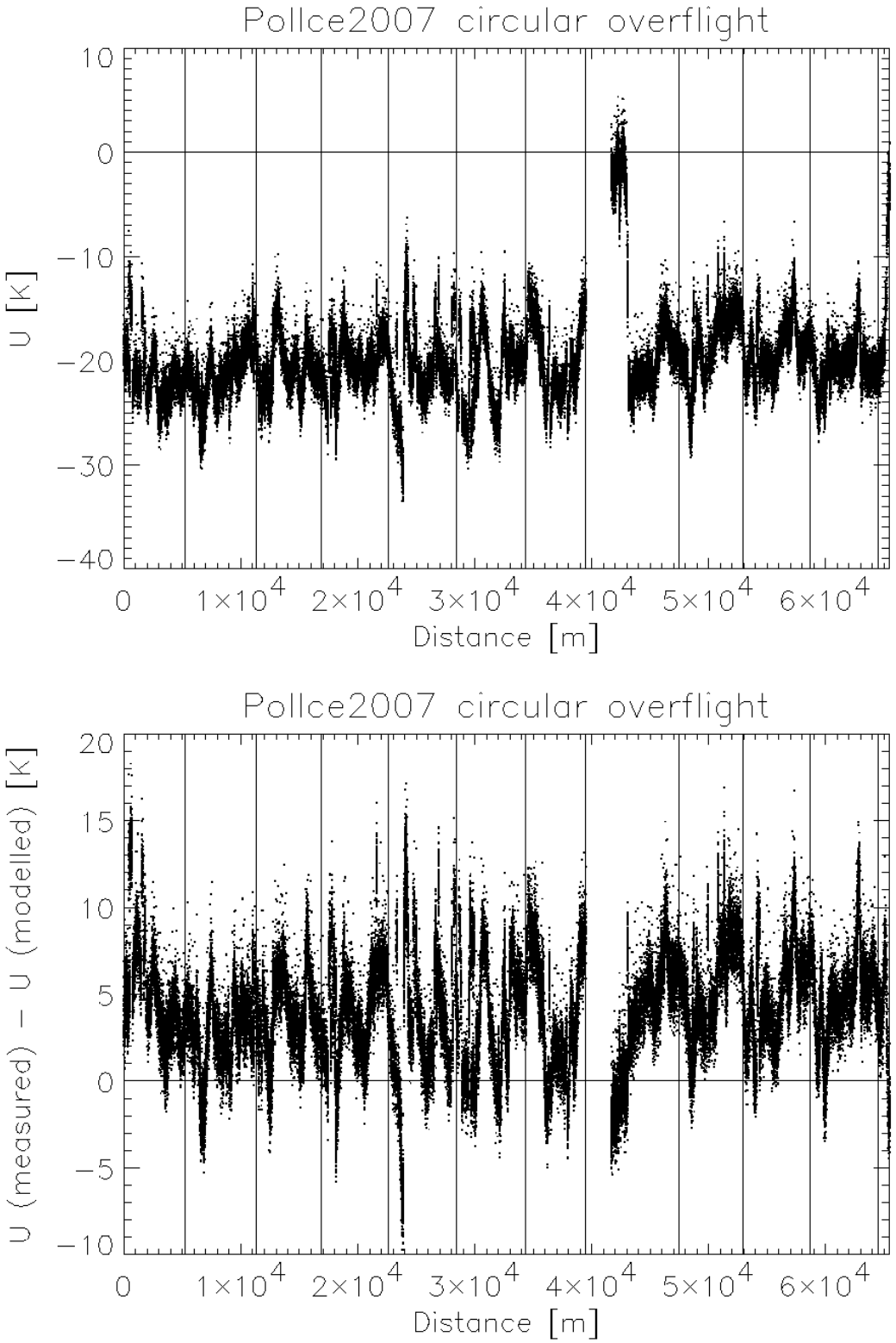

Figure 8.10: Time series of third Stokes component for circular fly-over. First figure is total signal, second figure has the component modelled from aircraft attitude removed. Vertical bars demarcate one 360 degree azimuthal rotation.

the same features.

8.5 Conclusion

The third Stokes component, U, is simply the polarisation difference in a coordinate axis rotated by 45 degrees (around the line of sight) from that in which the horizontal and vertical polarisations have been defined. Thus, if the polarisation axes defined by the instrument are rotated with respect to those defined by the surface—caused, for example, by a sloping surface or a tilted aircraft—this can give rise to a signal in U. A simple, geometric model of this effect has been developed which explains a large amount of the variance contained in aircraft measurements taken during the PolIce campaign.

Anisotropy in the slope will also induce a signal in U. For large-scale ridging, this can be modelled by simply integrating over the slope statistics. The resulting signal should be symmetric over 180 degrees azimuth with at least four zero crossings and two maxima and two minima over the full circle. When the U signal modelled from aircraft attitude is removed from measurement taken during a circular flyover, the resulting signal shows a similar functional form. While it is unclear whether this is due to ridging or some other phenomenon, it certainly results from some sort of horizontal anisotropy in the properties of the ice.

While it is clear that the above model is incomplete, nonetheless it can point in the direction of more sophisticated models which might take into account volume effects such as direct emission as well as surface reflection. It also implies that a complete model must be three-dimensional since complex ridging will produce numerous internal reflections resulting in a continual transfer of signal between the second and third Stokes components.

Chapter 9

Extrapolation to other salinities

Peter Mills and Georg Heygster

Institute for Environmental Physics, University of Bremen, Otto-Hahn-Allee 1, 28359 Bremen, Germany

9.1 Introduction

The Soil Moisture and Ocean Salinity instrument is a proposed new surface-detecting passive microwave radiometer measuring in the L-band (1.4 GHz). PolIce 2007 is so far the only source of field campaign measurements over ice using a fully polarimetric radiometer operating in L-band. It was conducted in the North Baltic which has a much lower salinity than the world oceans. Results must be generalized so that they are applicable to the Arctic and Antarctic. The purpose of this report is to explore how this might be accomplished.

9.2 Data

9.2.1 Pol-Ice campaign

The Pol-Ice campaign was conducted in March 2007 over the Bay of Bothnia in the Northern Baltic. It comprised two components: point-to-point and circular flyovers by an aeroplane carrying the fully polarimetric EMIRAD radiometer (Skou et al., 2007) operating at L-band, and point-to-point flyovers by a helicopter towing an ice thickness detector called the E-M bird. The E-M Bird instrument detects the ice-water transition using inductance variations in a pair of electromagnetic coils (similar to a metal-detector) while the ice surface height is measured with a laser altimeter as described in Chapter 3.

The coincident overflights of the EMIRAD and the E-M bird are summarized in Figure 2.5.Flights are labelled based on the waypoints. EMIRAD flights are also designated by a number, which can be found in Figure 9.4. Weather conditions during the campaign found temperatures at or above freezing with overcast skies and patches of fog. Only data from the aft-looking (40 degree) antenna will be used in this study.

9.2.2 Processing and collocation procedures

Because the radiometer was fixed on the aircraft, its pointing direction will be affected by changes in aircraft attitude. These must be corrected for before the measurements can be used. The following equations give the measurement coordinate as a function of the aircraft coordinates and attitude: pitch, roll and yaw:

$$\begin{aligned}
\zeta' &= P + \zeta && (9.1)\\
dx &= z \tan \zeta' && (9.2)\\
dy &= z \sin R && (9.3)\\
\psi &= \psi_a + \frac{1}{r_E \sin \psi_a}(dx \cos H + dy \cos H) && (9.4)\\
\phi &= \phi_a + \frac{1}{r_E}(dx \cos H - dy \sin H), && (9.5)
\end{aligned}$$

where P is the aircraft pitch, ζ is the instrument looking angle relative to the aircraft longitudinal axis, R is the aircraft roll, $(\psi_a,\ \phi_a)$ is the longitude, latitude coordinates of the aircraft, z is the aircraft altitude, H is the aircraft heading r_E is the radius of the Earth and $(\psi,\ \phi)$ are the ground coordinates of the measurement centre.

The same geometrical approach can be used to figure out the effective viewing angle. Many formulations are possible. Here is one of them:

$$\theta_1 = \sin^{-1} \sqrt{\tan^2 \zeta' + \sin^2 R}. \quad (9.6)$$

To simplify the analysis, an approximate conversion to Cartesian coordinates was applied, with the X coordinate denoting distance along the flight path while the Y is distance across it:

$$\begin{aligned}
X_0 &= r_E(\theta - \theta_0)\cos\phi && (9.7)\\
Y_0 &= r_E(\phi - \phi_0) && (9.8)\\
\gamma &= \tan^{-1}(\Delta\psi, \Delta\theta \cos\bar{\phi}) && (9.9)\\
X &= X_0 \cos\gamma + Y_0 \sin\gamma && (9.10)\\
Y &= -X_0 \sin\gamma + Y_0 \cos\gamma, && (9.11)
\end{aligned}$$

where $\Delta\theta = \theta_f - \theta_0$ is the total longitudinal travel of the reference flight track, $\Delta\phi = \phi_f - \phi_0$ is the total latitudinal travel and $\phi = (\phi_0 + \phi_f)/2$ is the avearge latitude of the referecne flight track. To collocate two or more approximately overlapping flight tracks, the transformation is applied first to a reference flight, the coefficients saved and the same transformation applied to all others. Distances can easily be calculated in two ways: since the X coordinate will vary much faster than the Y, for fast, crude collocations, a one-dimensional distance can be calculated based only on difference in the X dimension, while for more accurate collocations, we use the standard Cartesion metric.

9.2.3 EMIRAD instrument characteristics

Brightness temperature measurements will be affected not only by what is there, but also by the instrument characterisics. The half-power FOV of the EMIRAD instrument for the nadir-looking geometry is 31 degrees, translating to an footprint size of over 250 m for 500 m cruising altitude. This is much broader than the E-M Bird footprint, therefore we account for the smear-

ing produced by the EMIRAD instrument by weighting each of the thickness measurements based on its power-response function.

The angle from instrument boresight, δ, of a given ice thickness measurement can be calculated:

$$\delta = \cos^{-1}\left[\frac{(\mathbf{r_a}-\mathbf{r})\cdot(\mathbf{r_a}-\mathbf{r_t})}{|\mathbf{r_a}-\mathbf{r}||\mathbf{r_a}-\mathbf{r_t}|}\right], \tag{9.12}$$

where $\mathbf{r} = (X, Y, 0)$ is the radiometer measurement location, $\mathbf{r_a} = (X_a,\ Y_a,\ z)$ is the aircraft position and $\mathbf{r_t} = (X_t,\ Y_t,\ 0)$ is the ice thickness measurement location. The power-response function of the instrument is a Gaussian with respect to the angle from the boresight (Skou et al., 2007):

$$w = \exp\left(\frac{\delta}{2\sigma_{FOV}}\right), \tag{9.13}$$

where σ_{FOV} is the angular FOV of the instrument and w is used to weight the thickness measurements for collocation with a given radiometer measurement:

$$W = \sum_i w_i \tag{9.14}$$

$$\bar{h} = \frac{1}{W}\sum_i h_i w_i, \tag{9.15}$$

where $\{h_i\}$ are the set of ice thickness measurements, $\bar{h}$ is the average over the instrument footprint while the radiometer measurement location is held constant. The sum of the weights, W, gives the equivalent number of thickness samples and can be used to screen the quality of the collocation by admitting only those values larger than a certain threshold.

Since the algorithm to calculated thickness from E-M Bird measurements assumes infinite water depth, some of the thickness measurements were flagged because of shallow water. These were similarly averaged to form a "badness" rating.

The instrument characteristics will also need to be simulated in the Monte Carlo model by generating random deviates for the angle at the instrument head. It would seem to be a straightforward matter to simply generate Gaussian deviates, however the EMIRAD and E-M Bird measurements are not always perfectly coincident. Consider the measurement geometry shown in Figure 9.1 in which we need deviates along a line of measurements offset from the intrument dead-centre. We can simply transform normal deviates for the overall offset angle, δ to a corrected offset angle, δ' as follows:

$$\delta' = \mathrm{sgn}\delta \sin^{-1}\sqrt{\sin^2\delta - (\Delta Y/r)^2}, \tag{9.16}$$

where $\Delta Y/r$ is the offset (magnitude) of the line of measurements from the footprint centre normalized by the distance from the radiometer instrument head. However, we will need to discard all deviates for which $\sin|\delta| < \Delta Y/r$ or $|\delta| < \sin^{-1}(\Delta Y/r)$. This can be done by generating uniform deviates within a certain range and then transforming them to normal deviates by inverting the error function. The out-of-plane contribution to the incidence angle is ignored.

9.2.4 Calibration errors

As Figure 9.2 shows, there was a considerable discrepancy between the measured and modelled radiance values over open water, especially in the vertical polarisation. Open water points

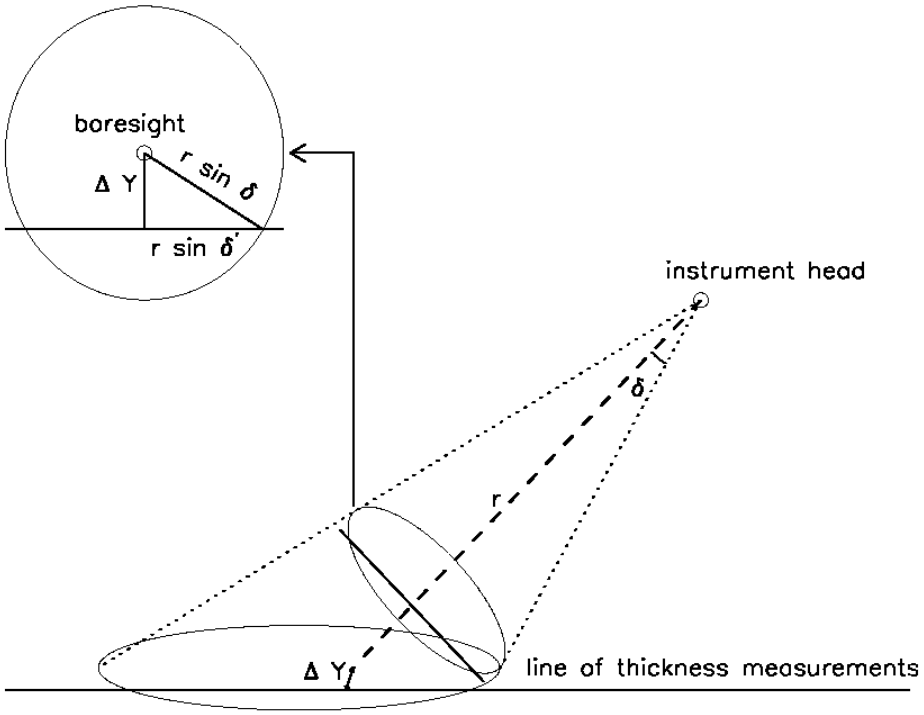

Figure 9.1: Diagram showing how to convert angle from instrument boresight to an equivalent angle along a line of measurements offset from the footprint centre.

were derived from the ARTIST Sea Ice algorithm (ASI) (Spreen et al., 2008) by taking ice concentrations of less than 1 %. Since the horizontal and vertical polarisations do not agree at the 0 degree viewing angle, it was assumed that this was due to a constant offset callibration error in the radiometer. It is apparent from Figure 9.3 which shows a detail of one of the Pol-Ice EMIRAD flights, however, that this calibration offset was not constant. The trace shows large discontinuities that are not likely due to changes in surface type. These shifts occur only in the vertical polarisation and produce a both a large polarisation difference and high radiance that do not appear even physically possible.

Figure shows 9.4 a map of all the EMIRAD measurements performed during the campaign with different surface types plotted in different colours. Since the open water points are so far distant from the collocated thickness measurements (upper right corner) and were performed four and five days prior (8th versus the 12th and 13th), it is unlikely that calibration offsets derived from the open water points will be applicable. Anomolous spiking was also observed, primarily within the vertical channel as reported in Chapter 4.

Because of these calibration errors, measurements and results derived from them must be treated with some caution. Nonetheless, we feel that the concepts treated within are valid and that emissivitiy calculations show meaningful statistical relationships with measured values.

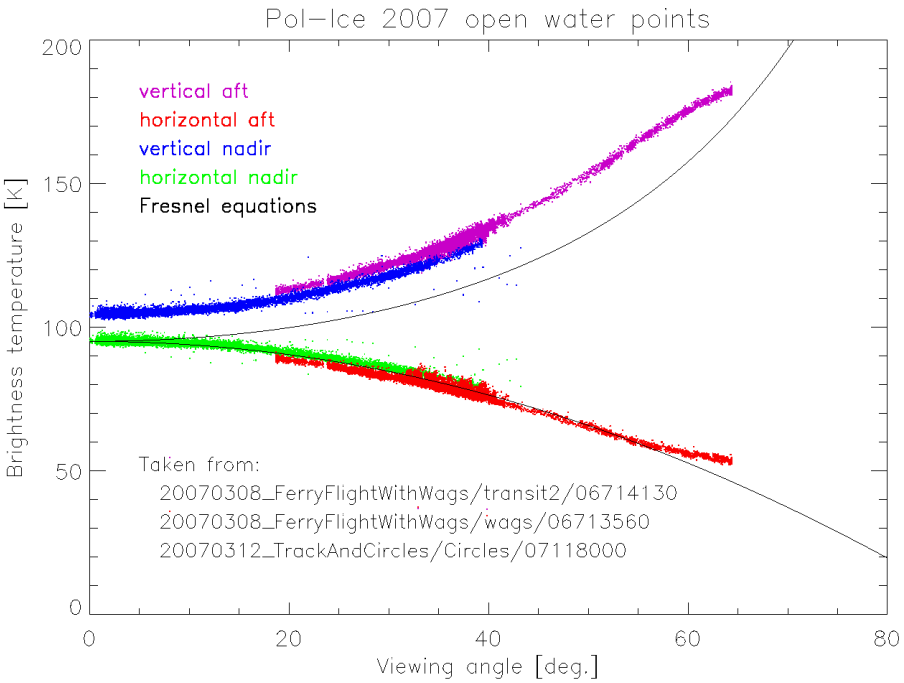

Figure 9.2: Measured (points) versus model (lines) brightness temperatures over open water as a function of viewing angle. Points with excessive polarization mixing have been filtered out based on the angle, α, defined in (8.5)

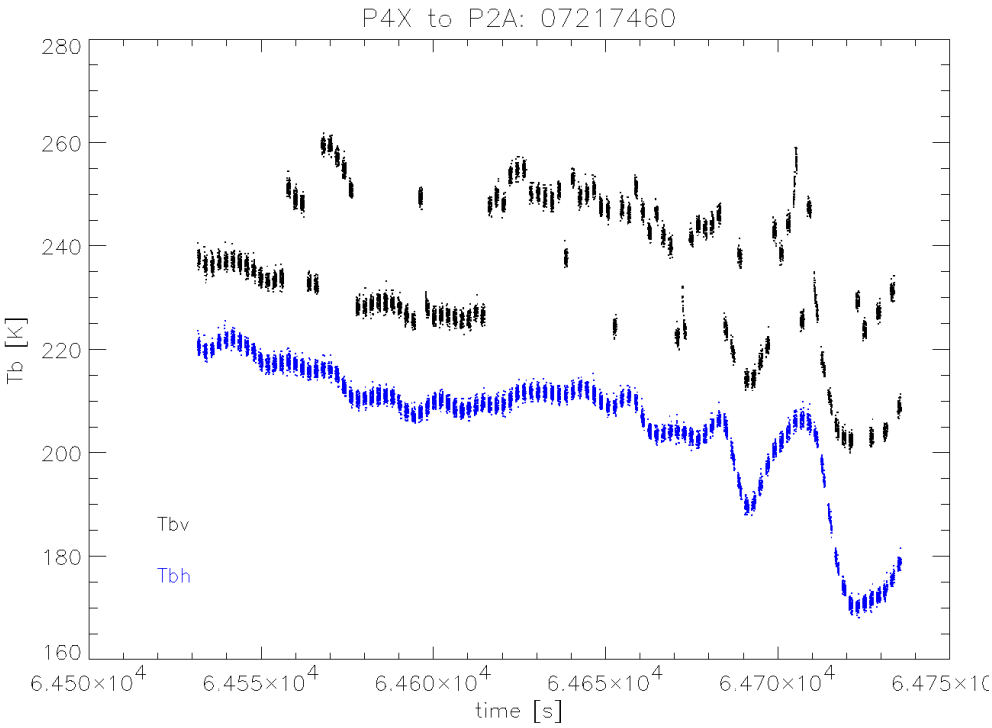

Figure 9.3: Detail of P4X to P2A flight showing shifting of calibration offset in the vertical polarisation.

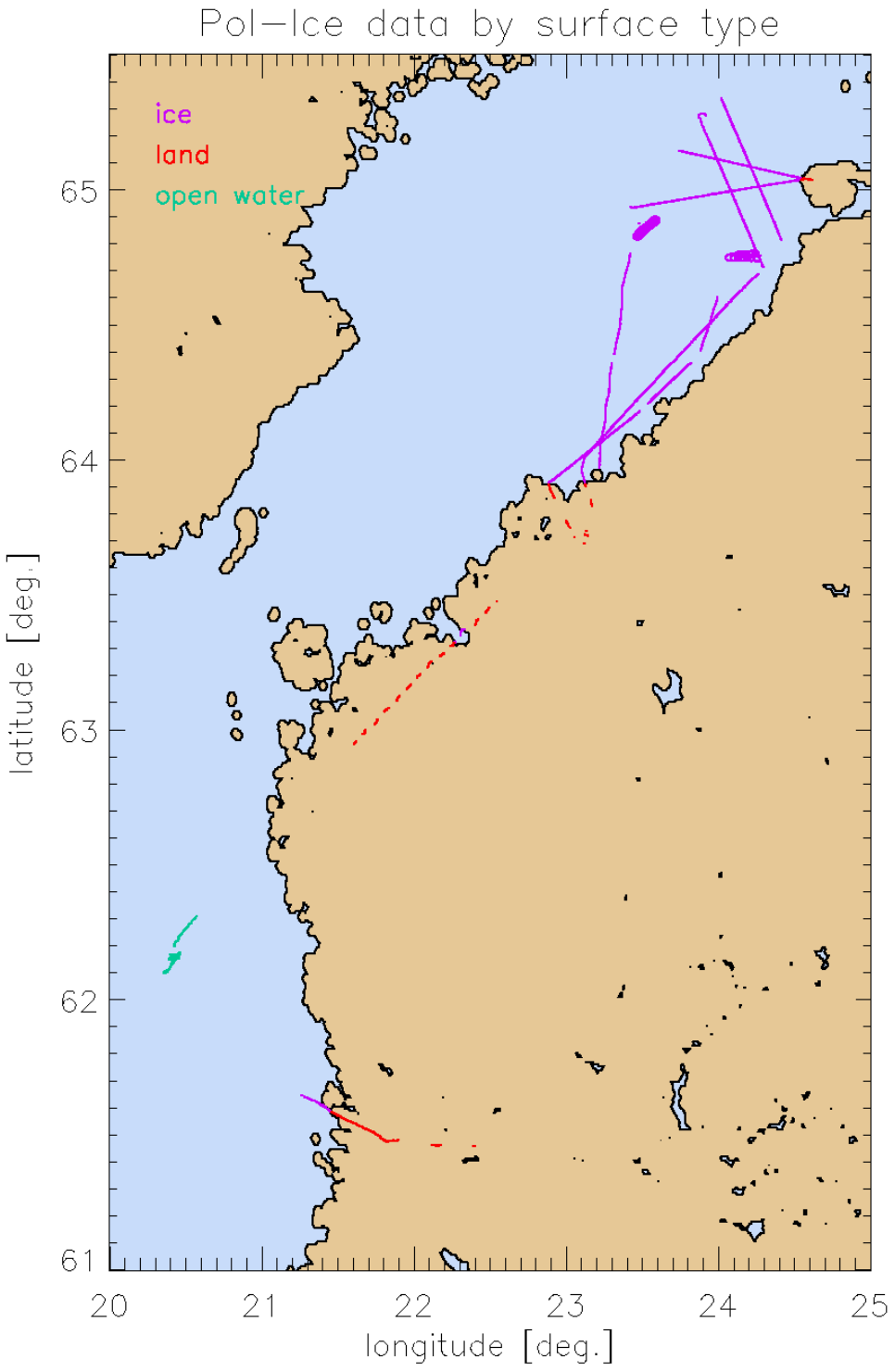

Figure 9.4: Map of all Pol-Ice EMIRAD measurements showing surface-type. Open water points were derived from ASI high-resolution sea ice concentrations. Land points were filtered using a landmask, which is also drawn as coastline.

9.2.5 Ice salinity profiles from Polarstern

Eicken (1992) has performed a statistical analysis to classify salinity profiles collected from the Antarctic on Polarstern cruises. These same ice cores have already been used in Chapter 6 to test the variability in forward model calculations for different parameterisations of the complex permittivities. We will use the same cores here to help understand the relationship between ice thickness, salinity and the variation of salinity with depth.

9.3 Deriving complex permittivities from Pol-Ice data

Figure 9.5 shows a plot of the brightness temperature and polarisation difference as a function of the complex permittivity for a 2.5 m thick ice sheet at 265 K. Especially within the central region of the plots, it is apparent that if all other parameters in the equation are known, inverting (6.22) to determine the complex permittivity from the measured brightness temperature is quite a well-posed problem. Consider: pick a given isoline in one plot, another one in the other and they will likely have a unique intersection. This central region determines the transition zone between ice which is transparent and that which is opaque, hence it is exactly the region of interest because of the translucency of sea ice at L-band. It can be understood from Figure 9.5a as follows: in transparent ice (bottom of plot), a higher real permittivity will increase the brightness temperature because there are more reflections within the ice layer. Conversely, as the ice becomes optically thick (top of plot), a higher real permittivity will decrease the brightness temperature because the ice now reflects more downwelling radiation from the sky.

The operation of the radiometer was cyclic, taking a cluster of measurements every 2 seconds as can be clearly seen in Figure 9.3. Averaging each cluster has several advantages: first, by removing points with a standard deviation greater than a certain threshold (10 K), many anomolous spikes, caused by a malfunction in the radiometer, may be discarded. Second, instrument noise is reduced thus the measurement becomes more stable. Finally, the smaller data set is far easier to work with and process. Further quality checks were applied: measurements with a total antenna weighting, or equivalent number of thickness measurements, W, had to be less than 1000, the "badness" rating had to be less than 0.01 (less than 1 % of thickness measurements were affected by shallow water).

Equation (6.22) was inverted using an iterated stochastic algorithm: several points are randomly chosen from a bounded region, the forward model is applied and the point with the smallest error chosen. The bounded region is reduced in size and the process repeated until the error is smaller than a pre-defined tolerance. In addition to being faster, this algorithm converged more reliably than a downhill simplex (Press et al., 1992). Since bad values will be thrown away, we need to carefully examine the convergence statistics to avoid introducing a selection bias. Figure 9.6 shows that all but a few points have converged and generated sensible estimates. While likely not reliable in and of themselves, we expect these estimates to be useful for generating statistics. Figure 9.7 compares the effective permittivity estimates with bounds calculated by analytic continuation for representative ice conditions.

9.4 Relationship of salinity to ice thickness

The relationship of salinity to ice thickness is well documented in the literature – see for instance Tucker et al. (1992), Weeks and Ackley (1985) and Ehn et al. (2007). First, because thin ice conducts heat more quickly, it freezes faster, meaning that less brine is expelled. Second,

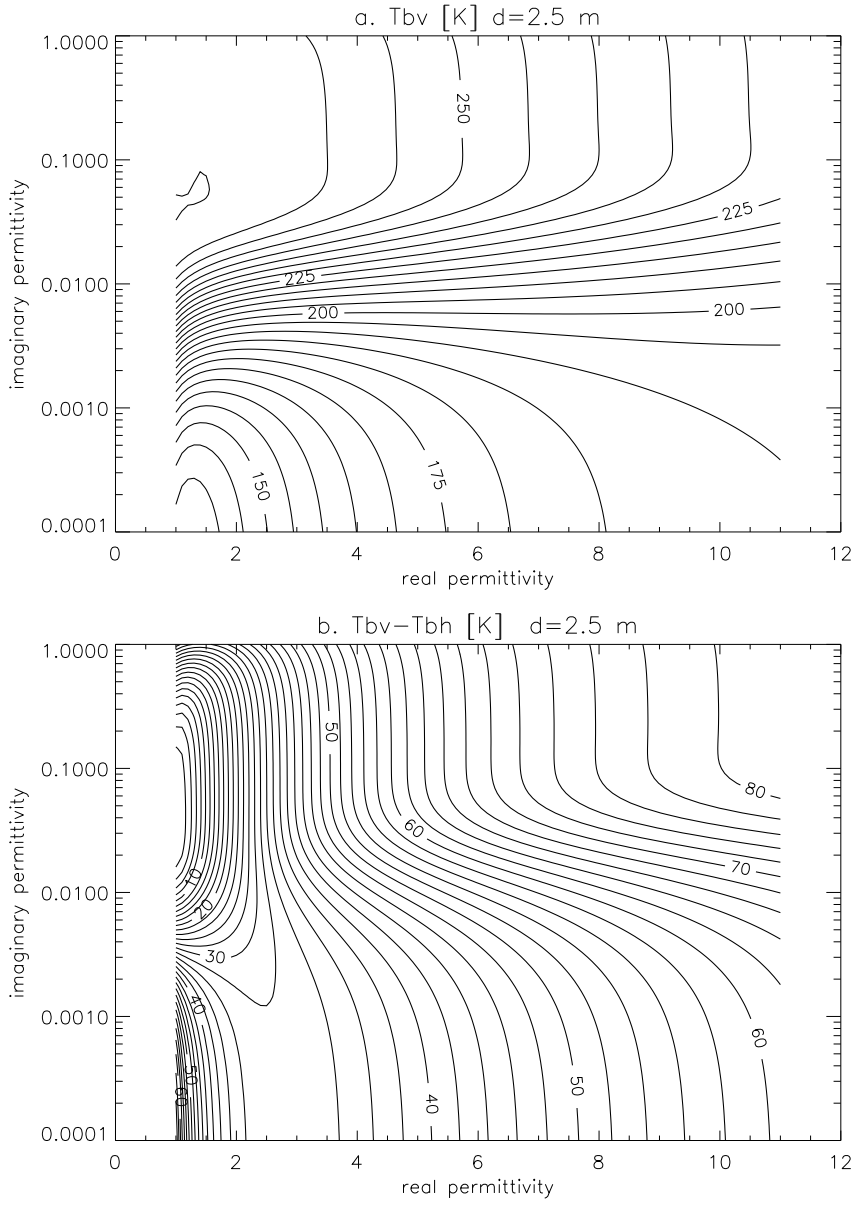

Figure 9.5: Emitted brightness temperature as a function of complex permittivity according to the emissivity model (6.22) for an ice temperature of 265K.

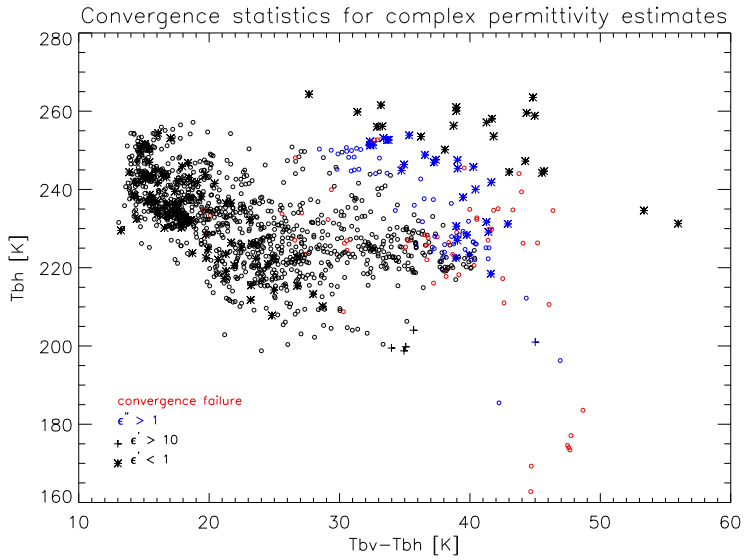

Figure 9.6: Convergence of complex permittivity estimates in measurement space. Red points have failed to converge. Blue points have converged but have a real permittivity greater than ten. Crosses have an imaginary permittivity greater than one, while asterisks have a real permittivity of less than one. Convergence, in this case, is defined as a summed square error of less than 1 K.

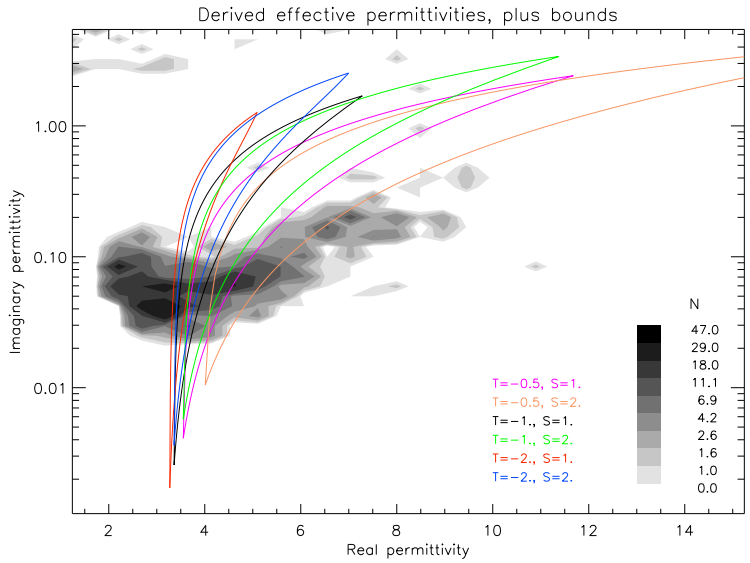

Figure 9.7: Derived effective permittivities from Pol-Ice campaign plus bounds calculated from analytic continuation. T temperature in °C, S salinity in psu.

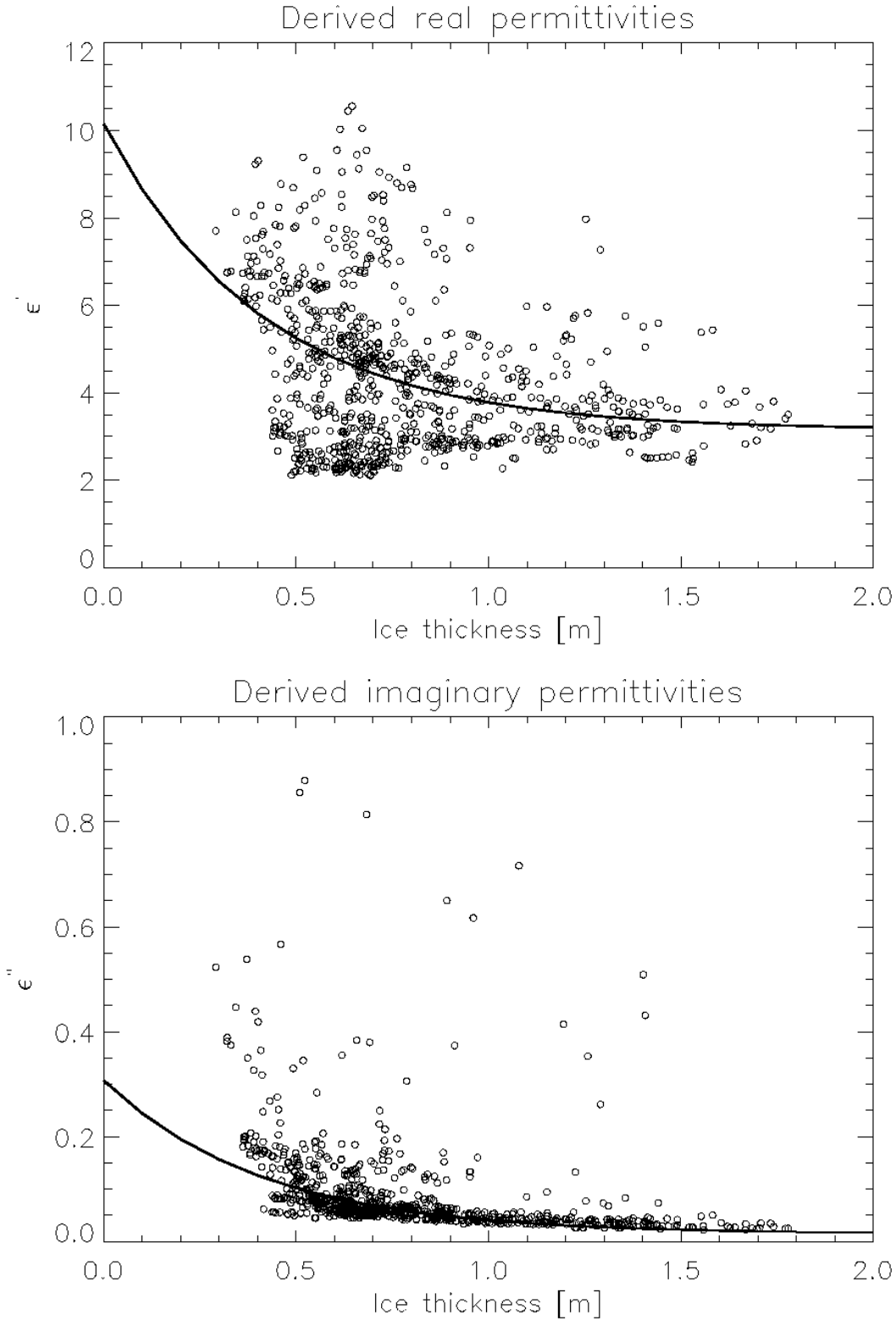

Figure 9.8: Derived permittivity versus ice thickness with statistical fits.

brine drainage and expulsion processes, which are qualitatively summarized in Section 2.2.1, will act to reduce the salt content of old ice (Cox and Weeks, 1988; Eicken, 1992). Because of changing weather conditions, however, ice growth is highly variable, regardless of thickness, thus there is much uncertainty in the relationship. Since more saline ice has lower emissivity, both Martin et al. (2005) and Naoki et al. (2008) attempt to use this property in order to determine ice thickness from passive microwave measurments.

Figure 9.8 shows the dependence of permittivity on ice thickness with the lines illustrating statisical fits of the form:

$$\epsilon^* = \exp(ah + b) + c, \tag{9.17}$$

where h is ice thickness and a, b and c are constants.

The imaginary component is used to infer the relationship of salinity to ice thickness using the formula for complex permittivity in Equation (6.16). Thus, salinity appears to have an approximately exponential relationship with ice thickness even for brackish waters like the Baltic. This is in line with the curves found in Tucker et al. (1992) (p. 15, Fig. 2-5), Weeks and Ackley (1985) (p. 93, Fig. 64) and in Chapter 5 Figure 5.13.

While the relationship of the imaginary permittivity to ice thickness is quite clear, although with large scatter, the plot for real permittivity is more ambiguous. Note that there appear to be two modes: in one case, the real permittivity shows either no relationship or an increasing relationship with ice thickness, while in the other, the permittivity increases with decreasing thickness, as expected. We hypothesize the following: in the case of the imaginary permittivity, pure ice has a value of almost zero so that the addition of brine, which is highly conductive, will always increase it. In the case of the real permittivity, pure ice already has a large value. In brackish waters the volume of the brine will be small and its salinity low producing little or no effect. Rather, the changes are the result of some other effect which is, as yet, not well understood.

Figure 9.9 shows a scatter plot of bulk salinity versus ice thickness for ice cores collected in the Weddell Sea in the Antarctic. An exponential has been fitted and the same exponential is shown together with that derived from the Baltic campaign data in Figure 9.10a. It would be reasonable to expect that the magnitude of the curves (as determined by the multiplication coefficient) is proportional to the salinity of the parent water as suggested by Figure 9.10c. Figures 9.10b and c could allow us to estimate the sea ice salinity versus thickness relation from the salinity of the surrounding ocean.

9.5 Validation using forward models

We test the parameterisation of complex permittivity by applying the forward models to the P4X to P2A overflight as in Section 6.7. Since this flight was omitted while fitting the permittivity versus thickness curves, we have here a form of cross-validation. Time series are shown in Figure 9.11 while scatter-plots are shown in Figure 9.12. A puzzling feature of both pairs of results is that while adding the permittivity dependence produces a positive correlation in the polarisation difference (Q), it does not improve the correlations in the components that comprise Q. Presumably, the parameterisation is not optimal.

In this instance, the Monte Carlo model is worse than the enemble model in predicting both horizontally polarised brightness temperature and polarisation difference. While it does not do a good job of *predicting* the polarisation difference, nonetheless, it does provide a possible *explanation* for the large variance in this signal, as Figures 9.13d and 9.15d suggest. Note that much of the scatter seen in the measured values of brightness temperature versus polarisation

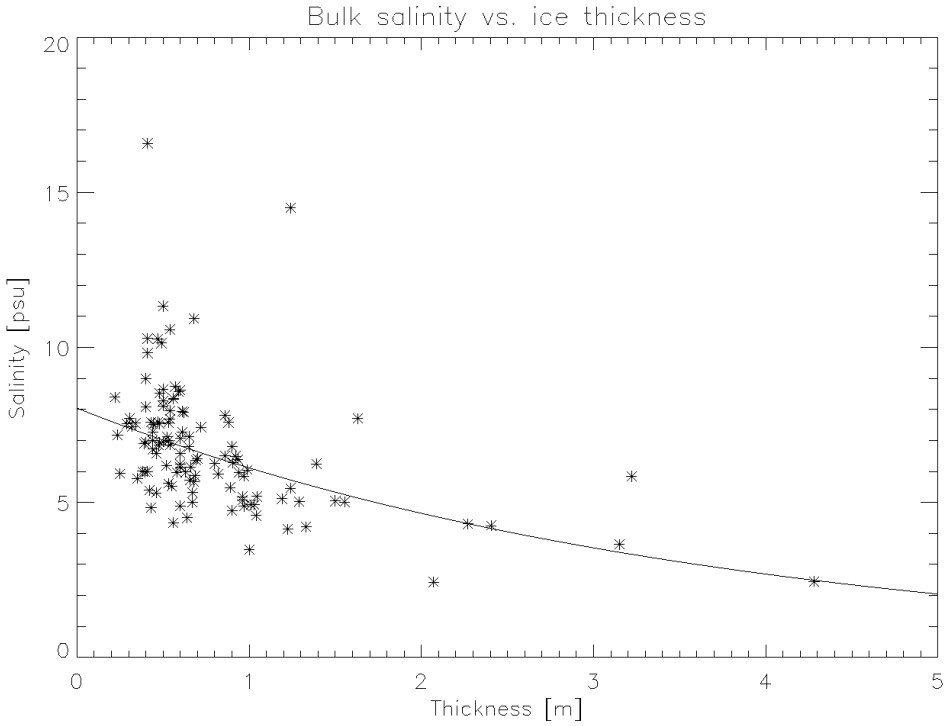

Figure 9.9: Bulk salinity as a function of ice thickness from cores taken from the Antarctic. Data from Eicken (1992)

difference seen in Figure 9.13a, particularly the points in the upper right corner, is the result of calibration problems.

9.6 Relationship of salinity profiles to bulk salinity and thickness

The surface ice layers will have the strongest contribution to the radiometric signal since they are not shielded by the layers above. Therefore, the salinity in the top few centimeters is particularly important: this is the approach taken in Naoki et al. (2008). It is not just the average salinity that varies with depth, it is also the shape of the salinity profile. Thinner ice will tend to have more variation of salinity with depth, with highly saline layers in both the top and bottom of the sheet generated by brine expulsion processes. Moreover, the salinity of the parent water will also affect the salinity profile; the latter tends to be flatter in ice from brackish waters like the Baltic (Granskog et al., 2006).

As a first crack at the problem, consider the following statistical model relating the surface salinity to both the bulk salinity and ice thickness:

$$S_0 = cS_{ave}^{k_1} \exp(k_2 h), \tag{9.18}$$

where c, k_1 and k_2 are constants. Figure 9.16 shows the results from such a model applied to the average salinity of the top 10 centimetres. This depth was chosen because it is just above the minimum resolution of the salinity profiles while just below the minimum ice thickness. Naturally, as this depth increases, the surface salinity will approach the bulk salinity. The rms error of the model was 5.02 psu while the correlation (without cross-validation) was 0.7.

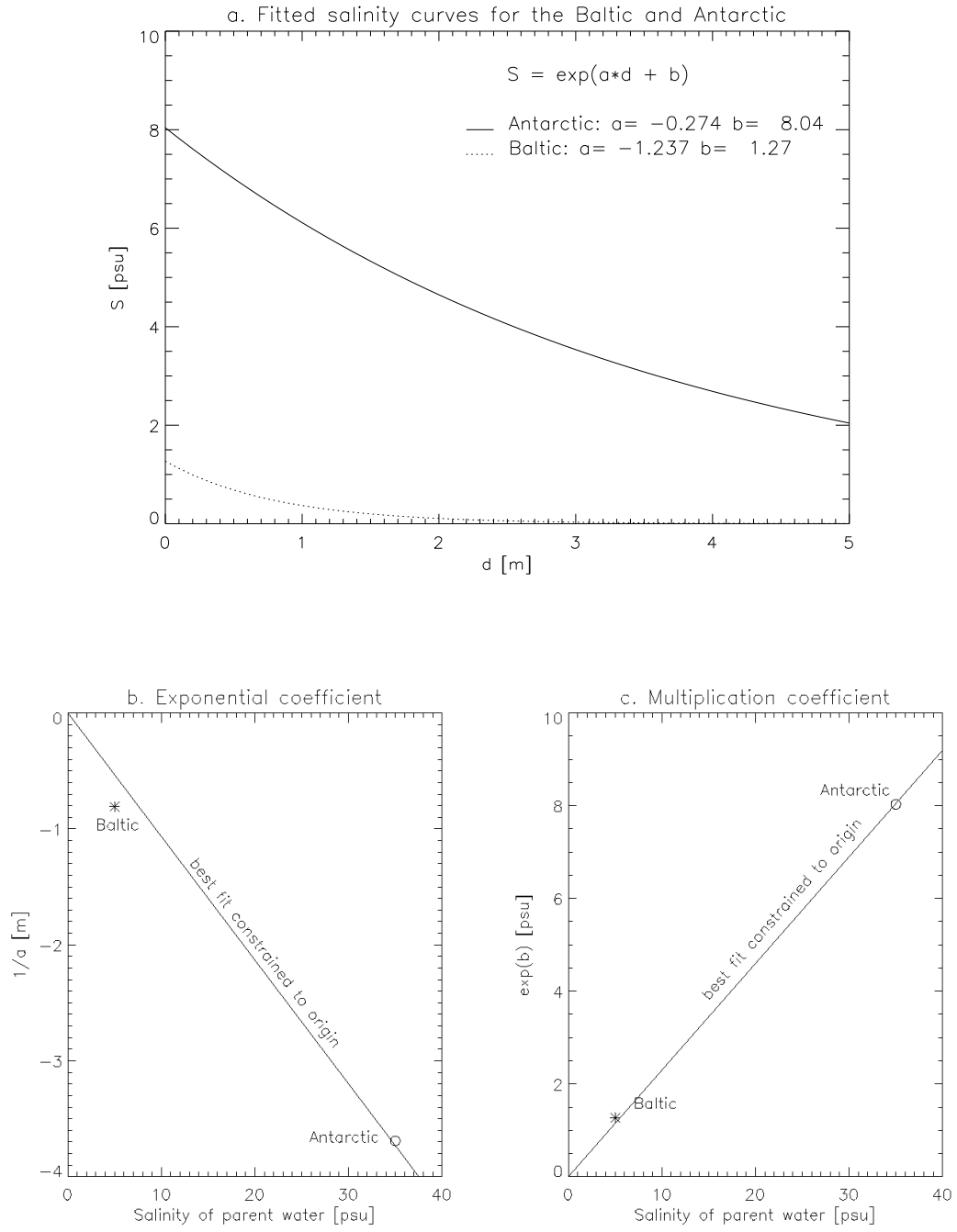

Figure 9.10: a. Fitted exponential curves for the Antarctic and the Baltic as a function of ice thickness. Figures b. and c. show the coefficients plotted with respect to the salinity of the parent waters with best-fit lines constrained to pass through the origin.

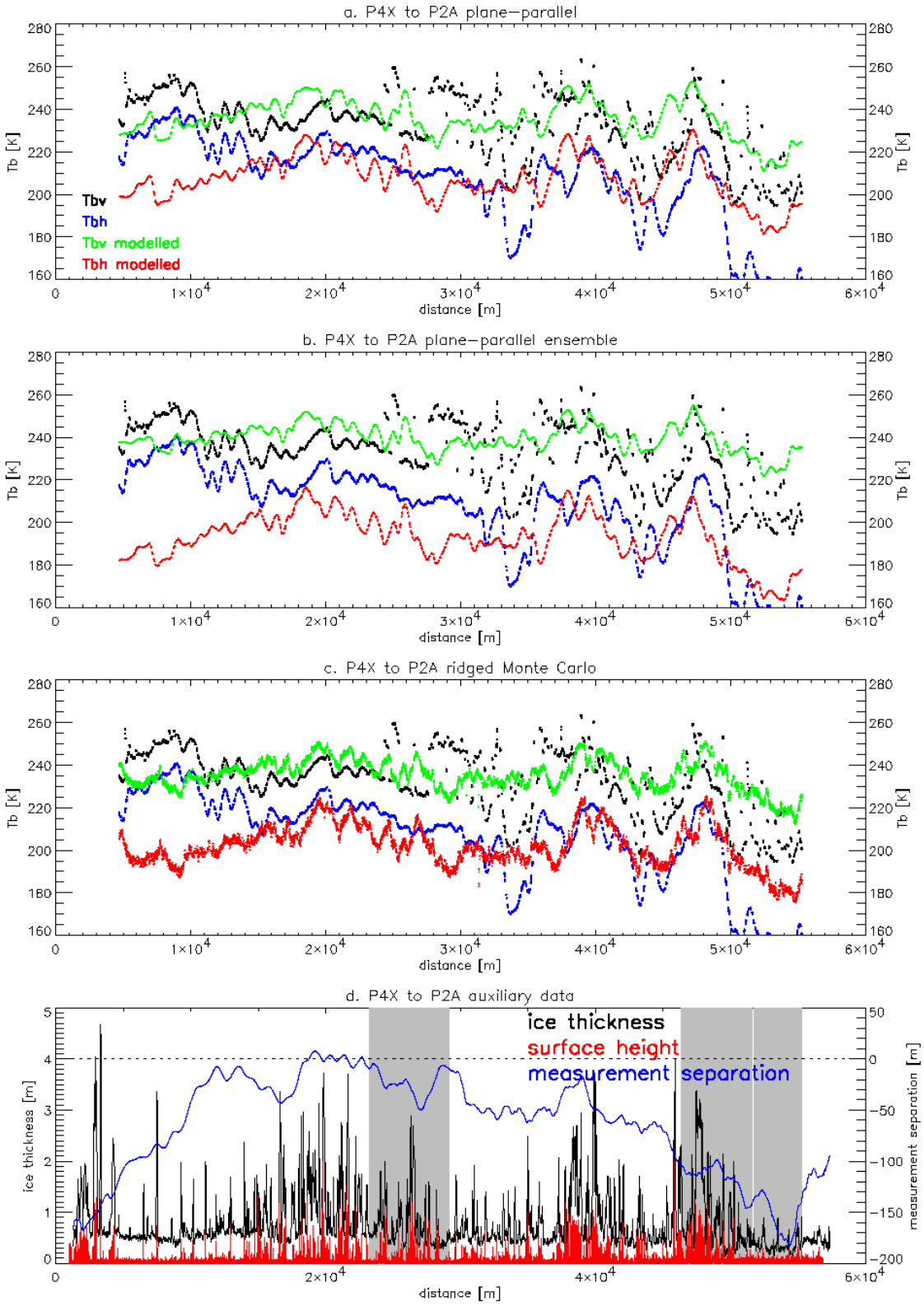

Figure 9.11: Same as Figure 6.24 except varying permittivity with ice thickness.

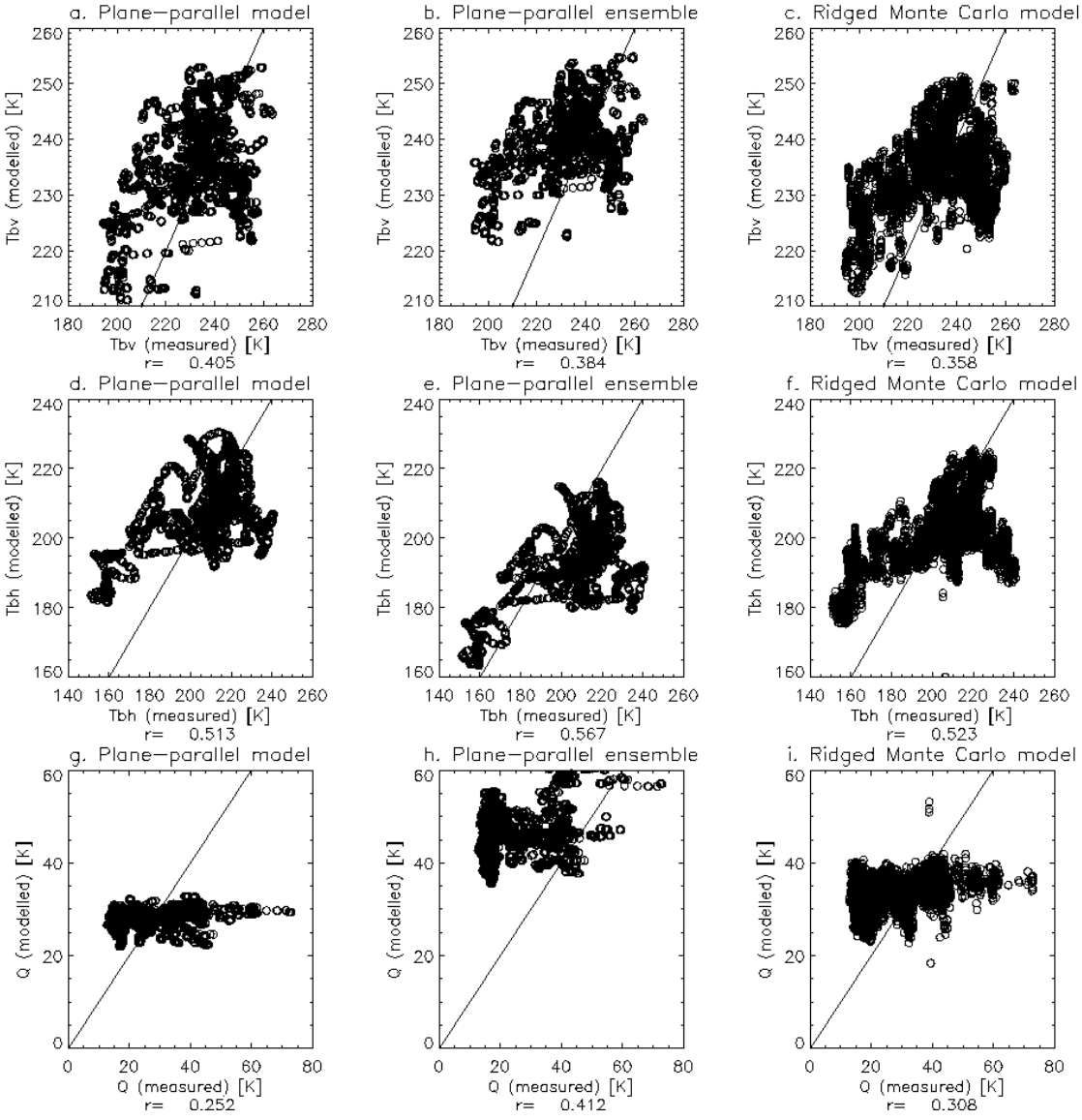

Figure 9.12: Same as Figure 6.25 except varying permittivity with ice thickness.

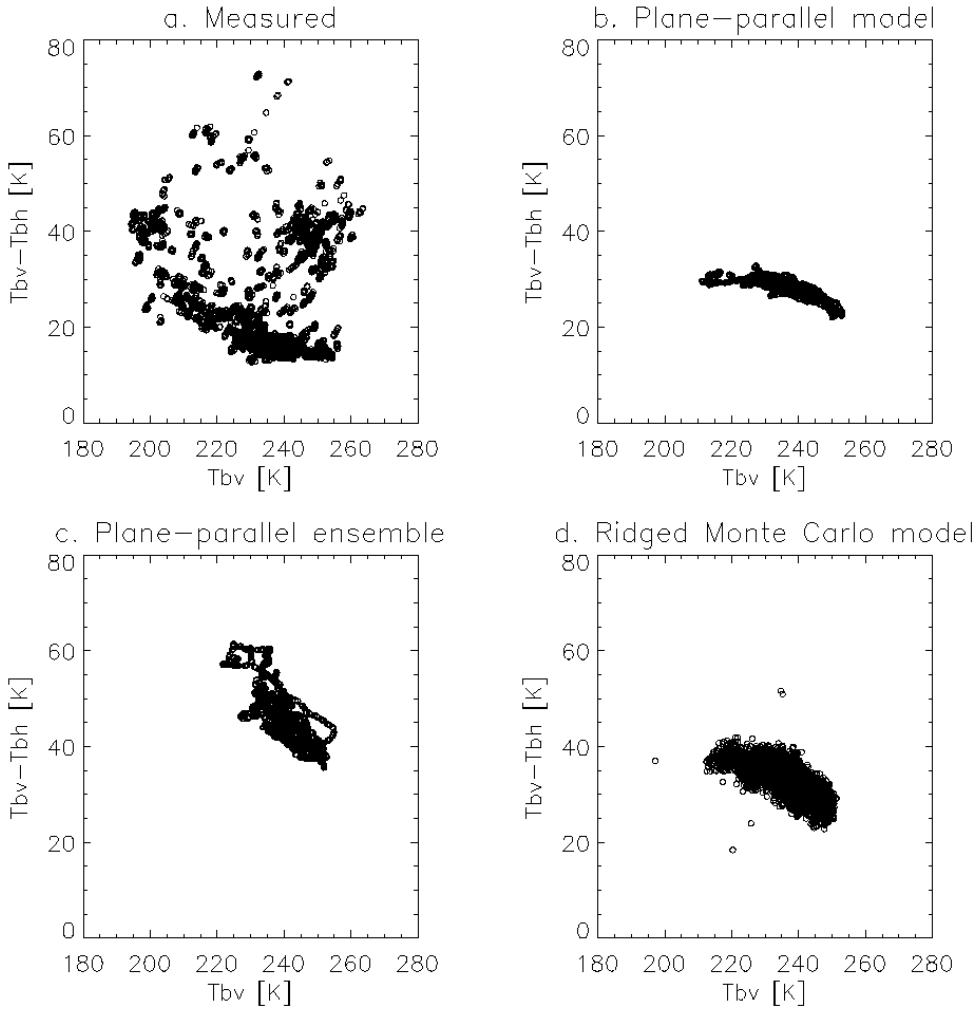

Figure 9.13: Scatter plots of polarisation difference versus brightness temperature for measurements and model results of P4X to P2A overflight.

9.7 Conclusion

Inversions of campaign data from the Baltic have demonstrated an approximately exponential relationship of sea ice salinity with ice thickness just like in more saline waters such as the Antarctic. This result was derived from complex permittivities estimated from campaign data and compared with ice thickness measurements. Applying the permittivity vs. thickness relations to forward model calculations improved estimation of polarisation difference. The magnitude of the thickness-salinity curves are roughly proportional to the salinity of the parent water, although it would be difficult to use them for any type of prediction or inversion work since the scatter is quite large. (See Figures 9.8b and 9.9.) Since it is not just the bulk salinity of the ice that varies with thickness and with the salinity of the water, but also the salinity profile, a simple statistical model for surface salinity was investigated. This related surface salinity to bulk salinity and thickness using ice core measurements taken in the Antarctic during Polarstern cruises.

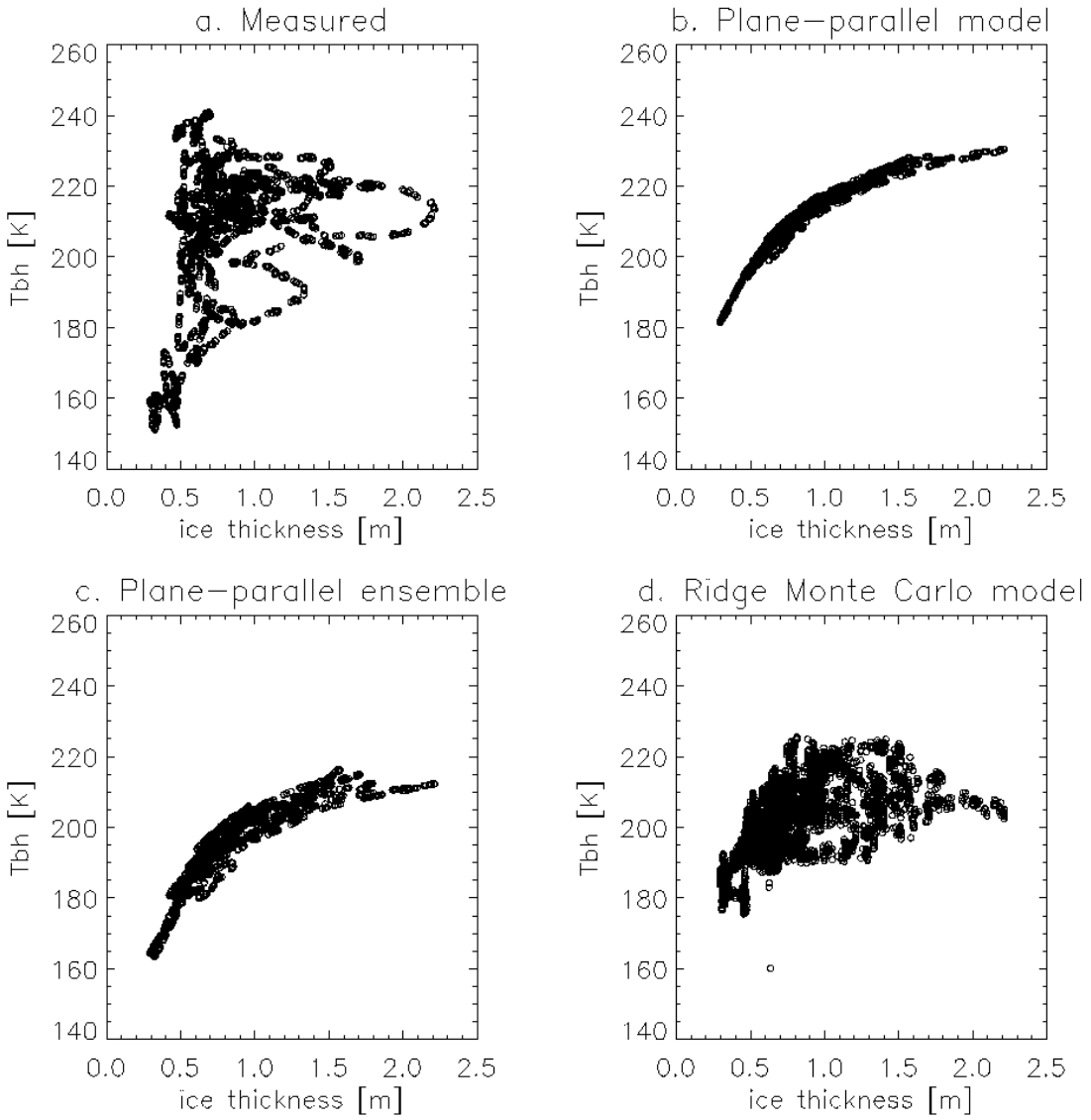

Figure 9.14: Scatter plots of brightness temperature versus ice thickness temperature for measurements and model results of P4X to P2A overflight.

Acknowledgements

Thanks to Hajo Eicken for sea ice core data (Eicken, 1992).

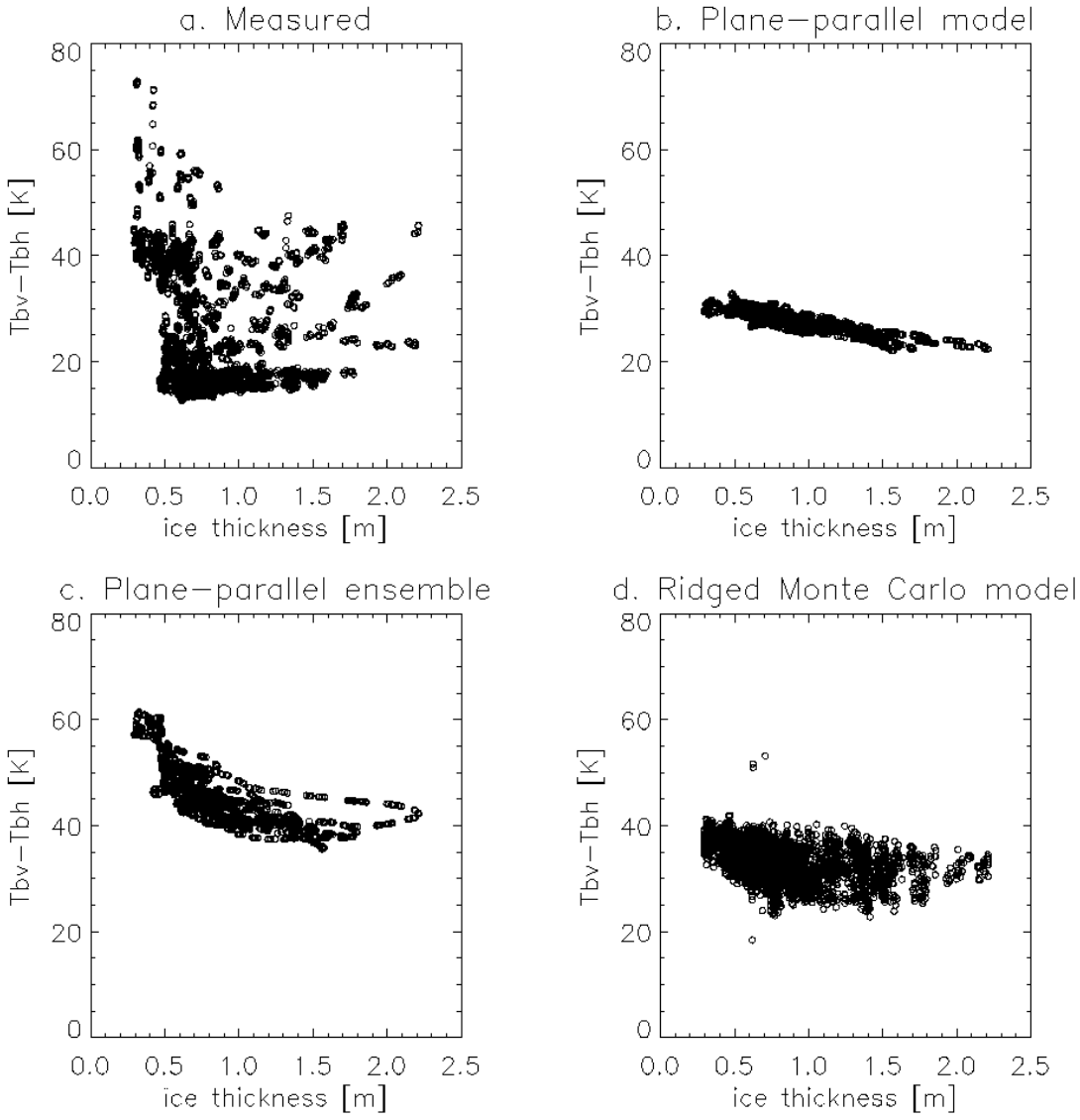

Figure 9.15: Scatter plots of polarisation difference versus ice thickness temperature for measurements and model results of P4X to P2A overflight.

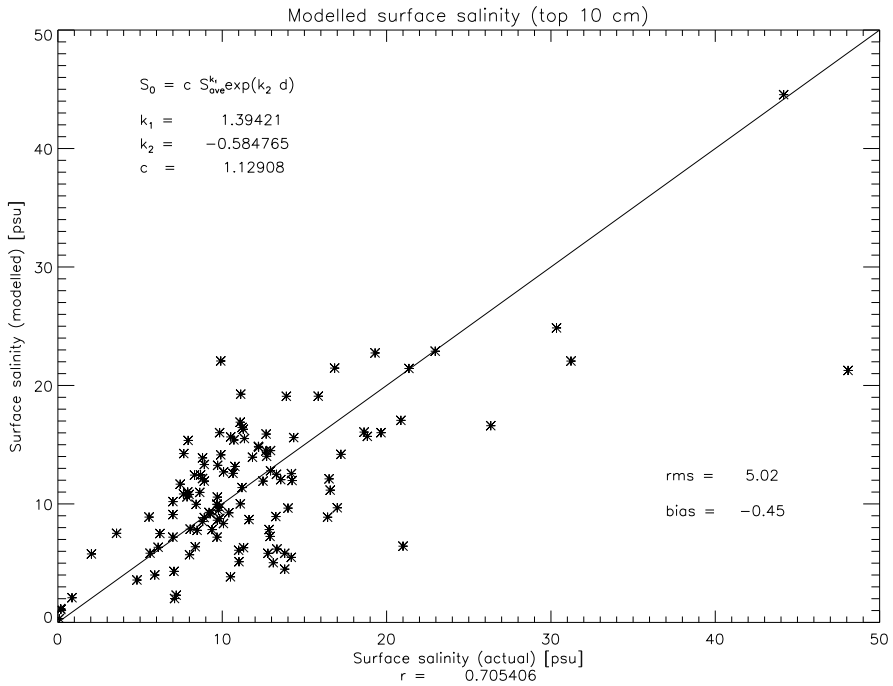

Figure 9.16: Sea ice surface salinity (top 10 cm) modelled from bulk salinity and ice thickness versus measured.

Chapter 10

WP 3: Retrieval Algorithms

Peter Mills and Georg Heygster

Institute for Environmental Physics, University of Bremen, Otto-Hahn-Allee 1, 28359 Bremen, Germany

10.1 Introduction

The Soil Moisture and Ocean Salinity instrument is a proposed new surface-detecting passive microwave radiometer measuring in the L-band (1.4 GHz). The SMOS Ice project aims to render, in addition to that from the pedosphere and the ocean surface, information about the cryosphere, sea ice in particular. Because of high transparency at such a low frequency, it is hoped that this may include the internal structure of the ice, such as salinity and thickness. Here we explore preliminary designs for a combined retrieval algorithm for ice concentration and thickness based on model results and thickness and emissivity measurements taken in the Northern Baltic during the Pol-Ice campaign, March 2007.

10.2 Proposed algorithm design

A schematic diagram of the proposed retrieval algorithm is shown in Figure 10.1. The open water point is located at the bottom, while the 100 % ice concentration points lie along a line at the top. The fractional distance along the line, from bottom right, is given as:

$$t = \frac{(Q - Q_{OW})T_{bOW} - (T_b - T_{bOW})Q_{OW}}{(Q - Q_{OW})(T_{b2} - T_{b1}) - (T_b - T_{bOW})(Q_2 - Q_1)} \tag{10.1}$$

where Q is the polarisation difference (second Stokes component), T_b is the brightness temperature and the subscripts 1, 2 and OW denote the bottom right, top left and open-water tie-points respectively. The ice concentration may be calculated either from the brightness temperatures:

$$C = \frac{T_b - T_{bOW}}{(T_{b2} - T_{b1})t + T_{b1} - T_{bOW}} \tag{10.2}$$

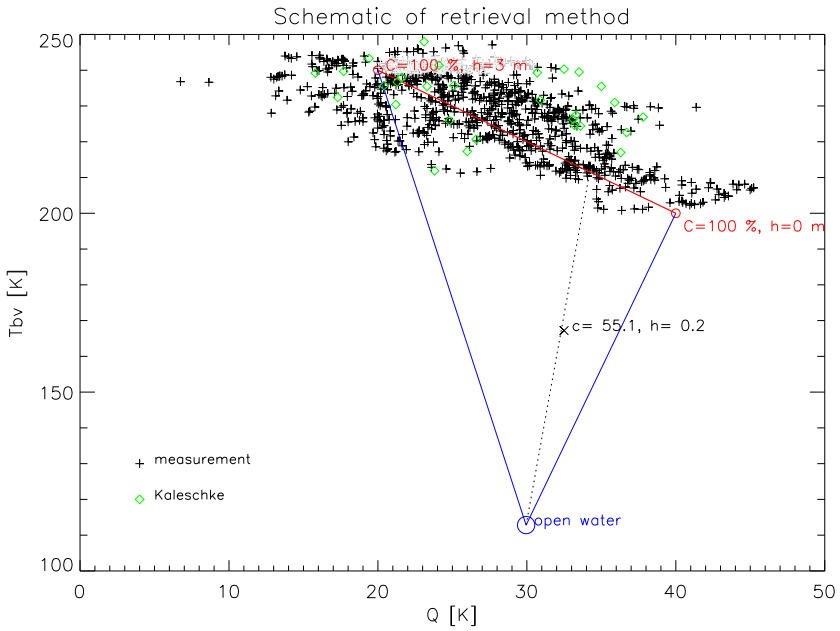

Figure 10.1: Schematic diagram of proposed retrieval algorithm at a 35 degree incidence angle. Black crosses are measurement points. Green diamonds are averaged values taken from Kaleschke and Maass (2008). c is concentration, h is thickness.

or from the polarisation differences:

$$C = \frac{Q - Q_{OW}}{(Q_2 - Q_1)t + Q_1 - Q_{OW}} \tag{10.3}$$

The $t = 0$ point corresponds to ice of zero or negligible thickness while $t = 1$ corresponds to ice of 3 metre thickness or more. We assume an exponential relationship between thickness and the distance parameter, t:

$$h = \ln(t - b)/a \tag{10.4}$$

where a and b are constants. This is at least partially supported by Figure 10.7, where the functional relations defined for the retrieval algorithm are traced by the red curves, while actual measurements are shown with points.

10.2.1 Zenith angle dependence

Since the synthetic aperture of SMOS will sample at different effective viewing angles – from between 0 and 50 degrees – the angular dependence will have to be determined. To determine this from theoretical considerations is straightforward: perform an inversion on the line segment between the two tie-points to determine the complex permittivities using the same

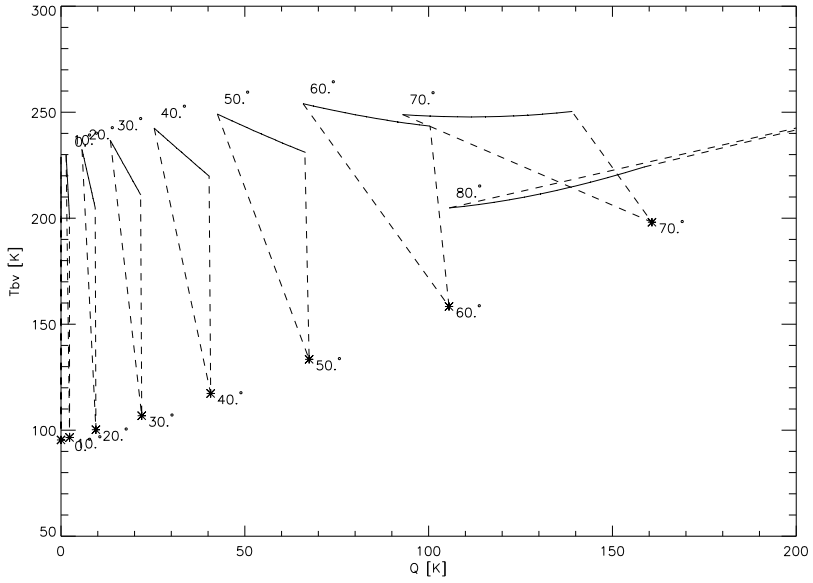

Figure 10.2: Retrieval curve for different viewing angles.

procedure described in Section 9.3. Then we run the model forward again for different zenith angles.

The modified geometry for zenith angles between 0 and 80 degrees in 10 degree increments is shown in Figure 10.2 while the location of the tie-points as a function of zenith angle is shown in Figure 10.3. The derived complex permittivies are shown in Figures 10.4 through 10.6 with those from the retrieval curves shown by the red circles. In an attempt to fit the designed retrieval curves to the theory, fits have been performed on the red curves: the real permittivity was hand fit to ice thickness using an exponential of the form:

$$\epsilon' = \exp(k_1 h + k_2) + c \tag{10.5}$$

where k_1, k_2 and c are constants. A linear least-squares fit was performed to relate the real and imaginary components of the complex permittivities:

$$\epsilon' = m\epsilon'' + b \tag{10.6}$$

This is consistent with Vant et al. (1978), although the constant of proportionality is about an order of magnitude higher. All the fitted curves, shown in blue and labelled as "model 1," are well within the scatter of the experimental data. Forward model runs of these fitted curves are shown in Figure 10.7, also in blue. Despite the close fit with the designed retrieval curves, when plotted in measurement space in Figure 10.7d, it traces out a voluptuous 'S'-shaped curve rather than a straight line. Thus even such a simple model displays a considerable degree of sensitivity to the input parameters.

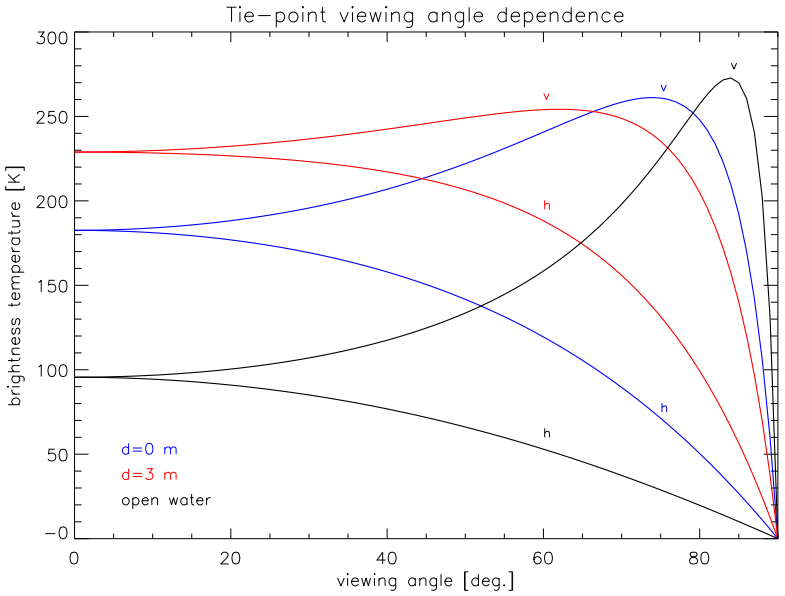

Figure 10.3: Dependence on viewing angle of the three tie-points.

10.2.2 Salinity and temperature dependence

The fitted curves described in the previous section are useful for determining the angular dependence. For determining the salinity dependence, we need a closer agreement with the theory. The ice models used in this study all have two modules: the first step calculates the effective complex permittivities of the ice from its bulk and microphysical properties, e.g. temperature, salinity, grain size and density, while the second computes the resulting brightness temperatures of the emitted radiation. To gain an idea of the salinity dependence, we need to go back to step one to the bulk properties of the sea ice.

The second fitted model, labelled "model 2" and designated with the brown curves, was created by first fitting the imaginary permittivities with an exponential of the same form as Equation (10.5) by subtracting the constant first and then performing a least-squares regression. Real permittivities were calculated by first solving for the brine volume using Equation (6.16) and then calculating the real part with Equation (6.17). It was shown in Chapter 9 that the magnitude of the curve relating ice salinity to thickness is approximately proportional to the salinity of the parent water. This allows us to extrapolate the curves for the world oceans.

The salinity of the Baltic Sea at the test site is about 5 psu, corresponding to a freezing temperature of -0.3 degrees Celsius. Figure 10.8 shows the resulting brightness temperature for several ice temperatures with ice thickness as the parameter. This figure suggests that a combined thickness and concentration retrieval, if possible at all, is only so at temperatures close to freezing. It also suggests that the brightness temperature converges to a more or less constant value for thick ice, regardless of temperature or salinity conditions, meaning that concentration retrievals should be fairly straightforward.

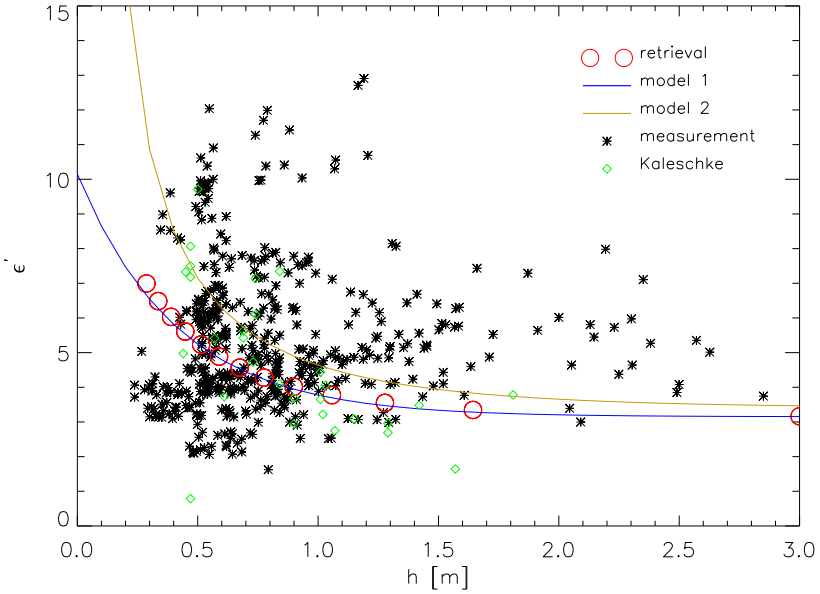

Figure 10.4: Real permittivity as a function of ice thickness. Blue and brown curves are two different parameterizations of the complex permittivity as a function of thickness. Red circles are the curves designed for the combined thickness-concentration retrieval. Black asterisks are derived from aft-looking campaign measurements (two polarizations, see Chapter 9) while green diamonds are derived from averaged values tabulated in Appendix A of Chapter 4.

10.3 Results

Validation of ice-concentration retrievals against the ASI algorithm (Spreen et al., 2008) are shown in Figures 10.9 and 10.10. All the Pol-Ice data was used for which there were corresponding ASI retrievals. The first scatter plot shows a direct comparison of ice concentrations derived from single measurement points with those interpolated at the same location from high-resolution (5 km) ASI ice concentration maps. Since the footprint size of the two instruments is so different, the two have also been compared by first binning all the ASI ice concentrations in one percent intervals and averaging the Pol-Ice retrievals. Correlations are, respectively, 0.39 and 0.72. While these are not brilliant, they are typical for comparisons of sensors whose footprints are different by orders of magnitude, e.g., Spreen et al. (2008) find correlation coefficients around 0.8 when comparing AMSR-E/ASI results with shipboard observations. Two other points should be kept in mind. First, there is a selection bias because of the linear flight path of the aircraft and because the pilot may be deliberately seeking either ice-covered or open-water areas. Second, the ASI algorithm is designed for the more saline water bodies of the Arctic and Antarctic.

Thickness retrievals do not fare quite so well and are shown in Figure 10.11. Overall, there

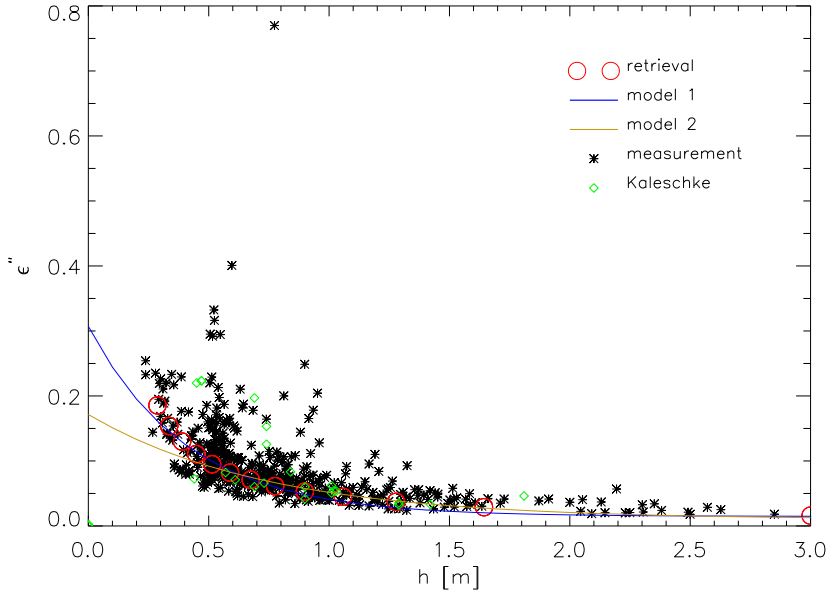

Figure 10.5: Imaginary permittivity as a function of ice thickness. Curve descriptions are the same as for Figure 10.4.

is essentially no correlation between measured and retrieved thicknesses. For the selected averages there is a weak correlation of 0.26 with open water points and 0.2 without. For the selected overflight, P4X to P2A, used in both the forward modelling studies (Sections 6.7 and 9.5) and the earlier retrieval study (Section 4.4.1. The time series in Figures 10.12 looks quite poor, but the scatter plot in 10.13 shows a non-negligible correlation of 0.27. These should be compared with Figure 4.16.

The calibration errors in the vertical channel will considerably hamper such a combined retrieval. These were discussed in considerable detail in Section 9.2.4. Other obstacles to accurate thickness retrieval will be discussed in the next section.

10.4 Discussion

It is clear from this work that it will be possible to estimate ice concentration from SMOS measurements. It is not so clear whether any information on ice thickness can be rendered. It should be understood that even at low frequencies with a large penetration depth like L-band, changes in the radiometric signature as a function of thickness result primarily from changes in effective permittivity. In the current models, the effective permittivity is a function only of brine-volume, which in turn is a function of salinity and temperature. As explained in Section 2.2.1, salinity is a function of ice thickness because of varying growth rates and because of expulsion processes. Since growth processes are highly variable, this function will have a great

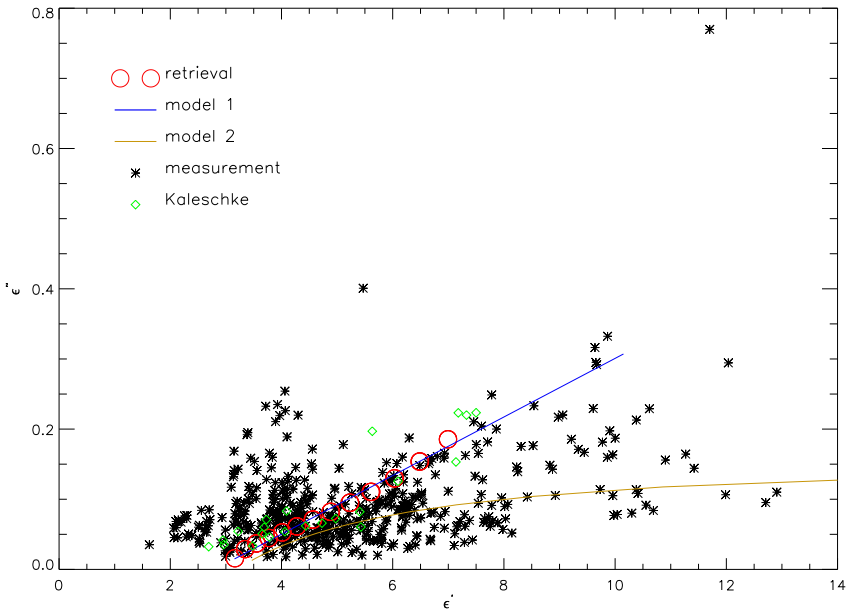

Figure 10.6: Imaginary permitivity versus real permittivity Curve descriptions are the same as for Figure 10.4.

deal of scatter, as shown in Chapter 9.

The melting conditions of the Pol-Ice campaign are particularly difficult. Figure 10.14 shows a plot of brine volume as a function of temperature for three different equations: (4.21) to (4.23) from Chapter 4 (Vant et al., 1978), (4.24) from Chapter 4 (Cox and Weeks, 1983) and the following empirical relation from Ulaby et al. (1986):

$$V_b = \frac{S}{1000}\left(-\frac{49.185}{T} + 0.532\right) \tag{10.7}$$

Because of the steepness of the curve and because the relations are empirical and approximate, calculations of brine volume close to melting conditions will be highly uncertain. In theory, at melting conditions the brine volume is 100%. From brine volume, we compute the permittivities. This is similarly fraught with uncertainty, as described in detail in Chapter 6, Section 6.5.

If we believe the mixture formulae from Vant et al. (1978) (Equation (6.16)) – shown in Figure 10.15 – the complex permittivity is quite stable at lower temperatures. E.g., at -2°C, we have ϵ'' about 0.1, corresponding to the maximum of the retrieved values in Figure 9.7. Moreover, the curves must be linearly adjusted up or down depending on salinity. This dependence will be particularly important in the case of the imaginary part since a change of one psu will produce a change in ϵ'' of roughly 0.005. Since the salinity of the top layers of thin ice can be higher than 15 psu under Arctic conditions, this means that the variability in complex permittivity, even at constant temperature, could be as high as 0.1.

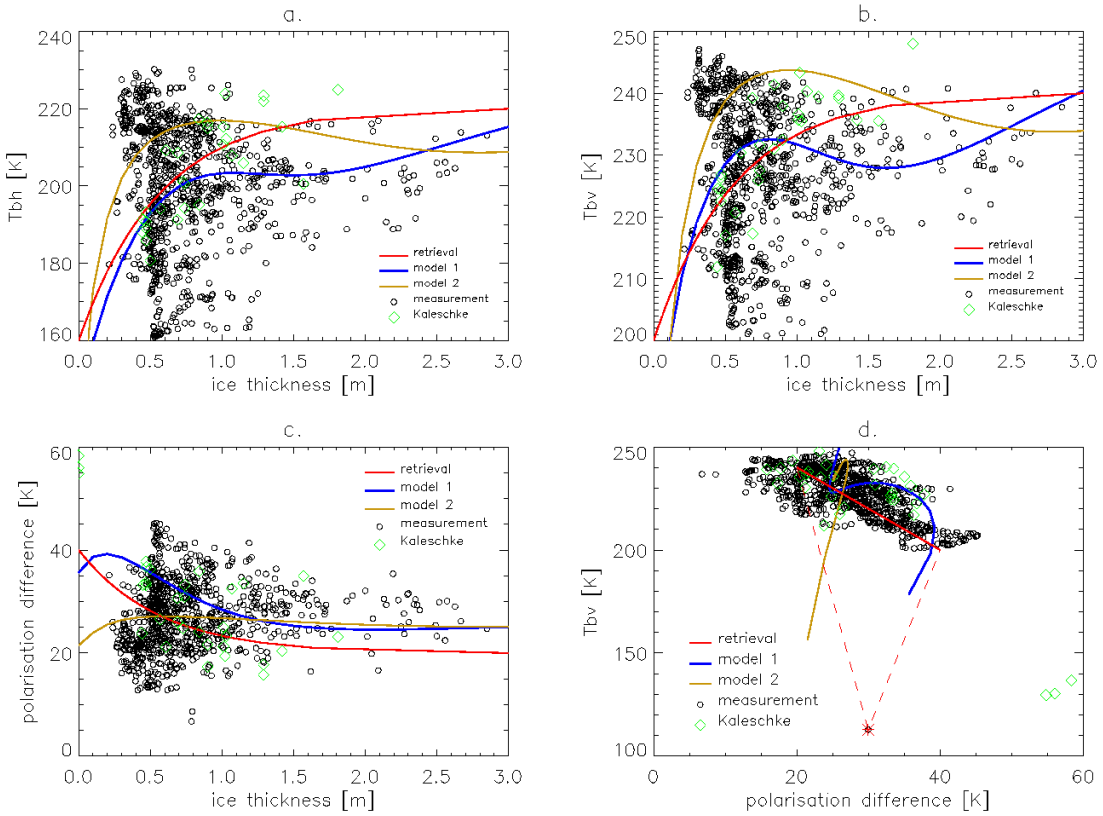

Figure 10.7: Retrieval and model curves in measurement space. Blue and brown curves are two different parameterizations of the complex permittivity as a function of thickness. Red is the designed curve for the combined thickness-concentration retrieval. Black circles are measured values while green diamonds are averaged values from the appendix of Chapter 4.

Further uncertainties will be introduced by aspects of the ice not accounted for in the models. We have no knowledge of the internal structure of the ice, for instance. The external structure, such as ridging, will also have an effect on the signal, as shown in Sections 6.7 and 9.5. Figures 9.13d, 9.14d and 9.15d show how much including ice ridging increases the scatter in the brightness temperature-thickness relation.

It will likely be difficult to retrieve more than one quantity from the horizontally and vertically polarised channels. While these results suggest that thickness and concentration are at least somewhat independent, this is likely not the case for the other quantities of interest. Figure 10.16 plots the brightness temperature and polarisation difference as a function of salinity and ice thickness while keeping the temperature constant. Because the isolines in the pair of diagrams intersect at small angles, retrieval of the salinity and thickness will be highly uncertain. Figure 10.17 plots the same thing but varying temperature while keeping salinity constant. Both assume 100 percent ice concentration.

Rather than retrieving those quantities most meaningful for climate research, such as salinity and temperature, it might make more sense to retrieve quantities that are more relevant to the models, much like our permittivity estimates, as an intermediate step. For instance, for media of constant temperature and reasonably high opacity, the polarisation difference will vary with the real permittivity, as Figure 10.18 shows. According to the mixture models of Vant et al.

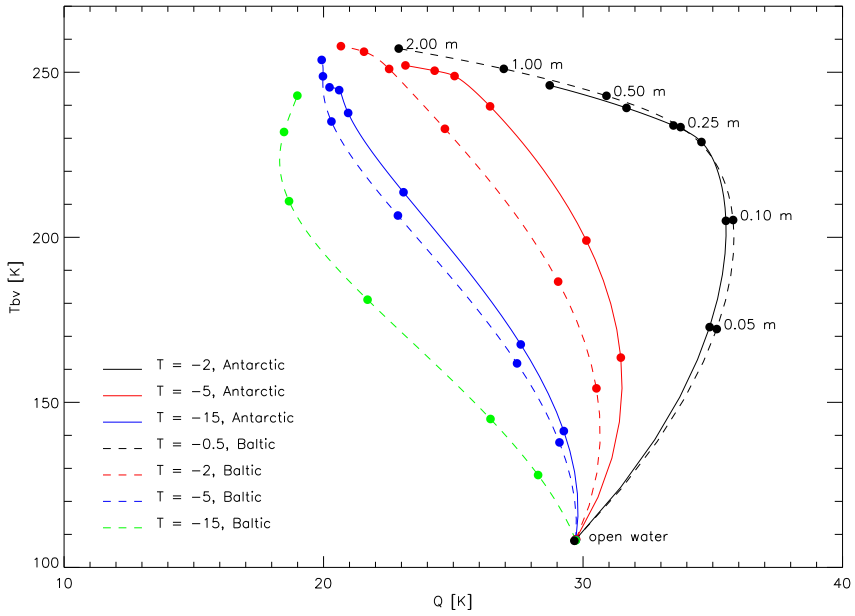

Figure 10.8: Model 2 curves for ice at different temperatures in the Baltic (S=5) and in the ocean (S=35).

(1978), real and complex permittivities are both linearly related to brine volume thus it makes sense to retrieve brine volume in conjunction with ice thickness. Figure 10.19 suggests that this may be possible in some regimes.

While L-band measurements may be of limited use on their own for retrieving more than ice concentration, they could well be used in conjunction with other satellite data, supplying, for instance, some knowledge of temperature. Figure 10.20 illustrates a "five-layer" dielectric slab model with an ocean layer, two ice layers and a snow layer. There are two ice layers because of the importance to the signal of the highly saline surface layer in first-year and new ice. As suggested in the previous paragraph, rather than retrieving the ice structural properties, we instead retrieve the complex permittivities, which are more fundamental from the stand-point of the models. There are four quantities per solid layer: real and imaginary permittivity, thickness and physical temperature, which makes twelve in total. These could be retrieved from a combination of SMOS data, and several low frequency channels of the AMSR-E instrument. To keep the problem fairly well-posed, the retrieved parameters could be partially constrained. The retrieval may proceed in one of two ways: either direct inversion using one of the many classical inversion algorithms, such as Levenberg-Marquardt iteration, or by constructing a direct inverse model from multiple runs of the forward model using machine-learning techniques. Ice emissivity models are quite interesting from the point of view of non-linear inverse theory: complex enough to be interesting, yet simple enough to be used as a sample test case.

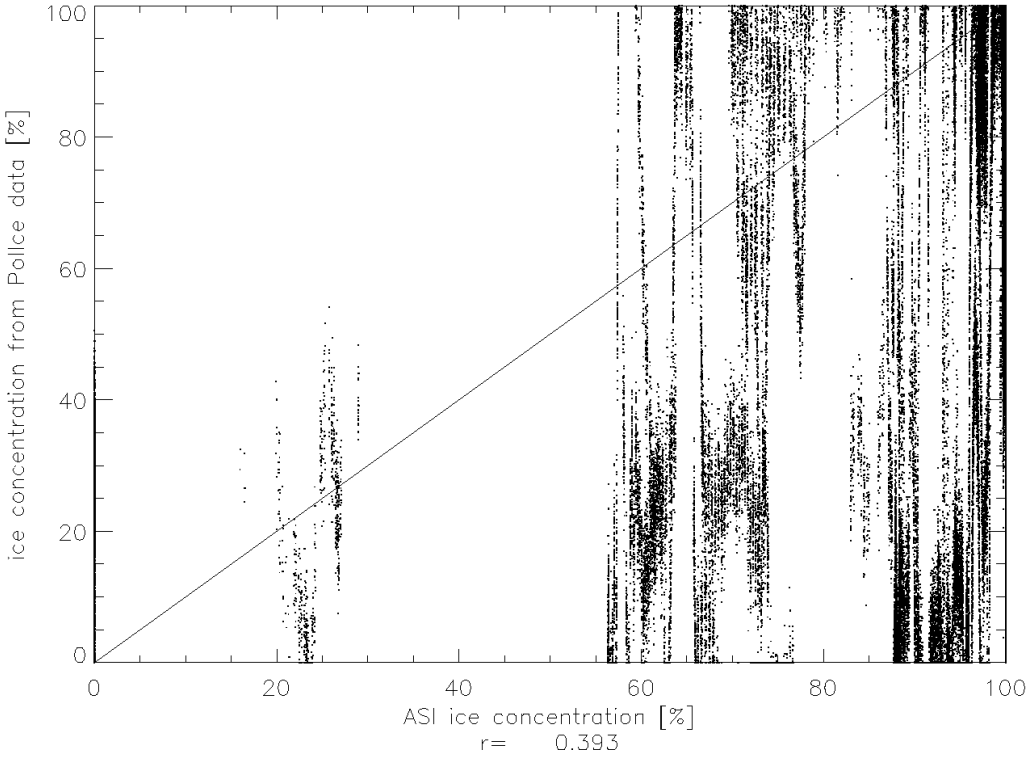

Figure 10.9: Point-by-point comparison of ice concentration retrieval from Pol-Ice 2007 measurements with ice concentration from ASI high-resolution AMSR-E retrievals.

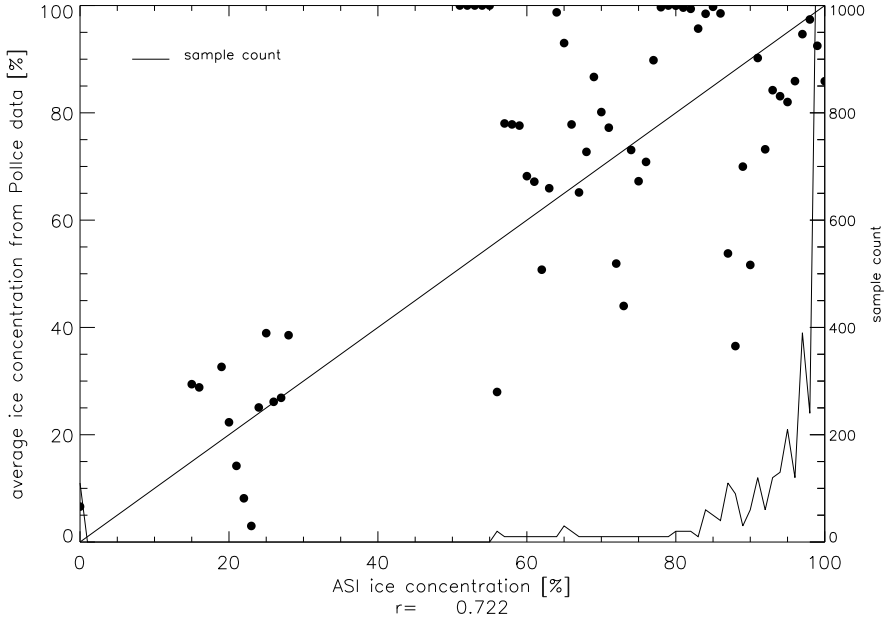

Figure 10.10: Average ice concentration retrievals from Pol-Ice 2007 compared with ASI binned in 1% intervals.

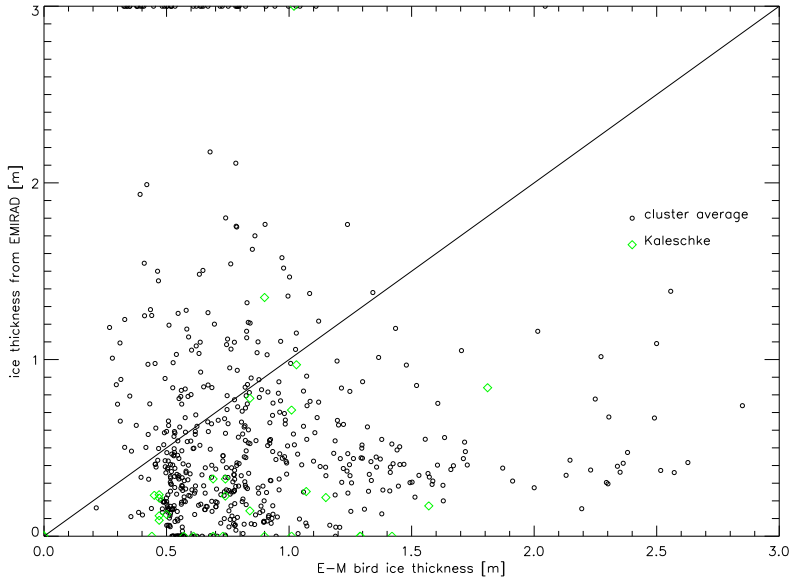

Figure 10.11: Validation of ice thickness retrievals. Circles are comparison with measured values averaged in the manner described in Chapter 9. Green diamonds test the retrieval against the averaged data described in Chapter 4.

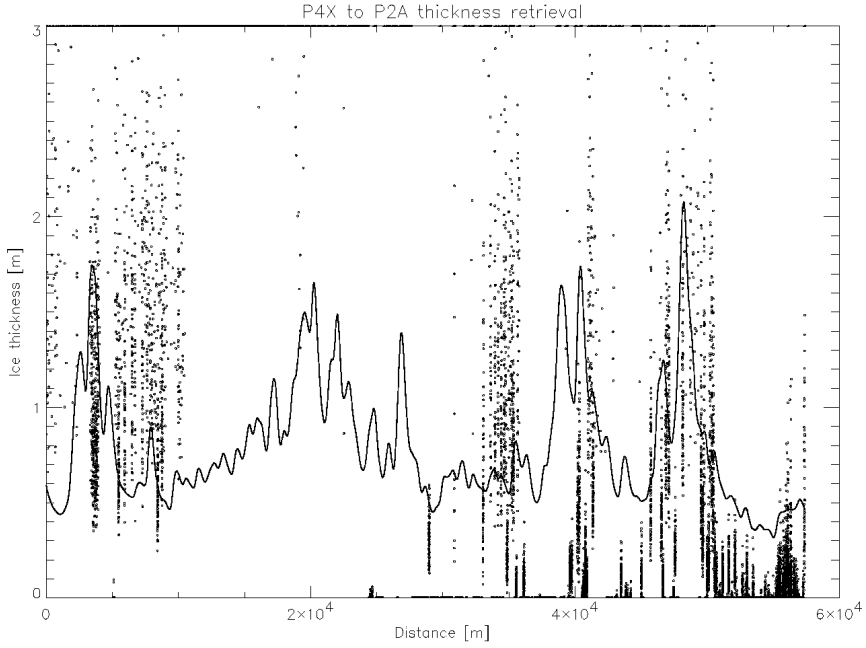

Figure 10.12: Validation of ice thickness retrievals for selected overflight. Line is measured ice thickness averaged over the instrument footprint. Circles are retrieved.

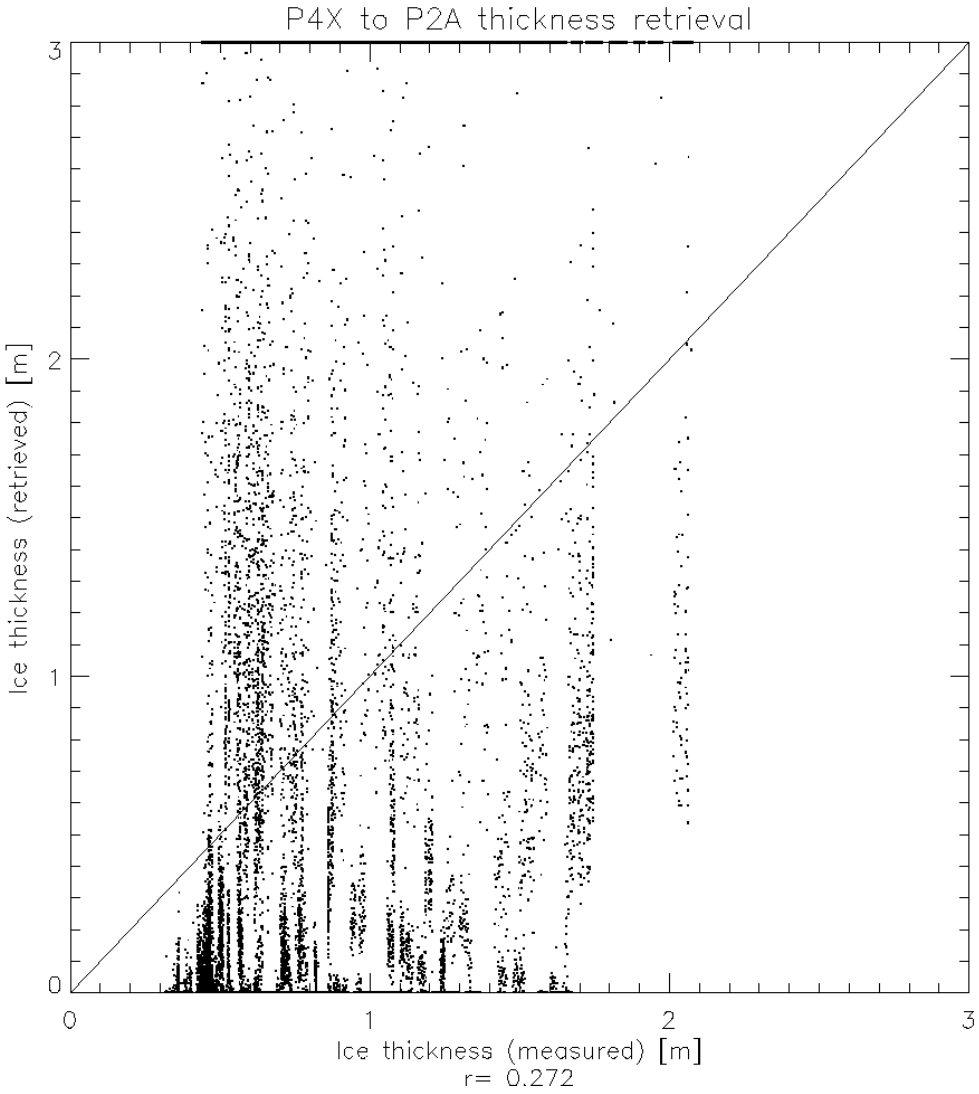

Figure 10.13: Scatter plot of ice thickness retrievals for selected overflight.

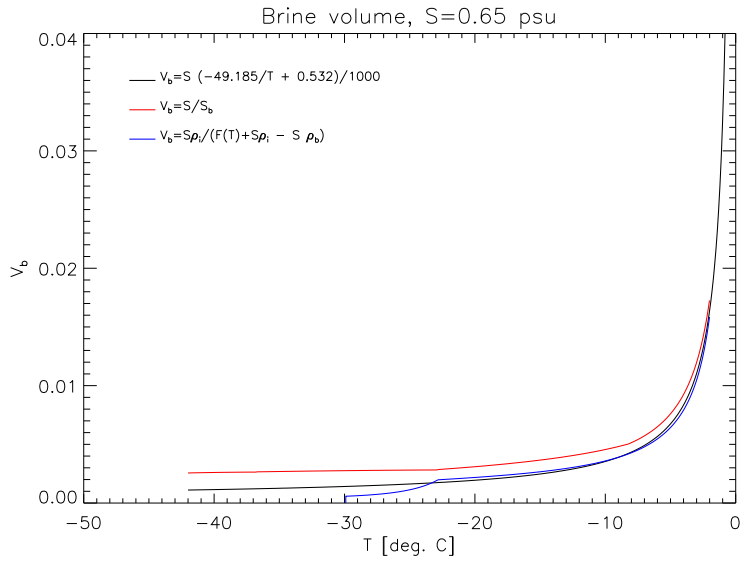

Figure 10.14: Plots of brine volume as a function of temperature.

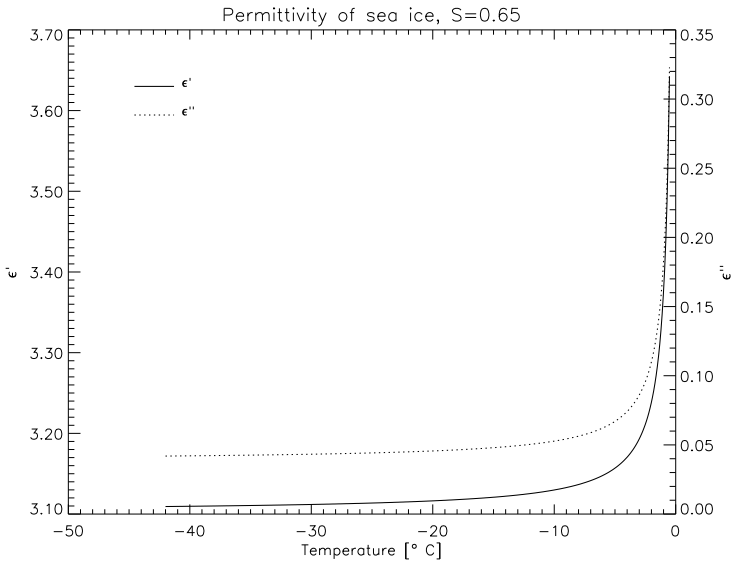

Figure 10.15: Complex permittivity as a function of temperature according to mixture models of Vant et al. (1978).

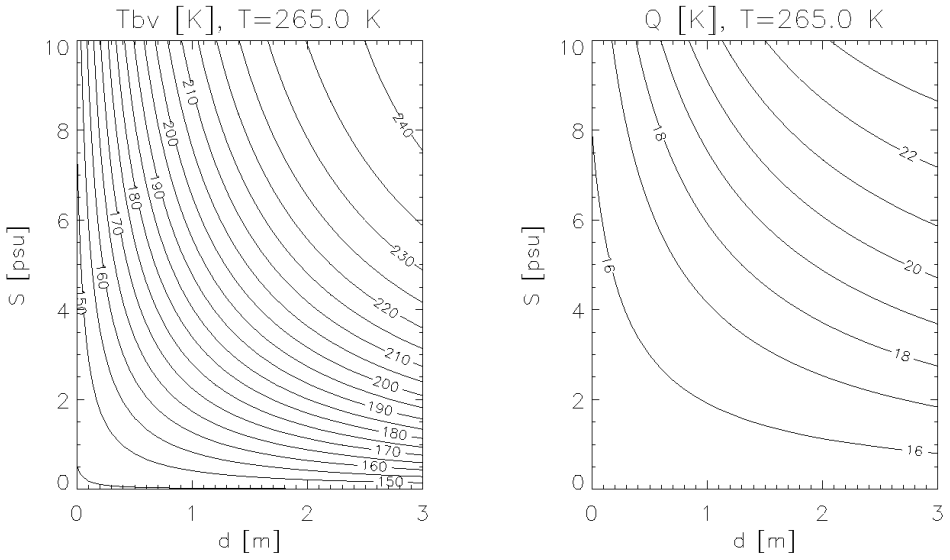

Figure 10.16: Modelled signal as a function of salinity and thickness, assuming constant temperature.

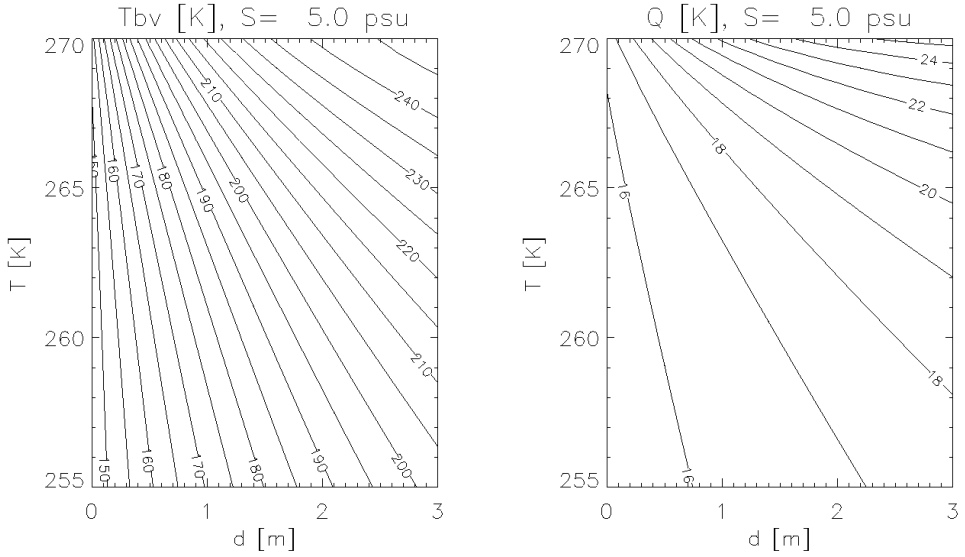

Figure 10.17: Modelled signal as a function of temperature and thickness, assuming constant salinity.

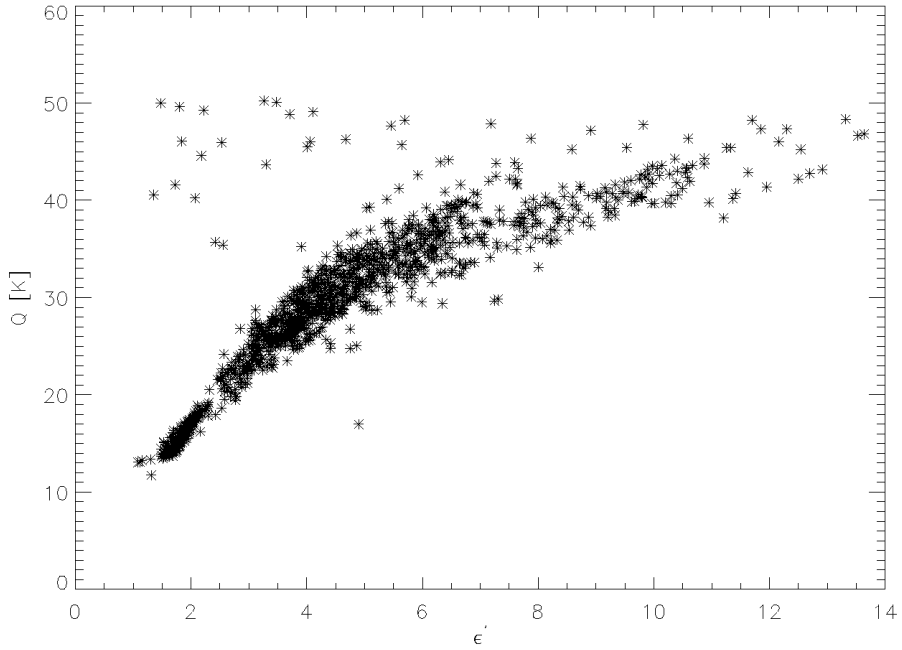

Figure 10.18: Polarisation difference for averaged EMIRAD measurements versus retrieved real permittivities.

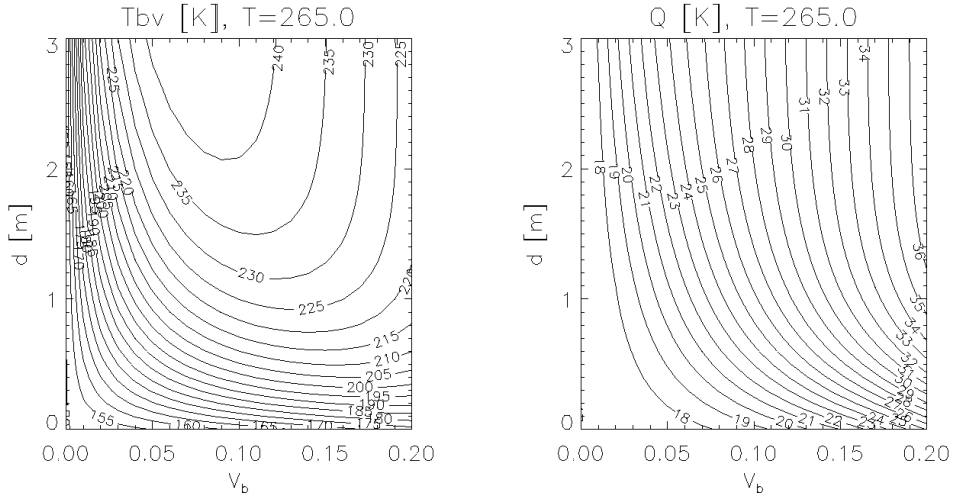

Figure 10.19: Modelled signal as function of brine volume and ice thickness using Vant et al. (1978) mixture formulae – (Equation (6.16)).

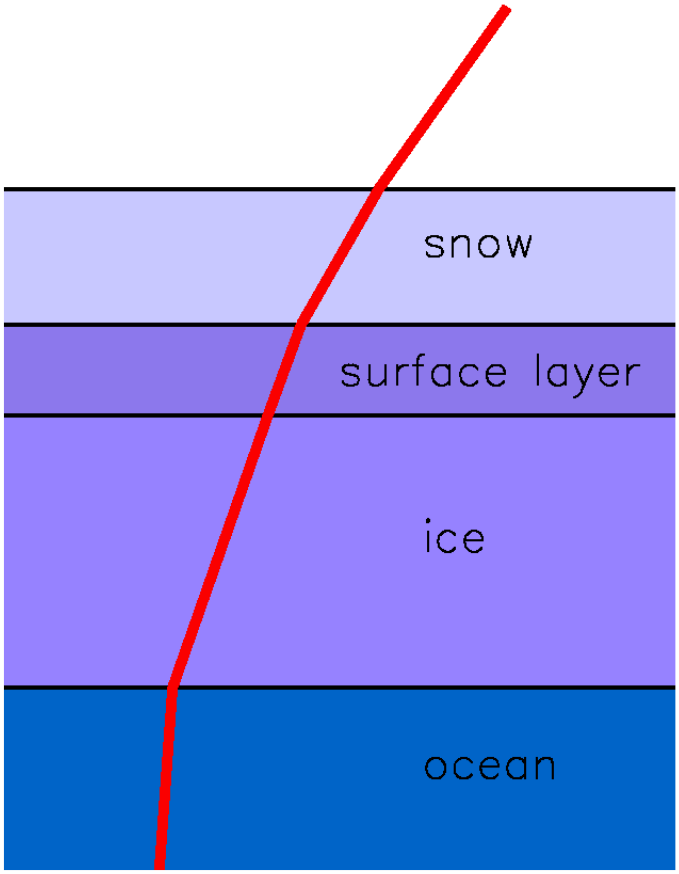

Figure 10.20: Five-layer ice emissivity model.

10.5 Conclusion

A preliminary ice concentration and thickness retrieval algorithm for a partially polarised (horizontal and vertical polarisations only) L-band receiver was presented and tested on campaign measurements. While the concentration retrievals showed fairly good agreement with AMSR-E derived satellite ice concentrations, the thickness retrievals were rather poor. In part, this is because of calibartion errors in the vertical channel of the radiometer, which were particularly noticeable in the overflight used to test the algorithm. These results do, however, suggest that a combined retrieval of concentration and thickness may be possible for some conditions.

Currently we cannot determine if this poor result is cause by technical or physical reasons, or a combination of both. The technical ones are the radiometer imperfections. All results need to be treated with caution because the additional sensor noise propagates into all subsequent analyses. The physical reason is the temperature near melting, leading to high brine volume and small microwave penetration depth in the ice. The imaginary part of the permittivity reaches values up to 0.35. However, the diagrams of Fig. 10.15 show that at ice temperatures of -2° and below, the relation between permittivity and both components of permittivity becomes much more stable. Unfortunately, such conditions were not met during the campaign. These uncertainties lead to a high variability in the retrieved complex permittivities, and thus thicknesses.

Improved retrievals would likely require some knowledge of ice temperature. While the SMOS instrument may not supply much useful information on its own, it would be valuable when used in conjunction with other passive microwave radiometers.

It is clear from this work that more research must be done. Relationships between the bulk properties and microstructure of sea ice and resultant electro-magnetic properties are still not well understood. For basic research, coincident radiometer measurements and ice core samples for direct validation of layered emissivity models will be helpful.

There are a number of factors that make retrievel of ice thickness difficult. As ice becomes thinner, it becomes more saline, particularly in the top layers. It also becomes warmer because of greater heat conduction. This means that the permittivities, both real and imaginary, become both higher and more variable as the ice becomes thinner, thus the penetration depth and our ability to predict it are both reduced. On the other hand, first retrievals as shown in Figure 4.9 are encouraging. As a first step, SMOS observations combined with a set of Arctic sea ice thickness data, best together with temperature information, would help to better explore the possibilities of sea ice thickness retrieval from SMOS.

Chapter 11

WP 4: External Calibration

Detlef Stammer

Institut fuer Meereskunde, KlimaCampus, University of Hamburg

11.1 Introduction

WP 4 is concerned with the question whether a region with stable temperature and salinity values can be identified in high latitudes where the surface temperature of the ocean then could be used as an external calibration source for SMOS L-band radiances without adding any extra in situ observations. The calibration of SMOS brightness temperatures against a cold target seems especially important for obtaining reliable results from SMOS applications over ice. In an earlier study, (Ruf, 2000) used the global minimum temperature observed by the TOPEX Ku microwave radiometer to calibrate this instrument and especially to identify its drift in time. A similar attempt could be followed here as well. However, in our case, we also have to consider changes in salinity, since temperature and salinity together will impact the brightness temperature seen at the antenna of an L-band radiometer. Without such a stable calibration site an in situ observing component will be necessary to calibrate the L-band radiances for any high-latitude ice applications.

To find areas with stable, or at least known, cold temperatures, one has to analyze existing prior (external) knowledge available from ocean observations (in situ and satellite) and from numerical models. Usually all of those data sets have uncertainties and their joint analysis therefore seems useful in high latitudes with waters close to the freezing point. On the other hand, one wants to stay out of dynamically active regions, which will be subject to significant variability in temperature and salinity. Such regions can be found close to dynamically active current regions but also close to the ice edge where salinity would also vary significantly due to melting sea ice in spring and freezing of sea water in winter.

Since our study is concerned with calibration sites in high latitudes, we focus our analysis on the European Polar Sea, also called the Greenland-Iceland-Norwegian (GIN) Sea, which encompasses most of the open waters available around the Arctic. The study area is roughly between 60°N and 80°N. Because salinity observations are hardly available over the ocean, we have to rely heavily on the analysis of a model output with respect to salinity variability. But to be credible in this step, we also need to inter-compare the model's temperature fields with the AMSR-E observations and thereby describe the model's quality.

The work summarized below is split into the following two tasks: WP 4.1: Identify regions

for external calibration targets WP 4.2: Statistical properties of calibration targets

11.2 WP 4.1: Identify regions for external calibration targets

The goal of this sub-task is to identify external calibration sites where stable salinity and temperature exist. More specifically, this WP aims to:

1. Define characteristics of temperature and salinity variability in cold waters of the Nordic Seas.
2. Discriminate highly variable regions from regions with low variability in both quantities.
3. Analyze temperature variability from an ocean circulation model and from AMSR-E SST fields.
4. Analyze SSS variations from model output and ship data where available.

As input to this WP we use the output of an ocean circulation model and satellite SST data available from AMSR-E. However, we will start with a description of climatological temperature and salinity conditions in the GIN Sea.

11.2.1 WOA Climatology:

A climatological description of temperature and salinity fields in the GIN Sea can be obtained from the WOA data base (Locarnini et al., 2005; Antonov et al., 2005). The associated climatological mean temperatures, as well as the standard deviation (STD) field as it follows from the twelve monthly temperature fields are shown in the top row of Fig. 11.1 and respective fields of salinity are shown in the lower row of the figure.

From the mean temperature and salinity fields the path of the inflowing North Atlantic water is visible along the Norwegian coast, bringing warm and salty water northward toward the Arctic. The return flow from the Arctic follows as East Greenland current along the Greenland shelf on the western side of the basin, indicated by very cold (close to the freezing point) and fresh water. It is also this latter region where we can find sea ice on a regular basis every winter, while the eastern side of the GIN Sea stays ice-free.

In terms of the STD of temperature, we find a large seasonal cycle in the central basin, indicating the seasonal heating and cooling. High seasonal variability can also be observed along the Norwegian coast in terms of temperature and salinity, which to some extent is due to the outflow of fresh water from the Baltic Sea, but also due to run-off from Norway. However, highest salinity variability can be found in the East Greenland current where the sea ice melting is causing a large seasonal cycle in salinity.

11.2.2 AMSR-E:

Traditionally, satellite SST data are available using the AVHRR technology. However, in high latitudes the presence of clouds ($> 80\%$) makes it impracticable to use those data for an accurate description of SST. Instead we need all-weather microwave measurements, as they are now available from the AMRS-E instrument operated on the EOS Aqua platform, providing microwave SST retrievals since 2002. The microwace sea surface temperature (SST) measurements describe the temperature of the top layer of water, approximately 1 millimeter thick in extension. Available to us are gridded fields obtained through an objective analysis of the swath

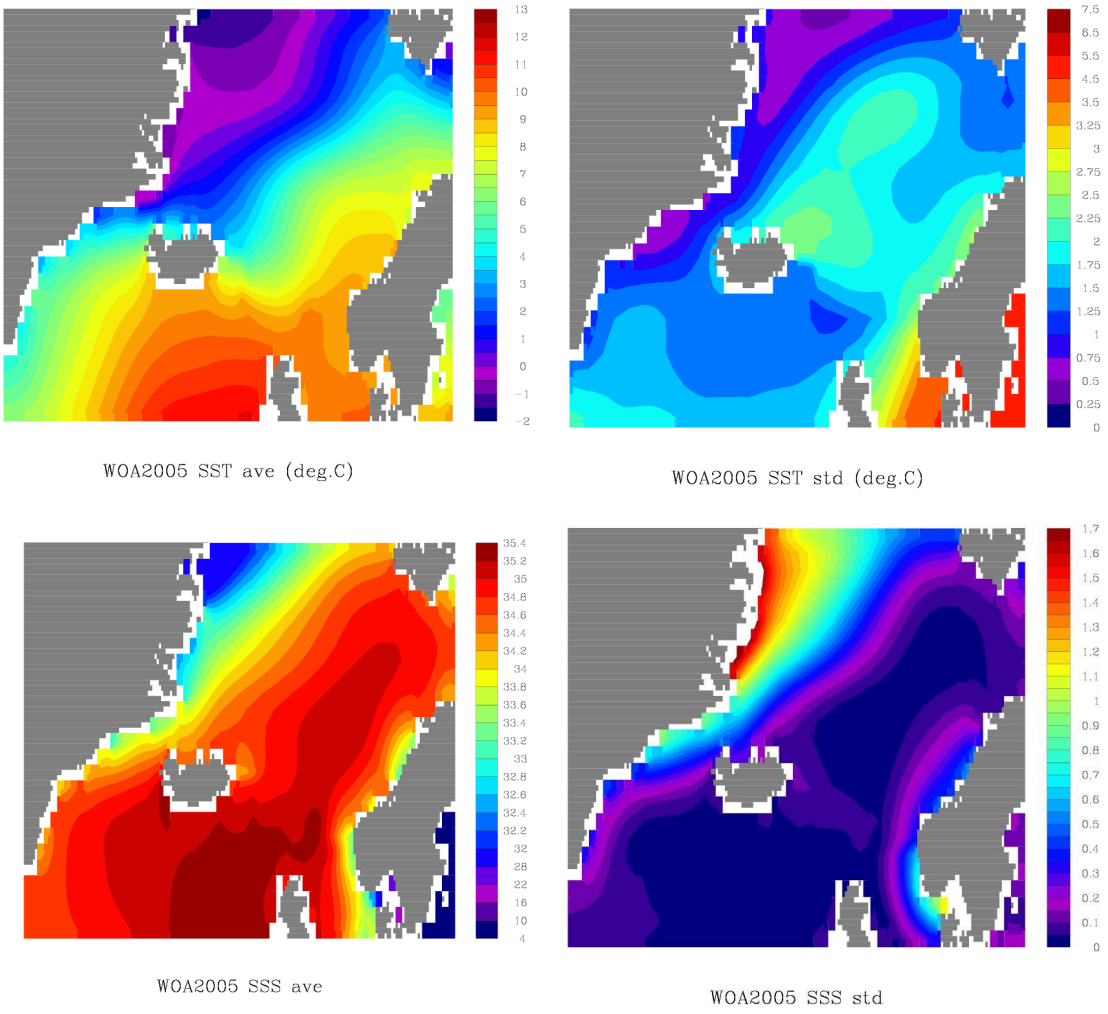

Figure 11.1: WOA (2005) temperature (top) and salinity (bottom) fields in terms of time mean (left) and STD (right) computed from the 12 monthly mean climatologies.

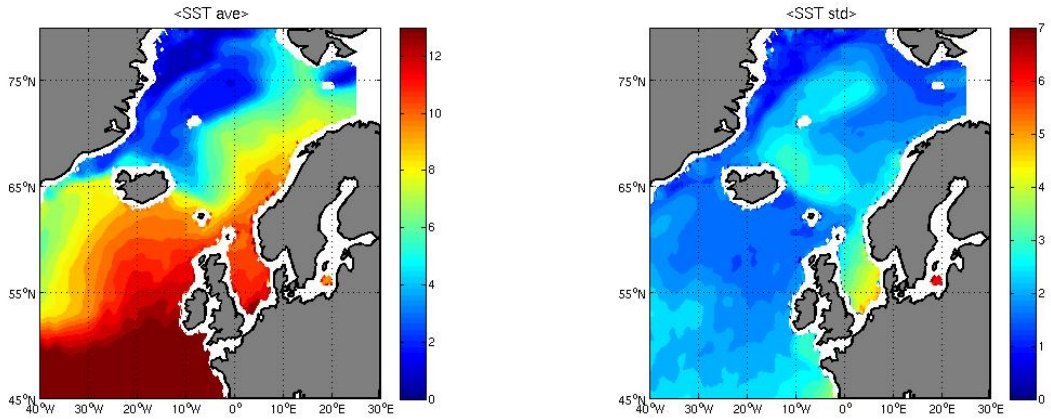

Figure 11.2: Time mean (left) and standard deviation (STD) SST (right), as they result from AMSR-E SST fields during the period 2002 through 2008 over the eastern subpolar North Atlantic and the European Polar Seas.

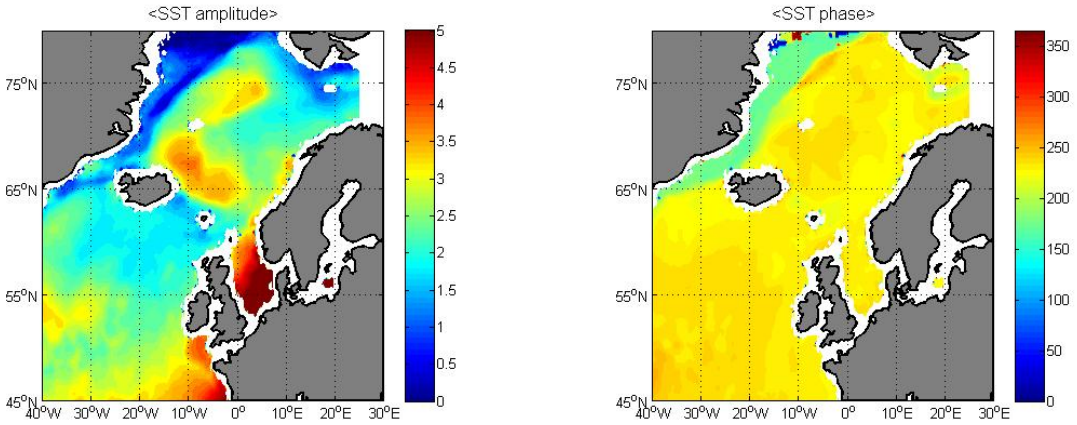

Figure 11.3: Annual harmonic of the AMSR-E SST data inferred during the period 2002 through 2008.

data. The data are available on a 0.25° geographical grid and combine data from ascending and descending paths. The SST data were recovered from

`http://www.remss.com/amsr/amsr_data_description.html`

.

Shown in Fig. 11.2 are the time mean and the standard deviation SST fields as they result from the daily gridded fields over the period 2002 through 2008.

In the time mean SST field (left panel), like in the climatological description, high SST values are aligned along the Norwegian Coast, following the path of the North Atlantic Water flowing from the subpolar North Atlantic into the GIN Sea. On the western side we see water with temperatures close to zero degrees on annual average. However, since no SST fields are available during the ice covered period, the time mean in that region is biased toward summer values. In terms of STD, we find variability around 2-3° over most parts of the basin. Lower variability - which is of specific interest for this study - is located only in areas of winter time ice cover and south of Svalbard. However, we have to keep in mind that due to missing data during ice cover the STD biased low in that region. But even there amplitudes of the STD are around 1° or larger.

As indicated already in the climatological fields, a large fraction of the SST variability is due to the seasonal cycle due to local heat and cooling through net surface heat fluxes. To investigate which fraction of the variability shown in Fig. 11.2b is related to the seasonal changes in SST associated with the annual warming and cooling of the sea surface, we analyzed the seasonal cycle present in the SST data by fitting a sine wave to the measurements. Results are shown in Fig. 11.3 in terms of amplitude and phase of the annual harmonic. The phase is fairly homogeneous (except under the winter sea ice in the western region) indicating a maximum temperature over the entire region to occur between year days 200 and 250. In contrast, the amplitude of the seasonal cycle varies around 1.5°C in regions with modest SST changes to close to 4°C in the western region and north of Island. In the later analysis of WP 4.2 the annual cycle needs to be removed from the data to obtain an important description of the eddy variability present in the GIN Sea.

11.2.3 Simulations of the North Atlantic circulation in the period 1950-present using the MITgcm model

An important element in this study is the analysis of model output from the subpolar North Atlantic and the GIN Sea. Those regions are not well observed, especially with respect to surface salinity. We therefore have to rely heavily on model simulations to quantify the impact of ocean variability on temperature and salinity fields. For our study we used the output of a model run, performed over the period 1950 -2007 as described by Serra and et al. (2009). The run is based on the MITgcm, configured with close to a $1/6^\circ$ resolution over the Atlantic Ocean, including the Arctic. The model has a southern boundary at 30° S, where it is nested into a global GECCO model run which was constrained by most available ocean observations (see Koehl and Stammer (2008) for details). In the vertical, the model has 50 layers. Initial conditions for temperature and salinity are obtained from the Gouretski and Koltermann (2004) Atlas. The forcing of the run is performed using 6 per day NCEP atmospheric state and Bulk formula. In the Arctic, the model has a dynamically active sea ice model.

Before using a model simulation for a quantitative study it is important to test its results. We show in Fig. 11.4a a snapshot field of SST as it results from Jan. 16, 1951. Also shown is the sea ice extent in red. Especially the latter shows a significant reality as compared to observations and the model is capable to essentially simulate the observed variations in sea ice extent, including the large retreat during 2007. Shown in the right panel of the figure is the speed of the near-surface current fields. Vigorous ocean currents are visible in the low latitudes and especially along the entire western boundary. However, enhanced currents are likewise visible in the GIN Sea. As we will see later, those currents are responsible for high eddy variability of salinity and temperature in those regions. As can be seen from the figure: eddy variability is ubiquitous over the world ocean and low eddy activity is limited in the model run for regions covered by sea ice.

To extract information about SST and sea surface salinity (SSS) variations from the model output, several steps are necessary which are summarized in Fig. 11.5. Those steps involve the de-trending of the model simulation to remove any numerical drift from the output. From the de-trended fields we computed time-mean and STD fields over two periods: (1950 - 2007) and (2002 - 2007). We also computed the annual harmonic from SST and SSS over both periods as well as the STD after removing the seasonal cycle from the model fields.

Shown in Fig. 11.6 are the time mean and STD SST and SSS fields as they result from the period (2002 - 2007) which can be directly compared with the AMSR-E results. Results are not unlike those obtained from the longer period (see also below).

In terms of time mean the SST field largely agrees with results obtained from AMSR-E. However, a few striking differences are obvious. Those include the presence of small-scale structures in the model fields, not seen by the microwave SST sensor, especially south of Iceland, but also along the Norwegian Current, where we see standing waves in the current structure and the split of the current into one branch flowing toward Fram Straight and one branch flowing into the Barent Sea. On the western side of the basin, temperatures are substantially lower in the model, because those fields are true time mean values and include winter estimates as well. For the time mean salinity, a similar spatial structure arises, indicating very fresh water on the Greenland shelf.

In terms of the STD(SST) field, we also see more spatial structures than can be seen from the fairly smooth AMSR-E SST fields, although the large scale structures do agree well between the model simulation and the satellite observations. Also available from the model is the STD field for SSS which shows substantial SSS variability in the western part of the basin, enhanced

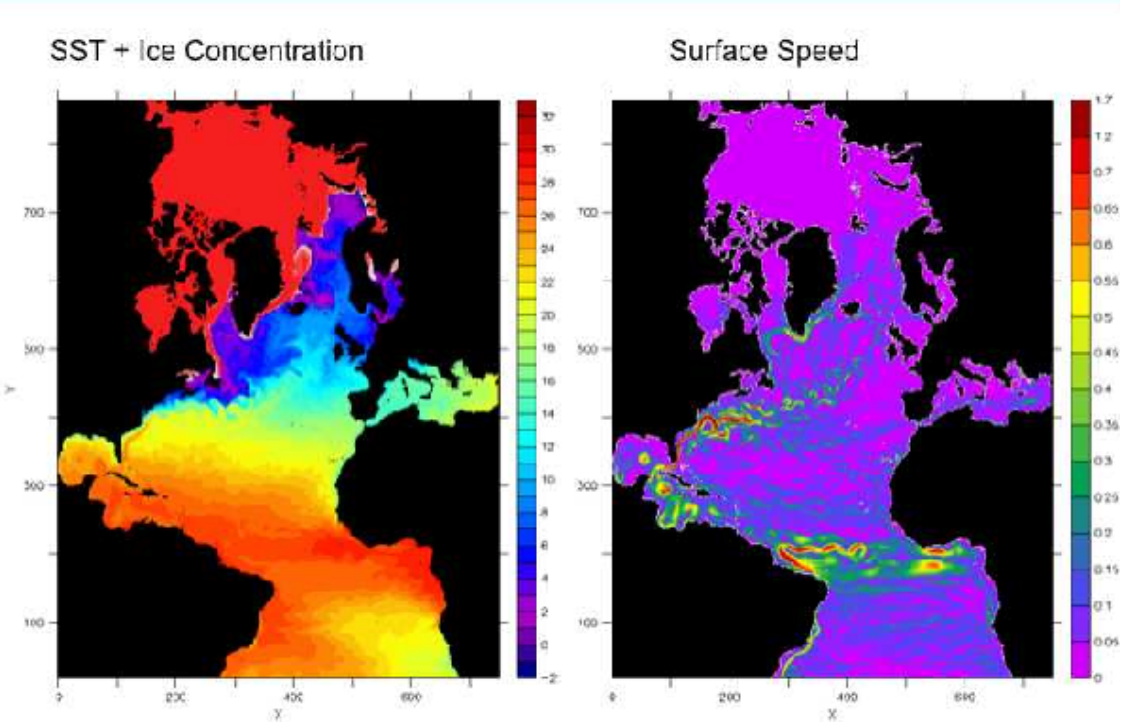

Figure 11.4: (left) Snapshot SST field plus sea ice cover simulated by a MITgcm forward run for day Jan. 16, 1951. (right) Speed of the near-surface currents of the same model simulation at the same day.

SSS variability along the Norwegian coast, and hardly any SSS variability (less than 0.1 psu) in some regions of the central basin. On top, we do see some agreements in the spatial pattern of the SSS variability with the STD(SST) map, indicating already a link between both fields through ocean dynamics.

To retrieve the purely random eddy variability component that, in contrast to the seasonal cycle, is unpredictable, we have to remove the annual harmonic SST and SSS fields from the model output. As can be seen from Fig. 11.7, the spatial pattern of the amplitude of the annual harmonic for SST are fairly similar to those seen in Fig. 11.3 before. We also see now that in the model the phase of the annual SST harmonic is homogeneous over the entire domain indicating maximum SST values to occur in August. For salinity, however, the picture is much more complex and consistent with the general circulation pattern in the basin, suggesting that salinity changes are primarily driven by changes in the advection terms plus ice melting.

11.3 WP 4.2: Statistical properties of calibration targets

The purpose of this sub-task is to synthesize the information obtained from task WP 4.1 and condense it into a recommendation about a potential external calibration site for SMOS L-band radiances. The aims of the task are specifically:

- From ocean circulation model output and satellite data identify regions in the Nordic Seas where a stable, cold surface temperature can be found.
- Identify regions with low and high SSS variability

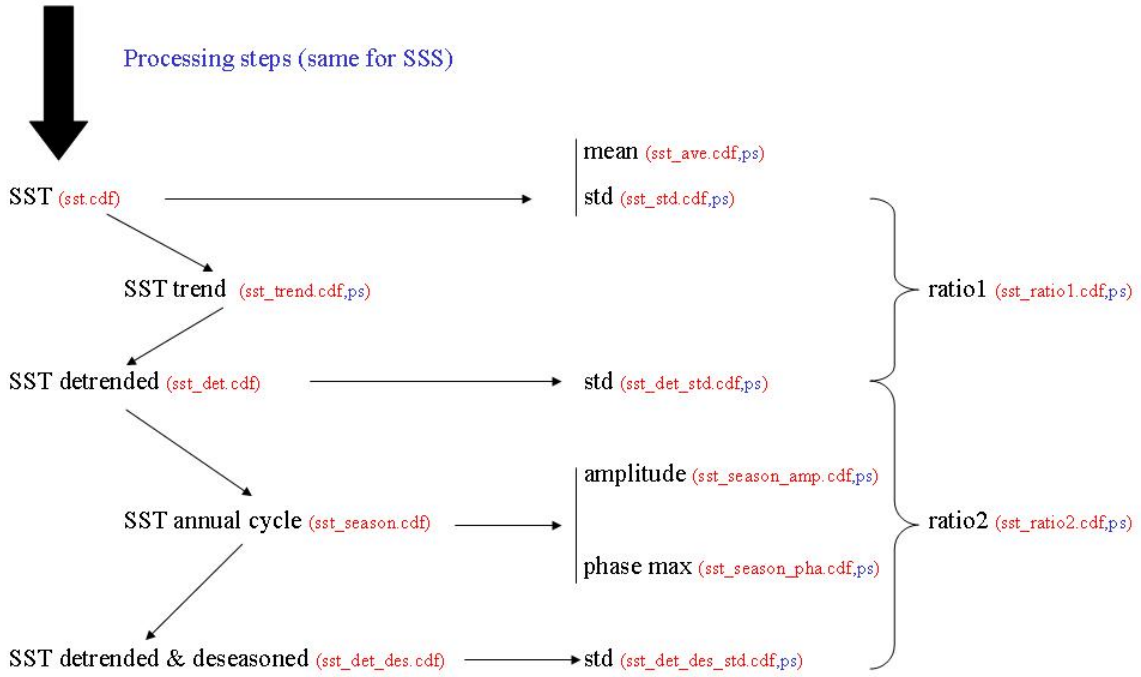

Figure 11.5: Schematic of processing steps for model output.

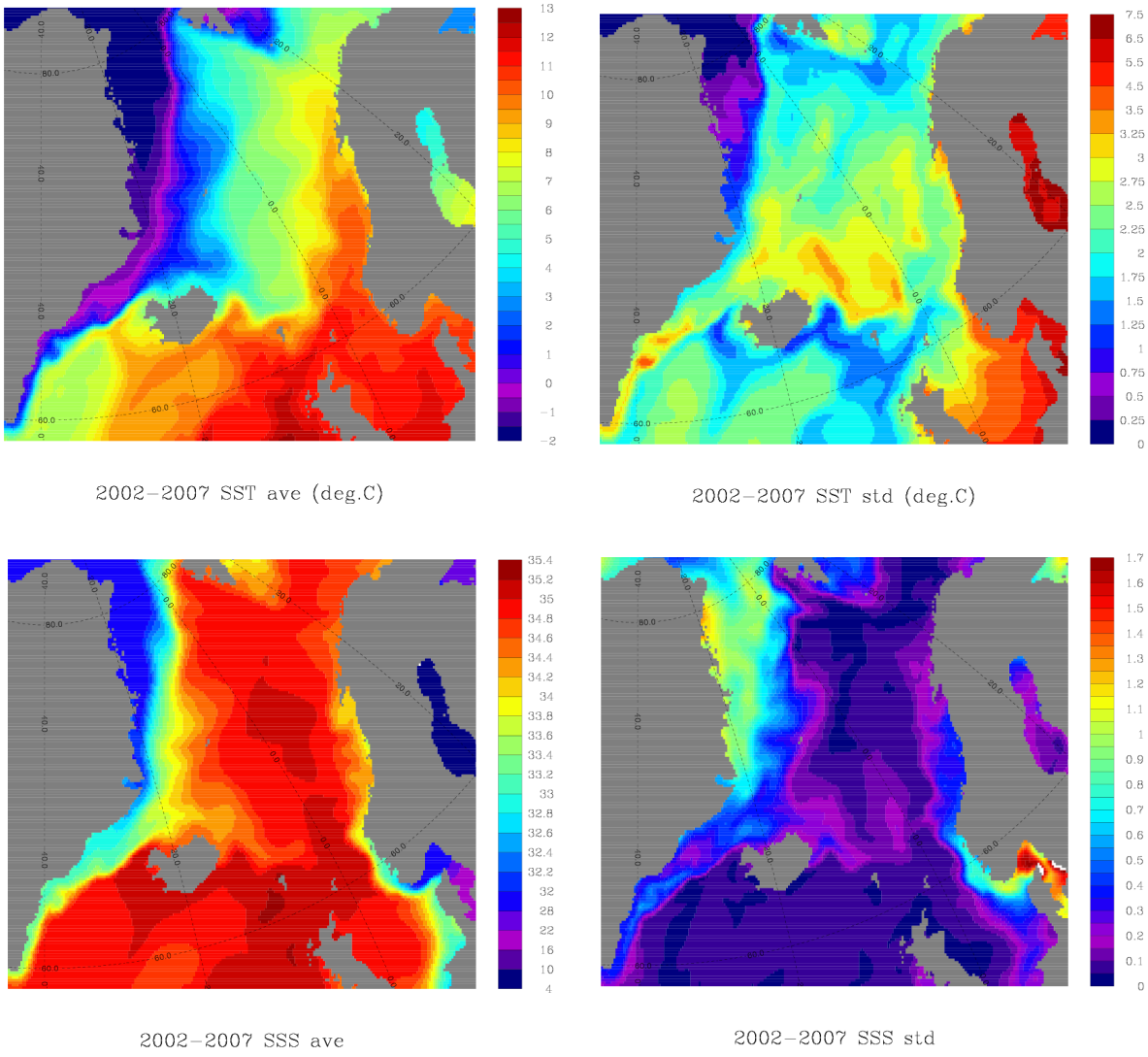

Figure 11.6: (top panel) Time mean average SST (left) and STD(SST) (right) computed from the model simulations for the period 2002-2007. (lower panels) Time mean average SSS (left) and STD(SSS) (right) computed from the model simulations for the period 2002-2007.

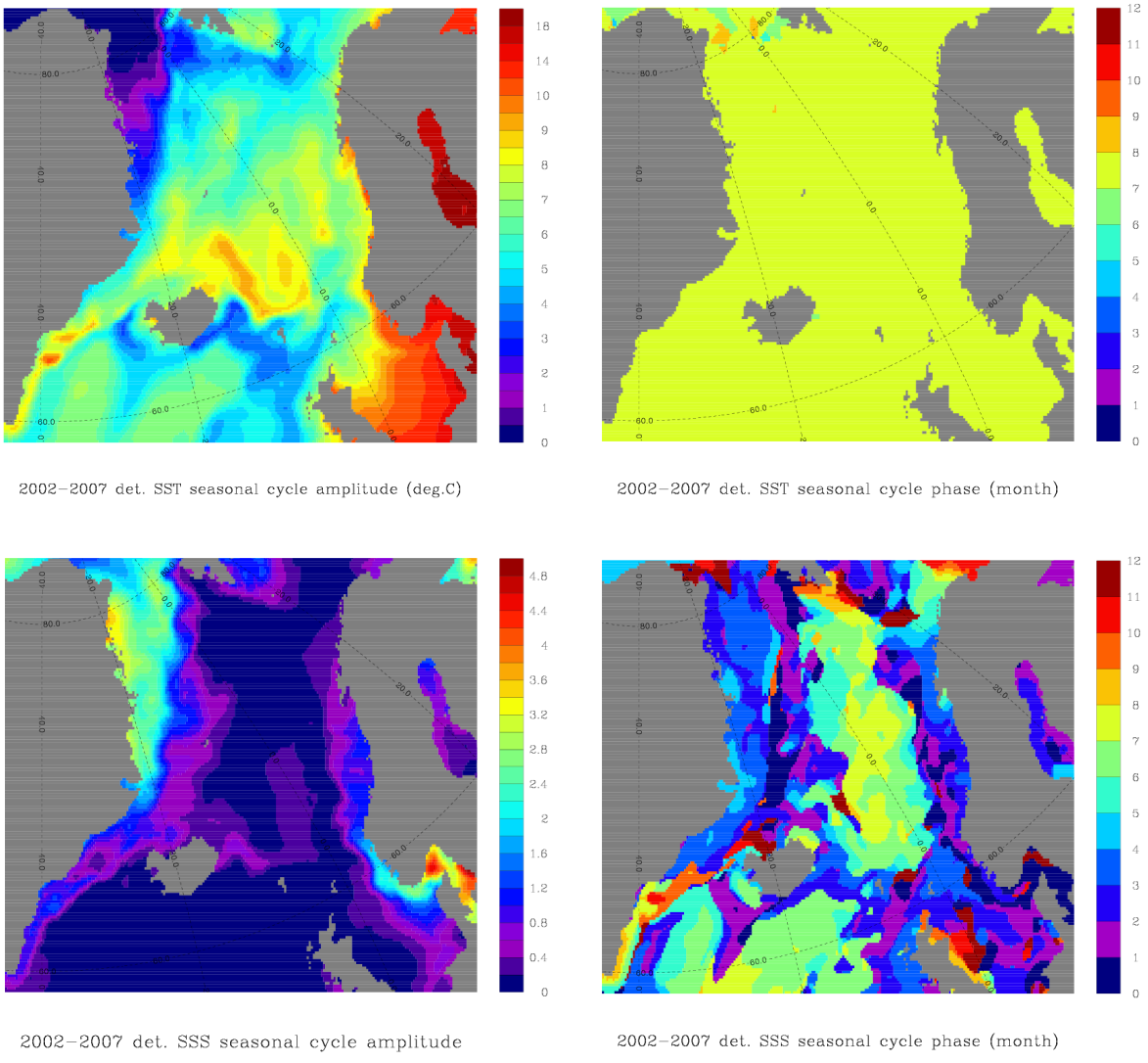

Figure 11.7: Amplitude (left column) and phase (right column) of the annual harmonic computed for (top) SST and (bottom) SSS from the model results over the period 2002-2007.

- Evaluate the statistical properties of the identified external calibration targets from model data.

To start with, we show in Fig. 11.8 the time-mean SST fields as they follow from the three data sets involved in this analysis: (a) AMSR-E, (b) the WOA climatology, and (c) MITgcm model. We can see from the figure a visual agreement between all three in the eastern basin of the GIN Sea. However, substantial differences occur in the western side, where the satellite SST fields don't see the ocean for a significant fraction of the year due to ice cover in that region. As a consequence, satellite SST fields are biased warm here, while model simulation lead to SST values close (but above) to the freezing point. Differences are also obvious between all three results regarding the spatial scales resolved. As an example, the Norwegian Current shows standing meanders in the model simulation which in the AMSR-E fields are smoothed out due to the low resolution. Other differences include the fact that in the model most of the North Atlantic water seems to enter the Arctic, where AMSR-E fields suggest a substantial recirculation into the east Greenland Current. We conclude, that the AMSR-E data are not sufficient to resolve eddy variability in the GIN Sea.

An inter-comparison of STD(SST) fields between satellite results and the model simulation is provided in Fig. 11.9. Again, the eastern portion of the basin seems to agree fairly well between the model and the satellite estimates in terms of amplitudes. However, the western side shows again substantial differences, partly due to differences in the sampling of the ocean by the satellite, partly due to errors in the model. In terms of the spatial pattern, however, we do find substantial differences between satellite observations and model simulations, again underlining the fact that the model simulation does show deficiencies in simulating all details that are being observed.

Nevertheless, the model is very valuable in providing a suggestion as to where salinity is varying in the GIN sea, how much and to what extent it co-varies with SST. The figure clearly illustrates the differences in low variability in SSS and SST: the eastern basin shows only very little SSS variability (< 0.1 psu) where SST shows maximum changes. Along the east Greenland shelf the situation is just the opposite leaving us with no region where both SST and SSS show low variability.

But because a substantial fraction of the variability shown in Fig. 11.9 could reside on the seasonal time scale, we show in Fig. 11.10 the variability in SST and SSS as it results from the satellite SST fields and the model SST and SSS fields, after the seasonal cycle was removed. Now a substantially different pattern in variability emerges with regions of high eddy variability being located where we know from the model and altimetry that the ocean currents in the area show large eddy activity (compare also Fig. 11.4). In terms of AMSR-E results, this is especially the Norwegian Current, north of the Greenland-Iceland-Scotland ridge and along the East Greenland Current. Likewise high SST variability is located south of the ridge where substantial eddy variability was observed in the overflow water. A substantial difference between satellite and model results is that the SST variability observed off Norway is not present in the model simulations. In that region SSS variability is also low and we have to suspect that the model under-represents reality here. Taking the model at face value, we see that the only region where the model's SST and SSS variability is low is situated south of Svalbard. On the other hand, a comparison with Fig. 11.8 shows that in this region cold temperature conditions are not being met. We likewise infer from Fig. 11.10, that the variability of SST and SSS, although low, is not zero in this region.

To demonstrate how large the remaining SST variability present even in the lowest-variability region, we show in Fig. 11.11 two timeseries of SST from one geographic location situated close to 75°N, 10°E.

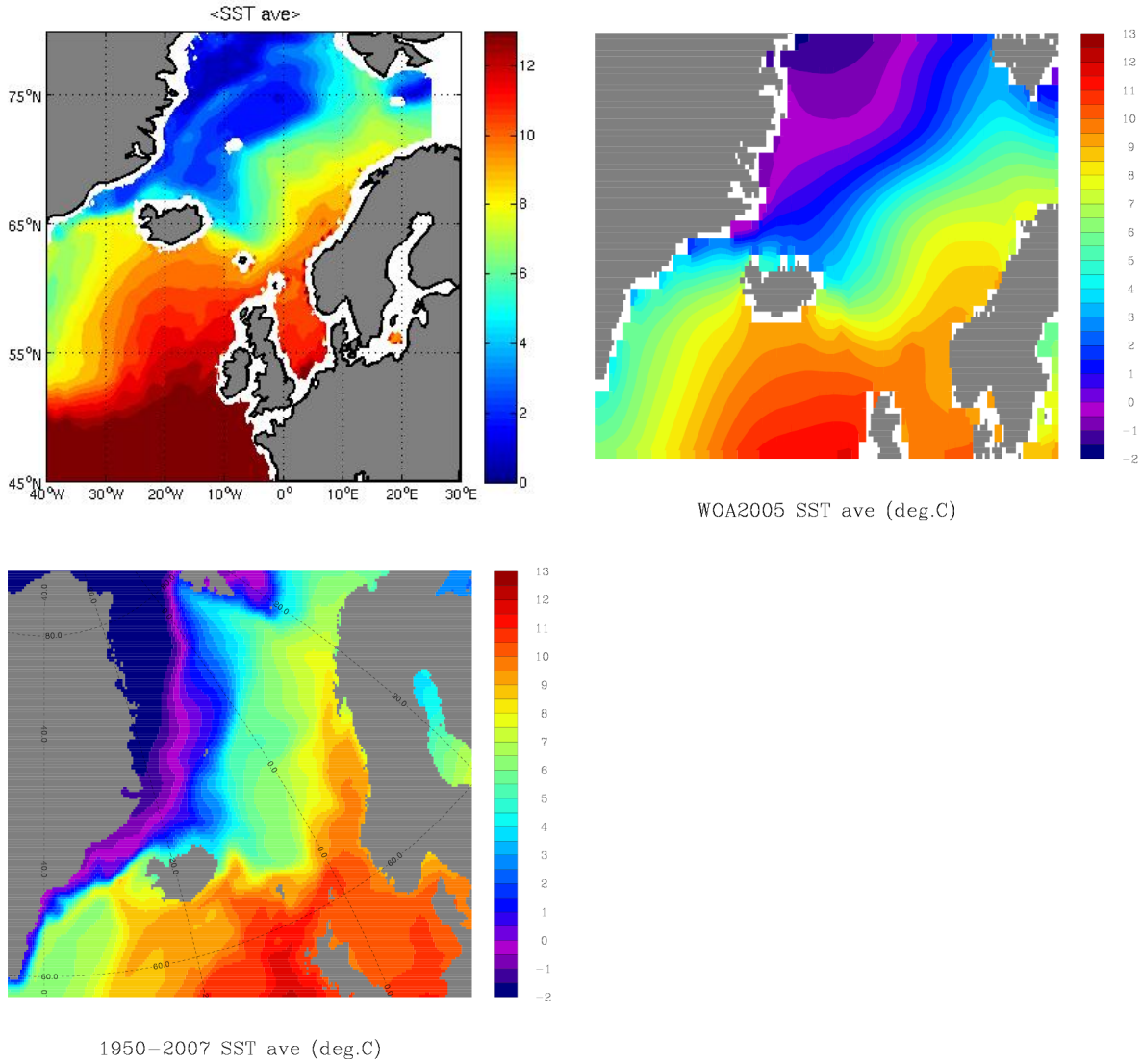

Figure 11.8: Inter-comparison of time-mean SST fields as they follow from (a) AMSR-E, (b) the WOA climatology, and (c) GIN Sea model. Note different color bars.

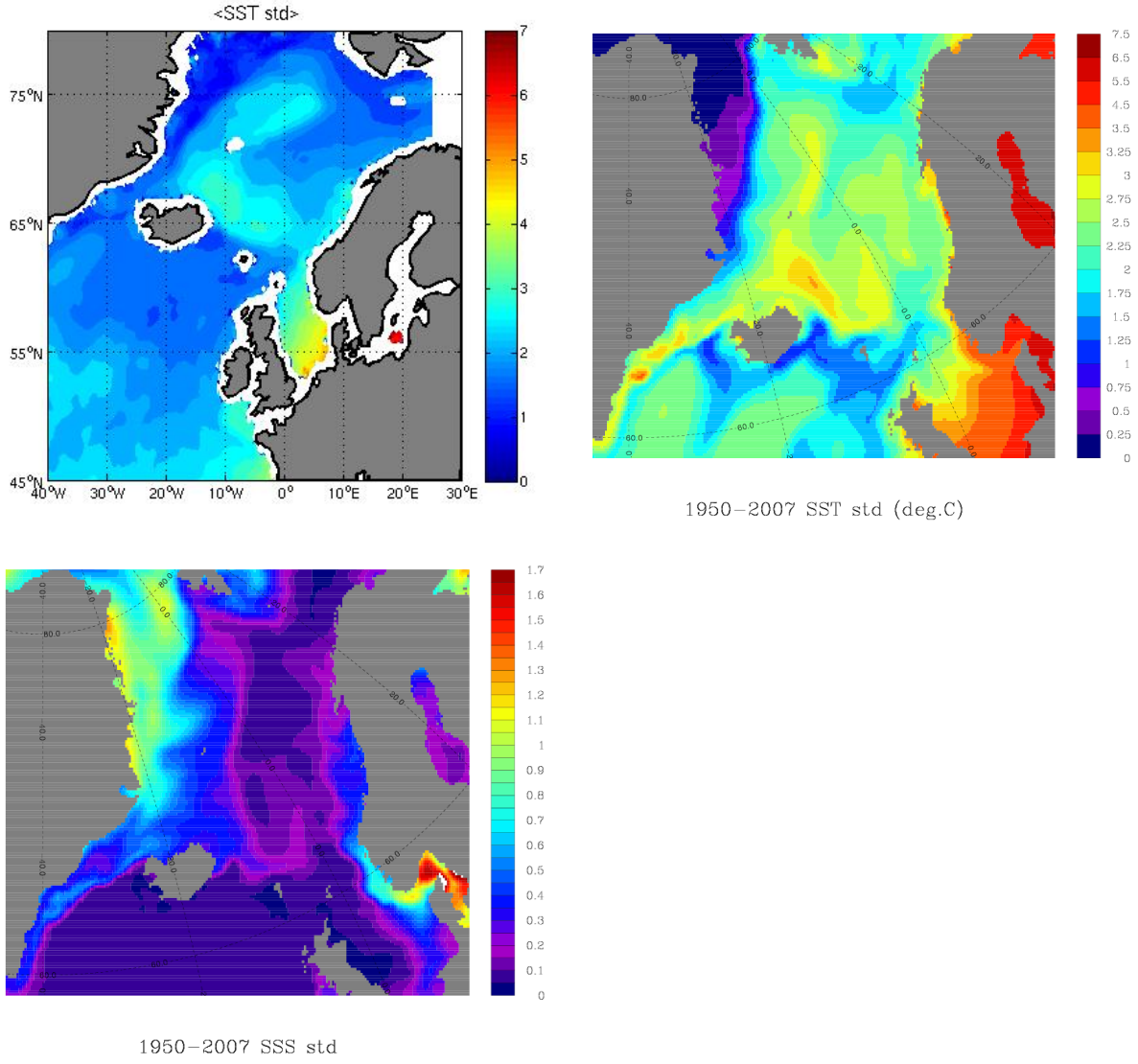

Figure 11.9: (top) STD of AMSR-E and model SST fields. (bottom) STD of model SSS field.

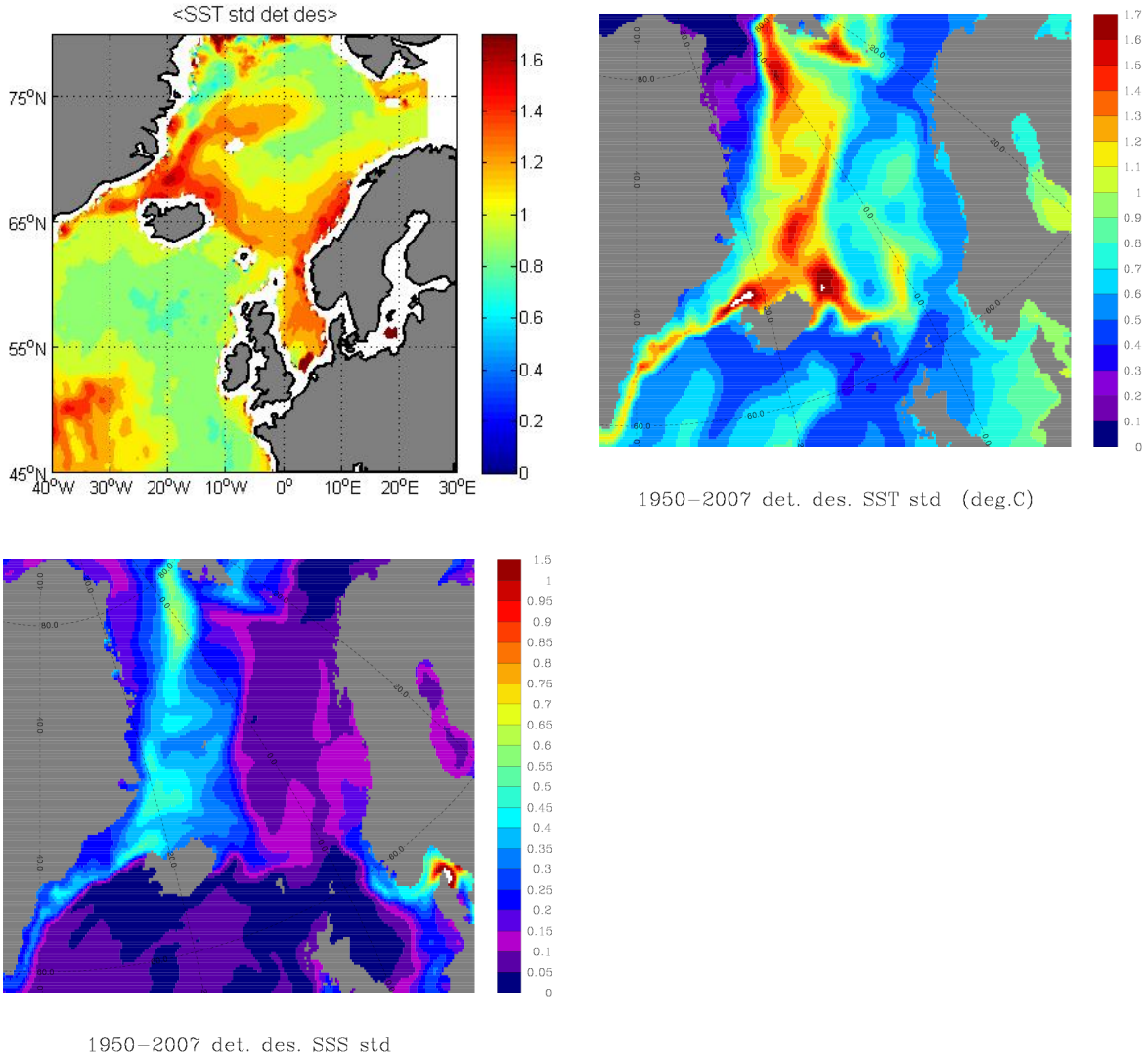

Figure 11.10: (a) STD of SST observations after removing the seasonal cycle and a trend in AMSR-E SST fields. (b) Same but as inferred from model results covering the period 1950-2007. (c) STD of SSS after removal of a trend and the seasonal cycle and analyzed other period 1950-2007 seasonal cycle.

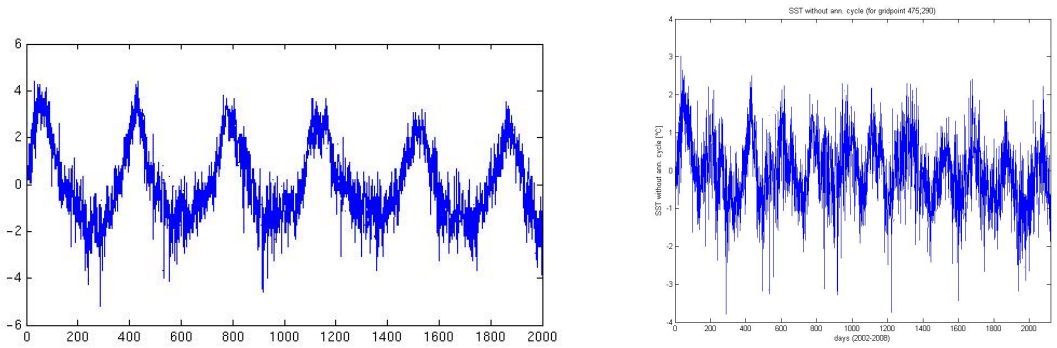

Figure 11.11: Time series of SST at the geographic location 75°N, 10° E left with the annual harmonic included and right without.

While in the left panel the seasonal cycle is still included, the right panel shows the same timeseries after an annual harmonic was removed. High-frequency variability of +/- 2° C is visible rendering the SST fields even in this region not stable enough to use them as external calibration sites.

11.4 Conclusion

From the results shown above we have to draw the following conclusions with respect to the question posed in the beginning:

Does a region exist in high latitudes where stable temperature and salinity values can be identified which can be used as an external calibration source for SMOS L-band radiances?

The conclusions can be summarized as follows:

- There is no location in the GIN Sea where SST is stable.
- Regions with low variability do not agree with regions of low SSS variability in a model simulation.
- Best way to calibrate SMOS L-band radiances seems to use the global SSS cal/val program (MW SST fields, drifter, ARGO floats plus estimates of wind and humidity).

Chapter 12

Conclusions and Recommendations

12.1 Conclusions

The potential of the spaceborne, polar orbiting L band radiometer SMOS to retrieve sea ice parameters has been explored by two means, a field campaign and with emissivity models.

The field campaign took place in March 2007 in the North Baltic Sea as an add-on to the POL-ICE campaign. The thickness was measured with the airborne electromagnetic probe EM-Bird of AWI, carried by a helicopter. The L band microwave signal was observed in coordinated flights of the EMIRAD radiometer of DTU, carried aboard the Sky Van airplane of HUT.

Two types of emissivity models have been used: first, several versions of so-called three layer models, describing the sea ice by just one layer, plus one layer for the atmosphere and one for the ocean. The three-layer models are specific for L band, with just one constant sea ice permittivity. Second, multi-layer and multi-frequency models have been used. By physical modelling of the interaction mechanisms, they allow to cover the full microwave range from L band to 100 GHz, namely MEMLS and the Strong Fluctuation Theory. As the wavelength is much larger than the size of the scatterers (air and brine inclusions), scattering can be neglected at L-band. This simplifies a lot the L-band only models.

The three-layer models consist of the layers air, sea ice and water, where within each layer all physical parameters are constant. This leads to a small number of parameters, namely incidence angle, thickness, sea ice concentration, temperature and salinity, and, via some parameterization, surface roughness.

With the first of the three-layer models, the brightness temperatures of a quality-selected subset of the campaign data can be prediced from the ice thickness with a standard deviation of about 7 K. Moreover, the model shows a reasonable sensitivity to thickness up to about 50 cm (Figure 4.7), and a one-channel retrieval, allowing for one separate retrieval based on each of the vertically (TBv) and horizontally (TBh) polarized brightness temperatures, has been applied to a selected part of one of the POL-ICE flights with promising results (Figure 4.9).

The second three-layer model starts from the well-known fact that the salinity and thus the permittivity of thin Arctic sea ice vary with thickness. Real and imaginary part of the permittivity are constructed based on pairs of TBv and TBh observations of the POL-ICE campaign. Then, the model can be used to predict brightness temperatures from the permittivity. Two versions of this model have been used. In the first version, both real and imaginary part of the permittivity as function of sea ice thickness, are determined by empirical fits to the campaign data. In the second model, only the imaginary part is fit to the campaign values, and the real part is then determined using the Mixture Model (Section 5.5), the empirical equations of Vant

(1978b) and Hoekstra and Capallino (1971), allowing us to adjust for the higher salinity of the global ocean.

At temperatures near melting, the influence of ice concentration and ice thickness may be distinguished (Fig. 10.8), but at the same time retrieval of ice thickness becomes more uncertain because of the strongly increasing imaginary part of the permittivity (Figs. 10.14 and 10.15). At low temperatures, these curves in Fig. 10.8 suggest a sensitivity of the brightness temperatures to thickness up to 50 cm. This lower sensitivity to thickness at both higher salinity and higher temperatures is in agreement with the intuitive expectation because in both cases the salt content in the ice increases, which reduces the penetration dept.

For young and thin sea ice, the condition of temperatures far below freezing, which is favorable for the detection of ice thickness, can be fulfilled at a reasonable percentage of the observed cases, e.g. during cold air outbreaks.

The second type of models are multi-layer and multi-frequency, and are much more sophisticated. The Strong Fluctuation Theory (SFT) by Strogryn (1987) in the implementation of Grenfell et al. (1992) describes the emissivity of an isothermal layer in the microwave region between 1 and 100 GHz. In view of the model, the sea ice consists of isothermal layers of snow and ice. For each of them, ten different parameters describe its structure and constituents. An improved version of the SFT, called Combined SFT (CSFT) avoids oscillations e.g. with ice thickness in the outgoing emission, by incoherent calculations.

The second multi-layer and multi-frequency model used is the sea ice version of the Microwave Emission Model of Layered Snowpacks (MEMLS, Wiesmann and Mätzler 1999), a multiple-scattering model allowing many layers in order to simulate snow cover emission including most of the known physical effects. Both MEMLS and the CSFT include scattering. Output of a thermodynamic sea ice model, driven with ECMWF ERA 40 atmospheric data, served as input data for MEMLS. The sea ice model data at 85°N, 180°East over a complete winter season were used to simulate the L band emission.

In a comparison study, these sea ice model data have also been used as input for the CSFT and mixture model. Most of the models showed for first-year ice consistently a sensitivity of the emitted L-band radiation to thickness up to about 0.5 m. The only exceptions are the mixture model where already at about 0.2 m saturation is reached, and the CSFT, where the sensitivity reaches up to over 1 m. The sensitivity limit of about 0.5 m is also found for the campaign data when using the three layer model with constant permittivity.

Effects of inhomogeneous ice parameters on the forward modelling and the retrieval have not yet been addressed. However, we have to expect that the ice conditions vary within the large footprint of about 50 km of the SMOS sensor. All model parameters, retrieved and input, need to be considered as effective parameters, averaged with some weight over the sensor's footprint. These parameters are sea ice concentration, thickness, temperature, salinity, roughness and other microphysical conditions.

On the other hand, each surface region will be observed several times during each overpass under different incidence angles. A consequence is that the retrieval algorithms have to be developed for all angles. This has been done (Fig. 10.3). These multiple observations at different incidence angles might be used to determine additional quantities if their variation with incidence angle is strong enough. However, model calculations show that the observed brightness temperatures vary only little in the range of incidence angles of SMOS. As a consequence, it is suggested to use multiple observations of a given scene to reduce the uncertainty in the retrieval by fitting a best retrieval to the observations at the various incidence angles.

The campaign data show that the contrast between open water is high enough to discriminate both surface types and to determine the sea ice concentration, and the empirical thickness

-salinity relations observed in the Arctic have been confirmed, however with much scatter, for the Baltic where the salinity is much lower.

An additional explanation for the higher scatter in the Baltic might be found in some imperfections in the campaign data, both technical and physical, limiting their use for the intended purpose. The radiometer was not working stable during the flights, so that only few subperiods of the flights of stable radiometer functioning could be used for data analysis. Moreover, the temperature during the campaign was rather constant and near melting so that the sea ice emission could only be observed for a narrow range of temperatures. Finally, the salinity in the Northern part of the Baltic is much lower than that of the global ocean, influencing the sea ice properties and emission. In order to draw conclusions from the campaign results about the SMOS retrievals over Arctic sea ice, they must be transferred from Baltic to Arctic conditions using emissivity models, which is not obvious.

For emission modeling and model-based retrieval, the sea ice permittivity is the most important quantity. Therefore it is interesting to compare its values found by and used in the different models. Using the thermodynamic sea ice model data in conjunction with MEMLS,the real part varies between 4.5 and 5.5, and the imaginary part between 0.1 and 0.5 (Fig. 5.12). For both the the CSFT and the mixture model, the corresponding values are 3.5 to 7 and 0.002 to 1, a much larger range. The values determined from the campaign data range from 2 to 8 for the real part and from 0.03 to 0.1 for the the imaginary part (Fig. 9.7). Thus, the values for the Arctic and the Baltic are less different than expected, probably due to the high temperatures during the POL-ICE campaign.

Two studies have been devoted to the higher Stokes components. First, a deviation of the sensor attitude from horizontal orientation will cause a crosstalk from the first two Stokes components to the third one, U. This influence has been quantified and compensated in the airborne data, demonstrating that about 60% of the observed U signal is cause be the aircraft attitude, and only 40% by geophysical influences. Second, a model of horizontally anisotrope permittivities has shown that it can generate nonzero U and V Stokes components.

Finally, an investigation for a region with stable temperature and salinity values of the high latitudes has been conducted where the surface temperature of the ocean could be used as an external calibration source for SMOS L-band radiances without adding any extra in situ observations. It has turned out that there is no location in the GIN Sea where SST is stable, and regions with low variability do not agree with regions of low SSS variability in a model simulation.

As overall conclusion we here repeat from Chapter 4 that t

The promising results of the project are that SMOS will have some potential for ice thickness and the lower boundary of ice volume retrieval. The sensitivity for Arctic ice thickness retrieval of up to half a meter is complementary to the capabilities of altimeter instruments. The thin ice plays an important role for heat exchange between the ocean and the atmosphere. Therefore, a SMOS based ice thickness product will be certainly useful for sea ice applications in climate research, meteorology, and perhaps even for operational services for the assistance of ship navigation in polar waters.

12.2 Recommendations

The sea ice emissivity models suggest a clear sensitivity of SMOS data to sea ice thickness. As on the other hand, during the POL-ICE campaign there have been several shortcomings, the assessment of the potential to retrieve ice thickness from SMOS data needs more effort. This

requires a ground truth data set with known ice thicknesses at a horizontal extent comparable to the SMOS sensor footprint. The best way to obtain such data would be a dedicated field campaign. Ideally it would take place in a region of fast growing thin ice, at a horizontal scale comparable to the SMOS footprint. Candidate regions and seasons are

1. Sea of Ohotsk, January,
2. Ross Sea, April,
3. North of Siberia, October/November, and
4. Hudson Bay, December.

Note that these are just rough indications. The exact region and period would have to be determined for the individual year. Moreover, observations take at a broader range of tempertures will be favorable. But even without a dedicated campaign, the situation is not hopeless. A more economic way would be to use data of regions where the large-scale formation of sea ice is known a priori, e.g. from meteorological conditions (see list above) and recurring polynyas.

Without doubt additional information, especially about the ice temperature, will be helpful in the retrieval process. Therefore it is suggested to use the SMOS data in conjunction with other passive microwave sensors, e.g. AMSR-E, and with atmospheric circulation model data such as ECMWF. As sea ice salinity and roughness are difficult to determine from the SMOS observations alone, other informations like climatology and ocean model (deformation) can also be helpful to restrict the variability range of retrieved quantities. It has become obvious that the sea ice emissivity models need more development in order to meet the best tradeoff between complexity required to reflect the important physical feature, and at the same time to be sufficiently simple to be handled and understood.

During the commissioning phase of SMOS, the information content of the third and fourth Stokes components over sea ice should be investigated. The best way for an external calibration of SMOS L-band radiances seems to use data from the global SSS cal/val program, such as MW SST fields, drifter, ARGO floats plus estimates of wind and humidity.

Bibliography

Andersen, S., Tonboe, R., Kaleschke, L., Heygster, G., and Pedersen, L. T. (2007). Intercomparison of passive microwave sea ice concentration retrievals over the high-concentration Arctic sea ice. *Journal of Geophysical Research*, 112(C08004).

Andersen, S., Tonboe, R., Kern, S., and Schyberg, H. (2006). Improved retrieval of sea ice total concentration from spaceborne passive microwave observations using numerical weather prediction model fields: An intercomparison of nine algorithms. *Remote Sensing of Environment*, 104:374–392.

Antonov, J. I., Locarnini, R. A., Boyer, T. P., Mishonov, A. V., and Garcia, H. E. (2005). Salinity. In *World Ocean Atlas 2005*, volume 2. U.S. Government Printing Office, Washington, D.C.

Barber, D. G., Fung, A. K., Grenfell, T. C., Nghiem, S. V., Onstott, R. G., Lytle, V. I., Perovich, D. K., and Gow, A. J. (1998). The role of snow on microwave emission and sacttering over first-year sea ice. *IEEE Transactions on Geoscience and Remote Sensing*, 36(5):1750–1763.

Belchansky, G. I., Douglas, D. C., Alpatsky, I. V., and Platonov, N. G. (2004). Spatial and temporal multiyear sea ice distributions in the arctic: A neural network analysis of SSM/I data, 1988-2001. *Journal of Geophysical Research*, 109(C10017).

Belchansky, G. I., Douglas, D. C., Eremeev, V. A., and Patonov, N. G. (2005). Variations in the Arctic's multiyear sea ice cover: A neural network analysis of SMMR-SSM/I data 1979-2004. *Geophysical Research Letters*, 32.

Brun, E., Martin, E., Simon, V., Gendre, C., and Coleou, C. (1989). An energy and mass model of snow cover suitable for operational avalanche forecasting. *Journal of Glaciology*, 35(121):333–342.

Burke, W. J., Schmugge, T., and Paris, J. F. (1979). Comparisons of 2.8- and 21-cm Microwave Radiometer Observations over Soils with Emission Model Calculations. *Journal of Geophysical Research*, 84(C1):287–294.

Cavalieri, D. J. (1994). A microwave technique for mapping thin sea ice. *Journal of Geophysical Research*, 99(C6):12561–12572.

Comiso, J. C., Cavalieri, D. J., and Markus, T. (2003). Sea Ice Concentration, Ice Temperature, and Snow Depth Using AMSR-E Data. *IEEE Transactions on Geoscience and Remote Sensing*, 41(2):243–252.

Comiso, J. C., Cavalieri, D. J., Parkinson, C. L., and Gloersen, P. (1997). Passive microwave algorithms for sea ice concentration: A comparison of two techniques. *Remote Sensing of the Environment*, 60:357–384.

Comiso, J. C. and Parkinson, C. L. (2008). Arctic sea ice parameters from AMSR-E data using two techniques and comparisons with sea ice from SSM/I. *Journal of Geophysical Research*, 113(C02S05).

Cox, G. and Weeks, W. (1974). Salinity variations in sea ice. *JG*, 13(67):109–120.

Cox, G. and Weeks, W. (1983). Equations for determining the gas and brine volumes in sea-ice samples. *Journal of Glaciology*, 29(102):306–316.

Cox, G. and Weeks, W. (1988). Numerical simulations of the profile properties of undeformed first-year sea ice during the growth season. *Journal of Geophysical Research*, 93(C10):12499–12460.

Davis, C., Emde, C., and Harwood, R. (2005). A 3d polarized reversed monte carlo radiative transfer model for mm and sub-mm passive remote sensing in cloudy atmospheres. *IEEE Transactions on Geoscience and Remote Sensing*, 43(6):1096–1101.

Dierking, W. and Busche, T. (2006). Sea ice monitoring by L-band SAR: An Assessment Based on Literature and Comparisons of JERS-1 and ERS-1 imagery. *IEEE Transactions on Geoscience and Remote Sensing*, 44(2):957–970.

Dinnat, E. P. and Boutin, J. (2003). Issues concerning the sea emissvity modeling at l band for retrieving surface salinity. *RS*, 38(4):8060, doi:10.1029/2002RS002637.

Drucker, R., Martin, S., and Moritz, R. (2003). Observations of ice thickness and frazil ice in the St. Lawrence Island polynya from satellite imagery, upward looking sonar, and salinity/temperature moorings. *Journal of Geophysical Research*, 108(C5).

Eagleman, J. R. and Lin, W. C. (1976). Remote Sensing of Soil Moisture by a 21-cm Passive Radiometer. *Journal of Geophysical Research*, 81(21):3660–3666.

Ehn, J. K., Hwang, B. J., Galley, R., and Barber, D. G. (2007). Investigations of newly formed sea ice in the Cape Bathurst polynya: 1. Structural, physical and optical properties. *Journal of Geophysical Research*, 112(C05002).

Eicken, H. (1992). Salinity Profiles of Antarctic Sea ice: Field Data and Model Results. *Journal of Geophysical Research*, 97(C10):15545–15557.

Emde, C. (2005). *A Polarized Discrete Ordinate Scattering Model for Radiative Transfer Simulations in Spherical Atmospheres with Thermal Source*. PhD thesis, University of Bremen.

Eppler, D. T., Farmer, L. D., Lohanick, A. W., Anderson, M. R., Cavalieri, D. J., Comiso, J., Gloersen, P., Garrity, C., Grenfell, T. C., Hallikainen, M., Maslanik, J. A., Maetzler, C., Melloh, R. A., Rubinstein, I., and Swift, C. T. (1992). Passive Microwave Signatures of Sea Ice. In *Microwave Remote Sensing of Sea Ice*, number 68 in Geophysical Monographs, chapter 4, pages 47–71. American Geophysical Union.

Fuhrhop, R., Simmer, C., Schrader, M., Heygster, G., Johnsen, K.-P., and SchÃijssel, P. (1997). Study of Passive Remote Sensing of the Atmosphere and the Surface Ice. Technical Report 297, Institute for Marine Science, Christian Albrechts University, Duestenbrooker Weg 20 D-24105 Germany.

Fung, A. K. (1994). *Microwave Scattering and Emission Models and Their Applications*. Artec House, Norwood MA.

Golden, K. (1995). Bounds on the complex permittivity of sea ice. *Journal of Geophysical Research*, 100(C7):13699–13711.

Golden, K. and Papanicolaou, G. (1983). Bounds for Effective Parameters of Heterogeneous Media by Analytic Continuation. *Communications in Mathematical Physics*, 90:473–491.

Golden, K. M., Borup, D., Cheney, M., Cherkaeva, E., Dawson, M. S., Ding, K.-H., iand D. Isaacson, A. K. F., Johnson, A., Jordan, A. K., Kong, J. A., Kwok, R., Nghiem, S. V., Onstott, R. G., Sylvester, J., Winebrenner, D. P., and Zabel, I. H. H. (1998a). Inverse Electromagnetic Scattering Models for Sea Ice. *IEEE Transactions on Geoscience and Remote Sensing*, 36(5):1642–1654.

Golden, K. M., Cheney, M., Ding, K.-H., Fung, A. K., Grenfell, T. C., Isaacson, D., Kong, J. A., Nghiem, S. V., Sylvester, J., and Winebrenner, D. P. (1998b). Forward Electromagnetic Scattering Models for Sea Ice. *IEEE Transactions on Geoscience and Remote Sensing*, 36(5):1642–1654.

Gouretski, V. V. and Koltermann, K. P. (2004). Woce global hydrographic climatology. Technical Report 35/2004, Berichte des Bundesamt fur Seeschifffart und Hydrographie (BSH), Hamburg and Rostock, Germany.

Grandell, J., Johannessen, J. A., and Hallikainen, M. T. (1999). Development of a Synergetic Sea Ice Retrieval Method for the ERS-1 AMI Wind Scatterometer and SSM/I Radiometer. *IEEE Transactions on Geoscience and Remote Sensing*, 37(2):668–679.

Granskog, M., Kaartokallio, H., Kuosa, H., Thomas, D. N., and Vainio, J. (2006). Sea ice in the Baltic Sea–A review. *Estuarine, Coastal and Shelf Science*, 70:145–160.

Granskog, M. A., Leppäranta, M., Kawamura, T., Ehn, J., and Shirasawa, K. (2004). Seasonal development of the properties and composition of landfast sea ice in the gulf of finland, the baltic sea. *Journal of Geophysical Research*, 109(C2). C02020, doi:10.1029/2003JC001874.

Grenfell, T. C., Barber, D. G., Fung, A. K., Gow, A. J., Jezek, K. C., Knapp, E. J., Nghiem, S. V., Onstott, R. G., Perovich, D. K., Roesler, C. S., Swift, C. T., and Tanis, F. (1998). Evolution of Electromagnetic Signatures of Sea Ice from Initial Formation to the Establishment of Thick First-Year Ice. *IEEE Transactions on Geoscience and Remote Sensing*, 36(5):1642–1654.

Grenfell, T. C., Comiso, J. C., Lange, M. A., Eicken, H., and Wensnahan, M. (1994). Passive microwave observationsof the weddell sea during austral winter and early spring. *Journal of Geophysical Research*, 99(C5):9995–10010.

Hallikainen, M. and Winebrenner, D. P. (1992). The physical basis for sea ice remote sensing. In Carsey, F. D., editor, *Microwave remote sensing of sea ice*, volume 68 of *Geophysical monographs*, pages 29–46. American Geophysical Union, Washington DC.

Hendricks, S. and Haas, C. (2008). SMOS Sea Ice Validation WP 2.2: Ice Thickness Deliverable Report. Technical report, Alfred Wegener Institute for Polar and Marine Research, Bremerhaven, Germany.

Hewison, T. J. and English, S. J. (1999). Airborne Retrievals of Snow and Ice Surface Emissivity at Millimeter Wavelengths. *IEEE Transactions on Geoscience and Remote Sensing*, 37(4):1871–1879.

Heygster, G. and Melsheimer, C. (2008). Retrieval of Sea Ice Emissivity and Integrated Retrieval of Surface and Atmospheric Parameters over the Arctic from AMR-E Data. Technical report, University of Bremen. Part of final report to JAXA AMSR-E 3rd Research Announcement.

Heygster, G., Wiebe, H., Spreen, G., and Kaleschke, L. (2008). AMSR-E Geolocation and Validation of Sea Ice Concentrations based on 89 GHz Data. *IEEE Transactions on Geoscience and Remote Sensing*. submitted.

Hoekstra, P. and Cappillino, P. (1971). Dielectric Properties of Sea and Sodium Chloride Ice at UHF and Microwave Frequencies. *Journal of Geophysical Research*, 76(20):4922–4931.

Hwang, B. J., Ehn, J. K., and Barber, D. G. (2006). Relationships between albedo and microwave emissions over thin newly formed sea ice during fall freeze-up. *Geophysical Research Letters*, 33(L17503).

Hwang, B. J., Ehn, J. K., Barber, D. G., Galley, R., and Grenfell, T. C. (2007). Investigations of newly formed sea ice in the Cape Bathurst polynya: 2. Microwave emission. *Journal of Geophysical Research*, 112(C05003).

Jackson, T. J., Hsu, A. Y., van de Griend, A., and Eagleman, J. R. (2002). Skylab L band Microwave Radiometer Observations of Soil Moisture Revisited. In *IEEE International Geoscience and Remote Sensing Symposium Proceedings*.

Johnsen, K.-P. (1998). *Radiometrische Messungen im arktischen Ozean–Vergleich von Theorie und Experiment*. PhD thesis, Universitaet Bremen, Otto-Hahn Allee 1, Bremen, Germany.

Jordan, R. (1991). A one-dimensional temperature model for a snow cover. Technical Report SP 91-16, CRREL.

Kerr, Y. H. (1998). Soil Moisture and Ocean Salinity: Radiometry applied to soil Moisture and Salinity Measurements. Technical report, CESBIO, 18 Avenue Edouard Belin 31401 Toulouse Cedex 4, France. The Living Planet Programme Earth Explorer Missions.

Klein, L. and Swift, C. (1976). An improved model for the dielectric constant of sea water at microwave frequencies. *IEEEJOE*, OE-2(1):104–111.

Klein, M. (2002). Meltpond 2000 PSR Processing–Final Report. Technical report, NASA Goddard Space Flight Center, Greenbelt, MD 20771-001 USA.

Klein, M., Gasiewski, A. J., Schuler, K., Cavalieri, D., Markus, T., and Yevgrafov, A. (2001). Sea Ice Brightness Imagery Observed During the Meltpond 2000 Experiment. In *IEEE International Geoscience and Remote Sensing Symposium Proceedings*. American Geophysical Union.

Koehl, A. and Stammer, D. (2008). Decadal sea level changes in the 50-year gecco ocean synthesis. *Journal of Climate*, 21:1876–1890.

Kwok, R., Comiso, J., Martin, S., and Drucker, R. (2007). Ross Sea polynyas: Response of ice concentration retrievals to large areas of thin ice. *Journal of Geophysical Research*, 112(C12012).

Kwok, R. and Cunningham, G. (2002). Seasonal ice area and volume production of the Arctic Ocean: November 1996 through April 1997. *Journal of Geophysical Research*, 107(C10).

Langlois, A., Barber, D., and Hwang, B. (2007). Development of a winter snow water equivalent algorithm using in situ passive microwave radiometry over snow-covered first-year sea ice. *Remote Sensing of Environment*, 106:75–88.

Leppäranta, M. and Manninen, T. (1988). The brine and gas contents of sea ice with attention to low salinities and high temperatures. Internal Report 2, Finnish Institute of Marine Research.

Liu, Q., Simmer, C., and Ruprecht, E. (1998). Monte Carlo simulations of the microwave emissivity of the sea surface. *Journal of Geophysical Research*, 103(C11):24983–24989.

Locarnini, R. A., Mishonov, A. V., Antonov, J. I., Boyer, T. P., and Garcia, H. E. (2005). Temperature. In *World Ocean Atlas 2005*, volume 1. U.S. Government Printing Office, Washington, D.C.

Maetzler, C. (1982). Microwave Signatures of Young Sea Ice and Its Influence on Ice Concentration Algorithms. In Laidet, L., editor, *Actes du Symposium International de la Commission VII de la Societe Internationale de Photogrammetrie et Teledetection*, pages 757–765, GDTA 18, avenue Ed. Belin 31055 Toulouse Cedex, France. International Society for Photogrammetry and Remote Sensing.

Maetzler, C. (1997). Autocorrelation functions of granular media with free arrangement of spheres, spherical shells or ellipsoids. *Journal of Applied Physics*, 81(3).

Maetzler, C. (1998). Improved born approximation for scattering of radiation in a granular medium. *Journal of Applied Physics*, 83(11).

Maetzler, C. (2001). Applications of smos over terrestrial ice and snow. In *Proceedings, 3rd SMOS Workshop*, DLR, Oberpfaffenhofen, Germany.

Maetzler, C., editor (2006). *Thermal Microwave Radiation: Applications for Remote Sensing*. The Institution of Engineering and Technology.

Maksym, T. and Markus, T. (2008). Antarctic sea ice thickness and snow-to-ice conversion from atmospheric reanalysis and passive microwave snow depth. *Journal of Geophysical Research*, 113(C02S12).

Markus, T. and Cavalieri, D. J. (2000). An Enhancement of the NASA Team Sea Ice Algorithm. *IEEE Transactions on Geoscience and Remote Sensing*, 38(3):1387–1398.

Martin, S., Drucker, R., Kwok, R., and Holt, B. (2004). Estimation of the thin ice thickness and heat flux for the Chukchi Sea Alaskan coast polynya from Special Sensor Microwave Imager data, 1990-2001. *Journal of Geophysical Research*, 109(C10012).

Martin, S., Drucker, R., Kwok, R., and Holt, B. (2005). Improvements in the estimates of ice thickness and production in the Chukchi Sea polynyas derived from AMSR-E. *Geophysical Research Letters*, 32(L05505).

Mathew, N. (2007). *Retrieval of Surface Emissivity of Sea Ice and Temperature Profiles over Sea Ice from Passive Microwave Radiometers*. PhD thesis, University of Bremen, Otto-Hahn Allee 1, Bremen, Germany.

Maykut, G., Grenfell, T., and Weeks, W. (1992). On estimating spatial and temporal variations in the properties of ice in the polar oceans. *Journal of Marine Systems*, 3:41–72.

Menashi, J. D., St. Germain, K. M., Swift, C. T., Comiso, J. C., and Lohanick, A. W. (1993). Low-frequency passive-microwave observations of sea ice in the weddell sea. *Journal of Geophysical Research*, 98(C12):22569–22577.

Nakawo, M. and Sinha, N. K. (1981). Growth rate and salinity profile of first-year sea ice in the high arctic. *Journal of Glaciology*, 27(96):315–330.

Naoki, K., Ukita, J., Nishio, F., Nakayama, M., Comiso, J. C., and Gasiewski, A. (2008). Thin sea ice thickness as inferred from passive microwave and in situ observations. *Journal of Geophysical Research*, 113(C02S16).

Narvekar, P. S., Heygster, G., and Tonboe, R. (2008). Analysis of windsat data over arctic sea ice. Technical report, EUMETSAT.

Notz, D., Wettlaufer, J. S., and Worster, M. G. (2005). A non-destructive method for measuring the salinity and solid fraction of growing sea ice in situ. *J. Glac.*, 51(172):159–166.

Press, W. H., Teukolsky, S. A., Vetterling, W. T., and Flannery, B. P. (1992). *Numerical Recipes in C*. Cambridge University Press, second edition.

Remund, Q. P., Long, D. G., and Drinkwater, M. R. (2000). An Iterative Approach to Multisensor Sea Ice Classification. *IEEE Transactions on Geoscience and Remote Sensing*, 38(4):1843–1856.

Reul, N. and Chapron, P. (2001). SMOS-Salinity Data Processing Study: Improvements in Emissivity Models. Technical Report WP 1100, CLS/IFREMER/NERSC. ESA contract N 15165/01/NL/SF.

Reul, N., Tenerelli, J., Chapron, B., and Waldteufel, P. (2008). Modeling sun glitter at l-band for sea surface salinity remote sensing with smos. *TGRS*, 45(7):2073–2087.

Rotboll, J., Sobjaerk, S. S., and Skou, N. (2003). A novel l-band polarimetric radiometer featuring subharmonic sampling. *Radio Sci.*, 38(3):DOI:10.1029/2002RS002666.

Ruf, C. (2000). Detection of calibration drifts in spaceborne microwave radiometers using a vicarious cold reference. *IEEE Transaction on Geoscience and Remote Sensing*, 38(1):44–52.

Schanda, E. (1987). Microwave modelling of snow and soil. *Journal of Electromagnetic Waves and Applications*, 1(1):1–24.

Serra, N. and et al. (2009). On the low-frequency phase relation between the denmark strait and the faroe-shetland channel dense overflows. to be submitted.

Shokr, M. E. (1998). Field Observations and Model Calculations of Dielectric Properties of Arctic Sea Ice in the Microwave C-Band. *IEEE Transactions on Geoscience and Remote Sensing*, 36(2):463–478.

Sihvola, A. H. and au Kong, J. (1988). Effective Permittivity of Dielectric Mixtures. *IEEE Transactions on Geoscience and Remote Sensing*, 26(4).

Skou, N., Sobjaerg, S. S., and Balling, J. (2007). EMIRAD-2 and its use in the CoSMOS Campaigns. Technical Report ESTEC Contract No. 18924/05/NL/FF, Electromagnetic Systems Section, Danish National Space Center, Technical University of Denmark.

Spreen, G., Kaleschke, L., and 2008, G. H. (2008). Sea ice remote sensing using AMSR-E 89 ghz channels. *Journal of Geophysical Research*, 113(C02S03).

St. Germain, K. M., Swift, C. T., and Grenfell, T. C. (1993). "determination of di-electric constant of young ice using microwave spectral radiometry". *Journal of Geophysical Research*, 98(C3):4675–4679.

Stogryn, A. (1985). Strong fluctuation theory for moist granular media. *IEEE Transactions on Geoscience and Remote Sensing*, GE-23(2):78–83.

Stogryn, A. (1986). A study of microwave brightness temperatures of snow from the point of view of strong fluctuation theory. *IEEE Transactions on Geoscience and Remote Sensing*, GE-24(2):220–231.

Svendsen, E., Maetzler, C., and Grenfell, T. C. (1987). A model for retrieving total sea ice concentration from a spaceborne dual-polarized passive microwave instrument operating at near 90 GHz. *International Journal of Remote Sensing*, 8(10):1479–1487.

Swift, C. T. (1980). Passive microwave remote sensing of the ocean – a review. *Bound. Lay. Meteorol.*, 18:25–40.

Tang, S., Qin, D., Ren, J., Kang, J., and Li, Z. (2007). Structure, salinity and isotopic composition of multi-year landfast sea ice in Nella Fjord, Antarctica. *Cold Regions Science and Technology*, 49:170–177.

Tedesco, M., Kim, E. J., England, A. W., Roo, R. D., and Hardy, J. P. (2006). Intercomparison of Electromagnetic Models for Passive Microwave Remote Sensing of Snow. *IEEE Transactions on Geoscience and Remote Sensing*, 44(10).

Tenerelli, J., Reul, N., Mouche, A. A., and Chapron, B. (2008). Earth-Viewing L-Band Radiometer Sensing of Sea Surface Scattered Celestial Sky Radiation - Part i:General Characteristics. *TGRS*, 46(3):659–674.

Thomas, M., Geiger, C., and Kambhamettu, C. (2008). High resolutions (400 m) motion characterization of sea ice using ERS-1 SAR imagery. *Cold Regions Science and Technology*. in press.

Tonboe, R., Andersen, S., and Heygster, G. (2006a). A 'first look' at the thermal microwave polarimetric signature of sea ice. In *MicroRad'06, 9th Specialist Meeting on Microwave Radiometry and Remote Sensing Applications*, San Juan, Puerto Rico.

Tonboe, R. T. (2005). A mass and thermodynamic model for sea ice. Technical Report SR05-10, Danish Meteorological Institute.

Tonboe, R. T., Heygster, G., Pedersen, L. T., and Andersen, S. (2006b). Sea ice emission modelling. In Maetzler, C., editor, *Thermal Microwave Radiation: Applications for remote sensing*, volume 52 of *Electromagnetic Wave series*, pages 382–400. IET, London.

Tucker, W. B., Perovich, D. K., Gow, A. J., Weeks, W. F., and Drinkwater, M. R. (1992). Physical Properties of Sea Ice Relevant to Remote Sensing. In *Microwave Remote Sensing of Sea Ice*, number 68 in Geophysical Monographs, chapter 2, pages 9–28. American Geophysical Union.

Ulaby, F. T., Moore, R. K., and Fung, A. K. (1981). *Microwave remote sensing, active and passive. Volume I: Fundamentals and Radiometry*. Addison Wesley Pub., London, U.K.

Ulaby, F. T., Moore, R. K., and Fung, A. K., editors (1986). *Microwave Remote Sensing: Active and Passive, Volume III, From Theory to Applications*. Artech House, Norwood, MA.

Vancoppenolle, M., Bitz, C. M., and Fichefet, T. (2007). Summer landfast sea ice desalination at Point Barrow, Alaska: Modeling and observations. *Journal of Geophysical Research*, 112(C04022).

Vant, M. R., Ramseier, R. O., and Makios, V. (1978). The complex-dielectric constant of sea ice at frequencies in the range 0.1-40 ghz. *Journal of Applied Physics*, 49(3):1264–1280.

Warren, S. G., Rigor, I. G., Untersteiner, N., Radionov, V. F., Bryazgin, N. N., Aleksandrov, Y. I., and Colony, R. (1999). Snow depth on arctic sea ice. *Journal of Climate*, 12:1814–1829.

Weeks, W. F. and Ackley, S. F. (1985). *The Geophysics of Sea Ice*, volume 146 of *NATO ASI Series B: Physics*, chapter 2. Plenum Press.

Wensnahan, M., Maykut, G. A., Grenfell, T. C., and Winebrenner, D. P. (1993). Passive microwave remote sensing of thin sea ice using principal component analysis. *Journal of Geophysical Research*, 98(C7):12453–12468.

Wiesmann, A., Fierz, C., and Mätzler, C. (2000). Simulation of microwave emission from physically modelled snowpacks. *Annals of Glaciology*, 31:397–405.

Wiesmann, A. and Maetzler, C. (1999). Technical Documentation and Program Listings for MEMLS 99.1, Microwave Emission Model of Layered Snowpacks. Technical report, Institute of Applied Physics, University of Bern, Sidlerstr. 5 CH-3012 Bern, Switzerland.

Wiesmann, A. and Mätzler, C. (1999). Microwave emission model for layered snowpacks. *Remote sensing of environment*, 70:307–316.

Wiesmann, A., Mätzler, C., and Weise, T. (1998). Radiometric and structural measurements of snow samples. *Radio Science*, 33(2):273–289.

Winebrenner, D. P., Bredow, J., Fung, A. K., Drinkwater, M. R., Nghiem, S., Gow, A. J., Perovich, D. K., Grenfell, T. C., Han, H. C., Kong, J. A., Lee, J. K., Mudaliar, S., Onstott, R. G., Tsang, L., and West, R. D. (1992). Microwave Sea Ice Signature Modelling. In *Microwave Remote Sensing of Sea Ice*, number 68 in Geophysical Monographs, chapter 8, pages 137–175. American Geophysical Union.

Xu, P., Tsang, L., and Chen, K. S. (2007). Emissivities of Rough Surface over Layered Media in Microwave Remote Sensing of Snow. In *Proceedings of the International Conference on Geoscience and Remote Sensing, Summer 2007*.

Yu, Y. and Lindsay, R. W. (2003). Comparison of thin ice thickness derived from RADARSAT Geophysical Processor System and Advanced Very High Resolution Radiometer data sets. *Journal of Geophysical Research*, 108(C12).